



HAL
open science

Quantum transport in novel superconducting hybrid junctions based on germanium nanowire heterostructures

Jovian Delaforce

► **To cite this version:**

Jovian Delaforce. Quantum transport in novel superconducting hybrid junctions based on germanium nanowire heterostructures. Materials Science [cond-mat.mtrl-sci]. Université Grenoble Alpes [2020-..], 2022. English. NNT : 2022GRALY009 . tel-03817688

HAL Id: tel-03817688

<https://theses.hal.science/tel-03817688>

Submitted on 17 Oct 2022

HAL is a multi-disciplinary open access archive for the deposit and dissemination of scientific research documents, whether they are published or not. The documents may come from teaching and research institutions in France or abroad, or from public or private research centers.

L'archive ouverte pluridisciplinaire **HAL**, est destinée au dépôt et à la diffusion de documents scientifiques de niveau recherche, publiés ou non, émanant des établissements d'enseignement et de recherche français ou étrangers, des laboratoires publics ou privés.

THÈSE

Pour obtenir le grade de

DOCTEUR DE L'UNIVERSITÉ GRENOBLE ALPES

Spécialité : **NANOPHYSIQUE**

Arrêté ministériel : 25 mai 2016

Présentée par

Jovian DELAFORCE

Thèse dirigée par **Olivier BUISSON**, Directeur de recherche,
Université Grenoble Alpes
et co-encadrée par **Cécile NAUD**, Chargé de recherche,
Université Grenoble Alpes

préparée au sein de l'**Institut Néel, CNRS**
dans l'**École Doctorale de Physique**

**Transport quantique dans des
jonctions hybrides superconductrices
à base d'hétérostructures dans des
nanofils de germanium**

**Quantum transport in novel
superconducting hybrid junctions
based on germanium nanowire
heterostructures**

Thèse soutenue publiquement le **4 février 2022**,
devant le jury composé de :

Madame Hélène BOUCHIAT

Directrice de recherche, Laboratoire de Physique des Solides,
Rapporteuse

Monsieur Georgios KATSAROS

Professeur Assistant, Institute of Science and Technology, Austria,
Rapporteur

Madame Julia MEYER

Professeur, Université Grenoble Alpes, Présidente

Monsieur Jesper NYGÅRD

Professeur, University of Copenhagen, Examineur

Monsieur Jean-Damien PILLET

Professeur Assistant, École Polytechnique, Examineur

Madame Cécile NAUD

Chargé de recherche, Institut Néel, Co-directeur de thèse

Monsieur Olivier Buisson

Directeur de recherche, Institut Néel, Directeur de thèse



Acknowledgements

My PhD journey of nearly four years took me through so many emotions. I have learnt to enjoy the moments of pleasure and push through the difficulties. These four years, have been awesome. Awesome, in the sense of a life changing, all encompassing and unbeatable experience.

Now I have the opportunity to acknowledge and say thank you. But, where does one begin. One doesn't often get the privilege to publish their gratitude. And this is my first time. So here we go...

It is said that a community raises a child. I wholeheartedly agree, for I could not be here, at the end of this awesome journey, without the love and support provided by family, friends, teachers, colleagues and many others.

Whether you are mentioned or not in the following text, if you have offered friendship, love or even just a laugh, then please accept my gratitude. I hope you know who you are.

I would first like to thank the members of the jury. Thank you Dr H el ene Bouchiat and Dr Georgios Katsaros for accepting to be *rapporteurs* of my thesis. Thank you Prof. Julia Meyer, Prof. Jesper Nyg ard and Dr. Jean-Damien Pillet for accepting to be *examineurs* of my thesis.

Doing a PhD at Institut N el is a great privilege. The fantastic technical, engineering and administrative staff provide great support, helping me to overcome many issues. Special thanks to Ang elique Simoes and Otmane Benhamed and Florence Pois for your support in all things that are the French state and one of its organs, the CNRS.

Of course the joys of N el life are made possible by the wonderful students, post-docs and researchers that bunker down in the labs and at times walk the corridors. Thank you to you all for making my N el experience memorable. Thank you to my office mate, J er mie. I enjoyed our varied discussions and fan optimisation. Thank you for the afternoon football matches and the great hikes at Les Houches.

Scientific research is now rarely achieved by a lone figure in their laboratory. It requires collaboration and open discussion. The research presented in this thesis is a result of successful collaboration. It was a great privilege to be apart of the germanium nanowire team. This collaboration between groups in Vienna and Grenoble included many. I would like to thank Roman Kramer, Martien den Hertog, and Alois Lugstein for their great support and collaboration during this project.

A special mention and thank you goes to Masiar Sistani, the clean room wizard. None of these results could be possible without you and your exceptional devices. It was a pleasure to share those weeks of intense but rewarding measurements with you, thank you. I look forward to seeing your further advances with aluminium-germanium heterostructures.

The lab. The team. The circuiteers. A place where colleagues became friends. A

team whose uplifting chats over lunch at H2 mark a joyful break in the day. There is much thanks to give. Thanks for your patience, to wait for me as I finished my lunch. As many of you are aware, eating and talking are my two favourite pastimes.

During my PhD, many students have passed through the superconducting circuits group. I have enjoyed working and discussing with you all, past and present. You have all added a special touch to my PhD experience. Javier and Rémy, as members of the old guard, you gave me a warm welcome on my arrival. Rémy, thank you for the great games of table tennis under the shadow of Mount Blanc. Karthik, it was a pleasure to share the experimental room with you. It was good to know there was some cricket love in the team. Maybe one day we will hit the nets! Vladimir, we began our PhDs two weeks apart. I am pleased that I could share the journey with you. Thank you for your fiercely independent character and your fantastic and entertaining stories. Gonzalo, it was fun to share an office with you in the first months of my PhD. I am grateful for your kind invitation to join your friends at Le Tonneau de Diogène for a beer one Tuesday night in May. For that was the night I met Suzy. Arpit, thank you for the interesting and frank political discussions over coffee/tea or beers. I am sure we will find each other at The Family's Pub. Kazi, thank you for the great evening chats and laughs in our shared office. Your acceptance of my de-stressing techniques after a long week was greatly appreciated. Be careful of the Sinnerman!! Thibault, thank you for sharing your diverse language skills. In particular, your Gaelic. You're ready for Ireland! Dorian, thank you for the stimulating conversations about your many mountain adventures. Your stories gave me a taste of climbing, while maintaining my feet firmly on the ground. Martina, thank you for your sense of humour and your tolerance of my special carbonara. To the recent arrivals, Samuel, Cyril, Nicolo and Giulio, it was a pleasure to have the opportunity get to know you in my final months. Samuel, thank you for introducing me to the funny but dangerous game of chifouséche. Don't worry, I am aware of our bet.

Sébastien and Luca. Your importance in my PhD journey is impossible to overstate. Four years ago we became colleagues and now you have become my lifelong friends. Thank you for being you. Thank you for keeping me sane during the six month Covid winter. P.S. We still have not finished Pirates of the Caribbean.

A lab team is developed and nurtured by its research directors. Olivier Buisson, Nicolas Roch, Wiebke Hasch and Cécile Naud have built a laboratory atmosphere that is inclusive, intellectually stimulating and above all, enjoyable. Thank you for welcoming me into this special team. Cécile, thank you for being a supportive co-supervisor. I greatly appreciated your support and feedback, especially during the writing of this manuscript. You brought greater clarity to this manuscript by pointing out my missing commas.

Olivier, I will be forever grateful that you provided me with the opportunity to complete a PhD in a great lab with fantastic people. The opportunity turned into an awesome experience. Thank you. Thank you for your enthusiastic interest in not only my scientific endeavours but also in my personal well-being and growth. Thank you for being an incredible person and a great supervisor.

I experienced so many emotions in the lab. From stress and frustration to relief, joy and laughter. However, I will always remember the feeling of comfort. The lab was my first community away from home. The comfort and homeliness that I felt has been the foundation of my awesome PhD experience. It has been the rock from which I have built my life in Grenoble. The city, which I now call home.

Thank you to my friends from Australia to Northern Ireland and inbetween. Though our conversations were infrequent, knowing that you will be there for a chat and a laugh has brought me great comfort over these years. Thank you to the friends and family who visited me in Grenoble. It was fun showing you around my new home.

Anissa, you were there from the very beginning. You picked me up from the airport and we managed to put my suitcases and bicycle into your little citroën. Thank you so much for your generosity and company.

Over the years in Grenoble I have made good friends. Thank you to the *Pétanque Tour* for the splendid evenings of coinche, pétanque and other activities. Let your hairs grow long and beautiful! Romy, thank you for entertaining me with you epic goals in Rocket League. Pap, thank you for the intense games of Warzone and resistance. Thank you to the *PsychoPots* for your enthusiasm to party. Thank you to all those who have helped me build a community outside the lab. I am truly thankful for the love, support and entertainment you have offered me.

Suzy, we met at the beginning of my PhD journey and you have been in my life ever since. Your presence has been so important to me. Thank you. Thank you for the many lovely evenings spent together. Where we listen, joke and laugh. These evenings, which sometimes led onto weekends were an essential distraction from my thesis. Merci à la famille de Suzy, ma famille adoptive. Merci pour les superbes déjeuners en famille. Vous m'avez fait me sentir chez moi. With lots of love, thank you Suzy. Our journey together has just begun

Finally, my dear family, Michelle, Walter and Orlanda. Your unequivocal love and support has been fundamental to the success of this journey, thank you.

Contents

1	INTRODUCTION & SUMMARY	1
1.1	Introduction	1
1.2	Summary	3
1.2.1	Fabrication	3
1.2.2	Transport Properties (Al-Ge-Al)	5
1.2.3	Transport Properties (Al-Ge/Si-Al core/shell)	11
2	THEORETICAL CONCEPTS	15
2.1	Introduction to charge transport	16
2.1.1	Drude Model	16
2.1.2	Free electron Model	17
2.1.3	Bloch's Theorem	20
2.2	Transport in nanowires	25
2.2.1	Coherent ballistic conductor	25
2.2.2	Conductance quantisation	26
2.3	Transport in quantum dots	29
2.3.1	Tunnel junctions	30
2.3.2	The constant interaction model	30
2.3.3	Case of zero-bias (Coulomb oscillations)	33
2.3.4	Case of varying V_G and V_{SD} (Coulomb Diamonds)	34
2.4	Superconductivity	38
2.5	Superconducting Junctions	42
2.5.1	Proximity Effect	42
2.5.2	Microscopic description of the proximity effect	43
2.5.3	Superconducting-normal junctions (S-N-S)	45
2.5.4	Superconducting Quantum Dot Junctions (S-QD-S)	55
3	FABRICATION	67
3.1	Superconducting quantum devices: Architectures and their challenges	68
3.2	Nanowire Growth Using VLS Growth	69
3.2.1	Intrinsic Germanium Nanowires	70
3.2.2	Germanium-Silicon core-shell nanowires	71
3.3	Field Effect Transistor FET	72
3.4	Diffusion through Thermal Annealing	75
3.5	Interface Quality	78
3.5.1	i-Ge Interface	78
3.5.2	Ge/Si core/shell Interface	78
3.6	Conclusion	79

4	EXPERIMENTAL SET-UP	81
4.1	Cryogenics	82
4.2	Le Fridge: Table-top pumped helium-3 cryostat	82
4.2.1	Advantages & Disadvantages	83
4.2.2	Cool-down procedure	84
4.2.3	Reducing cool-down time: Exchange Gas	86
4.2.4	Stabilising ^4He flow	86
4.3	Measurement Set-up	90
4.3.1	Electronic measurements	90
4.3.2	Thermalisation & Filtering	94
4.4	Performing Measurements & Data Processing	95
4.4.1	LabView Measurement Program	95
4.4.2	Measurement Feedback	97
4.4.3	Data Correction	97
4.5	Sample Installation	98
5	TRANSPORT PROPERTIES OF AL-GE-AL NANOWIRE HETEROSTRUCTURES	101
5.1	Al-Ge-Al heterojunction: A back-to-back Schottky diode	102
5.1.1	Schottky-Mott rule	102
5.1.2	Surface States	104
5.1.3	Charge transport through a Schottky barrier	106
5.1.4	Modeling Al-Ge-Al as a back-to-back Schottky diode	108
5.1.5	Quantum dot formation	110
5.2	Transport properties at high temperature	111
5.2.1	Long vs short Ge segment lengths	111
5.2.2	Temperature dependence on Al-Ge-Al transport ($G-V_G$)	113
5.3	Transport Overview at 400 mK	116
5.4	Coulomb Blockade	120
5.4.1	Addition Energy	124
5.4.2	Odd-even filling effect	127
5.4.3	Excited charge state resonant tunneling	128
5.4.4	Temperature evolution of Coulomb blockade	128
5.4.5	Coulomb blockade with superconducting leads	130
5.5	Supercurrent Regime	132
5.5.1	Multiple Andreev Reflection (MAR)	132
5.5.2	Supercurrent	139
5.6	Intermediate Regime	142
5.7	Sub-gap features in the Coulomb blockade regime	145
5.8	Conclusion	147
6	TRANSPORT PROPERTIES OF AL-GE/SI-AL CORE/SHELL NANOWIRE HETEROSTRUCTURES	151
6.1	Introduction	152
6.2	Transport Overview	152
6.3	Quantised Conductance	154
6.4	Low Conductance Regime	158
6.5	High Conductance Regime	159
6.6	Conclusion	164

7	CONCLUSION & PERSPECTIVES	167
	7.1 Conclusion	167
	7.2 Perspectives	168
	APPENDICES	171
A	INTRODUCTION TO BCS THEORY	173
B	MEASUREMENT FEEDBACK AND DATA CORRECTION PROCEDURE	181
	B.1 Measurement Feedback	181
	B.2 Data Correction	181
C	USING THE MONTE CARLO FITTING PROGRAM	183
D	ARTICLE IN HIGHLIGHTS 2019	185
	BIBLIOGRAPHY	187

Introduction & Summary

1

1.1 Introduction

The rich physics and promising future as a quantum technology has lead to significant research focus on superconducting hybrid structures. Superconducting hybrid mesoscopic or nanoscopic devices consist of a superconductor (S) in contact with a non-superconducting material (X). The electronic pairs of the superconducting state strongly influences the properties of the non-superconducting materials that are in contact with the superconductor. This phenomenon, known as the proximity effect, is understood as superconducting electronic pairs propagating into the non-superconducting material and giving it superconducting-like properties. Over the recent decades different architectures of superconducting hybrid structures with a variety of materials have been considered theoretically and realised experimentally.

By building a superconducting hybrid junction consisting of two superconducting leads coupled together through a non-superconducting weak-link, abbreviated as S-X-S, the proximity effect can be exploited to induce supercurrent through the weak-link. The most well known superconducting junction is the Josephson tunnel junction, where the weak-link is an insulating layer. Josephson tunnel junctions are the building blocks of superconducting circuits and are employed in many quantum devices including superconducting quantum bits [1], quantum limited traveling wave parametric amplifiers [2] and superconducting quantum interference devices (SQUIDS). The weak-link can be achieved in a variety of ways beyond an insulating including using a normal metal [3], a semiconductor [4] or even a constriction of the superconductor [5] and more recently carbon nanotubes [6] and graphene [7]. By introducing a semiconductor as the weak-link, the extra degree of freedom provided by the tunability of the semiconductor's charge density up to a single charge state opens even further avenues of physical investigation and applications.

One application of superconducting-semiconducting hybrid junctions is the Josephson field effect transistor (JoFET) which was first proposed by T. D. Clark et al. in 1980 [8] a few decades after Josephson's pioneering work on the Josephson effect [9]. A JoFET behaves similarly to the Josephson tunnel junction (JJ) having a non-linear inductance and a Josephson current-phase relationship. However, a JoFET has an additional feature; the supercurrent through the junction can be tuned using an electrostatic field of a gate. This is equivalent to the way the current through a transistor can be tuned, hence the inclusion of field effect transistor in the JoFET's name. By

[Link back to Table of contents →](#)

employing a JoFET, instead of a JJ, in a transom architecture one can use an electrostatic field to tune the resonance frequency of the transom qubit [10]. Such a device is known as a gatemon and has been only recently realised [11, 12, 13, 14].

Other quantum systems, including Andreev spin qubits [15] have been realised using superconducting hybrid junctions. Further, more exotic architectures have been theoretically proposed such as topologically protected quantum bits based on Majorana fermions or multi-terminal junctions.

The demand for qubit architectures is due to the attractive technological advancement that would be provided through effective quantum information processing (QIP) for which the qubit is the unit of information. QIP covers the domain where quantum entanglement is exploited to go beyond the limitations of classical computers [16].

Quantum simulation promises to solve the complex and computationally demanding many-body problems arising in physics and chemistry [17]. Experiments performed, in our group QuantECA, using Josephson junction chains coupled to a nonlinear oscillator has enabled the simulation of dissipation of a quantum system [18].

Potentially the most significant of the quantum information processing technologies is the quantum computer. The concept was first introduced by David Deutsch who developed a model of a universal quantum computer in 1985 [19] that could perfectly simulate any Turing machine, quantum computer or simulator. Quantum computing exploits the superposition of states in qubits to carry out computational processing in parallel, speeding up the processors considerably compared to the linear nature of current computer processing. Recently, claims of quantum supremacy, where a quantum processor outperforms a classical processor, have been published [20].

Though substantial progress in the realisation of quantum systems for QIP has been made since the first proposals at the end of the 20th century, considerable challenges must be overcome before the promised technological breakthroughs of QIP can be realised. Superconducting hybrid junctions could provide a solution to some of these challenges including reducing qubit relaxation and dephasing through topological protection, improved scalability through using electrically tuneable qubits and CMOS compatible materials and finally the development of alternative qubit architectures such as the Andreev spin qubit and Majorana qubits.

In this thesis, we investigate the low temperature transport properties of superconducting hybrid junctions with a nanowire architecture using germanium (Ge) for the semiconducting weak-link and aluminium (Al) for the superconducting leads. Ge is a group IV semiconductor that has a long history in experimental physics. Ge was used by J. Bardeen, W. Brattain and W. Shockley to demonstrate the first point-contact transistor in 1947. Their ground-breaking discovery was acknowledged by the Nobel committee who awarded them the 1956 Nobel Prize in Physics. Beyond its useful semiconducting properties, Ge has many advantageous properties for quantum devices. In particular, the strong spin-orbit coupling and strong g-factor make Ge attractive for topologically protected qubits and spin qubits. These important characteristics are further enhanced in Ge by the dominance of hole transport. Furthermore, Ge can be purified to reduce the presence of nuclear spins, which reduce spin qubit lifetimes. Importantly for scalability of quantum systems Ge is a CMOS compatible material, thus well established techniques from the microelectronic industry can be exploited. Finally, and crucially for this thesis Al and Ge are a diffusive match, which enables thermal diffusion to be exploited to reliably fabricate monolithic Al-Ge-Al nanowire heterostructures with unique high quality interfaces.

Ge is predominantly integrated with Si in the form of Ge/Si core/shell NW junctions [21, 22, 23, 24] or Ge hut wires [25] with Si caps and Ge/Si planar junctions [26, 27, 28]. However, the adoption of intrinsic Ge (i-Ge) NWs for the development of quantum devices, including superconducting hybrid junctions, has been limited. The lack of adoption is mainly associated with the difficulty in overcoming the metal-Ge Schottky barrier, which can prevent proximity induced supercurrent. Overcoming the Schottky barrier requires the fabrication of high quality electrical contacts to Ge nanostructures while simultaneously reducing the gate screening effect of the leads [29, 30]. This tremendous challenge has been recently achieved through intense research on the thermal diffusion of metals into semiconducting NWs, by our close collaborators [31, 32, 33]. The absence of an intermetallic phase formation and compatible diffusion rates between Al-Ge have been exploited extensively to form true metal-Ge heterostructures with abrupt interfaces [34] leading to the formation of self-aligned monocrystalline Al NWs contacting the monolithically integrated Ge QD.

1.2 Summary

This thesis will document our investigations of the low temperature transport properties of monolithic Al-Ge-Al nanowire heterostructures with different Ge segment lengths. We will also compare these novel i-Ge devices to the familiar Ge/Si core/shell NWs, which are employed in quantum devices by multiple research groups. By using a near identical fabrication technique for both Al-Ge-Al and Al-Ge/Si-Al core/shell devices we can truly compare their transport similarities and differences. The following is a summary that outlines the important aspects and results of this thesis.

Chapter 2 introduces the important theoretical concepts required to understand and appreciate the results of this thesis.

1.2.1 Fabrication

The Al-Ge-Al and Al-Ge/Si-Al core/shell nanowire heterostructure studied in this thesis were fabricated by our collaborators, Masiar Sistani and Alois Lugstein, at TU Wien in Vienna. Using a novel thermal annealing technique, which induced the exchange of Ge and Al through diffusion, our collaborators could fabricate monolithic Al-Ge-Al NW heterostructures with atomically precise interfaces. Figure 1.1 (a) shows a scanning electron microscope (SEM) image of an Al-Ge-Al NW heterostructure after the thermal annealing process. To enable investigations of their transport properties the NW heterostructures were integrated in a back-gated field effect transistor architecture. The exceptional results of this fabrication technique are evident; we clearly see the monolithic structure with a continuous NW consisting of two crystalline Al (c-Al) leads separated by a Ge segment. High-resolution high angle annular dark field (HAADF) scanning transmission electron microscopy (STEM) image of the Ge segment, shown in Figures 1.1 (b-c), reveals the uniform diameter and abrupt interface of the heterostructure. A zoom on the Al-Ge interface 1.1 (c) shows that the interface is nearly atomically sharp with the Ge lattice, orientated along the [110] direction, transitioning into c-Al in a single atomic layer. In the Fabrication chapter (Chapter 3) of this thesis, we will detail the fabrication process employed to achieve such high quality devices and discuss their structural characterisation carried out by our collaborators.

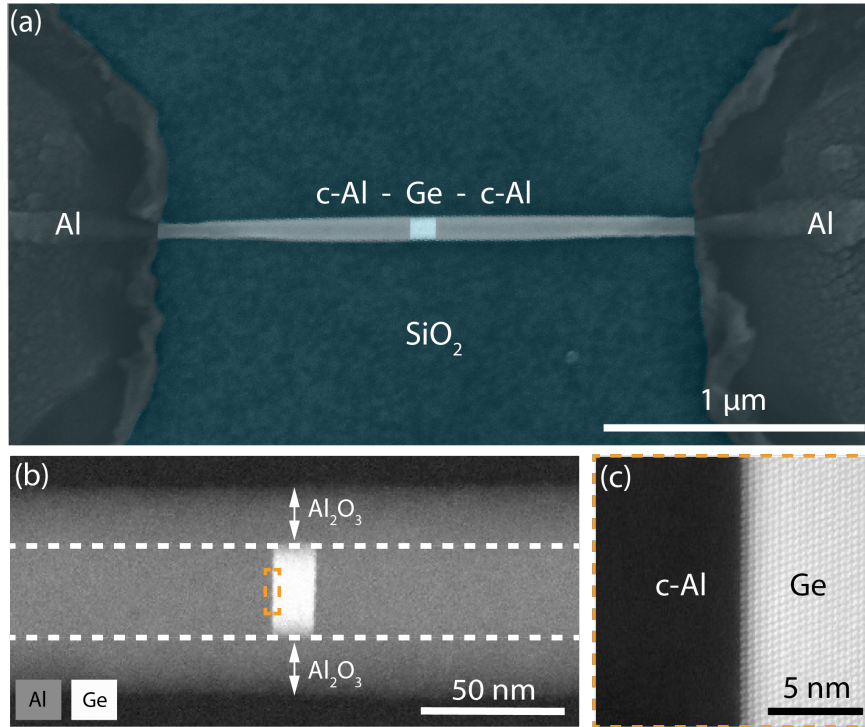


Figure 1.1 – (a) False color SEM image of an Al-Ge-Al NW heterostructure after the thermal annealing process. The NW is integrated in a back-gated field-effect transistor architecture. (b,c) High-resolution high angle annular dark field (HAADF) scanning transmission electron microscopy (STEM) image using a probe corrected FEI Titan Themis working at 200 kV of (b) a 15 nm long Ge segment embedded in an Al-Ge-Al NW heterostructure and (c) the abrupt Al-Ge interface of the Al-Ge-Al NW heterostructure orientated along the [110] direction.

To investigate the low temperature transport properties of Al-Ge-Al and Al-Ge/Si-Al core/shell nanowire heterostructures, we used a table-top pumped ^3He cryostat designed and built at Institut Néel. With a minimum working temperature of 350 mK, we could use the cryostat to investigate the influence of the superconducting c-Al leads on the NW transport. Further, these low working temperatures also enabled the investigation of the quantum transport properties of the Ge segment, including determining its quantum dot properties such as charging energy and mean-level spacing. The experimental set-up to realise these investigations is detailed in Chapter 4. As the first PhD student to carry out systematic and extensive measurements on the pumped ^3He cryostat, I present a detailed description of my optimal cool-down procedure that I have developed over the many cool-downs.

1.2.2 Transport Properties (Al-Ge-Al)

The results of the low temperature transport investigations are presented in detail in Chapter 5. We show that the high quality Al-Ge-Al and Al-Ge/Si-Al core/shell nanowire heterostructures shown through HAADF STEM and EDX analysis translates to rich transport physics that show quality interfaces. Our discussion will focus on three Al-Ge-Al nanowire heterostructures; one device which has a Ge segment length of $L_{\text{Ge}} \approx 162$ nm, labeled Sample L1 and two samples which are on the limits of the ballistic regime with L_{Ge} of 42 nm and 37 nm which are labeled Sample S1 and Sample S2, respectively.

Figure 1.2 (a-b) shows the differential conductance, in units of quantum conductance, versus bias voltage (V_{D}) of Sample S1 and S2 recorded at $T = 390$ mK and 410 mK respectively over an extended gate voltage (V_{G}) region. The plots reveal that the two devices display similar highly tuneable transport properties with four distinguishable regimes: 1) a full blockade regime for $V_{\text{G}} > 0.5$ V, 2) a CB regime from the first hole to a few tens of holes in the QD (-4.0 V $< V_{\text{G}} < 0.5$ V), 3) an intermediate regime with various sub-gap features (-15 V $< V_{\text{G}} < -4.0$ V) and 4) a supercurrent regime at very negative gate voltages. We also observe peaks in conductance due to Andreev reflections at $eV = 2\Delta/n$, where n is the order of reflection and $\Delta = 220$ μeV .

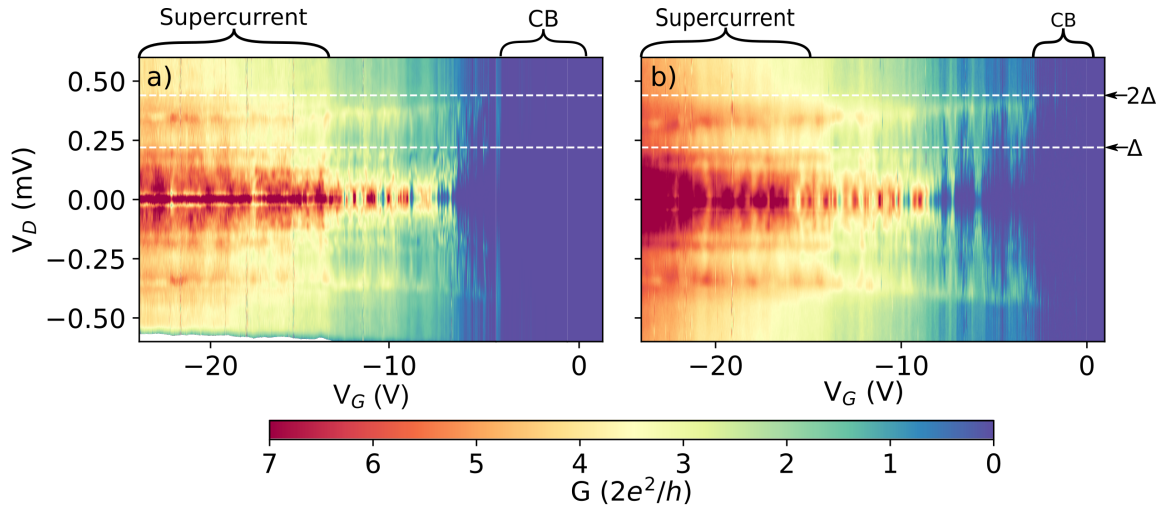


Figure 1.2 – **Transport Overview.** Density plot of differential conductance with respect to bias voltage V_{D} and gate voltage V_{G} of (a) Sample S1 recorded at 390 mK and (b) Sample S2 recorded at 410 mK. We observe four distinct regimes: A full blockade regime for $V_{\text{G}} > 0.5$ V. A Coulomb blockade regime (-4.0 V $< V_{\text{G}} < 0.5$ V), labeled an intermediate regime (-15 V $< V_{\text{G}} < -4.0$ V) and a supercurrent regime ($V_{\text{G}} < -15$ V), labeled. Horizontal dashed lines show the expected position ($eV_{\text{D}} = 2\Delta/n$) of the first two conductance peaks due to Andreev reflection for $\Delta = 220\mu\text{eV}$.

The high gate tuneability of the Al-Ge-Al nanowire heterostructures is evident by the multiple transport regimes observed in Figure 1.2. We associate this dynamic transport to the band structure of the Al-Ge-Al NW heterostructure. At the two Al-Ge interfaces, two Schottky barriers form back-to-back. However, in the Ge junction, the valence band (VB) is pinned close to the Fermi energy (E_{F}) of c-Al. This so

called Fermi level pinning results in a weak Schottky barrier for holes compared to a strong barrier for electrons. As such, hole states in the valence band dominate the transport. The valence band, forms a quantum dot (QD), where the tunnel barriers are defined by the back-to-back Schottky barriers. The QD hole states become available for resonance tunneling as VB is pushed above E_F by the electrostatic field of the back-gate V_G .

Coulomb Blockade

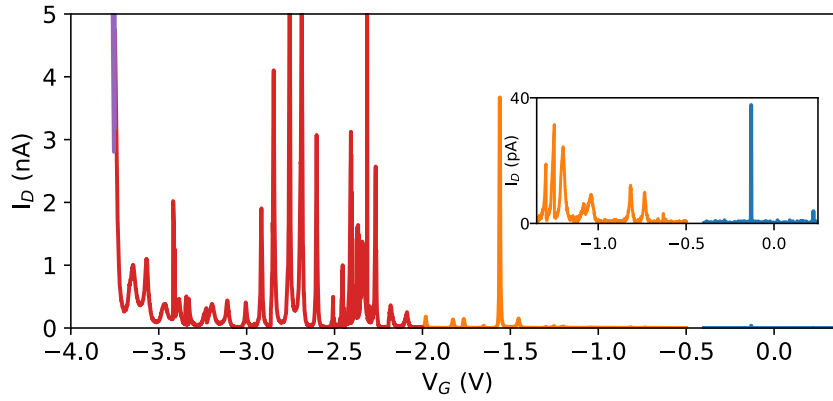
Figure 1.3 (a-b) shows a plot of I_D versus V_G of a Al-Ge-Al NW heterostructure with a short Ge segment (Sample S1) and a longer, 162 nm Ge segment (Sample L1). The curve is for a voltage bias of $V_D = 0.48$ mV focused on the CB regime. The plots reveal, for both samples, periodic current peaks separated by near-zero current regions typical of Coulomb blockade. The current peaks occur when a hole state of the QD is on resonance with the chemical potential of the c-Al leads and allows holes to tunnel through the QD.

Analysis of the CB regime reveals that the characteristic QD energies of the samples, the charging energy E_C and the tunnel rate Γ , are dependent on V_G . For Sample L1, E_C decreases from approximately 4.8 meV to 0.8 meV as V_G decreases from -3 V to -5 V. Whereas for Sample S1, E_C decreases from approximately 32 meV near pinch-off to 3 meV before the intermediate regime. The decrease in E_C as V_G becomes more negative is understood to be due to the increasing size of the QD, which occurs as the volume between the valence band (VB) and E_F increases.

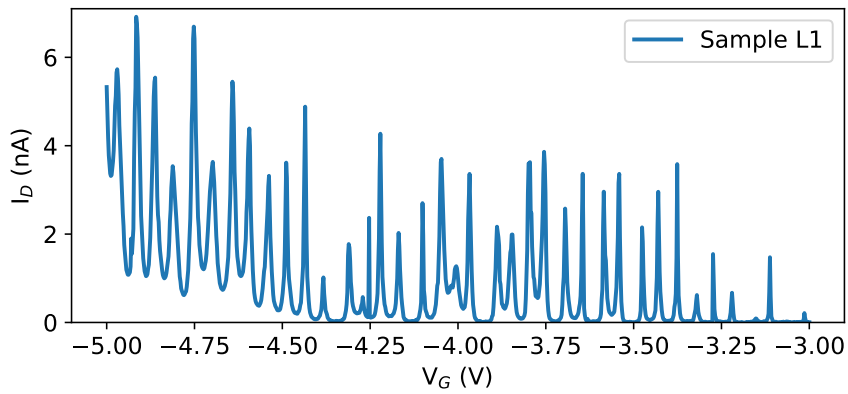
In addition to the E_C variations, the evolution of Γ as V_G decreases is evident in Figure 1.3 (a-b) by the increasing magnitude of the current peaks. From the stability diagrams of Sample S1, we estimated Γ to increase from 6.2 μeV near pinch-off to 250 μeV before the intermediate regime. We associate the increasing tunnel rate to the decreasing strength of the Schottky barriers as VB is pushed above E_F by the gate field. The strong Fermi level pinning fixes the edges of VB to below E_F of the c-Al leads. As such, to compensate for the negative electrostatic field VB can only bend above E_F . This bending reduces the depletion region at the Al-Ge interfaces, that defines the Schottky barriers, while simultaneously increasing the number of states above E_F , thus increasing the size of the QD. The intrinsic coupling of the charge density and Schottky barrier strength is fundamental to the transport dynamics of these Al-Ge-Al nanowire heterostructures and enables one to simultaneously tune E_C and Γ by modulating the back-gate voltage V_G .

Moreover, in the Coulomb blockade regime of Sample S1 & L1, we observe other features typical of strongly confined quantum dots including the odd-even effect and resonant tunneling through excited states. Details and analysis of these features can be found in the Results chapter, Chapter 5

1.2 SUMMARY



(a) Sample S1



(b) Sample L1

Figure 1.3 – I_D - V_G slice at $V_D = 0.48$ mV of (a) Sample S1 and (b) Sample L1. (a) For Sample S1 Each color represents a different measurement taken during the same cool-down. (Inset) zoom of I_D (V_G) for 0.25 V < V_G < -1.45 V.

Supercurrent Regime

At negative gate voltages, $V_G \lesssim -10$ V, the short Ge segments samples (Samples S1 & S2) enter the supercurrent regime. Figure 1.4 (a) shows a density plot of the differential resistance ($R = dV_D / dI_D$) with respect to the current bias (I_D) and V_G across Sample S1 at 390 mK. A continuous region of zero differential resistance is observed for a range of bias currents symmetric around $I_D = 0$, indicating dissipationless transport through the Ge segment. Figure 1.4 shows plots of V_D versus I_D at four gate voltages, highlighting the gate tunability and the similar values of the retrapping and critical current. For comparison, data of Sample S2 is plotted in orange. We observe gate tunable critical current up to 10 nA for Sample S1 and 6 nA for Sample S2. However, for Sample L1 we observe no evidence of supercurrent.

Outside this dissipationless current region of Figure 1.4 (a), we observe resonant features that are continuous with respect to V_G . We associate these features with multiple Andreev reflection (MAR) that is often observed in superconducting hybrid junctions with transparent interfaces. Figure 1.4 (c) shows G versus V_D curves of the same data as Figure 1.4 (b). We clearly see conductance peaks symmetric around $V_D = 0$ mV, which are consistent with MAR. Using the expected position of the conductance peaks associated with MAR, $V_D = 2\Delta/ne$, where Δ is the superconducting gap and n is the integer MAR order, we extracted an estimate for the effective superconducting gap of $\Delta^* = 185 \mu\text{eV}$. This extracted gap is nearly 20% less than the superconducting gap extracted in the Coulomb blockade regime of $220 \mu\text{eV}$. We associate the decrease of Δ to the superconducting proximity effect, which induces a gap in Ge that is smaller than the gap of the *c*-Al leads.

To estimate the transmission of the Ge nanowire's conducting channels we fit the MAR I_D - V_D curves using a Monte Carlo based fitting program, created by Gabino Rubio (see Ref. [35]). The fits of I_D - V_D curves of $V_G = -8.6$ V and $V_G = -15.5$ V, reveal transport through multiple Ge conduction channels with the first channel having exceptionally high transmission of 95 % and 96 %, respectively. The average transmission of the first three channels obtained from the fitting program was 60 % and 90 % for V_G slices -8.6 V and -15.5 V, respectively. This average transmission agrees quantitatively with transmission estimates obtained using the Blonder Tinkham and Klapwijk (BTK) model of 60 % and 80 %, respectively. The analysis of the supercurrent regime is described in greater detail in Section 5.5 in Chapter 5.

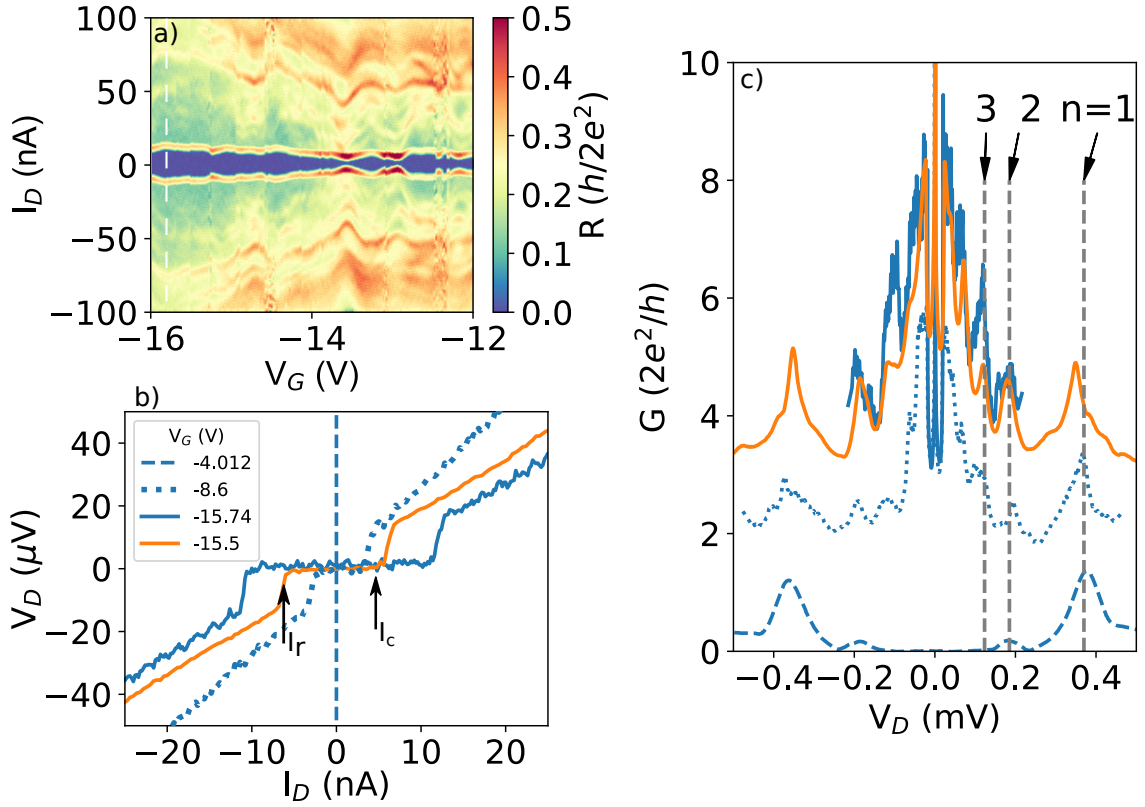


Figure 1.4 – (a) Density plot of differential resistance (dV_D/dI_D) with respect to bias current (I_D) and gate voltage (V_G), of Sample S1, in the supercurrent regime showing the gate-dependent supercurrent and MAR resonances. (b) V_D versus I_D for four V_G slices showing the onset of supercurrent. For comparison both Sample 1 (blue curves) and Sample 2 are shown (orange curve). Retrapping (I_r) and critical current (I_c) are labeled. (c) G (V_D) curves for the same V_G slices of Figure 5.33; we see clear conductance peaks which we associate with MAR. The vertical grey dashed lines indicate the expected voltage position ($V_n = 2\Delta/ne$) of the first three MAR peaks for $\Delta = 185\mu\text{eV}$.

Intermediate Regime

Between the Coulomb blockade (CB) and superconducting regimes of Samples S1 and S2, we observe an intermediate regime. The onset of the intermediate regime is marked by the fading of Coulomb blockade features as V_G becomes more negative. The transition from the Coulomb blockade regime to the intermediate regime is evident in Figure 1.3 (a), where the current rapidly diverges from the periodic current peaks of the CB regime. Figure 1.5 (b) shows the differential conductance versus V_D and V_G in the intermediate regime. The intermediate regime occurs when $\Gamma \sim \Delta$, which results in the observation of significant transport features within the superconducting gap. The nature of the sub-gap transport features suggests that in the intermediate regime, sub-gap transport does not solely occur by multiple Andreev reflection (MAR) but by a combination of MAR and resonant tunneling through the QD. For $V_G < -3.8$ V, sub-gap conductance peaks appear with periodic modulation with respect to V_G . These resonances, forming arcs bending towards zero-bias at the charge degeneracy points are interpreted as the experimental signature of single hole filling of the QD in the intermediate coupling regime. Similar to the CB regime, we estimate E_{add} from ΔV_G (see Figure 1.5 (a)) and observe a continuation of the even-odd filling with comparable addition energies. In this V_G range, we estimate the QD is filled by over thirty holes. More detail of the intermediate regime can be found in Section 5.6 of Chapter 5.

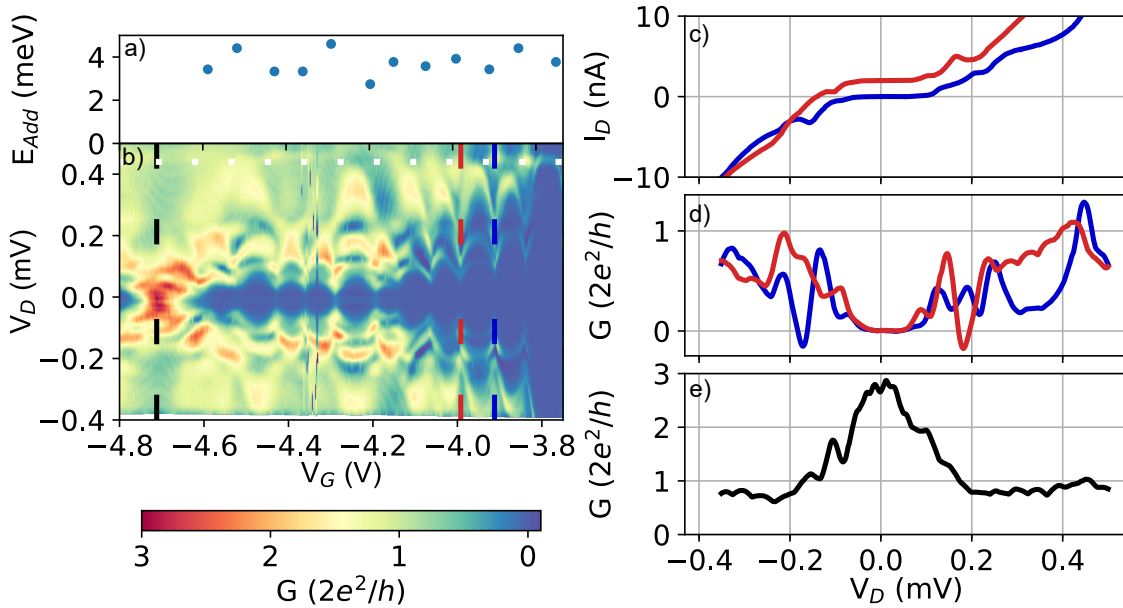


Figure 1.5 – **Intermediate regime**(a) E_{add} , calculated using $|\alpha_G|\Delta V_G$, versus V_G . (b) Density plot of differential conductance with respect to bias voltage (V_D) and gate voltage (V_G) in the intermediate regime. White dashed line shows $eV_D = \pm 2\Delta$ for $\Delta = 220 \mu\text{eV}$. We observe sub-gap conductance features that evolve with V_G . (c) $I_D(V_D)$ & (d) $G(V_D)$ slices at $V_G = -3.91$ V (dark blue) and $V_G = -3.99$ V (red). The red $I_D(V_D)$ curve has been offset by +5 nA for clarity. (e) $G(V_D)$ curve at $V_D = -4.72$ V.

1.2.3 Transport Properties (Al-Ge/Si-Al core/shell)

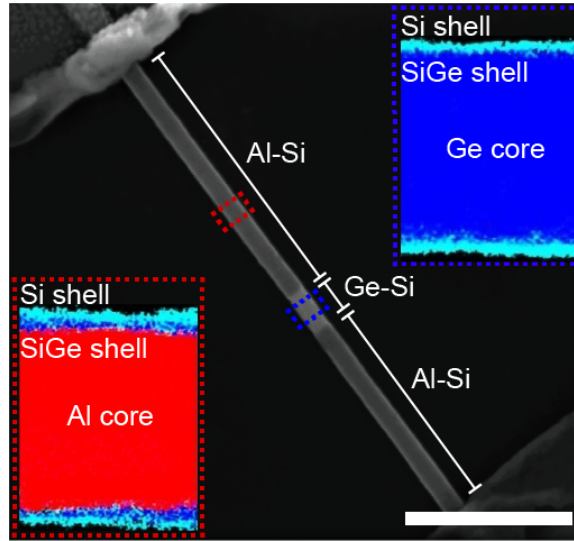


Figure 1.6 – Scanning tunneling electron microscope image of a monolithic Al-Ge-Al NW heterostructure core with a Si shell after the annealing process. Insets show energy dispersive X-ray measurements of the Ge segment and c-Al segment. Ge and Al cores with high purity are observed in the respective segments, which are wrapped by a continuous SiGe and Si shell. The scale bar is 200 nm.

In this section, I will summarise the results of the transport measurements on an Al-Ge/Si-Al core/shell nanowire heterostructure with a Ge/Si core/shell segment length of 40 nm. Figure 1.6 shows a scanning tunneling electron microscope image of a device. Energy dispersive X-ray measurements shown on the insets of Figure 1.6 reveal the purity of the c-Al and Ge components of the monolithic nanowire. Further, the insets show the structural integrity of the Si shell. The equal Ge segment length and similar fabrication process of the Al-Ge/Si-Al and Al-Ge-Al devices (Samples S1 and S2) enables a direct comparison of their transport properties.

The first distinction between the two devices is in the clear observation of quantised conductance in the Al-Ge/Si-Al core/shell NW heterostructure. Figure 1.7 shows $G-V_G$ characteristic curves of the Al-Ge/Si-Al core/shell NW heterostructure for various temperatures from 300 K to 5 K. In accordance with the i-Ge devices, the conductance increases as V_G goes from positive to negative. Notably, at $T = 150$ K the $G-V_G$ curve begins to reveal plateau-like features compared to the smooth curves at higher temperatures. The plateaus become more pronounced as the sample is cooled further. The position and nature of these features suggests that they relate to quantised conductance, confirming that we are observing, in the Ge/Si core/shell, system one-dimensional spin-degenerate sub-band-resolved quantum ballistic transport where steps of conductance occur at $G_0 = 2e^2/h$. In the literature, the reported mean free path of Ge/Si core/shell NWs ranges from 70 nm to 500 nm [36, 22], putting our Ge/Si device firmly in the ballistic regime. This is in contrast to the i-Ge device where we do not observe quantised conductance in the $L_{Ge} \approx 40$ nm devices even though they are near the ballistic limit given an estimated mean free path of approximately 45 nm.

Considering the Ge/Si core/shell segment is in the ballistic regime, we estimate the interface transparency from the resistance (R) of the conductance plateaus ($R =$

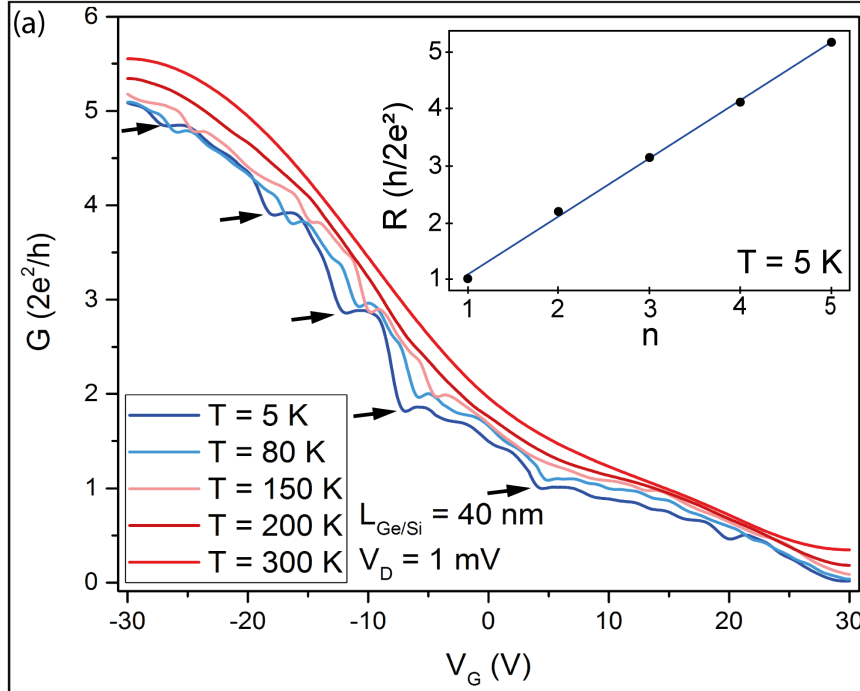


Figure 1.7 – G - V_G characteristics of the Al-Ge/Si-Al heterostructure device with a channel length of $L_{\text{Ge/Si}} = 40$ nm measured at different temperatures between $T = 5$ and 300 K. The conductance G was directly obtained from the measured current as the V_G is swept from -30 V to 30 V according to $G = dI_D/dV_D$ and is plotted in units of G_0 . The black arrows indicate the quantised conductance plateaus. The inset shows the resistance (R) of the quantised conductance plateaus vs the inverse of the conducting channel number ($1/n$). The linear fit is used to estimate the interface transparency.

$1/G$) retrieving an average transparency to be 96 %. This high transparency further endorses the high quality of the devices and supports the results from the structural analysis.

Low temperature transport measurements of the Al-Ge/Si-Al core/shell nanowire heterostructure are shown in Figure 1.8. Indeed, Figure 1.8 (a) reveals that we observe supercurrent at negative gate voltages in the Al-Ge/Si-Al core/shell devices. The top inset of Figure 1.8 (a) highlights the gate tuneability of the critical current (I_c), reaching a maximum I_c of 15 nA.

With a positive gate voltage, we enter the low conductance regime. Figure 1.8 (b) shows a density plot of the differential conductance $G = dI_D/dV_D$ versus V_D and V_G , for a positive gate voltage range. For $15 \text{ V} < V_G < 30 \text{ V}$, the transport is defined by a suppression of transport within the superconducting gap. The suppression of sub-gap transport has similarities to the superconducting gap observed in the Coulomb blockade regime of the i-Ge devices. However, in the Ge/Si core/shell devices we do not observe evidence of Coulomb blockade. As shown in the inset of Figure 1.8 (b), the I_D - V_D curves are linear in the normal regime ($|eV_D| > 2\Delta$) with a normal conductance around $0.3G_0$. Figure 1.8 (b) also shows continuous conductance resonances that run parallel to the V_G axis. These features are symmetric around $V_D = 0$ V and are similar to those observed in the i-Ge devices (see Figure 1.2). As with the i-Ge devices we

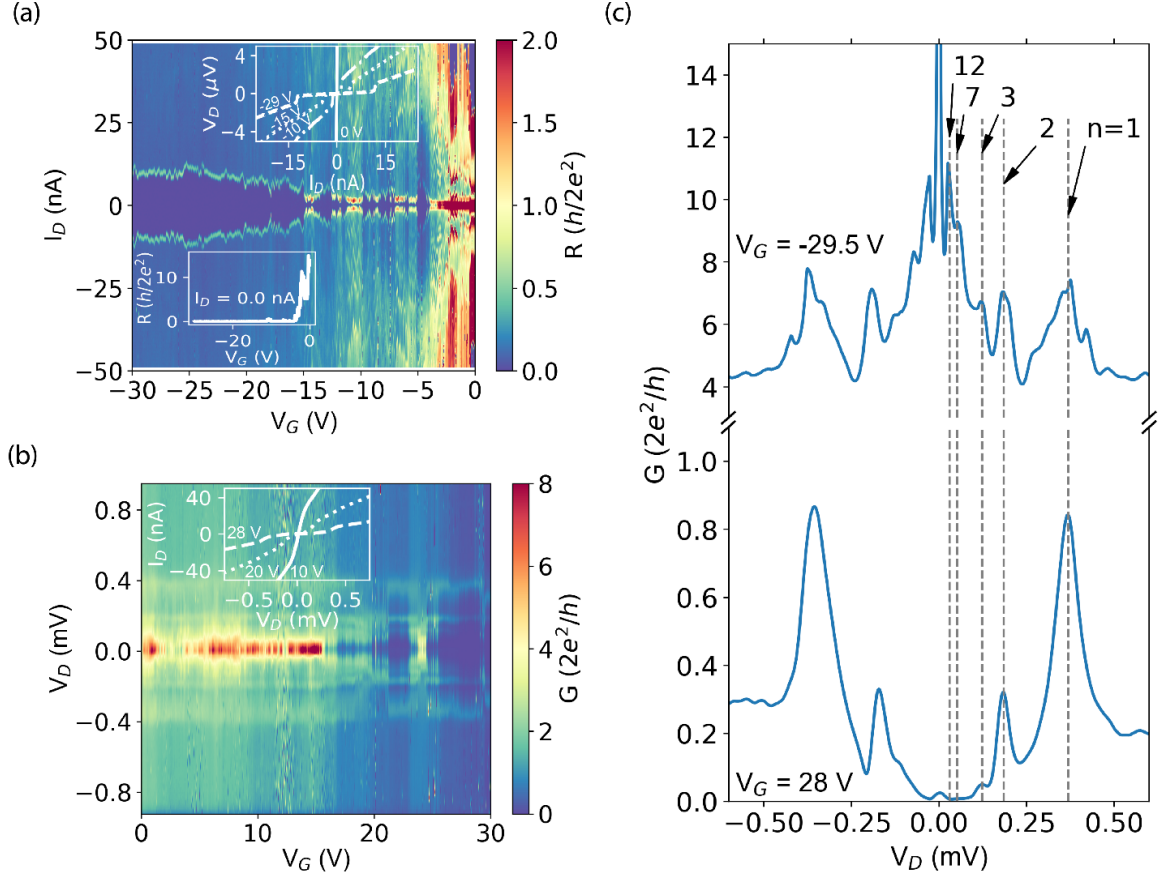


Figure 1.8 – (a) Density plot of differential resistance ($R = dV_D/dI_D$) with respect to bias voltage (V_D) and gate voltage (V_G), plotted in units of quantum resistance. The upper inset shows V_D - I_D curves for four different V_G (0 V, -10 V, -15 V, -29 V). The lower inset shows a slice of $R = dV_D/dI_D$ at $I_D = 0$ nA with respect to V_G . (b) Density plot of differential conductance ($G = dI_D/dV_D$) with respect to bias voltage (V_D) and gate voltage (V_G), plotted in units of quantum conductance. The inset shows I_D versus V_D curves for three different V_G (10, 20, 28 V). (c) Differential conductance slice (dI_D/dV_D) with respect to V_D for $V_G = -29.5$ V and 28 V measured at 450 mK.

associate these features with multiple Andreev reflection (MAR).

To better understand the conductance features due to MAR, we plot in Figure 1.8 (c) G - V_D slices from the low conductance regime ($V_G = 28$ V) and from the high conductance regime ($V_G = -29.5$ V) measured at $T = 420$ mK. The resonances appear as conductance peaks symmetric around a large conductance peak at $V_D = 0$ V. From the position of the first conductance peak at $V_D = 0.37$ mV, we estimate a superconducting gap of $\Delta = 185 \mu\text{eV}$. For $\Delta = 185 \mu\text{eV}$ three conductance resonances line up with the expected MAR position for consecutive MAR orders of $n = 1, 2, 3$. Impressively, the first three Andreev peaks of the $V_G = -29.5$ V curve align perfectly with the observed peaks at $V_G = 28$ V. The stability of the MARs through 60 V of gate tuning further endorses the exceptional interface quality of the Al-Ge/Si-Al core/shell nanowire heterostructures. Further conductance peaks at lower energy, $V_D < 0.1$ mV, are observed in the $V_G = -29.5$ V slice. These peaks line-up with

expected MAR positions of order $n = 7$ and 12 . However, as the peaks do not appear consecutively after the first three peaks it is not possible to rule out other causes of these lower energy features.

Applying the BTK model to the I_D - V_D curves in the supercurrent regime we retrieve an approximate transparency of 99%, which is consistent with the transparency calculated from the quantized conductance plateaus. More details on the transport properties of the Al-Ge/Si-Al NW heterostructures can be found in Section 6 of Chapter 5.

Theoretical concepts

2

Contents

2.1	Introduction to charge transport	16
2.1.1	Drude Model	16
2.1.2	Free electron Model	17
2.1.3	Bloch's Theorem	20
2.2	Transport in nanowires	25
2.2.1	Coherent ballistic conductor	25
2.2.2	Conductance quantisation	26
2.3	Transport in quantum dots	29
2.3.1	Tunnel junctions	30
2.3.2	The constant interaction model	30
2.3.3	Case of zero-bias (Coulomb oscillations)	33
2.3.4	Case of varying V_G and V_{SD} (Coulomb Diamonds)	34
2.4	Superconductivity	38
2.5	Superconducting Junctions	42
2.5.1	Proximity Effect	42
2.5.2	Microscopic description of the proximity effect	43
2.5.3	Superconducting-normal junctions (S-N-S)	45
2.5.4	Superconducting Quantum Dot Junctions (S-QD-S)	55

In this chapter, I will introduce the many physical quantities and concepts needed to discuss and understand the transport properties in our germanium based nanowire heterostructures. I will begin with an introduction to charge transport. This introduction incorporates aspects of an undergraduate (Honours) condensed matter course I attended^a and the textbook *Solid State Physics* by Ashcroft and Mermin [37]. I was motivated to begin from these fundamental concepts for a few reasons: to make a connection between my previous studies and the knowledge that I have gained through my PhD research, to help consolidate that knowledge and finally, to provide an approachable introduction for future students embarking on this project.

From the introduction of charge transport I discuss the important concepts regarding transport in nanowires. I will explain that in ballistic conductors it is possible to observe quantised conductance if the contacts between the leads and the nanowire are highly transparent. In the section that follows, I will consider a nanowire, which has highly opaque contacts to the leads. In this case, the nanowire forms a quantum dot. The key role a quantum dot plays in understanding our experimental observations motivates a detailed discussion of their transport properties.

In the final section, I present the theoretical concepts of superconducting junctions. The investigation of superconducting hybrid junctions based on germanium nanowire heterostructures is a major component of this thesis. As such, a solid understanding of superconducting junctions is necessary to appreciate the results. Before considering superconducting junctions, I provide a brief introduction to superconductivity.

Throughout this chapter, I maintained my goal of consolidating my knowledge, while providing a detailed introduction of the theoretical concepts required to follow this project and more importantly, push it forward in the future.

2.1 Introduction to charge transport

Before discussing the important aspects of charge transport in nanowire devices, we will first introduce the basics of charge transport in macroscopic systems. This introduction will be made within an historical context in order to appreciate the evolution of physicists' understanding of electronic transport in the early 20th century. We will begin with the Drude model, which explained Ohm's law through a microscopic particle model. We will then introduce the free electron model, which expanded upon the Drude model by considering electrons as quantum mechanical particles. Finally, we will present Bloch's theorem, which incorporates the effect of the periodic crystal lattice of solids into the electron transport model. This semiclassical model successfully explained some puzzling experimental observations of the time, including the existence of semiconductors and insulators and the suggestion of positive charge transport. We will conclude by describing the important electronic properties of germanium.

2.1.1 Drude Model

In 1900 Paul Drude introduced a microscopic model to describe the vast experiential observations of charge transport in metals during the 19th century. The Drude model applies the kinetic theory of gasses to metals. This simple "pinball" particle model considers a sea of negatively charged electrons^b that are continuously scattered by

^aPHYS4030, 4th year course by Prof. Ross McKenzie, University of Queensland, Brisbane (2017)

^bElectrons were recently discovered in 1897 by J. J. Thompson

positively charged ions that form the solid. Though the atomic model had yet to be proposed by Rutherford in 1909, Drude's model successfully explained many of the observations of the preceding decade. The Drude model is based on multiple assumptions; electrons are non self-interacting particles that only interact with the ions of the metal where collisions are instantaneous, collisions occur at a frequency of $1/\tau$ where τ is the average time between each collision, known as the scattering time.

Fundamental to the Drude model is the electron charge density of $n = \frac{N}{V}$, where N is the number of electrons and V is the volume. The charge density is commonly defined in terms of the volume per single conduction electron $\frac{4\pi}{3}r_s^3$, which has a radius of r_s . r_s is of the order of the Bohr radius $a_0 = \frac{4\pi\epsilon_0\hbar^2}{m_e e^2} \approx 0.5\text{\AA}$ and is defined in terms of the ratio $r_0 = r_s/a_0$. With $r_0 \approx 2 - 5$, the charge density of metals is of the order

$$n = \frac{N}{V} = \frac{1}{\frac{4\pi}{3}r_s^3} \approx 10^{23} \text{ cm}^{-3}. \quad (2.1)$$

By determining the equation of motion of electrons experiencing a constant electric field \vec{E} in the microscopic model, Drude produced a general expression for the conductivity σ of a metal,

$$\sigma = \frac{ne^2\tau}{m}, \quad (2.2)$$

where m is the electron mass. Conductivity defines the current density \vec{J} response of a wire that experiences an electric field \vec{E} , by $\vec{J} = \sigma\vec{E}$. Conductivity is related to the resistivity ρ by $\sigma = 1/\rho$. The resistivity of a wire of length L and cross-sectional area A is given by $\rho = RA/L$, where R is the resistance of the wire. We can retrieve Ohm's law by noting that $\vec{J} = I/A$, where I is the current, and $\vec{E} = V/L$, where V is voltage applied to the wire. Substituting the aforementioned definitions into $\vec{J} = \sigma\vec{E}$, we retrieve Ohm's law $V = IR$.

Importantly, the microscopic Drude model justifies the empirical Ohm's law. Drude's model was also successful at explaining other experimental phenomenon including; the Hall effect, the Drude peak in optical conductivity, the plasma frequency and the universal Lorentz number. However, this model has its shortcomings. The Drude model incorrectly predicts the sign of the Hall effect of some metals, and does not explain for the existence of insulators and semiconductors.

2.1.2 Free electron Model

Through treating the electrons as quantum mechanical particles obeying Fermi-Dirac statistics Arnold Sommerfeld expanded on the Drude model in 1927. This development became the free electron model of charge transport in metals and is also known as the Drude-Sommerfeld model.

Fermi-Dirac statistics was developed by Enrico Fermi in 1926 to describe the behavior of fermions, such as electrons. These particles obey the Pauli exclusion principle, which was formulated for electrons by Wolfgang Pauli in 1925 to explain the electron distribution in atoms. The principle states that two electrons of a system, such as an atom, can not exist in a state with the same quantum numbers.

As with any quantum system, treating electrons quantum mechanically requires

the application of the Schrödinger equation:

$$i\hbar \frac{\partial \Psi(\vec{r}, t)}{\partial t} = \left[-\frac{\hbar^2}{2m} \nabla^2 + V(\vec{r}) \right] \Psi(\vec{r}, t). \quad (2.3)$$

Considering a system in equilibrium we will apply the time independent Schrödinger equation

$$\hat{H}\psi(\vec{r}) = E\psi(\vec{r}), \quad (2.4)$$

to retrieve the eigenenergies and eigenstates of the electrons. Here, the Hamiltonian operator will be defined in terms of the momentum operator, giving

$$\frac{\hat{p}^2}{2m}\psi(\vec{r}) = -\frac{\hbar^2}{2m}\nabla^2\psi(\vec{r}) = E\psi(\vec{r}). \quad (2.5)$$

To solve the differential equation we simplify the model by breaking the metal conductor into cubes of volume L^3 and applying boundary conditions of the electron state being equal at each end of the cube which defines the volume of interest;

$$\psi(x, y, z) = \psi(x + L, y, z), \quad (2.6)$$

$$\psi(x, y, z) = \psi(x, y + L, z), \quad (2.7)$$

$$\psi(x, y, z) = \psi(x, y, z + L). \quad (2.8)$$

Eq. 2.5 is solve by describing the electrons as plane waves with eigenstates and eigenenergies of

$$\psi(\vec{r}) = \frac{1}{\sqrt{V}} e^{i\vec{k}\vec{r}} \quad (2.9)$$

and

$$\epsilon = \frac{\hbar^2 \vec{k}^2}{2m}, \quad (2.10)$$

respectively. Applying the boundary conditions the wavevectors of the allowed particle states are

$$\vec{k} = \frac{2\pi}{L} \vec{n}, \quad (2.11)$$

where

$$\vec{n} = (n_x, n_y, n_z) \quad n \in 0, \pm 1, \pm 2, \dots \quad (2.12)$$

Now that we have all the possible electron ground states, we can define important quantities in condensed matter physics: the Fermi energy E_F and Fermi wavevector k_F . The Fermi energy is the largest microscopic energy an electron of a macroscopic electronic system can have when it is in the ground state at $T = 0$ K. That is, the highest occupied energy level of the system in the ground state. The Fermi wavevector is defined by the Fermi energy using Eq. 2.10.

With E_F we can define the Fermi surface, which is the surface in k-space where $\epsilon(\vec{k}) = E_F$, for $|k| \leq k_F$. In the ground state the Fermi surface defines a boundary

in k-space between occupied ($\epsilon \leq E_F$) and unoccupied ($\epsilon > E_F$) states and aids in predicting the transport properties of the metal.

At finite temperatures, electrons near the Fermi surface are excited to higher energy levels. This leaves empty energy states near the Fermi surface where electrons are free to transition between, thus allowing the transport of charge and heat. Given that *free electrons* exist near the Fermi surface, they naturally have energy similar to that of the Fermi energy. By defining the Fermi velocity $v_F = \frac{\hbar k_F}{m}$, we can estimate the velocity of these free electrons. In metals, typically $v_F \approx 2 \times 10^6 \text{ ms}^{-1}$, which is significantly larger than Drude's estimate.

Fermi-Dirac Statistics

The internal energy U of the electronic system can be determined by summing over all the single-electron energy levels $E(\vec{k})$ multiplied by the mean number of electrons in that level. In the ground state this is quite simple as all the states up to $E(\vec{k} = k_F)$ are filled therefore the total energy is

$$U = 2 \sum_{k < k_F} \frac{\hbar^2 k^2}{2m}. \quad (2.13)$$

In the Drude model the classical Maxwell-Boltzmann distribution is used to define the electron filling. However, as the electrons are modeled as fermions which obey Fermi-Dirac statistics the electron filling of states is defined by the Fermi-Dirac distribution. Therefore the total internal energy at $T > 0 \text{ K}$ is given by

$$U = 2 \sum E(\vec{k}) f(E(\vec{k})), \quad (2.14)$$

where

$$f(E) = \frac{1}{e^{\left(\frac{E-\mu}{k_B T}\right)} + 1}, \quad (2.15)$$

is the **Fermi-Dirac distribution**.

The occupancy distribution of Fermi-Dirac statistics changes the velocity distribution of the free electron gas compared to the Drude model. Assuming an energy independent relaxation time τ , the mean free path, thermal conductivity and thermopower are adjusted by the new velocity distribution.

Characteristic lengths

The **elastic mean free path** (l) is the average length through which the electron transverses before elastic scattering due to collisions. Given that at most common temperatures free electrons have an energy similar to that of the Fermi energy the mean free path can be estimated from the Fermi velocity

$$l = v_F \tau. \quad (2.16)$$

If the dimensions of the system are larger than the elastic mean free path, then the electron trajectories will experience many collisions during their propagation through the system. This regime of transport is called diffusive. Whereas, if the dimensions of

the system are smaller than the elastic mean free path, then the electron trajectories will experience almost no collisions, this transport regime is called ballistic.

In addition to the elastic scattering, electrons can experience inelastic scattering events, where energy is lost to the crystal. During such an event, the phase of the wave function describing the electron is randomised. The **phase coherence length** ξ , measures the distance that the electrons propagate before losing their phase due to inelastic collisions. The phase coherence length is the relevant length scale for determining if coherent transport can be observed.

Density of States (DOS)

The density of states ($g(E)$) is an abstraction used to simplify the modeling of electronic systems and is defined as the density of single electron states per unit volume per unit energy at energy E . Taking $\tilde{N}(E)$ to be the total number of energy levels with energy less than E . The density of states (DOS) is defined as

$$g(E) = \frac{d\tilde{N}(E)}{dE}. \quad (2.17)$$

Though simple the free electron model accounts for many metallic properties. The use of Fermi-Dirac statistics, to account for the fermionic behavior of electrons, resolved some of the deficiencies of the Drude model. The Drude-Sommerfeld model successfully predicted the coefficients in some metals of the specific heat, mean free path, thermal conductivity among other properties. However, the free electron model makes significant assumptions that clearly oversimplify the model resulting in inadequate physical predictions.

2.1.3 Bloch's Theorem

Though solids form different shapes, at the microscopic level they all share a crystalline structure formed by the periodic arrangement of atoms or molecules. Significant model improvements can be made by taking into account the effect of the metal's crystalline structure on electrons. The incorporation of the crystal structure into modeling a material's electronic properties is at the heart of Bloch's theorem.

In Bloch's theorem the complex interaction between the periodic lattice ions and the electrons is modeled as a simple periodic potential given by

$$V(\vec{r}) = V(\vec{r} + \vec{R}), \quad (2.18)$$

for all Bravais lattice points \vec{R} .

Given the quantum mechanical nature of the system, the single electron states are determined by solving the Schrödinger equation (Eq. 2.3) with the periodic potential of Eq. 2.18. Bloch's theorem provides conditions to the solutions of the Schrödinger equation with a periodic potential. Stating that the eigenstates are of the form

$$\psi_{n\vec{k}}(\vec{r}) = e^{i\vec{k}\cdot\vec{r}} u_{n\vec{k}}(\vec{r}), \quad (2.19)$$

where

$$u_{n\vec{k}}(\vec{r}) = u_{n\vec{k}}(\vec{r} + \vec{R}), \quad (2.20)$$

for every \vec{R} in the Bravais lattice. An equivalent form of the solution is that the eigenstates satisfy

$$\psi(\vec{r} + \vec{R}) = e^{i\vec{k}\cdot\vec{R}}\psi(\vec{r}), \quad (2.21)$$

for every \vec{R} in the Bravais lattice.

Combining Bloch's theorem with von Karman boundary conditions, the expression for the Bloch wavevectors of Eq. 2.19 can be determined for a 3D crystal

$$\vec{k} = \sum_{j=1}^3 \frac{M_j}{N_j} \vec{b}_j, \quad (2.22)$$

where $M_j = 0, \pm 1, \pm 2, \dots$ is the coefficient of the reciprocal lattice primitive vector \vec{b}_j , which represents the reciprocal lattice vector points. Whereas $N_j = 0, \pm 1, \pm 2, \dots$ is the coefficient of the real space lattice vectors.

It must be noted that Bloch wavevectors \vec{k} of Eq. 2.22 are not proportional to momentum in the same way that the plane wave wavevectors of the free electron model are. This is due to the periodic potential in the Hamiltonian \hat{H} , which means that the eigenstates of \hat{H} are not eigenstates of the momentum operator \hat{p} . The momentum $\vec{p} = \hbar\vec{k}$ of Bloch wavevectors is called the crystal momentum.

Bloch bands and band structure

Comparing the wavefunction of Bloch's theorem (Eq. 2.19) with the solutions of the free electron model (Eq. 2.11) reveals that Bloch's solutions have an extra quantum number, n . In Bloch wavefunctions, n is an integer and iterates over the different possible eigenstates for a given wavevector \vec{k} . This range of eigenstates, results from the periodic boundary conditions of Bloch's theorem, which restricts the eigenvalue problem to determine the eigenstates $u_{n\vec{k}}$ and eigenenergies $\epsilon_{n\vec{k}}$ to a single primitive cell. This condition results in an infinite set of discrete solutions labeled by the quantum number n for a given \vec{k} . Conversely, a set of solutions designated by n will vary with \vec{k} . For continuous \vec{k} , restricted to a single primitive cell, we would expect a set of continuous functions given by $\epsilon_{n\vec{k}}$, which are called Bloch bands or energy bands.

The eigensolutions of Bloch's theorem can be extended to all k-space by exploiting the periodicity of the reciprocal lattice giving the solutions

$$\psi_{n,\vec{k}+\vec{K}}(\vec{r}) = \psi_{n\vec{k}}(\vec{r}), \quad (2.23)$$

$$\epsilon_{n,\vec{k}+\vec{K}} = \epsilon_{n\vec{k}}, \quad (2.24)$$

where \vec{K} is the reciprocal lattice vector. See Ref. [37] for details on the reciprocal lattice.

This complete result of Bloch's theorem shows that the energy states of an electron in a periodic potential are a set of continuous functions which are periodic with the reciprocal lattice. The combination of the single functions $\epsilon_{n\vec{k}}$ for all of k-space is referred to as the band structure of the solid.

Electron Velocity

The mean velocity of an electron in a stationary state $\psi_{n\vec{k}}(\vec{r})$ in a periodic potential can be determined from the energy bands of Bloch's theorem by

$$\vec{v}_n(\vec{k}) = \frac{1}{\hbar} \frac{\partial \epsilon_{n\vec{k}}}{\partial \vec{k}}. \quad (2.25)$$

This result reveals that the electrons have a non-zero and non-vanishing velocity that is not effected by static ions of the lattice. This is contrary to the predictions of the Drude model and explains the long mean free paths observed in metals.

Fermi Surface

The ground state of a crystal with N Bloch electrons is constructed by filling the single-electron energy states that are given by the Bloch band energies $\epsilon_n(\vec{k})$. Furthermore, the Bloch wavevectors must be restricted to a single primitive cell to ensure that the \vec{k} states are not double counted. The Fermi energy E_F is defined, as in the free electron case, as the energy below which all the single-electron states are filled by all the available electrons, N .

However, the continuous nature of the band structure results in different filling arrangements of the energy bands for different solids, which leads to different electronic properties. In general there are two global arrangements:

1 The Bloch bands $\epsilon_n(\vec{k})$ below the Fermi energy are completely full where as the higher energy bands are empty. In this configuration the energy between the highest energy filled Bloch band and the lowest energy empty Bloch band is called the *band gap*. By definition the Fermi energy exists within the band gap.

2 Some Bloch bands are partially filled, this occurs when the Fermi energy lies within the energy of multiple bands. This will result in occupied and unoccupied regions in a single Bloch band. In k -space, the combined surfaces that border the region of occupation of the Bloch band defines the Fermi surface. Each partially filled band is referred to as a branch of the Fermi surface. The Fermi surface of the partially filled Bloch bands can be described as a constant energy surface where

$$\epsilon_n(\vec{k}) = E_F. \quad (2.26)$$

The occupancy of the bands in the ground state and the subsequent position of the Fermi surface defines the conductive properties of the crystal. Figure 2.1 shows how the band filling and E_F position defines whether a crystal is a metal, insulator or semiconductor. This is an important result of Bloch's theorem and explained the huge variation in conductive properties observed in different solid state crystals.

In this thesis we will investigate the transport properties of germanium (Ge) and germanium/silicon (Ge/Si) core/shell nanowires. Germanium is a type IV semiconductor with an indirect band-gap of $E_G = 0.66$ eV and a direct band-gap at the Γ -point of 0.8 eV[38]. Figure 2.2 shows the band structure of bulk Ge, showing the direct and indirect band gaps. In the valence band Ge has light and heavy hole bands that are degenerate near $\vec{k} = 0$. This degeneracy can be lifted by confinement.

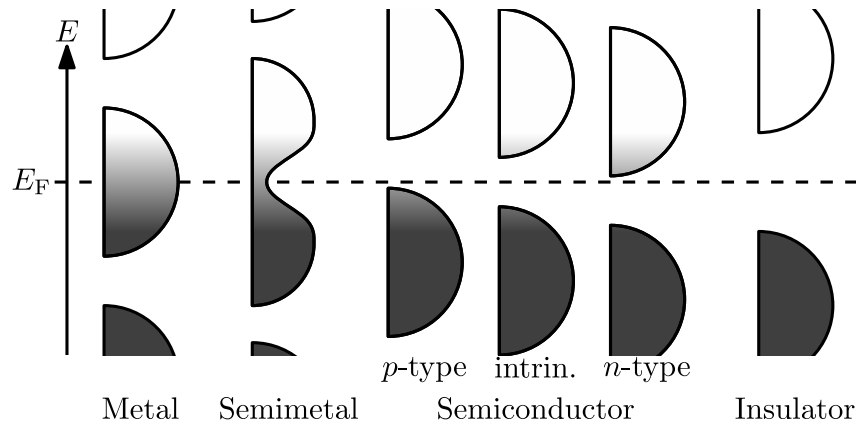


Figure 2.1 – Schematic representation of the band filling of different crystals. The electron filling of the bands and therefore the position of E_F defines the conductive properties of the crystal. In metals, E_F lies within partially filled bands. In semiconductors E_F is inside the band-gap. The collection of bands below E_F , which are filled with electrons is called the valence band. The collection of bands above E_F , which are empty of electrons is called the conduction band. In insulators E_F is also in the band-gap. However, the band gap is too large for conduction to occur. Figure taken from *Nanite, CC0, via Wikimedia Commons*.

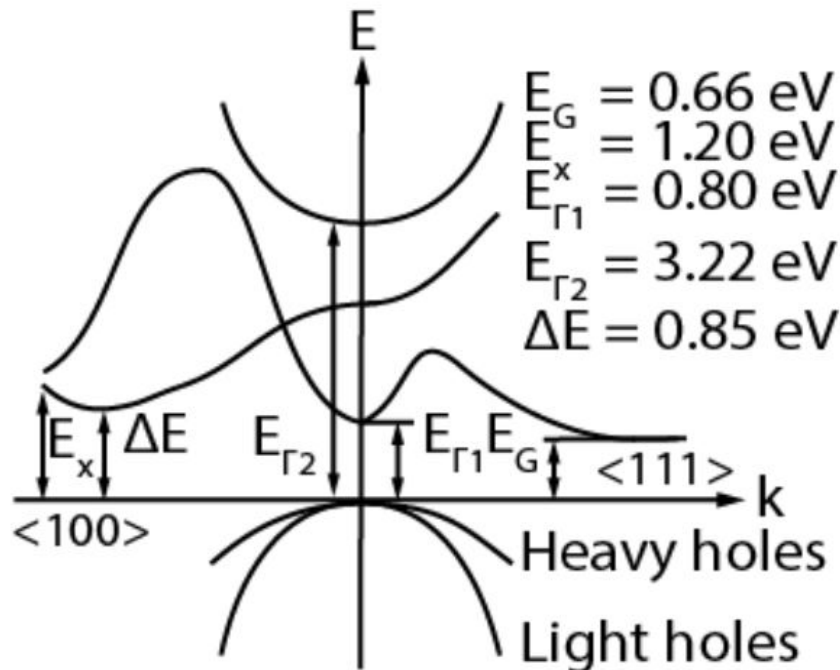


Figure 2.2 – Band structure of bulk germanium at 300 K. We can see the indirect band-gap labeled E_G and the direct band gap labeled E_{Γ}^x . We also observe light hole and heavy hole bands, which are degenerate near $\vec{k} = 0$. Figure taken from Ref. [39].

In intrinsic Ge, nanowires surface states result in E_F being close to the valence band. As suggested in Figure 2.1, this leads to p -type semiconducting behavior. In p -type semiconductors electronic transport occurs through charges in the valence band.

Unlike in metals and *n-type* semiconductors where transport occurs through electrons in the conduction band, the charge carriers in the valence band are holes. Holes are positive charge carriers, and can be thought of as the absence of electrons. The description of charge transport through positive charge carriers (holes) was another important break through of Bloch's theorem.

2.2 Transport in nanowires

In the previous section, we considered the transport properties of macroscopic solids. Such systems are usually in the diffusive transport regime, where the dimensions of the system are much greater than the mean free path. Diffusive transport is characterised by charge carriers scattering with phonons, impurities, crystal defects and crystal boundaries. The continuous scattering events leads to incoherent transport, where the phase of the charge carriers is lost as they traverse the large conductor.

Nanostructures, such as nanowires, can reduce the conductor's dimension to limits where ballistic transport as well as coherent transport can be observed. As a result, the wavefunction of the charge carriers has direct implications on the transport properties of the conductor. The classical values describing the transport, such as the Drude conductivity, must be corrected due to the impact of the quantum interference between the charge carrier trajectories.

In the Landauer formalism, the conductance of a coherent sample is calculated as a function of the transmission probability through the system. In the following, we will first present the Landauer formalism in the particular case of a ballistic quasi-one dimensional conductor. The Landauer formula explains the experimental observation of quantised conductance that has been measured in quantum conductors, such as quantum point contacts. Secondly, we will present how analysis of the conductance quantisation enables one to estimate the transmission of the conductor.

2.2.1 Coherent ballistic conductor

Rolf Landauer studied the case of a one-dimensional coherent conductor connected to two leads, which act as large reservoirs. In order to describe the system, using a scattering approach, Landauer considered the conductor to have an electron transmission probability T and reflection probability $R = 1 - T$. In this two probe measurement configuration, the conductance of the sample is directly related to the transmission through the system and is given by the Landauer formula [40]:

$$G = \frac{2e^2}{h}T. \quad (2.27)$$

For a perfect ballistic conductor, there is no scattering event, thus $T=1$ and the conductance is equal to the quantum of conductance. Further, given that no collisions occur in the ballistic conductor, we would expect there to be no dissipation and therefore no resistance. However, measurements of ballistic conductors reveal a finite resistance. This resistance comes from the contact, where the many channels of the macroscopic leads must converge to the few channels of the ballistic contact. The resulting resistance, referred to as the contact resistance, is given by

$$R_C = \frac{h}{2e^2} \approx 12.9\text{k}\Omega. \quad (2.28)$$

This resistance is fundamental to all ballistic conductors. One can consider that a ballistic conductor with a single conducting channel, has a fundamental minimum resistance of $R_0 \equiv \frac{h}{2e^2} \approx 12.9\text{k}\Omega$, which is called the resistance quantum. In the literature, the conductance quantum is often used when investigating the transport of

nanostructures, which is given by $G_0 \equiv \frac{2e^2}{h} \approx 7.75 \cdot 10^{-5}$ S. In this thesis, I will make regular use of G_0 and R_0 .

In the case of a quasi-one-dimensional conductor, the sample has M conduction channels. The Landauer formula (Eq. 2.27), can be expanded to the case of a quasi-one-dimensional conductor. This is achieved by summing over the transmission of each channel T_i , giving

$$G = \frac{2e^2}{h} \sum_i T_i. \quad (2.29)$$

2.2.2 Conductance quantisation

In this thesis, I have performed transport measurements on Al-Ge-Al nanowire heterostructures. These unique hybrid junctions feature crystalline quasi-one-dimensional Al leads which are connected to crystalline Ge segments by near atomically abrupt interfaces. The nanowires studied have diameters of approximately 25-30 nm and the Ge central segment can have a length down to 40 nm. In this paragraph, I want to show that our Al-Ge-Al nanowires can be an experimental realization of a coherent quasi-ballistic conductor.

Ballistic transport occurs when the dimensions of the conductor are shorter than the mean free path ℓ . The mean free path is given by,

$$\ell = v_F \tau. \quad (2.30)$$

where v_F is the Fermi velocity and τ is the average time between scattering events. By taking

$$v_F = \frac{\hbar}{m^*} \sqrt{2\pi n}, \quad (2.31)$$

where $m^* = 0.041m_e$ is the effective mass of heavy holes and $n = 5 \times 10^{13} \text{ cm}^{-3}$ is the charge density, the mean free path of Ge is estimated to be $\ell_{\text{Ge}} = 37.2 \text{ nm}$ for $\tau = 0.26 \text{ ps}$ [41]. This puts the Al-Ge-Al nanowire heterostructures with Ge segment lengths of 40 nm at the edge of the ballistic limit.

To observe conductance quantisation, the transverse dimensions of the conductor such as its diameter, must be reduced such that the conductance or valence band states are discrete rather than continuous. In this regime, the usually continuous bands form discrete sub-bands. Each sub-band forms single conductance channel. To achieve band discretisation, the width of the conductor must be of the order of the Fermi wavelength λ_F . λ_F can be estimated from the Fermi energy E_F by $\lambda_F = \frac{\hbar}{\sqrt{2m^*E_F}}$. Taking the effective mass of holes in Ge to be $m^* = 0.041m_e$ we retrieve a $\lambda_F = 10.7 \text{ nm}$. With a nanowire diameter of $d = 25 \text{ nm}$, we are in the limit where quantum ballistic transport can be observed.

By modeling the radial confinement of the nanowires (NWs) as a saddle potential, an estimate of the maximum number of sub-bands N available in a NW of diameter d is given by [39]

$$N = \frac{\pi d}{2\lambda_F}. \quad (2.32)$$

Using $\lambda_F = 10.7\text{nm}$ and $d = 25\text{ nm}$, we retrieve $N \approx 7$. Therefore, in an ideal Ge NW sample within the quantum ballistic limit, which experiences radial confinement according to a saddle potential, we would expect to observe the conductance saturate at a final conductance plateau at $7G_0$. Therefore, we would expect our Al-Ge-Al nanowire junctions with Ge segment lengths of 40 nm to be coherent ballistic conductors with around 7 conducting channels.

As our nanowires are semiconductors, we can tune their charge density using an electrostatic gate field. In a nanowire with discrete sub-bands, this translates to controlling the number of active sub-bands by applying a gate voltage V_G . The number of active sub-bands then defines the conductance G of the system. To aid in the understanding of this phenomenon we will consider hole transport in an ideal quantum ballistic nanowire (NW) with spin degeneracy. Figure 2.3 shows a schematic of G versus V_G of hole transport in an ideal quantum ballistic NW with perfect transmission, $T = 1$ (blue). For the ideal NW, by decreasing the gate voltage V_G from 0 V , the conductance increases in steps of $G_0 = \frac{2e^2}{h}$. The conductance steps occur because more sub-bands (conducting channels) become available for transport as V_G becomes more negative.

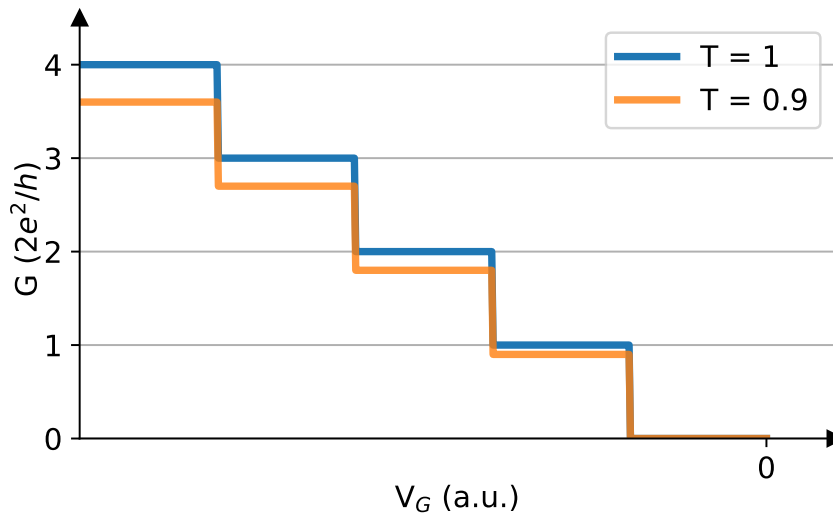


Figure 2.3 – Schematic of G versus V_G for hole transport in a quantum ballistic nanowire with transmission $T = 1$ (blue) and $T = 0.9$ (orange).

However, observing conductance plateaus, especially up to its confinement defined maximum G_0 , is experimentally quite challenging. Beyond having sufficient confinement, the nanostructures are usually very sensitive to crystal defects and surface states. These defects induce disorder, which in devices with strong radial confinement often results in back-scattering of charger carriers that prevents the observation of conductance plateaus [42].

In the Landauer model, the barrier transmission takes into account scattering within the ballistic conductor due to defects and also finite barrier transparency. In Figure 2.3, a G - V_G curve of a non-ideal NW with $T = 0.9$ transmission is plotted in orange. G is determined using Eq. 2.29. The effect of non-ideal transmission is clearly observable in the G - V_G curve. The conductance of the plateaus is reduced compared to the ideal NW. However, in most nanowire transport measurements, excessive de-

fects that result in considerable back-scattering will prevent the observation of clear conductance plateaus, rendering this conductance model futile.

Since our Ge segment is ballistic, we associate the transmission through the Al-Ge-Al nanowire to the transparency of the Al-Ge interface for the samples showing quantisation. Using an electrostatic gate, I have the possibility to tune the Al-Ge interface of the Al-Ge-Al junctions from a quasi-ohmic behavior to the equivalent of a tunnel barrier. In this last configuration, the Ge segment is equivalent to a dot with a well define number of charges.

2.3 Transport in quantum dots

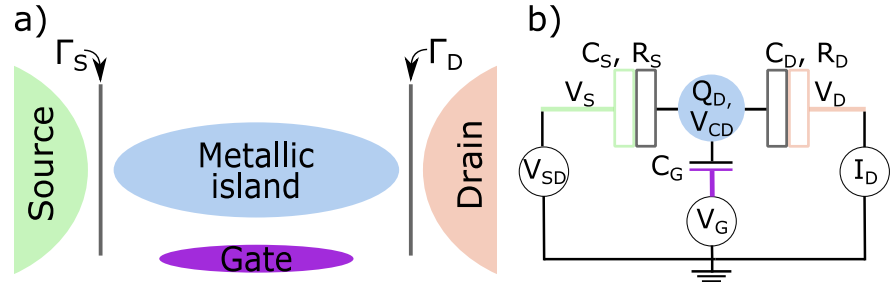


Figure 2.4 – (a) Schematic of a quantum dot, which consists of a small metallic island that is coupled to a source and drain through tunnel junctions with tunnel rates of Γ_L and Γ_R , respectively. (b) Circuit diagram of a QD in the constant interaction model. The QD has a charge Q_D and potential V_{CD} . The QD is capacitively coupled, by a gate capacitance C_G , to a gate electrode with potential V_G . The source and drain reservoirs have defined potentials of V_S and V_D , respectively. The tunnel junctions to the source and drain are modeled as leaky capacitors with a capacitance $C_{S,D}$ and resistance $R_{S,D}$.

In the previous section we discussed the interesting transport properties of ballistic nanowires (NWs) connected to macroscopic leads. In particular, we discussed the possibility to observe conductance plateaus in quantum ballistic NWs. However, their observation requires transparent interfaces between the leads and the NWs. Interestingly, if one reduces the transparency of the contacts such that opaque barriers form between the source & drain and the NW one can form a quantum dot (QD). In Chapter 5, it will be shown that the Al-Ge-Al nanowire heterostructures, studied in this thesis, form QD devices. As such, we will introduce the important concepts of QDs in this section.

A QD, depicted schematically in Figure 2.4, is a small metallic island that is coupled to a source and drain through tunnel junctions. The tunnel coupling to the source Γ_S and drain Γ_D must be sufficiently small that the tunnel junction resistance is $R \gg \frac{h}{e^2} \approx 25.8\text{k}\Omega$ [43]. If this criteria is met and the capacitance to the leads is small enough, then a fixed and quantised charge is confined on the metallic island. By introducing an electrostatic gate that is capacitively coupled to the metallic island, the number of charges on the dot can be controlled. With sufficient control, the device can be tuned such that only a single electron passes through the metallic island from the source to the drain. Such a device is known as a single electron transistor (SET) and was first demonstrated by Smith *et al.* [44] in 1988.

The size of the metallic region is also critical to its function. To observe artificial atomic signatures, the region defining the QD must be of the order of λ_F of the trapped charge. Another important consideration when designing QDs is the magnitude of the charging energy E_C . E_C is the energy required to overcome the electrostatic repulsion of the dot and is given by $E_C = \frac{e^2}{C_\Sigma}$, where C_Σ is the total capacitance of the QD device. To observe single electron tunneling it is necessary that $E_C \gg k_B T$, where T is the system temperature, otherwise thermal fluctuations induce uncontrolled electron tunneling. The total capacitance of the QD C_Σ increases with QD volume, there-

fore there is a maximum size the metallic island can have to observe single electron tunneling. This size is defined by the working temperature of the system.

The confinement required to observe QD effects can be achieved by using electrostatic gates on a 2D electron gas (2DEG) [44, 45] or under a 1D nanowire [46, 47] or carbon nanotube [48]. It can also be achieved by fabricating nanostructures where the charge is confined by physical barriers such as a small NW segment [49], a molecule [50] or nanocrystals [51]. QDs can be considered as artificial atoms as they have discrete electronic states similar to that of actual atoms.

2.3.1 Tunnel junctions

Tunnel junctions that couple the QD to the source and drain are based on the tunnel effect. The tunnel effect is a quantum mechanical phenomenon where particles, such as electrons or holes, have a non-zero probability of tunneling through a potential barrier. This phenomenon is due to the existence of wavefunction solutions to the Schrödinger equation when the particles energy E is less than the potential barrier V_0 . The wavefunctions are [52]

$$\psi(z) = \psi(0)e^{-\frac{\sqrt{2m^*(V_0-E)}}{\hbar}z}, \quad (2.33)$$

where $\psi(0)$ is the wavefunction at the edge of the barrier and z is perpendicular to the barrier in real space. Though decaying rapidly, the wavefunction permits a particle to pass through a barrier, which would not be possible in classical mechanics. The tunnel effect is an important phenomenon in nanotechnology and will be referred to throughout this thesis.

The tunnel junction can be represented in terms of a conventional circuit element, through which a small current, such as a single electron passes. The tunnel junction can be described as a leaky capacitor, with a capacitance C in parallel with a resistance R . The resistance describes the opacity of the barrier, whereas the capacitance characterises the capacitance between the conducting or semiconducting elements that are separated by an insulating barrier. Like in a standard capacitor, charge accumulates at the potential barrier, which justifies its description as a leaky capacitor

2.3.2 The constant interaction model

The constant interaction model is widely used to model a quantum dot in order to describe its transport properties. This model has been described in detail in Refs. [53, 43]. In the following, I will outline the constant interaction model. My discussion is based on Refs. [54, 55].

Figure 2.4 (b) shows a circuit representation of the QD system. In this model, the source and drain reservoirs have defined potentials of V_S and V_D , respectively. Further, the QD is capacitively coupled, by a gate capacitance C_G , to a gate electrode with potential V_G , which adjusts the electrostatic potential of the QD. The tunnel junctions to the source and drain are modeled as leaky capacitors with a constant capacitance $C_{S,D}$ and resistance $R_{S,D}$. The resistance defines the tunnel rates $\Gamma_{S,D}$ between the leads and the QD. Finally, the QD has a potential V_{CD} and charge Q_D .

The major benefit of the constant interaction model is the simplification of the complex electron-electron interactions. Electron-electron interactions occur not only

between existing electrons on the dot but as well as between the charges of the QD and the environment. In the constant interaction model this interaction is parameterised by the total capacitance of the system C_Σ , which is assumed to be constant. The total capacitance is the sum of the three contributing capacitances:

$$C_\Sigma = C_S + C_D + C_G. \quad (2.34)$$

In this model the QD is considered as a classical dot with a potential of V_{CD} . Applying the definition of charge on a capacitor to the respective capacitances and fixed voltages of the leads and gate electrode, we can estimate the charge on the dot by

$$Q_D = C_S(V_{CD} - V_S) + C_D(V_{CD} - V_D) + C_G(V_{CD} - V_G). \quad (2.35)$$

The electrostatic energy of a capacitor, defined as $U = \frac{1}{2}CV^2$, is combined with Eq. 2.35 to determine the electrostatic energy of the dot, which is

$$U_{CD}(N) = \frac{1}{2C_\Sigma} [-|e|(N - N_0) + C_S V_S + C_D V_D + C_G V_G]^2, \quad (2.36)$$

where the charge of the dot has been described in terms of the number of charges on the dot N by $Q_{CD} = -|e|(N - N_0)$, where N_0 takes into account background charges from donors or acceptors in the dot's structure.

Eq. 2.36 suggests that the electrostatic potential of the dot can be continuously tuned by varying the source, drain and gate voltages. For instance, by increasing V_G U_{CD} increases quadratically. However, to maintain the system in the ground state the electrostatic potential must be minimised. At critical gate voltages, it becomes energetically favorable to increase N by loading a charge onto the dot. This reduces U_{CD} by reducing the quadratic term by $|e|$, see Eq. 2.36, thus maintaining the ground state. As such, V_G can be used to tune the number of charges on the dot.

The discussion so far has only considered the QD system classically. The charging energy is a classical parameter and is associated with the Coulomb interaction between the charges of the QD, reservoirs and gate electrode. In the constant interaction approximation, E_C is modeled classically in terms of capacitances and is defined as

$$E_C = \frac{e^2}{C_\Sigma}. \quad (2.37)$$

This approach is sufficient to model classical dot systems such as single electron transistors (SETs), however it does not take into account quantum effects associated with confinement such as the atom-like quantised energy spectrum. The constant interaction model incorporates such quantum effects by introducing the single-particle energy levels of the QD E_N . With this the total energy of the system becomes

$$U_{QD}(N) = U_{CD}(N) + \sum_{n=1}^N E_n. \quad (2.38)$$

The electrochemical potential of the QD $\mu_{QD}(N)$ denotes the energy change of the QD due to the transition between the N charge ground state and the $N - 1$ charge

ground state. $\mu_{\text{QD}}(N)$ is defined as:

$$\mu_{\text{QD}}(N) = U_{\text{QD}}(N) - U_{\text{QD}}(N - 1) \quad (2.39)$$

$$= E_C \left(N - N_0 - \frac{1}{2} \right) - \frac{E_C}{|e|} (C_S V_S + C_D V_D + C_G V_G) + E_N. \quad (2.40)$$

Charge tunneling through the QD depends on the alignment of the electrochemical potential of the QD with respect to those of the source μ_S and drain μ_D . If $\mu_{\text{QD}}(N)$ is smaller than μ_S , then a charge can tunnel from the source to the QD, giving rise to a QD with N charges. If $\mu_{\text{QD}}(N)$ is larger than μ_D , then this charge can tunnel from the QD to the drain giving rise to a QD with $N - 1$ charges. The number of charges alternate between $N - 1$ and N . If $\mu_{\text{QD}}(N)$ does not satisfy these conditions, then the number of charges in the dot is fixed.

The electrochemical potentials of the transition between successive ground states form a ladder. The gate voltage can moved up or down the whole ladder. The difference between two electrochemical potentials, so between two successive levels of the ladder is constant and called the addition energy. With this, we introduce the addition energy $E_{\text{add}}(N)$, the energy cost of adding an additional charge to the QD with N charges. $E_{\text{add}}(N)$ is expressed by

$$E_{\text{add}}(N) = \mu(N + 1) - \mu(N) = E_C + \delta_N, \quad (2.41)$$

where $\delta_N = E_{n+1} - E_n$ is the energy spacing between two discrete quantum levels, known as the single-particle level spacing.

In the case of a classical dot, the addition energy is equal to the charging energy E_C , which is the electrostatic energy associated to the Coulomb repulsion between a charge and the charges in the QD, the reservoir and the gate. If the dimension of the dot is small enough to induce quantization of the energy of dot, then the addition energy is the sum of the charging energy plus the energy spacing between two discrete quantum level

In the spin-degenerate case, δ_N can be zero when consecutive electrons are added to the same orbital. This is due to the Pauli exclusion principle, which permits two electrons of opposite spin to exist in the same orbital. It should be noted that E_{add} incorporates both the classical electrostatic part, the charging energy E_C and the quantum effect, the single-particle level spacing δ_N .

Gate lever arm

The gate lever arm (α_i) translates the gate voltage into the energy of the QD. Given the capacitive coupling between the gate and the QD, the potential energy of the gate electrode does not translate 1-1 to the energy applied to the QD. The gate lever arm defines the translation between the gate voltage V_i and the electrochemical potential $\mu(N)$ of the QD by

$$\alpha_i = \frac{C_i}{C_\Sigma}. \quad (2.42)$$

2.3.3 Case of zero-bias (Coulomb oscillations)

To describe the transport properties of a QD, we will consider the system in terms of electrochemical potential energies of the source μ_S , drain μ_D and dot $\mu(N)$. For simplicity, we assume that the QD system is at zero temperature and $\mu_{S,D} = -|e|V_{S,D}$. The electrochemical potentials of the reservoirs can be adjusted by applying a voltage bias to the respective metallic leads. As discussed above a gate voltage is used to adjust the electrochemical potential of the dot. By adjusting the voltages, different transport effects can be obtained.

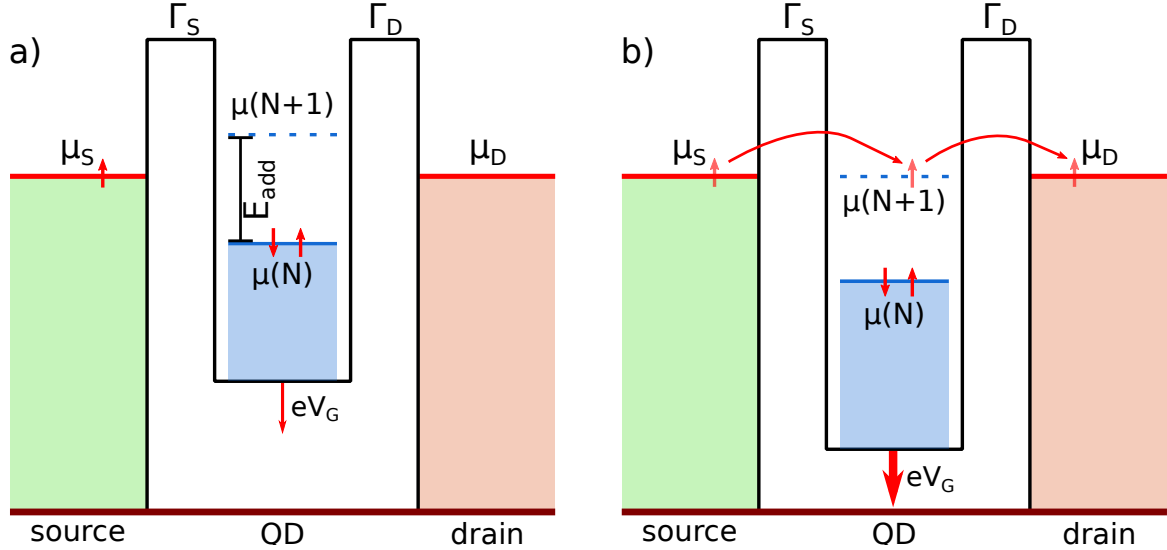


Figure 2.5 – Energy diagram showing the quantum dot (QD) (a) when the energy level $\mu(N+1)$ is off resonance and no charge can transfer from the source to the QD or from the QD to the drain. (b) By increasing the gate voltage V_G , the QD's energy level $\mu(N+1)$ is shifted down to be on resonance with the source and drain. A charge can now tunnel from the leads into the QD and vice-versa. When on resonance the QD is in a degenerate charge number state of N and $N+1$ charges, hence this point is referred to as the charge degeneracy point. By applying a small voltage bias, a measurable current through the QD will be induced.

First, we will consider the case when $\mu_S = \mu_D$, here the voltage bias across the QD approaches zero, therefore $V_S = V_D = 0$. Figure 2.5 (a) shows a typical energetic scenario of the QD system at zero-bias. Two consecutive energy levels of the QD are labelled $\mu(N)$ and $\mu(N+1)$. Energy levels that are below the electrochemical potential of the leads $\mu(N) < \mu_{S,D}$ are filled with charges. The filled orbitals below $\mu(N)$ are represented collectively by the shaded blue region.

In Figure 2.5 (a) the quantised energy levels of the QD are misaligned with the electrochemical potentials of the leads as $\mu(N) < \mu_{S,D} < \mu(N+1)$. This misalignment prevents charges from tunneling into the QD, thus blocking the flow of charge through the dot. This phenomenon is referred to as Coulomb blockade.

By adjusting the potential applied to the electrostatic gate V_G , the electrochemical potential of the QD's energy levels can be aligned with that of the leads. Figure 2.5 (b) shows such alignment where $\mu(N) = \mu_{S,D}$. In this scenario charges can tunnel in and out of the QD through resonant tunneling. By applying a small voltage bias current

will be induced in a certain direction. We can generalise the loading and unloading of charges on and off the QD by the following: for $\mu_S = \mu(N)$ the QD will transition from an N to $N - 1$ state whereas when $\mu_S = \mu(N + 1)$ the QD will transition from an N to $N + 1$ state. Given the tunneling of charge, we would expect to see current peaks at certain gate voltages V_G when the condition that,

$$\mu_S = \mu(N) = E_C \left(N - N_0 - \frac{1}{2} \right) - \frac{E_C}{|e|} (C_G V_G) + \delta_N \quad (2.43)$$

is met. This condition is equivalent for μ_D . When this condition is met, the QD's energy level $\mu(N)$ is on resonance with the leads. The QD is in a degenerate charge number state of N and $N+1$ charges. This point of resonance is referred to as the charge degeneracy point.

Eq. 2.43 can be solved for V_G , giving

$$V_G = \frac{1}{e\alpha_G} \left[E_C \left(N - N_0 - \frac{1}{2} \right) + E_N - \mu_S \right] \quad (2.44)$$

where we have introduced the gate lever arm $\alpha_G = \frac{C_G}{C_\Sigma}$. With this we can conclude that two consecutive current peaks of N and $N + 1$ have the gate voltage spacing of

$$\Delta V_G(N) = \frac{1}{e\alpha_G} E_{\text{add}}(N), \quad (2.45)$$

where E_{add} is the addition defined in Eq. 2.41.

The constant interaction model assumes that E_C is constant with respect to charge number. Though not completely valid for semiconductors, in the many-charge regime such an assumption is reasonable. In the case of SETs, the conductance peaks are generally equidistant in V_G due to the dominance of E_C over the single-particle level spacing δ_N . As the single-particle level spacing of the QD becomes comparable to E_C the fluctuations in ΔV_G are associated with fluctuations in δ_N .

2.3.4 Case of varying V_G and V_{SD} (Coulomb Diamonds)

By lifting the restriction on the voltage bias V_{SD} richer transport features are observed in QD systems. To understand such features, we will consider the conductance as a function of V_G and $V_{S,D}$. To simplify the description the source lead is considered to be grounded. As such, μ_S is constant and $\mu_D = \mu_S - eV_{SD}$ is tuned by an applied voltage bias. From the discussion of the constant interaction model, we know that current only occurs when the chemical potential of the dot is aligned with or within the bias window of the leads i.e. $\mu_S \geq \mu(N) \leq \mu_D$. As such, there is a boundary that is dependent on V_G and $V_{SD} \equiv V_D$, which defines a region of zero current. By definition of conductance $G = \frac{dI}{dV}$, this boundary is a line of finite conductance.

To be in the Coulomb blockade region with fixed charge, a QD with N charges must satisfy

$$\mu(N) < \mu_S - eV_D \quad (2.46)$$

and

$$\mu(N + 1) > \mu_S, \quad (2.47)$$

2.3 TRANSPORT IN QUANTUM DOTS

for $V_D > 0$. From the conditions of Coulomb blockade, we can define an expression for the border lines which mark out the blockade region. For positive bias we obtain

$$V_G = \frac{1}{e\alpha_G} \left[E_C \left(N - N_0 - \frac{1}{2} \right) - \mu_S + e(1 - \alpha_D V_D) + \delta_N \right], \quad (2.48)$$

$$V_G = \frac{1}{e\alpha_G} \left[E_C \left(N - N_0 + \frac{1}{2} \right) - \mu_S - e\alpha_D V_D + \delta_{N+1} \right]. \quad (2.49)$$

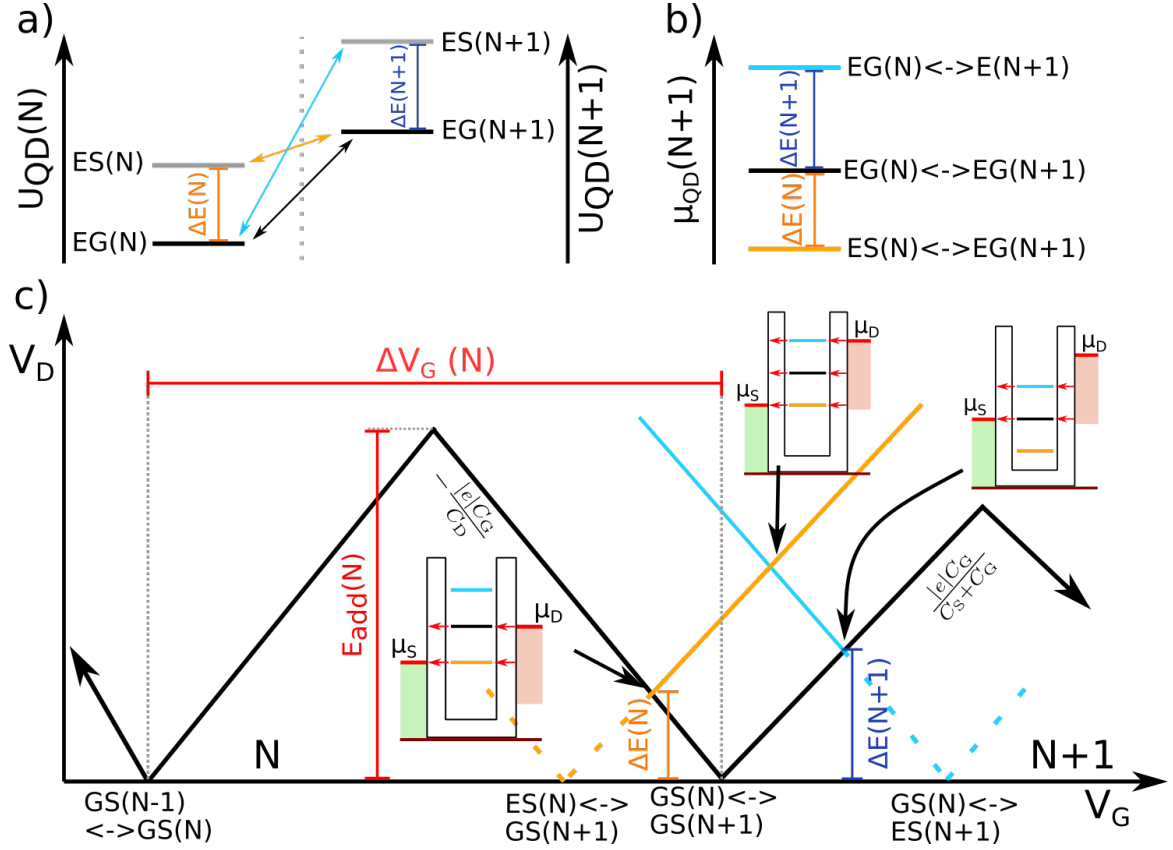


Figure 2.6 – Schematic describing transport in a QD under V_G and V_D bias. (a) Energy diagram of QD with N electrons $U_{QD}(N)$ and with $N+1$ electrons $U_{QD}(N+1)$. Possible QD energy transitions are designated by arrows. (b) Schematic showing the electrochemical potential of the QD for the transitions shown in (a). (c) Schematic plot of a typical QD stability diagram showing differential conductance dI_D/V_D versus V_G and V_D . The energy diagram of the QD associated with the observed conductance feature is depicted at certain locations. Further, the way $E_{\text{add}}(N+1)$ and $\Delta V_G(N+1)$ are extracted from the stability diagram is depicted in red.

Figure 2.6 (c) illustrates, schematically, a typical stability diagram of a QD, which is biased by V_D and V_G . In Figure 2.6 (c) the conductance boundary lines given by Eqs. 2.48,2.49 are plotted in black. Below the V-shaped boundary lines, the system is in the Coulomb blockade regime where the charge on the QD is fixed.

When the V-shape boundary lines meet the V_G axis, $V_D = 0$ V, the QD electrochemical potential $\mu(N)$ is on resonance with the leads. This permits resonant tunneling between the QD and the leads. At this point, labeled $GS(N) \longleftrightarrow GS(N+1)$

in Figure 2.6 (c), the QD is in a charge degeneracy state of $\text{GS}(N)$ and $\text{GS}(N + 1)$, where GS is the ground state. The QD charge degeneracy state of $\text{GS}(N - 1)$ and $\text{GS}(N)$ is also depicted in Figure 2.6 (c) and is labeled, $\text{GS}(N - 1) \longleftrightarrow \text{GS}(N)$.

The gate voltage difference between these two charge degeneracy points, labeled ΔV_G , is related to E_{add} by Eq. 2.45. As such, if one has an estimate for the gate lever arm α_G , one can estimate the addition energy $E_{\text{add}}(N)$. On the other hand, $E_{\text{add}}(N)$ can be extracted directly from the stability diagram by reading off the V_D at which the V-shape boundary lines meet for $V_D > 0$. See the $E_{\text{add}}(N)$ annotation on Figure 2.6 (c).

From the slopes of the boundary lines dV_D/dV_G , we can determine a ratio between the source and drain capacitance and the gate capacitance. The derivative of the positively sloped boundary gives the ratio

$$|e| \frac{\alpha_G}{1 - \alpha_D} = |e| \frac{C_G}{C_S + C_G}, \quad (2.50)$$

whereas the negatively sloped boundary gives the ratio

$$-|e| \frac{\alpha_G}{\alpha_D} = -|e| \frac{C_G}{C_D}. \quad (2.51)$$

The slopes are labeled on Figure 2.6 (c).

Tunneling through excited states

In QD systems charge tunneling can also occur through excited charge states of the QD. These excited charge states can be accessed by increasing V_D such that the excited charge state $\text{ES}(N)$ falls within the bias window. The availability of another channel, through which charge can tunnel, increases the probability of charge tunneling, which leads to an increase in current. This increase in current results in a finite conductance that can be observed in stability diagrams.

Figure 2.6 (c) shows the expected conductance features due to excited state tunneling. The orange conductance curve that intersects the black boundary line of the N th fixed charge state results from the availability of the excited charge state of the N th charge $\text{ES}(N)$. Along the orange conductance line charge can pass through $\text{ES}(N)$ and $\text{GS}(N + 1)$. The energy diagram on Figure 2.6 (c) depicts the tunneling of charge through the QD via two charge states. Here, there are two possible QD state transitions; $\text{GS}(N) \longleftrightarrow \text{GS}(N + 1)$ or $\text{ES}(N) \longleftrightarrow \text{GS}(N + 1)$. The transitions between the ground and excited states are depicted using an energy diagram in 2.6 (a). Figure 2.6 (b) shows the the electrochemical potential ladder of the QD. The three energy levels through which tunneling occurs are shown with their associated QD transitions. It should be noted that the electrochemical potential of the transition $\text{ES}(N) \longleftrightarrow \text{GS}(N + 1)$ is smaller than $\text{GS}(N) \longleftrightarrow \text{GS}(N + 1)$.

Above the stability region of the $N + 1$ charge state another conductance feature is observed (blue line) that intersects the positively sloped border line. This conductance feature results from the availability of the excited charge state of the $N + 1$ th charge $\text{ES}(N + 1)$. Along the blue conductance line transport can occur via charge tunneling into the $\text{GS}(N + 1)$ state or into the additional $\text{ES}(N + 1)$ state. In this case, the possible QD state transitions are either $\text{GS}(N) \longleftrightarrow \text{GS}(N + 1)$ or $\text{GS}(N) \longleftrightarrow \text{ES}(N + 1)$. At the

point where the blue and orange lines cross; the large voltage bias window makes all three channels available for transport.

Importantly, the energy difference between the ground and excited states can be determined directly from the stability diagrams. By reading off the bias voltage, where a conductance line that involves excited state tunneling (orange or blue) meets the V-shape boundary (black), one can estimate energy spacing between the GS (N) and ES (N), ΔE . Annotations on Figure 2.6 (c) show how ΔE can be retrieved.

In Chapter 5 we will show that at certain gate voltages the Al-Ge-Al nanowire heterostructure behaves like a QD system. We will make use of the concepts that have been described to characterise our system.

2.4 Superconductivity

Superconductivity came as a surprise to the physics community when it was experimentally discovered in 1911 by Heike Kamerlingh Onnes, while measuring the low temperature conductivity of mercury. After its discovery, many other superconducting solids, including Aluminium (Al), which was observed to transition into a superconducting state at 1.2 K in 1958 [56]. Another property of superconductors other than zero resistance, is the expulsion of a magnetic field in a metal transitioning from a normal to a superconducting state. This phenomenon was discovered by Meissner and Ochsenfeld in 1933 [57]. This Meissner-Ochsenfeld effect could not be explained by perfect conductivity, making it an important characteristic of superconductivity. In light of these experimental discoveries, the London brothers adapted Maxwell equations to describe the superconducting electrodynamics [58]. This suggestive approach assumed the existence of superconducting electrons that move within the lattice without resistance. This understanding, evolved into a phenomenological theory in 1950 with the Ginzburg-Landau theory. A complete microscopic description of superconductivity arrived in 1957 when Bardeen, Cooper and Schrieffer proposed BCS theory [59].

In Appendix A, I have provided an introduction to BCS theory, which is partly based on Ref. [60]. I have written this introduction with the goal of improving my own understanding of BCS theory and to provide an introduction useful to a master or PhD student embarking on a project on superconducting hybrid junctions. In this section, I will discuss the important concepts and formalism that are needed to understand the discussion on superconducting junctions.

At very low temperatures it is possible for attractive interactions between electrons to overcome the Coulomb repulsion and form a bound pair. This bound electronic pair, known as a Cooper pair, is the basis of BCS theory of superconductivity. In BCS theory, the superconductor is modeled using second quantisation and is defined by the Hamiltonian

$$\hat{H} = \sum_{k,\sigma=\uparrow,\downarrow} \xi_{k\sigma} \hat{c}_{k\sigma}^\dagger \hat{c}_{k\sigma} + \sum_{\vec{k},\vec{k}'} V_{\vec{k}\vec{k}'} \hat{c}_{\vec{k}\uparrow}^\dagger \hat{c}_{-\vec{k}\downarrow}^\dagger \hat{c}_{\vec{k}'\uparrow} \hat{c}_{-\vec{k}'\downarrow}, \quad (2.52)$$

where, $\xi_{\vec{k}} = \epsilon_{\vec{k}} - \mu$, is the energy of the particle state above the chemical potential μ . μ is taken to be the point of zero kinetic energy. Here, $V_{\vec{k}\vec{k}'}$ is the interaction potential between the electron pair.

The Hamiltonian of Eq. 2.52 makes use of second quantisation operators, which are defined as

- $\hat{c}_{\vec{k}\uparrow}^\dagger$ **creation operator**: Creates a fermion with momentum \vec{k} and spin $\frac{1}{2}$ (up).
- $\hat{c}_{\vec{k}\downarrow}$ **annihilation operator**: Destroys a fermion with momentum \vec{k} and spin $-\frac{1}{2}$ (down).
- $\hat{n}_{k\sigma} = \hat{c}_{k\sigma}^\dagger \hat{c}_{k\sigma}$ **particle number operator**: counts the number of particles with momentum \vec{k} and spin $\sigma = \uparrow, \downarrow$.

Importantly, these fermionic operators must obey the anti-commutator relation

$$\{\hat{c}_{k\sigma}, \hat{c}_{k'\sigma'}^\dagger\} = \delta_{\vec{k}\vec{k}'} \delta_{\sigma\sigma'}, \quad (2.53)$$

2.4 SUPERCONDUCTIVITY

where $\delta_{i,j}$ is the Kronecker delta, defined as

$$\delta_{i,j} = \begin{cases} 0 & \text{if } i \neq j \\ 1 & \text{if } i = j. \end{cases} \quad (2.54)$$

By applying a mean field approximation to the attractive interaction the \hat{H} of Eq. 2.52 can be simplified to

$$\hat{H}_{\text{BCS}} = \sum_{\vec{k}, \sigma=\uparrow, \downarrow} \xi_{\vec{k}\sigma} \hat{c}_{\vec{k}\sigma}^\dagger \hat{c}_{\vec{k}\sigma} - \sum_{\vec{k}} \left(\Delta_{\vec{k}}^\dagger \hat{c}_{-\vec{k}\downarrow} \hat{c}_{\vec{k}\uparrow} + \Delta_{\vec{k}} \hat{c}_{\vec{k}\uparrow}^\dagger \hat{c}_{-\vec{k}\downarrow}^\dagger \right). \quad (2.55)$$

Here, the complex pairing term $\Delta_{\vec{k}}$ has been introduced to describe the attraction interaction that defines superconductivity. One can consider that $\Delta_{\vec{k}}$ is the *source* of the superconductivity.

The ground state of the BCS Hamiltonian is given by

$$|\psi_G\rangle = \prod_{\vec{k}} (u_{\vec{k}} + v_{\vec{k}} \hat{c}_{\vec{k}\uparrow}^\dagger \hat{c}_{-\vec{k}\downarrow}^\dagger) |\phi_0\rangle, \quad (2.56)$$

where $|v_{\vec{k}}|^2$ is the probability that a pair ($\vec{k} \uparrow, -\vec{k} \downarrow$) is occupied, whereas the probability of not being occupied is $|u_{\vec{k}}|^2$. By the nature of probabilities, the condition $|u_{\vec{k}}|^2 + |v_{\vec{k}}|^2 = 1$ must be met.

In order to determine the coefficients $u_{\vec{k}}$ and $v_{\vec{k}}$ \hat{H}_{BCS} is diagonalised using a canonical transformation, known as the Bogoliubov transformation. In the canonical transformation the particle creation $\hat{c}_{\vec{k}\uparrow}^\dagger, \hat{c}_{-\vec{k}\downarrow}^\dagger$ and annihilation $\hat{c}_{\vec{k}\uparrow}, \hat{c}_{-\vec{k}\downarrow}$ operators in terms of creation $\gamma_{\vec{k}\sigma}^\dagger$ and annihilation $\gamma_{\vec{k}\sigma}$ operators of quasiparticle excitations, given by:

$$\hat{c}_{\vec{k}\uparrow} = u_{\vec{k}}^* \hat{\gamma}_{\vec{k}\uparrow} + v_{\vec{k}} \hat{\gamma}_{\vec{k}\downarrow}^\dagger \quad \hat{c}_{-\vec{k}\downarrow} = u_{\vec{k}}^* \hat{\gamma}_{\vec{k}\downarrow} - v_{\vec{k}} \hat{\gamma}_{\vec{k}\uparrow}^\dagger \quad (2.57)$$

$$\hat{c}_{-\vec{k}\downarrow}^\dagger = -v_{\vec{k}}^* \hat{\gamma}_{\vec{k}\uparrow} + u_{\vec{k}} \hat{\gamma}_{\vec{k}\downarrow}^\dagger \quad \hat{c}_{\vec{k}\uparrow}^\dagger = v_{\vec{k}}^* \hat{\gamma}_{\vec{k}\downarrow} + u_{\vec{k}} \hat{\gamma}_{\vec{k}\uparrow}^\dagger. \quad (2.58)$$

Using the canonical transformation, the diagonalised Hamiltonian becomes

$$\hat{H} = \sum_{\vec{k}} (E_{\vec{k}} \hat{\gamma}_{\vec{k}\uparrow}^\dagger \hat{\gamma}_{\vec{k}\uparrow} + E_{\vec{k}} \hat{\gamma}_{\vec{k}\downarrow}^\dagger \hat{\gamma}_{\vec{k}\downarrow}) + \Xi, \quad (2.59)$$

where $E_{\vec{k}} = \sqrt{(\xi_{\vec{k}}^2 + |\Delta_{\vec{k}}|^2)}$. Here, Ξ can be considered as a constant offset energy. From the Bogoliubov transformation the coefficients are found to be

$$|v_{\vec{k}}|^2 = 1 - |u_{\vec{k}}|^2 = \frac{1}{2} \left(1 - \frac{\xi_{\vec{k}}}{E_{\vec{k}}} \right), \quad (2.60)$$

which is in agreement with the original variational method of BCS.

For superconductors with s-wave pairing, such as aluminium, the order parameter is defined by $\Delta_{\vec{k}} = |\Delta| e^{i\varphi}$, where φ is the superconducting phase. At T = 0 K, there are no quasiparticle excitations and the order parameter reduces to the same expression

as that in the variational method, given by

$$\Delta = \frac{\hbar\omega_D}{\sinh(1/\rho(0)V)} \approx 2\hbar\omega_D e^{-1/\rho(0)V}. \quad (2.61)$$

The order parameter is dependent on the state of the system, thus it depends on how many quasiparticles exist. The number of quasiparticles depends on the temperature of the superconductor. As the temperature increase, the number of quasiparticles increases, which reduces the order parameter. The temperature at which $\Delta(T) \rightarrow 0$ defines the critical temperature T_C of the superconductor. According to BCS theory, T_C is given by

$$T_c = \frac{\Delta(0)}{1.764k_B}. \quad (2.62)$$

The temperature dependence of the gap can be determined numerically. The result, which is universal for superconductors in the weak coupling regime, reveals that near $T = 0$ the decay of $\Delta(T)$ is exponentially slow and nearly insensitive to T . As T approaches T_c , $\Delta(T)$ decays rapidly, reaching a vertical tangent. In fact, near T_c , $\Delta(T)$ is approximated by

$$\frac{\Delta(T)}{\Delta(0)} \approx 1.74 \left(1 - \frac{T}{T_c}\right)^{1/2}, \quad T \approx T_c. \quad (2.63)$$

BCS Density of States

Now we have a definition for the superconducting gap, we can define the density of states (DOS) of a superconductor. From our theoretical analysis, we understand that there exists a region where no quasi-particles can exist. From the density of states of a normal metal $\rho_N(0)$, which we assume to be constant, we obtain the DOS of a superconductor by introducing the energy states of the superconductor giving

$$\rho_S(E) = \frac{1}{2}\rho_N(0) \begin{cases} \frac{|E|}{\sqrt{E^2 - \Delta^2}} & \text{if } |E| > \Delta \\ 0 & \text{otherwise.} \end{cases} \quad (2.64)$$

Figure 2.7 shows the DOS of a superconductor.

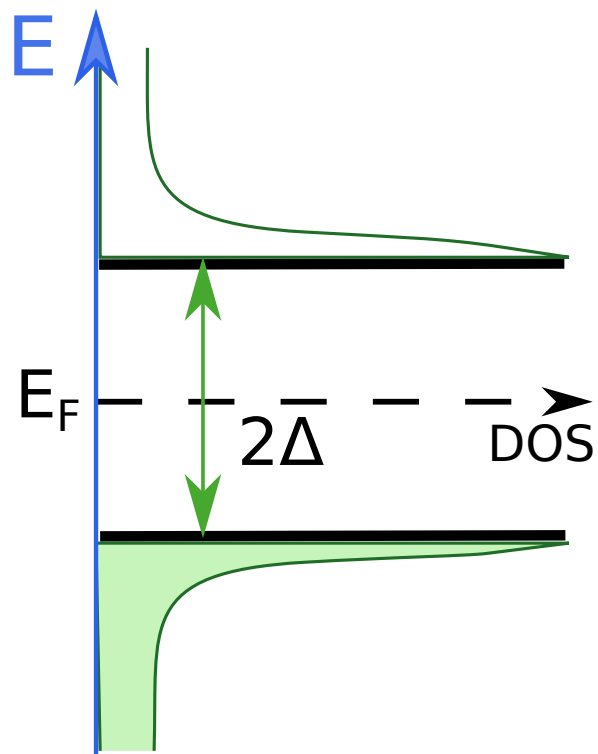


Figure 2.7 – Quasiparticle spectrum of the superconducting ground state in the one-particle representation. In the ground state, all the quasiparticle states below E_F are filled, whereas all states above E_F are empty. Notably, all quasiparticle states of energy $|E - E_F| < \Delta$ are forbidden. This defines the superconducting gap.

2.5 Superconducting Junctions

In the previous section, superconductors were considered in their isolated bulk form. In this section, we will consider the effects of introducing non-superconducting materials in contact with superconductors. Superconducting hybrid junctions are created by connecting two superconductors S via a weak-link X. S-X-S junctions are a focus of extensive research thanks to their interesting physics and potential application as quantum devices. In this thesis, we investigate the transport properties of superconducting-semiconducting-superconducting junctions based on germanium nanowires. Therefore, it is important that the reader has a good understanding of the transport physics of such systems.

We will first introduce the superconducting proximity effect, which is the general name used to describe the effect that superconductors have on non-superconductors when in contact. Then, we will provide a microscopic description of the proximity effect, which is based on Andreev reflection at the S-X interface. We will use this phenomenon to describe the transport properties of superconducting hybrid junctions. We will focus on two different junctions: S-N-S junctions, where the weak-link is a normal metal and S-QD-S junctions, where the weak-link is a quantum dot (QD).

The considerable research conducted on superconducting hybrid junctions has produced a plethora of noteworthy theses and publications. The theses of Pillet, Bretheau and Szombati [61, 62, 63] have been particularly useful in aiding my understanding of this subject. These theses have provided motivation for parts of the following discussion.

2.5.1 Proximity Effect

When a superconductor is in contact with a non-superconducting material, such as a normal metal, there is a leakage of Cooper pairs from the superconductor S to the normal metal N and a leakage of quasiparticles from N to S [64]. The diffusion of Cooper pairs into N results in a superconducting gap being induced in the region of the normal metal near the superconductor. This is known as the superconducting proximity effect. On the other hand, quasiparticle diffusion into S, reduces the magnitude of the superconducting order parameter near the interface. This is referred to as the inverse proximity effect. Furthermore, the transition temperature of an S-N system is reduced by the presence of the contaminating normal charge states. It has been shown, that by contacting normal metals with very thin superconducting films, superconductivity can be completely suppressed by the non-superconducting metal [65].

The proximity effect was first observed by R. Holm and W. Meissner in 1932, where they observed zero resistance through superconducting-normal-superconducting layers [66]. Before detailing the microscopic explanation of the proximity effect in terms of Andreev states, I will provide a qualitative description of the proximity effect.

Figure 2.8 shows a schematic plot of the order parameter near an N-S interface. We can see that the superconducting order parameter Δ is non-zero in N. This describes the leakage of Cooper pairs into N, which decay at length scales defined by the normal metal's coherence length ξ_N . Close to the N-S interface $|x| < \xi_N$, superconducting properties are induced in the normal metal, this includes an induced superconducting gap Δ^* . Furthermore, we observe the inverse proximity effect, the reduction of the

order parameter in S due to the leakage of quasi particles from N. This reduction is non-negligible at length scales less than the superconducting coherence length ξ_0 .

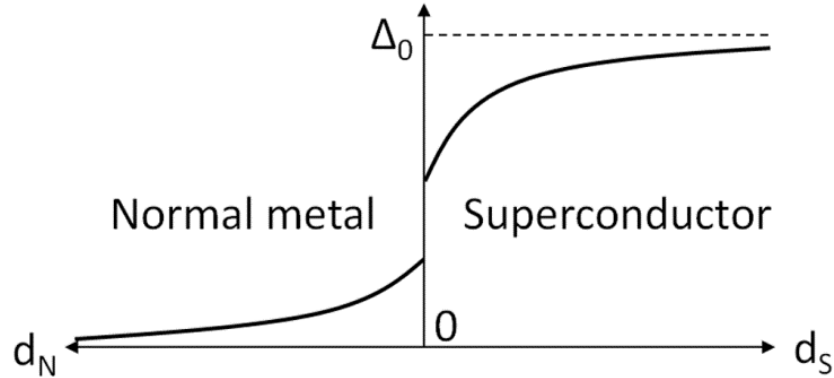


Figure 2.8 – Schematic plot showing the superconducting order parameter Δ near a normal metal N and superconductor S interface. We observe the leakage of Δ in N, close to the N-S interface. Though not shown on the figure, Δ exists in N up to a distance of the normal coherence length ξ_N away from the interface. We also observe the reduction of Δ from the bulk superconducting order parameter Δ_0 , near the N-S interface. This reduction is non-negligible at length scales less than the superconducting coherence length ξ_0 .

2.5.2 Microscopic description of the proximity effect

To help model the dynamics near the interface between a normal metal and a superconductor, we will first define the BCS variational coefficients $u_{\vec{k}}$, $v_{\vec{k}}$ in terms of electron-like and hole-like states. This new formalism means that normal charge states and superconducting states can be defined using the same terms. This allows the use of scattering methods to describe charge transport through a superconducting-metal interface.

Superconducting states to electron-like and hole-like states

One-particle states of superconductors and normal metals share a four-fold degeneracy. This four fold degeneracy stems from the wavevector degeneracy $\pm\vec{k}$ and the kinetic energy degeneracy $\pm\xi$. Recalling the plane wave solutions of electrons and holes in normal metals, it is reasonable to consider superconducting solutions of the form of

$\begin{pmatrix} u_e \\ v_e \end{pmatrix} e^{\pm ik_e x}$ and $\begin{pmatrix} u_h \\ v_h \end{pmatrix} e^{\pm ik_h x}$ for electron-like and hole-like states, respectively. Such solutions would also be valid in the normal regime of a superconductor when $\Delta \rightarrow 0$ or when $|E_{\vec{k}}^e| \gg \Delta$. In this description, electron-like states have positive excitation energy $E_{\vec{k}}^e > 0$, whereas hole-like states have negative excitation energy $E_{\vec{k}}^h < 0$. The adapted variational parameters are determined by expressing $u_{\vec{k}}$ and $v_{\vec{k}}$ in terms of

excitation energy $E_{\vec{k}}$, rather than in terms of wavevectors \vec{k} , giving [62]

$$\left\{ \begin{array}{l} u_{e,h}(E, \varphi) = e^{i\frac{\varphi}{2}} \left(\frac{1}{2} \left[1 + \eta_{e,h} \sqrt{1 - \left(\frac{\Delta}{E} \right)^2} \right] \right)^{1/2} \\ v_{e,h}(E, \varphi) = e^{-i\frac{\varphi}{2}} \operatorname{sgn}(E) \left(\frac{1}{2} \left[1 - \eta_{e,h} \sqrt{1 - \left(\frac{\Delta}{E} \right)^2} \right] \right)^{1/2} \\ k_{e,h}(E) = k_F \left(1 + \eta_{e,h} \operatorname{sgn}(E) \frac{\sqrt{E^2 - \Delta^2}}{\mu} \right)^{1/2} \end{array} \right\}. \quad (2.65)$$

Here, $\eta_{e,h} = \pm 1$, depending on whether an electron or hole is being described and φ is the superconducting phase. Naturally, $\eta_{e,h}$ is defined by the sign of the energies, that is $\eta_{e,h} = \operatorname{sgn}(E_{\vec{k}}) \operatorname{sgn}(\xi)$, as $E_{\vec{k}}$ is negative for holes.

Defining the charge of an excitation as

$$\frac{qE}{|e|} = u_k^2 - v_k^2 = -\eta_{e,h} \sqrt{1 - \left(\frac{\Delta}{E} \right)^2}, \quad (2.66)$$

where e is the electron charge, helps reveal the electron-like and hole-like properties of the variational parameters. As $\frac{\Delta}{|E|} \rightarrow 0$ ($|E| \gg \Delta$ or $\Delta \rightarrow 0$), the eigenstates converge to pure electron-like or pure hole-like states, depending on η , as in a normal metal. However, for an excitation near the superconducting gap edge ($|E| \approx \Delta$) the eigenstate is a superposition of electrons and holes.

Analysing $k_{e,h}(E)$ of Eq. 2.65, we observe that for $|E| > \Delta$, we have $k_{e,h}(E) \in \mathbb{R}$, thus the eigenstates are purely propagating plane waves. Whereas for $|E| < \Delta$, the wavevectors are imaginary, resulting in exponentially growing or decaying solutions. Such solutions are physically allowed in instances where the states are bounded by domain walls, such as an interface with a normal metal. This results in inhomogeneity of the order parameter Δ in space.

By applying a first order Taylor expansion to $k_{e,h}(E)$, when $|E| < \Delta$, Alexander Andreev revealed that electrons can reflect as holes at an N-S interface. This phenomenon is now known as Andreev reflection and is the basis of the microscopic description of transport through superconducting junctions.

2.5.3 Superconducting-normal junctions (S-N-S)

In this section, we will consider the transport properties of superconducting junctions, where the weak-link is a normal metal N.

Transport through N-S interface: Andreev Reflection

Here, we will consider a normal metal N connected to a superconductor S. The interface of the N-S junction, depicted in the schematic of Figure 2.9, is a thin barrier of arbitrary transparency. The following discussion of this scenario is based on the BTK model established by Blonder, Tinkham and Klapwijk in 1982 [68]. In the transport domain, we will consider an incident electron e^- traveling towards the superconductor. At the N-S interface, at $x = 0$, the electron meets a thin barrier, which is represented by a delta function of strength Z . At the N-S interface, there are multiple possible outcomes depending on the electron's incident energy:

- The electron can undergo full Andreev Reflection, where it reflects as a hole of opposite spin and energy. This process is labeled A in Figure 2.9. By this process, a Cooper pair is created in the superconductor, resulting in the transport of $2e$ of charge.
- For a barrier of finite transparency, where $Z > 0$, there is a finite probability that the electron undergoes normal reflection. This process is labeled B in Figure 2.9. Under normal reflection the incident electron reflects back into the normal metal as an electron with energy E , thus no charge is transported.
- For $|E| \geq \Delta$, the electron enters the superconductor as a quasiparticle of energy E . This process is labeled C in Figure 2.9. Taking into account the degeneracy of \vec{k} , the newly created quasiparticle has either positive or negative k -momentum. To maintain charge conservation partial Andreev reflection also occurs in this scenario.

The BTK model provides a mechanism to estimate the probability of the various processes, outlined above, with respect to the incident electron energy E and the strength of the interface barrier Z . Here, I will provide a summary of the important results of the BTK model. Figure 2.10 (a) presents the probability of each of the three possible processes occurring, versus incident electron energy E for different barrier strengths. The processes are labeled A, B, and C and are in agreement with Figure 2.9. The resulting conductance from the three processes are plotted in Figure 2.10 (b) in units of normalised conductance, $R_N \frac{dI}{dV}$. Here, R_N is the normal resistance, the resistance of the N-S devices at $e|V| \gg \Delta$.

For a perfectly transparent barrier ($Z = 0$), there is no scattering at the interface. As such, for $|E| < \Delta$, Andreev reflection (process A) occurs with probability equal to 1, resulting in a conductance of $2R_N \frac{dI}{dV}$. As $|E|$ increases above Δ , the process that creates quasiparticles (process C), begins to dominate, reducing the system conductance until it plateaus at R_N for $|E| \geq 2\Delta$.

At intermediate barrier transparencies, $Z = 0.3$, normal electron reflection can occur (process B). The probability of normal reflection occurring is at a minimum at $|E| = \Delta$. Further, at this point the probability of Andreev reflection peaks. This results in a large conductance peak at $eV = \Delta$. This feature is due to the peak in

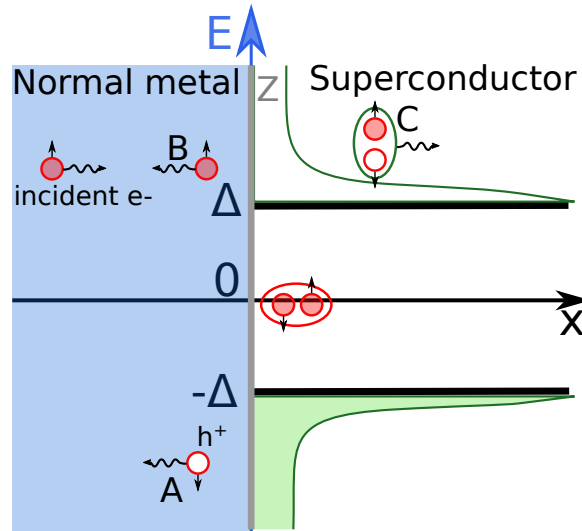


Figure 2.9 – Schematic showing Andreev reflection at the N-S interface. Depicted is an incident electron e^- of energy E travelling towards the N-S interface. At the interface multiple processes can occur. The electron can undergo Andreev reflection, where it reflects as a hole h^+ and creates a Cooper pair in S (Process A). The electron can undergo normal reflection and reflect back as an electron (Process B). Finally, for energies $|E| > \Delta$ the electron can enter the continuum of S as a quasiparticle pair (Process C).

density of states at $|E| = \Delta$. Therefore, there are many quasiparticle states available for transport, thus reducing the probability of normal reflection. As $|E|$ decrease below Δ the probability of normal reflection increases, reducing the sub-gap conductance. For very low barrier transparencies, $Z \geq 5.0$, process B dominates for $|E| < \Delta$, as such we observe no sub-gap transport.

The BTK model can be used to estimate the transparency of the interface between the superconductor and the normal metal. The I-V curve in the superconducting regime of an N-S junction, is non-linear for voltages $e|V| < \Delta$ and linear for voltages $e|V| \gg \Delta$. In the linear regime, the gradient is $1/R_N$. The difference in linearity between the two regimes is highlighted by fitting the high voltage part of the I-V curve by $I = R_N^{-1}V$. The extrapolation of the linear fit reveals that, at $V = 0$ V, the current is finite. It is defined as the excess current I_{exc} . The normalised excess current $\frac{eI_{\text{exc}}R_N}{\Delta}$ can be used to estimate the interface transparency by directly mapping onto the Z parameter, see Figure 2.10 (c). In Chapter 5 we make use of the BTK model to estimate the transmission of our Al-Ge-Al nanowire heterostructures.

2.5 SUPERCONDUCTING JUNCTIONS

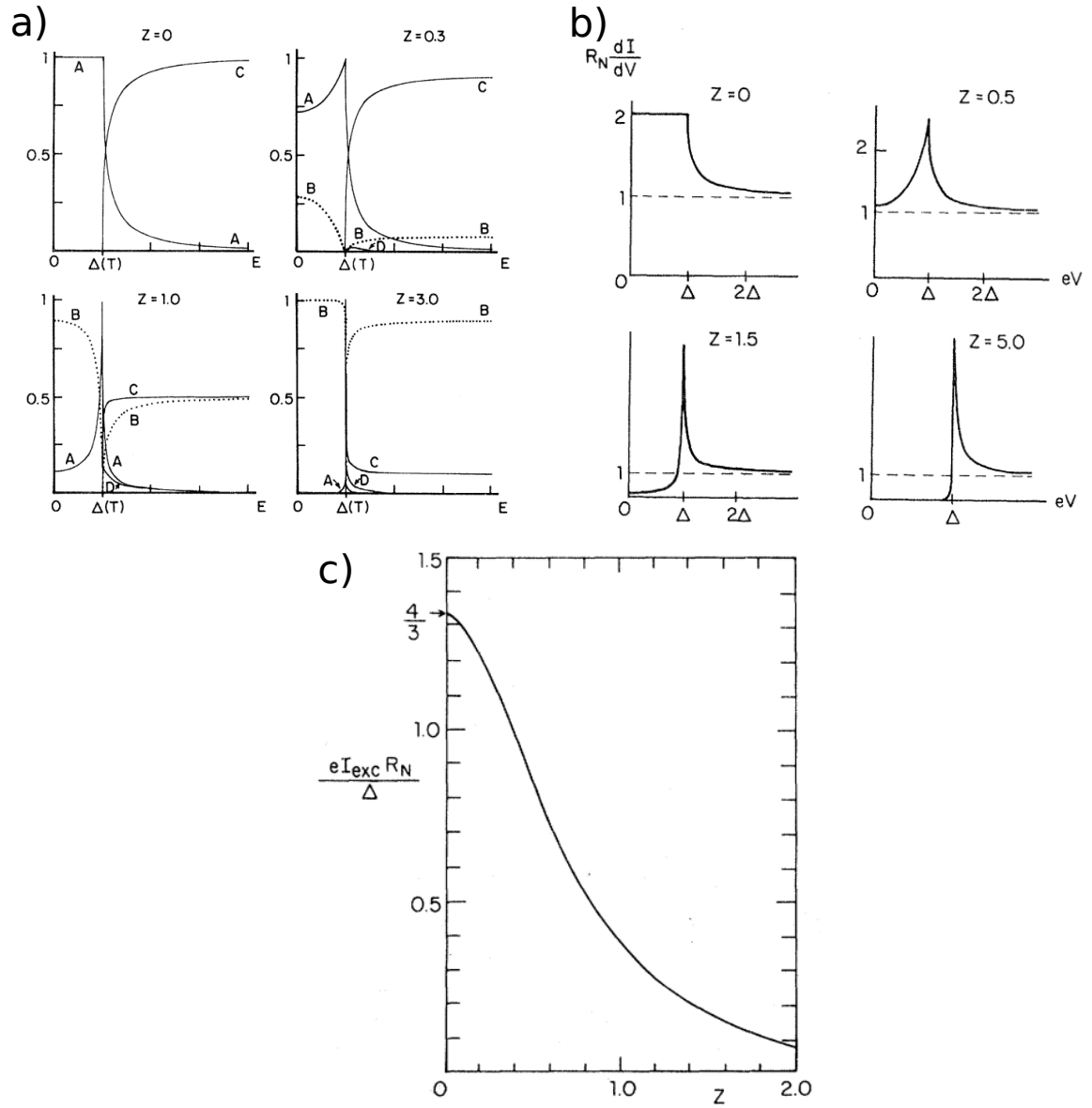


Figure 2.10 – Results of the BTK model for charge transfer and reflection about an NS interface. Figures taken from Ref. [68].

Transport through S-N-S junctions

Andreev Bound States

In the previous section, we discussed the charge transport dynamics at an N-S boundary. We showed that an electron in a normal conductor reflects as a hole at the superconducting interface through Andreev reflection. By adding a second S-N interface, opposite to the original, such as to construct an S-N-S junction, a cycle of Andreev reflections at each boundary would be expected. That is, an electron from the normal conductor would reflect as a hole at the right N-S interface and then reflect back as an electron at the left S-N interface, thus completing a cycle. This electronic cycle is shown schematically in Figure 2.11. This process is analogous to a Fabry-Perot cavity, where traveling waves reflect off two mirrors placed opposite to each other, resulting in constructively interfering waves that form bound states with discrete energies.

To achieve bound states in an S-N-S junction, the phase gained after a full cycle of two reflections, must be an integer multiple of 2π . Owing to the requirement of Andreev reflection, these bound states are called Andreev Bound States (ABS). In terms of charge transport, a single cycle results in the transfer of a charge of $2e$ from the left (source) to the right (drain) lead.

The energies of ABS can be determined by different approaches, including matching the phase of the incoming and outgoing electrons after a full cycle or a scattering matrix approach [69].

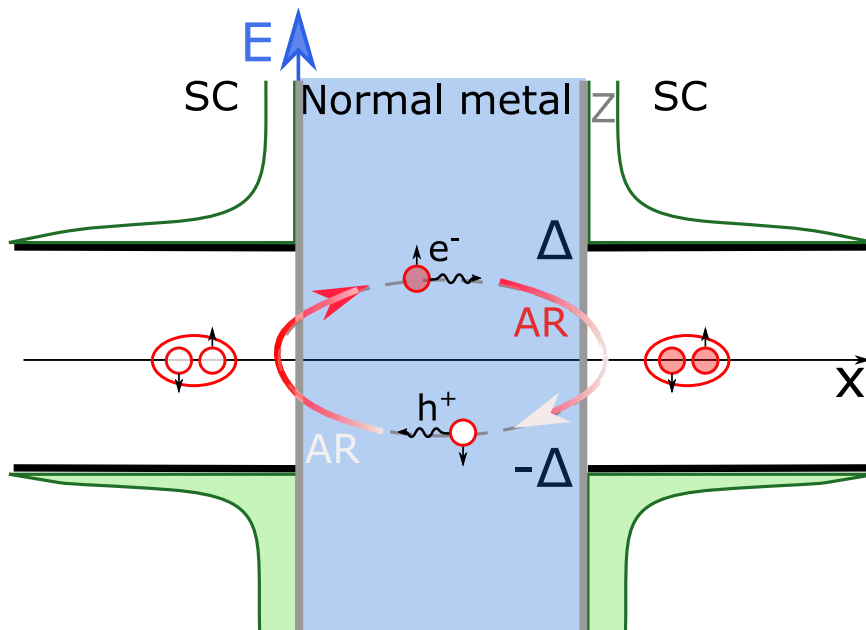


Figure 2.11 – Schematic of the formation of an Andreev Bound State (ABS) in an S-N-S junction. The ABS forms due to cycles of Andreev reflections (AR), which causes the superposition of the propagating electrons and holes in N. Each cycle results in the charge transfer of $2e$, a Cooper pair.

Calculating ABS

Developed by Beenakker and Van Houten, the scattering matrix technique to determine the dispersion relation of ABS [69] is an adaption of the Landauer-Büttiker scattering approach that was used for normal conductors [70]. This approach treats the weak link X of an S-X-S system, as a scatterer, which is described by matrices. The superconductors are treated as reservoirs, which are sources and drains of electron and hole modes.

The Beenakker and Van Houten differentiated the normal and Andreev scattering events into separate matrices. The Andreev scattering probabilities, which are determined using the BTK model, are dependent on Δ and the phase φ_L and right φ_R of the left and right superconducting leads. By applying the condition that ABS occur when the phase shift after a single cycle is an integer multiple of 2π , Beenakker and Van Houten determined the ABS solutions. For a single conducting channel there are two spin-degenerate solutions given by

$$\pm E_{A,\sigma} = \pm\Delta\sqrt{1 - \tau\sin^2\frac{\varphi}{2}} \quad \text{for } 0 < \tau < 1. \quad (2.67)$$

For a system with perfect transmission $\tau = 1$, the solutions reduce to

$$\pm E_{A,\sigma} = \pm\Delta\cos\frac{\varphi}{2} \quad (2.68)$$

The energy solutions are dependent on the phase difference between the two superconducting leads φ , the transmission of the weak link τ and the superconducting gap Δ . Figure 2.12 shows the energy spectrum of ABS with respect to φ for different transmissions. For each τ there are pairs of spin-degenerate ABS with energies $+E_{A,\sigma}$ and $-E_{A,\sigma}$. The positive and negative ABS carry current in opposite directions.

For transmissions of $\tau < 1$, backscattering in the weak link causes coupling between the ABS pairs resulting in an effective anti-crossing at $\varphi = \pi$. The resulting energy gap between the ABS pairs at $\varphi = \pi$ is $2\Delta\sqrt{1 - \tau}$. The lack of backscattering for $\tau = 1$ leaves the ABS pairs decoupled, thus there is no anti-crossing and the energies are equal at $\varphi = \pi$.

Outside the superconducting gap $E > \Delta$, there exists a continuum of traveling wave solutions. These solutions are delocalised and in the short junction limit independent of φ compared to the localised and phase dependent ABS.

Supercurrent Through ABS

The Andreev description is the microscopic mechanism through which supercurrent passes through a superconducting weak link. At high transmission and a phase difference of $\varphi \sim \pi$ one can consider the ABS to be isolated from the continuum as $E_A \ll \Delta$. This simplifies the model Hamiltonian into the form of an Andreev two-level system. The ABS of the two-level system are typically represented in the excitation picture,

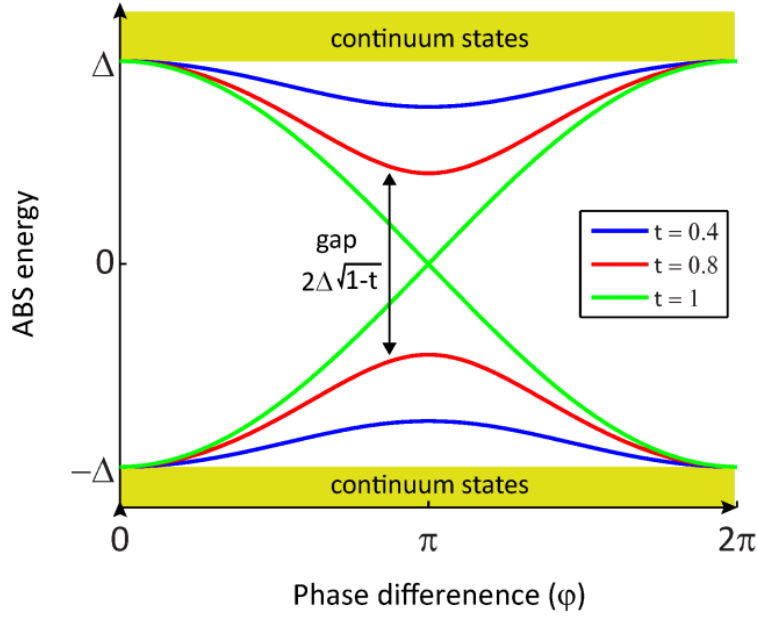


Figure 2.12 – ABS energy spectrum as a function of phase difference across the junction for various transmission. Here, transmissions are labeled by t . Taken from Ref. [63].

where the basis states are

$$\begin{aligned}
 |GS\rangle &\equiv |-\rangle, \\
 \gamma_{E_A\uparrow}^\dagger |GS\rangle &\equiv |\uparrow\rangle, \\
 \gamma_{-E_A\downarrow} |GS\rangle &\equiv |\downarrow\rangle, \\
 \gamma_{E_A\uparrow}^\dagger \gamma_{-E_A\downarrow}^\dagger |GS\rangle &\equiv |+\rangle,
 \end{aligned} \tag{2.69}$$

which have energies relative to the ground state of 0 , E_A , E_A and $2E_A$.

It can be shown that the current field operator restricted to an isolated ABS has even eigenstates of $|-\rangle$ and $|+\rangle$, with current eigenvalues of I_A and $-I_A$, respectively. I_A is the Andreev current for a single channel and is given by [69]:

$$I_A(\varphi, \tau) = -\frac{2e}{\hbar} \frac{dE_A}{d\varphi} = \frac{e\Delta}{2\hbar} \frac{\tau \sin(\varphi)}{\sqrt{1 - \tau \sin^2(\varphi)}}. \tag{2.70}$$

On the other hand, the odd ABS of $|\uparrow\rangle$ and $|\downarrow\rangle$ produce no current. This can be qualitatively understood by the fact that the even states are half filled. Therefore, they have an available ABS through which transport can occur, whereas the odd states have no available ABS (completely filled) or no particles available for transport (completely empty), preventing transport.

These results reveal that at low energy there exists current through a superconducting junction without a voltage bias. The only requirement is a finite phase differ-

ence φ and that the ABS is even; either in the ground $|-\rangle$ or the excited $|+\rangle$ state. The absence of voltage means that the current is dissipationless. Therefore, under certain conditions supercurrent passes through a normal weak link, this is known as the dc Josephson effect.

The expression of Eq. 2.70 defines the Andreev current for a single conducting channel. Thanks to the coherent nature of Andreev reflection, I_A can be easily expanded to N conducting channels by summing the contribution of each occupied channel giving

$$I_A^{total}(\varphi) = \frac{e\Delta}{2\hbar} \sum_{i=1}^N \frac{\tau_i \sin(\varphi)}{\sqrt{1 - \tau_i \sin^2(\varphi)}}, \quad (2.71)$$

where τ_i is the transmission of conducting channel i .

This general approach, to the dc Josephson effect in superconducting weak-link junctions of arbitrary transmission, can be reduced to the limit of the prominent tunnel Josephson junction, where $\tau \ll 1$. The tunnel Josephson junction is a superconducting junction, where the weak-link is a thin insulating layer. Such junctions, labeled S-I-S, are key components of quantum devices based on superconducting circuits.

The important and well known current-phase relationship of a Josephson junction can be determined from Eq. 2.71, by taking the limit of $N \rightarrow \infty$ and $\tau_i \rightarrow 0$ giving

$$I(\varphi) = \frac{e\Delta}{2\hbar} \sin(\varphi). \quad (2.72)$$

The coefficient of the sinusoidal defines the critical current I_c of a tunnel Josephson junction, $I_c = \frac{e\Delta}{2\hbar}$. The critical current is the maximum dissipationless current that can pass through a superconducting junction. A current that is larger than I_c will result in a voltage drop across the junction that results in dissipation.

Dissipative current

In the previous section, we discussed how a superconducting junction can transport dissipationless current. Nonetheless, it is important to understand the sub-gap transport dynamics at finite voltage bias. In superconducting hybrid junctions, dissipative sub-gap current requires non-negligible Andreev reflection at the superconducting interfaces.

Given the existence of Andreev reflection requires non-negligible τ , it is correct to expect minimal sub-gap current in tunnel Josephson junctions. Indeed, for a perfect tunnel Josephson junction the current is vanishingly small for $|eV| < 2\Delta$. This results in a large step current at $eV = \pm 2\Delta$, where the peak in the DOS induces a large current due to the high density of quasiparticles available for tunneling across the barrier.

For junctions with non-negligible transmission, dissipative sub-gap transport occurs through either an equilibrium or a non-equilibrium process. The equilibrium process occurs at low energy and involves the transport of current through ABSs and is described as a "quasiparticle elevator". The non-equilibrium process occurs at higher energies and involves the transport of current through repeated Andreev reflections and is known as multiple Andreev reflection (MAR).

Quasiparticle elevator

At low bias energies quasiparticles are transported through the junction via ABS pairs, $E_A = \pm \Delta \sqrt{1 - \tau \sin^2 \left(\frac{\varphi}{2} \right)}$. The transport mechanism relies on the time evolution of the superconducting phase difference φ at fixed voltage bias, defined by

$$\frac{d\varphi(t)}{dt} = \dot{\varphi}(t) = \frac{V}{\varphi_0}, \quad (2.73)$$

where $\varphi_0 = \hbar/2e$ is the magnetic flux quantum. This characteristic of superconducting junctions results in the phase oscillating at the Josephson frequency (\mathcal{V}_J) by

$$\varphi(t) = 2\pi \mathcal{V}_J t, \quad (2.74)$$

where $\mathcal{V}_J = \frac{2eV}{\hbar}$.

Thanks to their dependence on φ , the ABS energies migrate within the superconducting gap as φ evolves. If the energy is sufficiently small, this migration process can be considered adiabatically. The system is initially in the ground state $|-\rangle$ with energy $-E_A(\varphi)$, where a particle fills the lower ABS. The energy of the particle migrates as a function of φ according to Eq. 2.68, see Figure 2.12. As φ approaches π the energy difference between the ground $|-\rangle$ and excited $|+\rangle$ states decreases, thus increasing the probability that a non-adiabatic Landau-Zener transition from ground to excited state occurs. If the excited state is filled then the particle will decay into the continuum of the ABS when $\varphi = 2\pi$. From there the particle will migrate into the continuum of the superconducting drain as a quasiparticle. The now empty ground state is available to be filled by a $-k$ particle from the ABS continuum. The lost particle is replaced by a quasiparticle from the $-k$ continuum of the superconducting source. This cyclical process transports quasiparticles from the source superconductor to the drain superconductor through a "quasiparticle elevator", thus providing a mechanism for dissipative sub-gap current [62].

Multiple Andreev Reflection

At higher bias energies, dissipative sub-gap current is transported through superconducting hybrid junctions by Multiple Andreev reflection (MAR). MAR requires sufficiently high transmission through the superconducting weak link. As the name suggests, MAR involves Andreev reflections at the two opposing superconducting-weak-link interfaces.

Figure 2.13 sketches out the MAR process in the semiconducting picture of superconductivity, which aids to describe this phenomenon qualitatively. Suppose a bias voltage of V is applied across the junction; given the higher impedance of the weak link compared to the superconducting leads, an electron (hole) gains (loses) energy of eV when traversing left to right across the weak link. Suppose a quasiparticle of energy E , from the lower and full quasiparticle band of the source superconductor, enters the weak link as an electron. In the weak link, the quasiparticles behave as an electron or hole. The probability of such an event is given by $|P| = \sqrt{1 - |a(E)|^2}$ where $a(E)$ is the probability of Andreev reflection. The electron will traverse across the weak link, gaining energy of eV , where it will experience a scattering event at the boundary with the drain superconductor. As described by the BTK model, there is

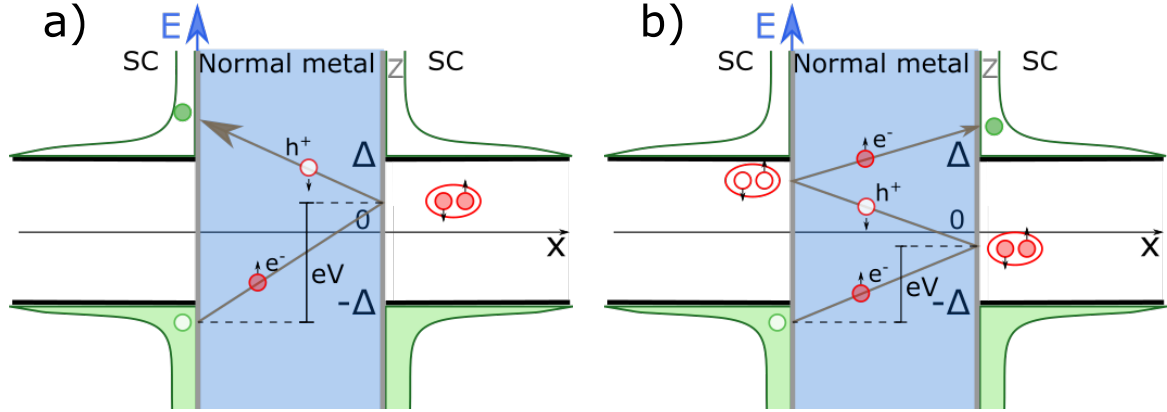


Figure 2.13 – Schematic representation of Multiple Andreev Reflection (MAR) in a S-N-S junction. (a) Shows 2nd order MAR, where a single Andreev reflection occurs ($n = 1$) at the right N-S interface. Here, $\Delta \geq eV < 2\Delta$ and a charge of $2e$ is transferred across the junction and a quasiparticle is excited to the upper continuum of the source. (b) Shows 3rd order MAR, where two Andreev reflections occur ($n = 2$), one at each N-S interface. Here, $\Delta/2 \geq eV < \Delta$ and a charge of $4e$ is transferred across the junction and a quasiparticle is excited to the upper continuum of the drain.

a finite probability that the scattering event will be an Andreev reflection. Andreev reflection will result in the reflection of a hole and the creation of a Cooper pair in the drain superconductor. The active particle, now a hole, traverses towards the source superconductor, gaining further energy.

At the interface with the source superconductor, the active particle has gained an energy of $2eV$ from its original energy of E . If $2eV < 2\Delta$, then another Andreev reflection is possible, which results in the hole reflecting as an electron and the annihilation of a Cooper pair in the source superconductor. However, if $2eV > 2\Delta$, then the traversing hole will recombine as a quasiparticle and enter the upper and empty branch of the source superconductor.

The number of reflections n required for a quasiparticle of energy E to reach the upper band from the lower band is given by $n(E, V) = \left\lfloor \frac{\Delta - E}{eV} \right\rfloor$. The parity of n determines the final location of the excited quasiparticle. For even (odd) n an electron (hole) recombines as a quasiparticle in the drain (source) superconductor. The probability of recombination after n reflections is $\sqrt{1 - |a[E + n(E, V)eV]|^2}$. The MAR order $M = n + 1$, allows one to track the charge transfer across the junction with $Q = Me$. First order MAR is the transfer of a single quasiparticle across the junction. Supposing that the energy of the introduced quasiparticle is $E = -\Delta$ (which is justified given the peak of DOS at the gap edge) the lowest possible order of MAR is

$$M(V) = \left\lceil \frac{2\Delta}{eV} \right\rceil. \quad (2.75)$$

Considering current due to MAR

As discussed in the case of ABS, an electron or hole has a finite probability τ to be transmitted across the weak link. Each trajectory across the weak link compounds this probability, thus the intensity of a MAR process of order M varies with τ^M . Generally $\tau < 1$, consequently the sub-gap current induced by a voltage $|V|$ is dominated by MAR of the lowest order. For a process at $\frac{2\Delta}{M} \geq |eV| < \frac{2\Delta}{(M-1)}$ the current is dominated by the MAR process of order $(M-1)$ as $\tau^{M-1} > \tau^M$. In the limit of $\tau = 1$, all MAR orders contribute coherently to the current.

The MAR process can be considered in terms of the inelastic tunneling of Cooper pairs from the source superconductor to the drain superconductor. For even M , $M/2$ Cooper pairs tunnel inelastically across the junction through which an energy of MeV is dissipated via the excitation of a quasiparticle from the lower continuum to the upper continuum of the source superconductor. For consistency $MeV > 2\Delta$. For odd M , $(M+1)/2$ Cooper pairs tunnel inelastically across the junction through which an energy of MeV is dissipated via the excitation of a quasiparticle from the lower continuum of the source superconductor to the upper continuum of the drain superconductor. For consistency $MeV > 2\Delta - eV$.

The I-V curve of a single channel S-N-S junction supporting MAR have been calculated using a variety of techniques [71, 72, 73]. Their calculations, which are beyond the scope of this thesis, allow one to determine the I-V curve for arbitrary transmission τ of a single channel S-N-S junction.

As MAR is a coherent process, each conducting channel of the weak link contributes independently to the total current. Therefore, the calculation of an I-V curve due to MAR can be extended to an S-N-S junction with multiple conducting channels. In this the current-voltage relation is given by

$$I(V) = \sum_i^N i(\tau_N, V), \quad (2.76)$$

where $i(\tau_N, V)$ is the current response of the Nth channel with transmission τ_N . $i(\tau_N, V)$ is calculated using the techniques cited above.

The coherent nature of MAR allows one to determine each channel transmission of a S-N-S junction by fitting the measured MAR I-V curve. In this thesis we will use a Monte Carlo based fitting program realised by the group of Gabino Rubio. For more details about the program see Ref. [35]. The program allows one to estimate the number of channels involved in the transport and the transmission of each channel.

2.5.4 Superconducting Quantum Dot Junctions (S-QD-S)

In the previous section, we considered a general S-N-S junction where the weak-link was a normal metal characterised by its transmission τ and number of channels. In the following section, we will focus the discussion on S-QD-S junctions, where the weak-link is a quantum dot (QD). In such a junction the properties of the QD, discussed in Section 2.3, have a significant influence on the superconducting transport properties. In writing this section I take inspiration from Refs. [74, 75, 63].

A QD with single-level spacing δ_N much larger than the tunnel coupling Γ and the working temperature $k_B T$, can be adequately modeled by an Anderson impurity model [76]. This model has a Hamiltonian description of

$$\hat{H}_{\text{QD}} = \sum_{\sigma} \epsilon_0 d_{0\sigma}^{\dagger} d_{0\sigma} + E_C n_{0\uparrow} n_{0\downarrow}, \quad (2.77)$$

where $d_{0\sigma}^{\dagger}$ creates an electron of spin σ on the orbital level ϵ_0 and $n_{0\sigma} = d_{0\sigma}^{\dagger} d_{0\sigma}$ is the number operator. The second term, describes the Coulomb interaction characterised by its charging energy E_C . The Hamiltonian of Eq. 2.77, describes a system of a single spin degenerate level of energy ϵ_0 .

To build a Hamiltonian of the complete S-QD-S system one combines \hat{H}_{QD} with the BCS pairing Hamiltonian of Eq. 2.52, which represents the left \hat{H}_L and the right \hat{H}_R superconducting leads and a tunneling Hamiltonian \hat{H}_T that describes the tunneling of charge between the leads and the QD. This system Hamiltonian is given by,

$$\hat{H}_{\text{sys}} = \hat{H}_L + \hat{H}_R + \hat{H}_T + \hat{H}_{\text{QD}} \quad (2.78)$$

Assuming a pairing of $\Delta = |\Delta|e^{i\varphi}$, the Hamiltonians \hat{H}_L and \hat{H}_R are given by the BCS Hamiltonian (Eq. 2.55),

$$\hat{H}_v = \sum_{\vec{k}, \sigma=\uparrow, \downarrow} \xi_{\vec{k}, v} \hat{c}_{\vec{k}\sigma, v}^{\dagger} \hat{c}_{\vec{k}\sigma, v} + \sum_{\vec{k}} \Delta_v \hat{c}_{\vec{k}\uparrow, v}^{\dagger} \hat{c}_{-\vec{k}\downarrow, v}^{\dagger} \Delta_v^{\dagger} \hat{c}_{\vec{k}\uparrow, v} \hat{c}_{-\vec{k}\downarrow, v}, \quad (2.79)$$

where $v = L, R$ defines the lead at which the Hamiltonian and its operators apply. $\hat{c}_{\vec{k}\sigma, v}^{\dagger}$ creates an electron with spin σ in the leads at the single-particle energy level $\xi_{\vec{k}, v}$. The energy level is defined with respect to the lead's chemical potential, $\xi_{\vec{k}, v} = \epsilon_{\vec{k}, v} - \mu_v$, where $\epsilon_{\vec{k}, v}$ is the electron energy.

The tunneling Hamiltonian \hat{H}_T , is given by

$$\hat{H}_T = \sum_{\vec{k}\sigma, v} \left(t_{\vec{k}, v} c_{\vec{k}\sigma, v}^{\dagger} d_{0\sigma} + h.c. \right), \quad (2.80)$$

where $t_{\vec{k}, v}$ is the hopping potential between the leads and the QD. To simplify \hat{H}_T , it is assumed that the hopping potential is \vec{k} independent, $t_{\vec{k}, v} \approx t_v$. Further, by assuming a constant normal density of states $\rho_v(\omega)$ around the Fermi energy, for energies of the order of the gap, the tunneling rate Γ between the leads and the QD can be defined in terms of t_v by $\Gamma_v = \pi |t_v|^2 \rho_v$.

The complexity of \hat{H}_{sys} due to electron-electron interactions, leading to many body physics, makes it very difficult to solve. In certain limiting cases, approximations can

be made to enable analytical or numerical solutions. These approximations are dependent on the energy scales of the system, which dictate the strength of the influence of each component on the total dynamics of the system.

We can consider that the order parameter Δ , defines the "strength" of the superconducting condensate and the coherence of the Cooper pairs. Whereas, in the case of the QD, the charging energy E_C , defines the strength of the Coulomb repulsion of adding an extra charge to the established QD. Finally, the tunnel coupling Γ , defines the rate of exchange between these two opposing systems. For simplification, we will consider identical tunnel coupling for the left and right leads. The difference between these opposing systems is further highlighted by considering their respective uncertainties with regard to charge number N . A superconductor has characteristically delocalised charge, with the charge number N having a large variability. Whereas, a QD is of the opposite nature, having highly localised charge with well defined N .

By considering the relative energy scales of Δ , E_C and Γ , the transport dynamics of an S-QD-S junction has been categorised into three regimes [74]:

- Weak coupling regime: $\Gamma \ll \Delta, E_C$. The large charging energy dominates the system dynamics, preventing Cooper pairs from tunneling onto the QD. In this regime, charge is transferred by the tunneling of single quasiparticles through the QD, with a characteristic time scale of h/Γ . The dominance of the characteristic tunneling time over the coherence time h/Δ of Cooper pairs, prevents the recombination of the tunneling quasiparticles into Cooper pairs. Therefore, in this regime, the observed transport consists of Coulomb blockade and no supercurrent. See Section 2.3 for details on transport in the Coulomb blockade regime.
- Strong coupling regime: $\Gamma \gg \Delta, E_C$. The dominance of Γ results in strong coupling between the superconducting leads and the QD. Consequently, Cooper pairs can resonantly tunnel across the QD, transporting supercurrent. The uncertainty in N , associated with Cooper pair tunneling, breaks down the well defined localised charge expected for a QD. This results in charge population fluctuations in the QD. In this regime, Andreev bound states (ABS) can form in the QD. However, in this case, the ABS have an extra degree of freedom; the gate tuneable orbital energy ϵ_0 of the QD. It will be shown that tuning ϵ_0 in an S-QD-S system is equivalent to tuning the transmission τ of an S-N-S junction.
- Intermediately coupled regime: $\Gamma \sim \Delta \sim E_C$. The similar energy scales results in a combination of the two aforementioned regimes, making it the most complex regime. When the condition that $\Gamma \sim \Delta$ is met and the QD's orbital ϵ_0 is on resonance with the leads, then a sizable supercurrent can be observed in the system. Moreover, if the condition $\Gamma \sim E_C$ is met, supercurrent can also be observed when ϵ_0 is off resonance. Here, supercurrent is transported by fourth-order co-tunneling processes. In this process, single quasiparticle tunneling into the QD from the left lead can recombine as Cooper pairs in the right lead. Furthermore, the non-negligible E_C means that the QD experiences Coulomb blockade when ϵ_0 is off resonance. Under the conditions of Coulomb blockade, the quantum dot can have reasonably well-defined spin and charge states.

We will now discuss the equilibrium properties of QDs coupled to superconducting leads. We will first consider the non-interacting approximation, where a QD with a

single orbital at ϵ_0 and $E_C = 0$, is considered. In this approximation, we can examine the effects of a QD orbital on ABS and make comparisons to the equilibrium states of the S-N-S junction.

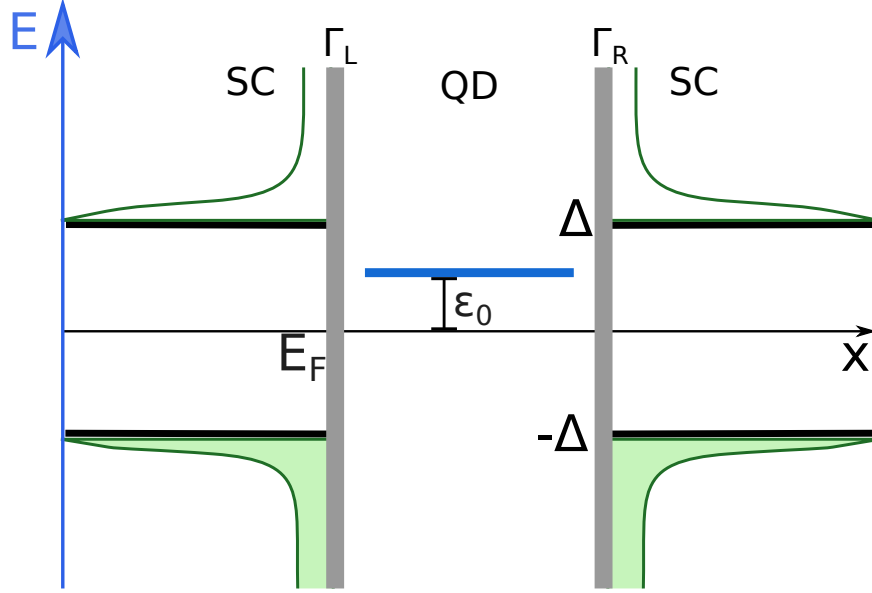


Figure 2.14 – Energy diagram of a S-QD-S junction in the non-interacting approximation. In this approximation the QD is modeled as a single orbital with position ϵ_0 with respect to the Fermi energy E_F .

The Non-interacting approximation ($E_C = 0$)

The non-interacting approximation is valid when the QD system has a large single particle level spacing δ_N that is much larger than the tunnel coupling Γ and the working temperature T . By neglecting electron-electron interactions, achieved by setting $E_C = 0$ in \hat{H}_{QD} . The S-QD-S system is modeled as a single QD orbital at energy ϵ_0 , coupled to the left and right superconducting leads by Γ_L and Γ_R , respectively. This scenario is depicted schematically in Figure 2.14.

In a QD system with $E_C = 0$ the conductance due to resonant tunneling is given by [77]:

$$G = \frac{2e^2}{h} \frac{\Gamma_L \Gamma_R}{\epsilon_0^2 + \frac{1}{4}\Gamma^2} \quad (2.81)$$

As expected, the conductance is maximum when the orbital is aligned with E_F of the leads, which corresponds to $\epsilon_0 = 0$.

In this approximation, the ABS in an S-QD-S junction can be determined by first calculating the normal scattering probability through the QD due to finite Γ and ϵ_0 . Secondly, by meeting the ABS condition that during a full cycle of Andreev reflections, a quasiparticle gains a multiple of 2π in phase. Ref. [75] provides an expression for ABS energy E , with respect to the phase difference between the superconducting leads φ :

$$E \pm \Delta \cos\left(\frac{\varphi}{2}\right) + \frac{E\sqrt{\Delta^2 - E^2}}{\Gamma} = 0. \quad (2.82)$$

Here, the coupling is symmetric $\Gamma_L = \Gamma_R$ and the orbital is on resonance $\epsilon_0 = 0$. In the strong coupling regime $\Gamma \gg \Delta$, Eq. 2.82 reduces to

$$E \approx \pm \tilde{\Delta} \cos\left(\frac{\varphi}{2}\right), \quad (2.83)$$

where $\tilde{\Delta} = \Delta \left[1 - 2\frac{\Delta^2}{\Gamma^2}\right]$ is the reduced gap parameter.

When the orbital is off resonance and $\Delta/\Gamma \rightarrow 0$, the ABS spectrum of a QD can be described similarly to the spectrum of a S-N-S junction, by defining a normalised transmission of $\tilde{\tau} = \frac{1}{1+(\epsilon_0/\Gamma^2)}$, giving:

$$E \approx \pm \Delta \sqrt{1 - \tilde{\tau} \sin^2\left(\frac{\varphi}{2}\right)}. \quad (2.84)$$

In the off resonance case, there is a gap in the ABS energy spectrum, similar to the ABS spectrum of a single channel S-N-S junction with finite transmission, see Figure 2.12.

Figure 2.15 shows the ABS energy spectrum of a S-QD-S junction with respect to φ for various tunneling rates, where $\Gamma_L = \Gamma_R = \Gamma$ for a QD on and off resonance, in the non-interacting approximation. When the QD is on resonance, Figure 2.15 (a), the ABS spectrum behaves similarly to that of a perfectly transmitting single channel S-N-S junction, see Figure 2.12. Whereas, in the off resonance case, Figure 2.15 (b), there is a gap in the ABS energy spectrum similar to the ABS spectrum of a single channel S-N-S junction with finite transmission, see Figure 2.12. The main difference of the S-QD-S ABS spectrum, is the reduced maximum amplitude of the ABS energy at $\varphi = 2n\pi$. The ABS energy is detached from the continuum due to the reduced gap parameter $\tilde{\Delta}$.

In the limit of $\Delta/\Gamma \rightarrow 0$, the zero temperature current phase relation of the S-QD-S superconducting junction is given by [75]

$$I_A(\varphi) = \frac{e\Delta}{2\hbar} \frac{\tilde{\tau} \sin \varphi}{\sqrt{1 - \tilde{\tau} \sin^2 \varphi/2}}. \quad (2.85)$$

This is identical to the current phase relation of a single channel S-N-S junction (Eq. 2.70), except here $\tilde{\tau}$ is the effective transmission that is dependent on ϵ_0 and Γ .

In conclusion, it has been shown that a S-QD-S junction, in the non-interacting approximation, has qualitatively the same ABS behavior as a single channel S-N-S junction. However, the main differences are the reduced I_c and the extra degree of freedom provided by the position of the orbital ϵ_0 , which can be experimentally tuned via electrostatic gates.

Co-tunneling approximation

The co-tunneling approximation, developed by Glazman and Mateev [78], provides a way to estimate the supercurrent through a QD junction for finite Δ/Γ . By applying perturbation theory to \hat{H}_T to the lowest order in Γ and finding the expectation values, the supercurrent through the left lead is determined by the expectation:

$$I = e \left\langle \frac{d}{dt} \xi_{\vec{k},L} \hat{c}_{\vec{k}\sigma,L}^\dagger \hat{c}_{\vec{k}\sigma,L} \right\rangle. \quad (2.86)$$

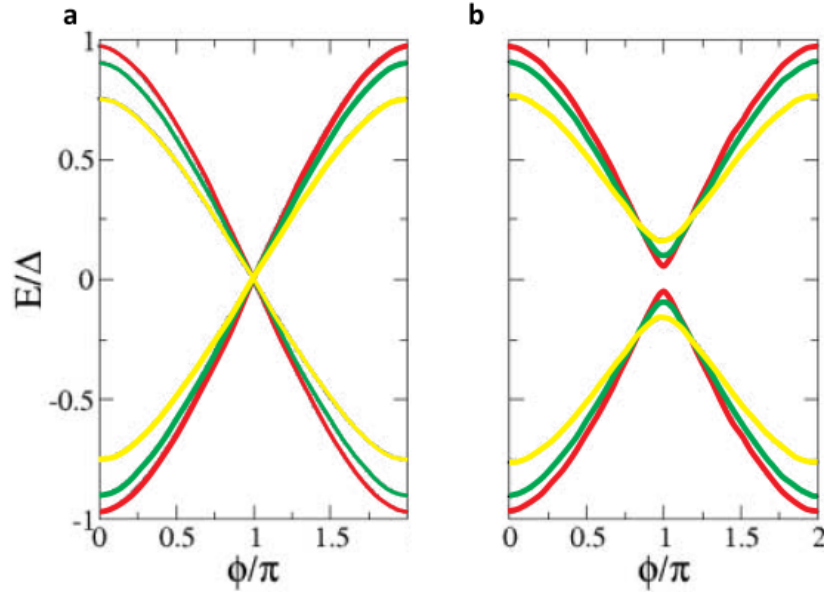


Figure 2.15 – Energy spectrum of ABS in a S-QD-S as a function of phase across the junction for a QD orbital of (a) $\epsilon_0 = 0$, on resonance and (b) $\epsilon_0 = 0.5\Delta$, off resonance. The tunneling coupling used were $\Gamma = \Delta$ (yellow), $\Gamma = 2\Delta$ (green) and $\Gamma = 4\Delta$ (red). Taken from Ref. [63].

By summing the co-tunneling events, that occur through virtual levels, which contribute to the supercurrent and taking the limit $E_C \rightarrow \infty$ the current is determined to be

$$I(\varphi) = \lambda \frac{e}{\hbar} \frac{\Gamma_L \Gamma_R}{\Delta} F\left(\frac{|\epsilon_0|}{\Delta}\right) \sin(\varphi), \quad (2.87)$$

where $F(x) = \frac{1}{\pi^2} \int \frac{dt_1 dt_2}{(\cosh t_1 + \cosh t_2)(x + \cosh t_1)(x + \cosh t_2)}$. The factor λ defines the direction of the supercurrent and depends on the occupation of the dot. For $\epsilon_0 > 0$ (empty dot), $\lambda = 2$ and for $\epsilon_0 < 0$ (singly occupied dot), $\lambda = -1$. This dependence of the supercurrent on the ground state of the QD reveals that the S-QD-S junction can transition between a 0- and π - junction [79].

In this approximation the current-phase relation remains sinusoidal like the tunnel Josephson junction (Eq. 2.72). However, the magnitude of I_c is proportional to Γ^2 . Its dependence on ϵ_0 , allows I_c to be tuned by electrostatic gates.

There are other methods to determine the current phase relationship for a range of Γ/Δ . An overview of these methods with appropriate references can be found in Ref. [75].

Voltage biased S-QD-S junction

In the previous discussion, we focused on the properties of S-QD-S junctions under equilibrium conditions. We showed that S-QD-S junctions exhibit supercurrent at energy scales of $\Gamma \gg \Delta$ and finite Δ/Γ . Further, we observed significant similarities between the S-N-S and S-QD-S junctions under equilibrium conditions, including a similar current phase relationship. In the following, we will consider the transport

properties of a voltage biased S-QD-S system. Under a voltage bias, we enter a non-equilibrium transport regime. Here, the theory becomes more complex due to the time dependence of the ac Josephson effect. The following discussion is based on the article by A. Levy Yeyati et al, Ref. [80] and the review article by A. Martin-Rodero and A. Levy Yeyati, Ref. [75]. I will introduce their main results because we will consider them when interpreting the transport properties of our Al-Ge-Al nanowire heterostructures in Chapter 5.

Resonant Tunneling

In 1997 A. Levy Yeyati et al. [80] theoretically investigated the voltage bias transport characteristics of a S-QD-S junction. They considered the effects of resonant tunneling in a small quantum dot. The analysis is nonperturbative in the coupling, contrary to the co-tunneling approximation, as such the results can be extended to both the weak coupling and the strong coupling regimes.

The energy regimes of the two studied cases are: in the weak coupling regime $\delta_1 \gg \Delta \gg \Gamma$ and in the strong coupling regime $\Gamma \gg \Delta$. In their analysis they assume that the orbital of the QD lies within the superconducting gap and Coulomb blockade can be neglected, that is $E_C = 0$. Similar to the study of S-QD-S junctions in equilibrium, Yeyati et al. used a model Hamiltonian, equivalent to Eq. 2.78, based on the Anderson impurity model.

To solve the Hamiltonian the authors use non-equilibrium Green function techniques that were used in Ref. [72]. To take into account the applied bias voltage across the superconducting leads V_v , the authors used a gauge that is equivalent to time-dependent phase factors modulating the hopping potential t_v . In this gauge, $t_v \rightarrow e^{ieV_v\tau/\hbar}$, where τ is the device transmission. In terms of the hopping potential the normal elastic tunneling rate is $\Gamma_v = \pi|t_v|^2\rho_v(\mu)$, where $\rho_v(\mu)$ are the normal spectral densities of the leads. The detail of the calculations are outside the scope of this thesis, nonetheless we will present their important conclusions, which will be relevant for understanding the results presented in this manuscript.

In the weak coupling regime, where the energy scales are $\delta_N \gg \Delta \gg \Gamma$, the double occupancy of a single resonant level is unlikely to occur, as such charge degeneracy can be neglected. Further, the weak coupling strongly suppresses Andreev reflection, thus only single quasiparticle processes need to be considered. The resulting expression for dc current versus voltage is

$$I_0(V) = \frac{4e}{h} \int_{-\infty}^{\infty} d\omega \frac{\Gamma_L^S(\omega)\Gamma_R^S(\omega)}{(\omega - \epsilon_0)^2 + [\Gamma_L^S(\omega) + \Gamma_R^S(\omega)]^2} \times [n_F(\omega - eV/2) - n_F(\omega + eV/2)], \quad (2.88)$$

where $\Gamma_{L,R}^S$ are the superconducting tunneling rates and $n_F(\omega)$ is the Fermi distribution. Eq. 2.88 is similar to that of normal resonant tunneling. The superconducting tunneling rates are defined in terms of the normal tunneling rates by $\Gamma_{L,R}^S(\omega) = \Gamma_{L,R}\tilde{\rho}_S(\omega \pm eV/2)$, with $\tilde{\rho}_S$ being the dimensionless BCS spectral density given by $\tilde{\rho}_S(\omega) = |\omega|/\sqrt{\omega^2 - \Delta^2}$. Note that ϵ_0 is the effective position of the resonant level of the QD, with respect to E_F of the leads.

Figure 2.16 shows the zero temperature I-V curves, determined using Eq. 2.88 for a resonant level at $\epsilon_0 = 5\Delta$. Different tunneling rates are considered, with a constant ratio of $\Gamma_R = 4\Gamma_L$, in the weak coupling regime. For comparison, systems with either

normal or superconducting leads are considered. The results predict the existence of superconducting resonances at a threshold voltage of $eV = 12\Delta$. The threshold voltage in the superconducting regime is 2Δ larger than in the normal regime. This is due to the gap, of 2Δ , in the density of states of the superconducting leads. This gap must be overcome for quasiparticles to tunnel from the source into the drain and through the QD's resonant level. The threshold voltage of the normal leads of $eV = 10\Delta$, maybe surprising given that $\epsilon_0 = 5\Delta$. However, this is a consequence of the model used to determine Eq. 2.88. In this model, the leads are assumed to be floating, as such a voltage bias of eV shifts the chemical potential of the source and drain by $eV/2$ and $-eV/2$, respectively. Therefore, for the source to reach the orbital ϵ_0 and allow charge transport, $eV/2$ must be equal to 5Δ , which is equivalent to the threshold voltage of $eV = 10\Delta$ in the normal regime.

The superconducting resonances have a finite height and width that are dependent on Γ_L rather than a phenomenological broadening parameter. As Γ_L is reduced, the resonant feature increasingly resembles that of a BCS spectral density, expected for tunneling experiments on superconducting junctions. Of further note, is the difference in threshold voltage of 2Δ between the superconducting and normal leads; this is associated with the superconducting gap of the leads, where propagating states are forbidden, thus no current is observed.

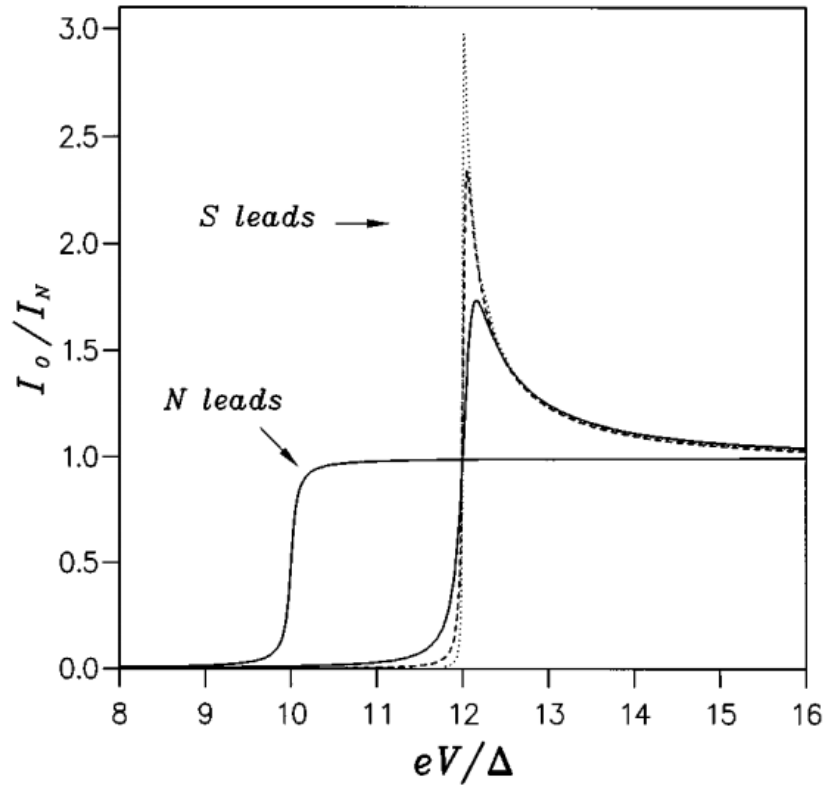


Figure 2.16 – Plot of calculated I-V curves for a resonant level of a QD coupled to superconducting leads in the weak coupling regime, for various tunneling rates: Full line for $\Gamma_L = 5 \times 10^{-3}\Delta$, dashed line for $\Gamma_L = 10^{-3}\Delta$ and dotted line for $\Gamma_L = 2 \times 10^{-4}\Delta$. In all cases $\Gamma_R = 4\Gamma_L$ and $\epsilon = 5\Delta$.

In the intermediate regime, the comparative energy scales of E_C and Γ requires that both Andreev reflection and single quasiparticle processes are considered when calculating the current. The importance of Multiple Andreev reflection (MAR) is highlighted in Figure 2.17, where sub-gap states become increasingly apparent as Γ approaches Δ . In the simulation shown in Figure 2.17, ϵ is fixed at $\epsilon = 0$ and the coupling is symmetric ($\Gamma_L = \Gamma_R$).

Some important characteristics of the results should be noted. For strong coupling $\Gamma \gg \Delta$, the sub-gap features are smoothed out, and the dominate feature is the saturation current as $V \rightarrow 0$ of $I_0 \sim 4e\Delta/h$, for a single conductance channel. The curves in the strong coupling regime resemble those of a superconducting junction where the weak-link is a quantum point contact (QPC) and the contacts are highly transparent. For weaker coupling $\Gamma \sim \Delta$, the sub gap features exhibit oscillations, which result in the appearance of negative differential conductance. Such features are a consequence of the combination of MAR and resonant tunneling through the orbital of the QD. These features are not normally observed in standard S-N-S junctions. Furthermore, the current jumps due to MAR occur most strongly at the condition $eV = 2\Delta/n$ for odd integer n . Whereas MAR processes at even integer n are suppressed.

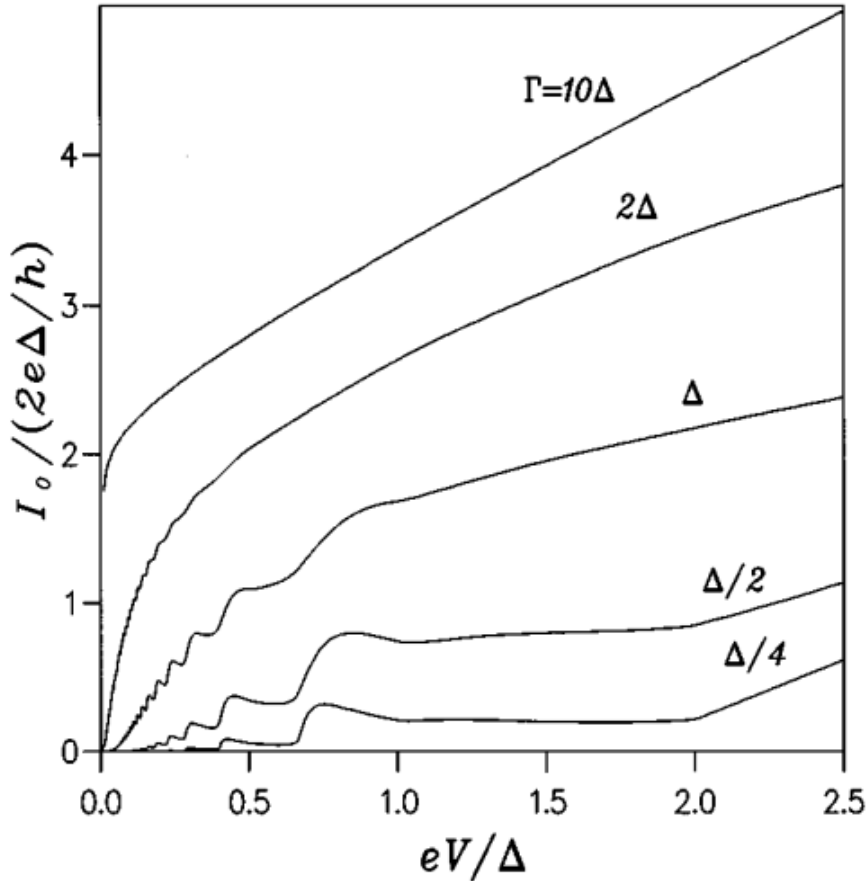


Figure 2.17 – Plot of analytically and numerically calculated I-V curves for a resonant level coupled to superconducting leads. We observe the combined effects of resonant tunneling and multiple Andreev reflection.

The deviation from standard MAR, due to the presence of a resonant level, can be

understood through the following explanation. In the energy regime $|eV| < 2\Delta$, the current flows through the junction via MAR, as with S-N-S junctions, singularities, observed as jumps in the I-V curves, occur at certain voltages when another Andreev reflection can occur; i.e. at energies $eV = 2\Delta/n$. However, the presence of a resonant level, rather than a continuum of states, modifies the current amplitude, resulting from MAR processes, by filtering the possible MAR trajectories. Only MAR trajectories that connect the resonant level to the spectral densities of the leads give a significant contribution to the current.

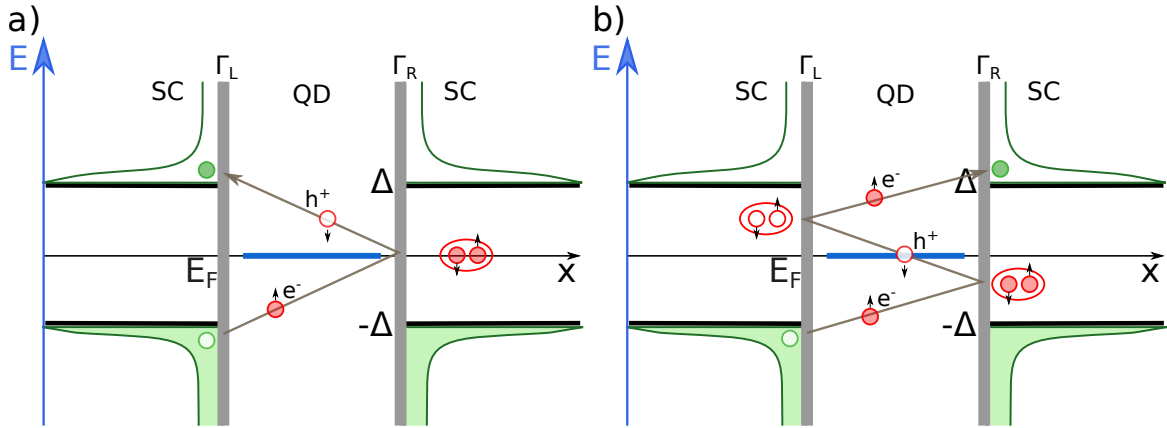


Figure 2.18 – Schematic showing resonant MAR processes of 2nd (a) and 3rd (b) order MAR through a S-QD-S junction. The QD orbital ϵ_0 , defined by the thick blue line, is on resonance with E_F of the leads. In (a) the 2nd order MAR does not align with ϵ_0 as such the usual MAR current jump is suppressed. However, in (b) the 3rd order MAR process does align with ϵ_0 as such the current jump is enhanced and we observe a current peak.

Figure 2.18 illustrates the trajectory of a quasiparticle undergoing 2nd (a) and 3rd (b) order MAR processes. Figure 2.18 (a) shows a MAR trajectory under a voltage bias in the range of $\Delta \leq eV < 2\Delta$. The MAR trajectory, depicted by the arrows does not align with the resonant level of the QD. This off resonance trajectory results in a reduced current compared to the on resonance trajectory that is depicted in Figure 2.18 (b). Here, the third order MAR trajectory aligns with the QD orbital, resulting in a peak in current at $eV = 2\Delta/3$, the onset of the third order MAR process.

The sub-gap features due to resonant MAR tunneling, shown in Figure 2.17, are dependent on the orbital position. Figure 2.19 shows the variation of the sub-gap features for different orbital positions ϵ_0 in the QD. For $\epsilon_0 = 5\Delta$, far from the superconducting gap, the sub-gap features look like standard MAR for an S-N-S junction with low transmission. However, as ϵ_0 gets closer to Δ the sub-gap features become more pronounced and the current peaks depend on eV and ϵ_0 .

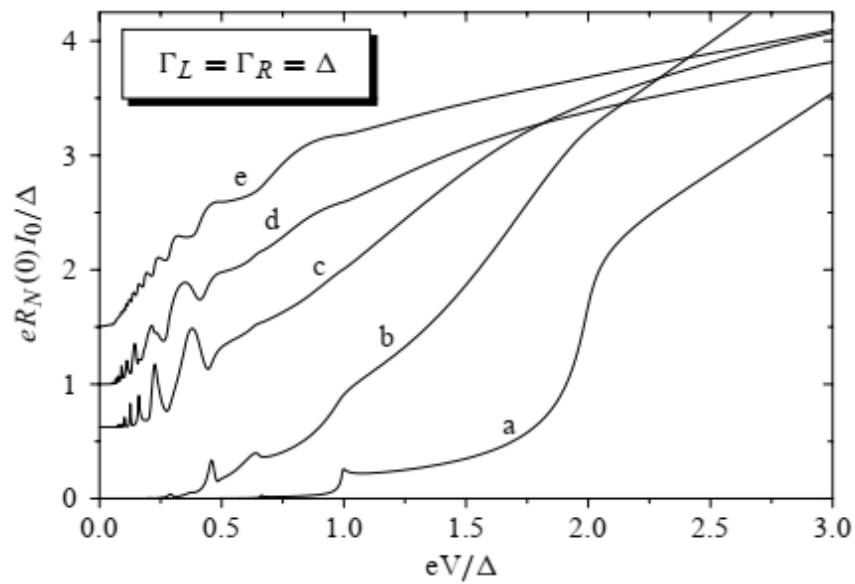


Figure 2.19 – I-V characteristic curves of S-QD-S junction with $\Gamma_L = \Gamma_R = \Delta$, for different orbital positions: (a) 5Δ , (b) 2Δ , (c) Δ , (d) 0.5Δ , (e) 0. Figure taken from Ref. [81].

Andreev Reflections and Kondo correlations

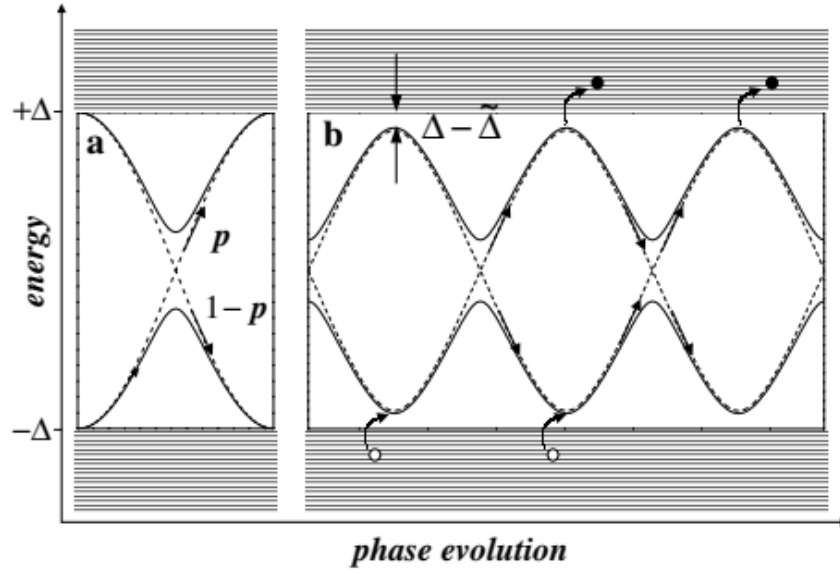


Figure 2.20 – Schematic showing the low bias charge transport through ABS, (a) for a single channel S-N-S junction and (b) for S-QD-S junction in the Kondo regime. Figure taken from Ref. [82].

Another non-equilibrium effect that must be considered in S-QD-S systems is the interplay between MAR and Kondo correlations [75]. The Kondo effect is a magnetic impurity effect, that can be observed in small QD systems. In a QD with large δ_N , where an isolated resonant level can be considered, the single charge on the orbital can behave like a magnetic impurity due to the charge's spin.

In S-QD-S systems, the Kondo effect becomes important when $T_K \gg \Delta$, where T_K is the Kondo temperature. T_K is related to the system energy scales by [83]

$$T_K = \sqrt{\frac{E_C \Gamma}{2}} e^{-\frac{\pi |\epsilon_0 (\epsilon_0 + E_C)|}{2 E_C \Gamma}}, \quad (2.89)$$

where $\Gamma = \Gamma_L + \Gamma_R$.

Ref. [82] theoretically investigated the transport properties in a S-QD-S in the Kondo regime. They showed that the sub-gap transport properties could be understood due to Andreev states. Here, the ABS are to those in the non-interacting case, except that here, the tunneling rate and orbital position are renormalised.

Figure 2.20 (b) shows a schematic of the ABS in a S-QD-S junction in the Kondo regime. The low voltage charge transport occurs through a Landau-Zener transition between the lower and upper ABSs. This is similar to the quasiparticle elevator of an S-N-S junction, see 2.20 (a). However, in the S-QD-S case, a transition between the continuum and the ABS must also occur. This is due to the detachment of the ABS from the continuum by $\Delta - \tilde{\Delta}$.

We will show that under certain conditions we observe evidence of this effect when the germanium quantum dot contains an odd number of holes.

Fabrication

3

Contents

3.1 Superconducting quantum devices: Architectures and their challenges	68
3.2 Nanowire Growth Using VLS Growth	69
3.2.1 Intrinsic Germanium Nanowires	70
3.2.2 Germanium-Silicon core-shell nanowires	71
3.3 Field Effect Transistor FET	72
3.4 Diffusion through Thermal Annealing	75
3.5 Interface Quality	78
3.5.1 i-Ge Interface	78
3.5.2 Ge/Si core/shell Interface	78
3.6 Conclusion	79

3.1 Superconducting quantum devices: Architectures and their challenges

The generic nature of the superconducting proximity effect that underscores the transport properties of superconducting hybrid junctions, enables their realisation using a diverse range of materials and architectures. There are two approaches to fabricating mesoscopic and nanoscopic devices; the top down approach and the bottom-up approach. The former approach is employed in the fabrication of devices that use planar 2D electron/hole gases (2DEG/2DHG) in epitaxially grown heterostructures. Such planar heterostructures have been realised in group III-V semiconductors including GaAs/AlGaAs [84] and group IV semiconductors including SiGe/Ge/SiGe [26, 27, 28]. Quantum devices such as quantum dots and quantum point contacts are achieved by electrostatic gates that are typically deposited on the surface of the heterostructure. Through gate voltage tuning confinement of the 2DEG/2DHG is induced and quantum devices can be realised. To electronically probe these quantum devices metallic contacts to the 2DEG/2DHG must be fabricated. By using superconducting metals for these contacts superconducting hybrid junctions can also be realised.

The bottom-up approach uses grown nanostructures such as nanowires (NWs) or carbon nanotubes which are placed on prepared substrates. Before the arrangement of the nanostructures, substrates are typically prepared with a distribution of metallic structures which are used for gating or electrical contacts. The superconducting contacts to the nanostructure weak-links are usually defined using electron beam lithography and deposited onto the nanostructures using evaporative techniques. A benefit of the bottom-up approach is that the nanowire weak-links already experience significant confinement due to the strong radial confinement provided by their dimensions; typically having diameters of the order of tens to hundreds of nanometers. To achieve a quantum dot, these quasi-1D systems require only confinement in the longitudinal direction. This confinement can be achieved by electrostatic gates or by reducing the length of the NW, which will be shown, in this chapter, to be possible through thermal annealing induced diffusion.

However, the bottom up approach comes with significant challenges. One of the major challenges is achieving transparent and impurity free superconducting-semiconducting interfaces. This implies etching the NW shell and/or the native oxide that forms on the NW surface when exposed to ambient air, before depositing the superconducting metal. This etching process is never perfect and can lead to poor quality contacts with impurities which can lead to unintentional potential barriers at the interfaces. The imperfect nature of this process reduces the reproducibility of these devices. Devices fabricated under similar conditions can exhibit, unintentionally, significantly different transport features; from supercurrent in one device with transparent interfaces to Coulomb blockade in another device with opaque interfaces defined by strong potential barriers resulting from interface impurities [85]. Moreover, this contact transparency issue is not limited to the bottom up approach. Devices fabricated using the top down approach also face difficulties with contact transparency and reliability [26].

Further, interface disorder can cause spurious transport states within the superconducting gap. These sub-gap states (SGS) are independent of superconducting Andreev states and can form a continuum of SGS, resulting in a "soft" superconducting gap [86]. The quest to observe non-trivial superconducting states such as Majorana zero

modes requires minimal impurity induced SGS, which demands high quality superconducting contacts.

An important step forward was taken with the epitaxial growth of Al thin films on pristine facets of InAs nanowires without breaking the vacuum [87]. Tunnel spectroscopy measurements of the InAs/Al devices revealed a "hard" superconducting gap, suggesting minimal spurious SGS and high quality superconducting-semiconducting contact. Beyond InAs nanowires (NWs) other group III-V high mobility compound semiconductors such as InSb [88, 89], InP [90] and InAs/InP core/shell [91] NWs have been employed in superconducting-semiconducting junctions with various levels of success.

Group IV semiconducting nanostructures including carbon nanotubes (CNTs) [92, 6] and Si NWs [49] have also been used for the development of quantum devices. However, more recently Ge based NWs have received significant attention due to its exceptional material properties including large hole mobility, strong spin-orbit coupling, and tuneable g-factors which are important traits for quantum devices. Until now, Ge has been predominantly integrated with Si in the form of Ge/Si core/shell NW junctions [21, 22, 23, 24] or Ge hut wires [25] with Si caps and Ge/Si planar junctions. However, the adoption of intrinsic Ge (i-Ge) NWs for the development of quantum devices, including superconducting hybrid junctions, has been limited. The lack of adoption is mainly associated with the difficulty in overcoming the metal-Ge Schottky barrier which, despite forming close to the valence band due to Fermi level pinning [93], can prevent proximity induced supercurrent. Overcoming the Schottky barrier requires the fabrication of high quality electrical contacts to Ge nanostructures while simultaneously reducing the gate screening effect of the leads [29, 30]. This tremendous challenge has been recently achieved through intense research on the thermal diffusion of metals into semiconducting NWs [31, 32, 33]. The absence of an intermetallic phase formation and compatible diffusion rates between Al-Ge have been exploited extensively to form true metal-Ge heterostructures with abrupt interfaces [34] leading to the formation of self-aligned Al NWs contacting the monolithically integrated Ge QD.

In this thesis, we investigated the low temperature transport properties of Ge NW and Ge/Si core/shell NW based quantum devices. In this chapter, I will outline the fabrication processes undertaken by our collaborators Masiar Sistani and Alois Lugstein, at TU Wien in Vienna, to construct these Ge NW devices. I will also discuss the high resolution imaging and structural investigation of the devices carried out by Masiar Sistani in collaboration with Minh Anh Luong and Martien den Hertog of Institut Néel and Eric Robin of CEA, Grenoble.

3.2 Nanowire Growth Using VLS Growth

The myriad of applications and interesting physical properties of nanowires from single photon sources to superconducting hybrid junctions has stimulated significant research into a vast range of NW fabrication techniques including electron beam lithography [94], laser ablation [95], template [96], vapor-liquid-solid (VLS) growth [97], and vapor-solid-solid growth [98, 99].

The intrinsic germanium (i-Ge) nanowires used in this thesis were grown by our collaborators in Vienna using the vapor-liquid-solid (VLS) growth mechanism, which bears its name thanks to the phase evolution the semiconducting material experi-

ences as it forms a NW. VLS growth, depicted schematically in Figure 3.1, was first demonstrated by R.S Wagner and W.C. Ellis in 1964 [97]. Since its first demonstration significant research interest has established VLS as a common fabrication technique for growing semiconducting NWs.

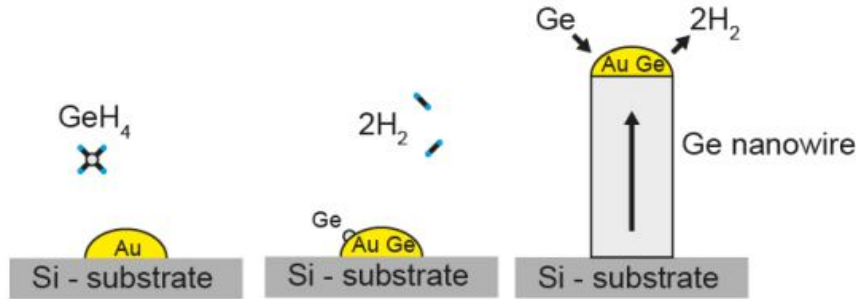


Figure 3.1 – Schematic representation of the vapor-liquid-solid growth mechanism used to grow Ge NWs nanowires. *Left* The Au nano-droplet that catalyses the Ge NW growth forms after annealing. Once annealed the substrate is heated to 539 K and the precursor gas, GeH_4 , is introduced. *Middle* Collision between Au nano-droplet and GeH_4 molecule causes the molecule to decompose into Ge and 2H_2 . The Ge atom is absorbed into the Au-Ge liquid and solidifies at the liquid-solid interface driving vertical Ge NW growth. Figure taken from Ref. [39].

3.2.1 Intrinsic Germanium Nanowires

The germanium nanowires are described as intrinsic because the Ge is not intentionally doped during the growth process. As such the nature and density of the charge carriers depends on the properties of the Ge NW. The ultra-scaled dimensions of the Ge NWs results in surface states having a significant effect on its transport properties [100]. It will be shown in Chapter 5 that the accumulation of negative charges in these interband trap levels combined with the Schottky barrier being pinned close to Ge's valence band leads to an overall p -type behavior.

The VLS growth process commences with the deposition of a thin film of gold (Au) onto a silicon wafer. The Au layer is forced into forming nano-droplets, through dewetting, by successive annealing procedures. The Au nano-droplets become the catalysts for NW growth with their diameter defining the final NW diameter. Having successfully seeded the Au nano seeds, the NW growth is initiated by heating the substrate to 539 K and the introduction of the precursor gas, GeH_4 . The heating temperature is not arbitrary and is chosen to be above the eutectic temperature of an Au-Ge mixture. Critical to the success of VLS growth, the eutectic temperature is the minimum temperature at which a heterogeneous mixture of chemicals (Au-Ge) melts. Importantly, the eutectic temperature occurs at a critical concentration of the constituents and is lower than the melting points of the individual constituents or a differing concentration of the constituents.

In these conditions, collisions between the GeH_4 vapour molecules and Au nano-droplets induces chemical decomposition of GeH_4 into its volatile components Ge and 2H_2 . The Ge diffuses through the liquid phase of the AuGe droplet until reaching the liquid-solid interface between the droplet and Si substrate. This diffusion process

concentrates Ge at the lower edge of the AuGe droplet. When the Ge concentration is sufficient to shift the concentration ratio of the AuGe mixture away from the critical concentration of the eutectic temperature, the Ge begins to solidify. This supersaturation of Ge results in the formation of a Ge nanowire with a diameter equal to that of the nano-droplet growing vertically. To improve their electrical properties and to prevent oxidation, the Ge NWs were passivated, just after growth, with a 20 nm Al_2O_3 shell by atomic layer deposition (ALD).

The NW length can be tuned by the chamber conditions; temperature, partial pressure and growth time [101]. There are multiple techniques to control and optimise the NW growth process. The Ge NWs grown by our collaborators exhibit typical lengths of approximately 7 μm and Ge diameters ranging between 25 nm and 75 nm. See Masiar Sistani's PhD thesis [39] for more details on Ge nanowire growth.

3.2.2 Germanium-Silicon core-shell nanowires

The Ge/Si core/shell nanowires used in this thesis were fabricated by the Lieber group of Harvard University. They used a similar VLS technique to grow Ge NWs from Au nano-droplets. After Ge NW growth, they deposited the Si shell by introducing SiH_4 gas within the same reactor. For more details see Ref. [102]. The Ge/Si core/shell NWs used in this thesis have a Ge core diameter of 30 nm and a Si shell thickness of 3 nm.

Figure 3.2 shows schematics of the two germanium based nanowires (NW) studied in this thesis. Though having a similar i-Ge core, the implementation of a Si shell results in significantly different transport properties compared to the Al_2O_3 shelled Ge NWs. The first major difference between the NWs is the formation of a quantum well in the Ge due to the valence band (VB) offset of ≈ 500 meV between Ge and Si at the interface, see Figure 3.2 (a). The accumulation of free holes between E_F and VB of the Ge core induces a quasi-1D hole gas in the Ge/Si core/shell NWs. Whereas, the inert Al_2O_3 shell of the i-Ge NWs has no effect on the band structure of the Ge core, thus the i-Ge NWs behave according to its semiconducting properties.

The quasi-1D hole gas of the Ge/Si core/shell NWs leads to significantly higher mobility μ and longer mean free path ℓ compared to the i-Ge NWs. The Ge/Si core/shell NW has a reported mobility and mean free path of $\mu_{\text{Ge/Si}} \approx 730\text{cm}^2\text{V}^{-1}\text{s}^{-1}$ and $\ell_{\text{Ge/Si}} \approx 500$ nm [36]. Whereas the i-Ge NWs have a mobility around half of $\mu_{\text{Ge/Si}}$ of $\mu_{\text{Ge}} \approx 370\text{cm}^2\text{V}^{-1}\text{s}^{-1}$ [103] and a mean free path orders of magnitude smaller than $\ell_{\text{Ge/Si}}$ of $\ell_{\text{Ge}} \approx 45$ nm [104]. As will be shown in the Results chapters these different electronic properties lead to differences in their transport properties at low temperature.

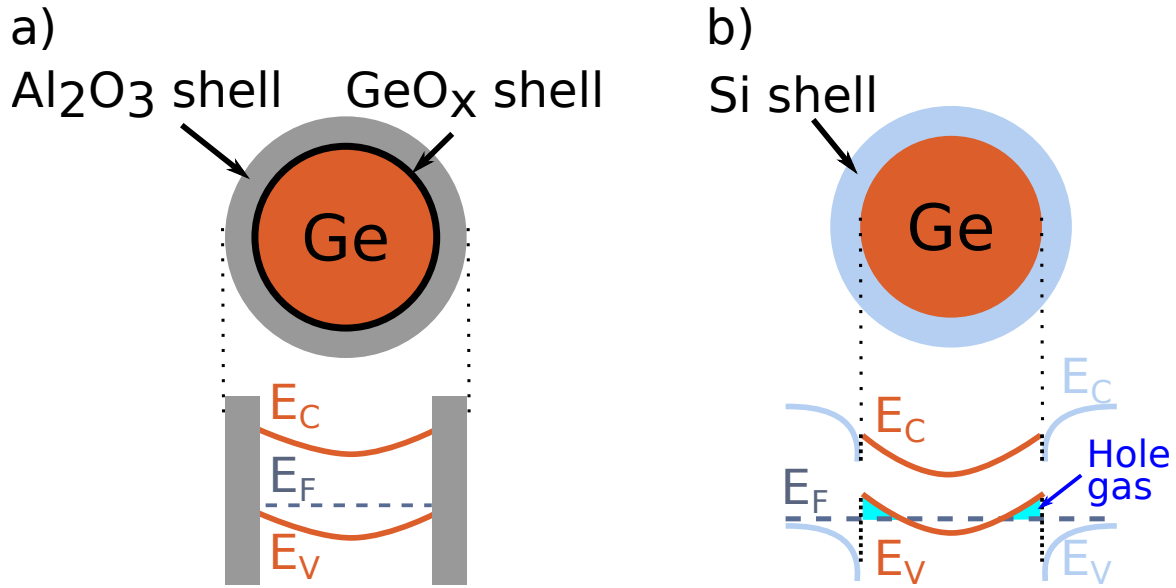


Figure 3.2 – Schematics of the (a) i-Ge and (b) Ge/Si core/shell nanowires used to fabricate gate tuneable superconducting semiconducting hybrid junctions studied in this thesis. (a) *Upper* Cross-section view of the i-Ge NW after VLS growth and ALD deposition of Al_2O_3 shell. *Below* Band diagram of the cross section of the i-Ge NW, the inert Al_2O_3 shell does not effect the band structure of the Ge core. The Fermi level E_F sits below the conduction band E_C and just above the valence band E_V [103]. (b) *Upper* Cross-section view of the Ge/Si core/shell NW after VLS growth and deposition of Si shell. *Lower* Band diagram of the cross-section of the Ge/Si core/shell NW. The band offset between Ge and Si results in the formation of a hole-gas in the Ge NW [105].

3.3 Field Effect Transistor FET

The grown Ge NWs with diameters between 20 nm and 30 nm with a 20 nm ALD grown Al_2O_3 passivating shell are extracted from the Si substrate and stored in solution. To enable electrical characterisation, the Al-Ge-Al heterostructures are fabricated using a field effect transistor (FET) architecture where the electrostatic gate field is established by a back-gate. The FET architecture was realised by drop-casting Ge NWs on a highly p-type doped 500 μm thick Si $\langle 100 \rangle$ wafer with 100 nm of thermally grown SiO_2 insulating layer. The drop-casting was carried out using a micropipette.

Figure 3.3 shows schematically the fabrication process. Before drop casting the substrate is prepared with macroscopic Ti/Au pads using photolithography techniques. The pads provide bonding contacts for the source, drain and back-gate. To access the p-doped layer that forms the global back-gate buffered hydrofluoric acid was used to etch the SiO_2 layer.

After drop-casting, appropriate Ge NWs are selected and contacted to the Ti/Au pads by the deposition of Al contacts, which are defined by electron-beam lithography. To ensure transparent contacts to the Ge NWs a two step etching process is used before the sputter deposition of Al. First, the Al_2O_3 shell is etched using buffered hydrofluoric acid. However, this results in a native oxide forming on the exposed Ge. In order to

3.3 FIELD EFFECT TRANSISTOR FET

improve contact transparency, the oxide layer is removed before Al sputtering using 14% diluted hydroiodic acid. For further details on the integration of Ge NWs into FET including the etching process see Ref. [39].

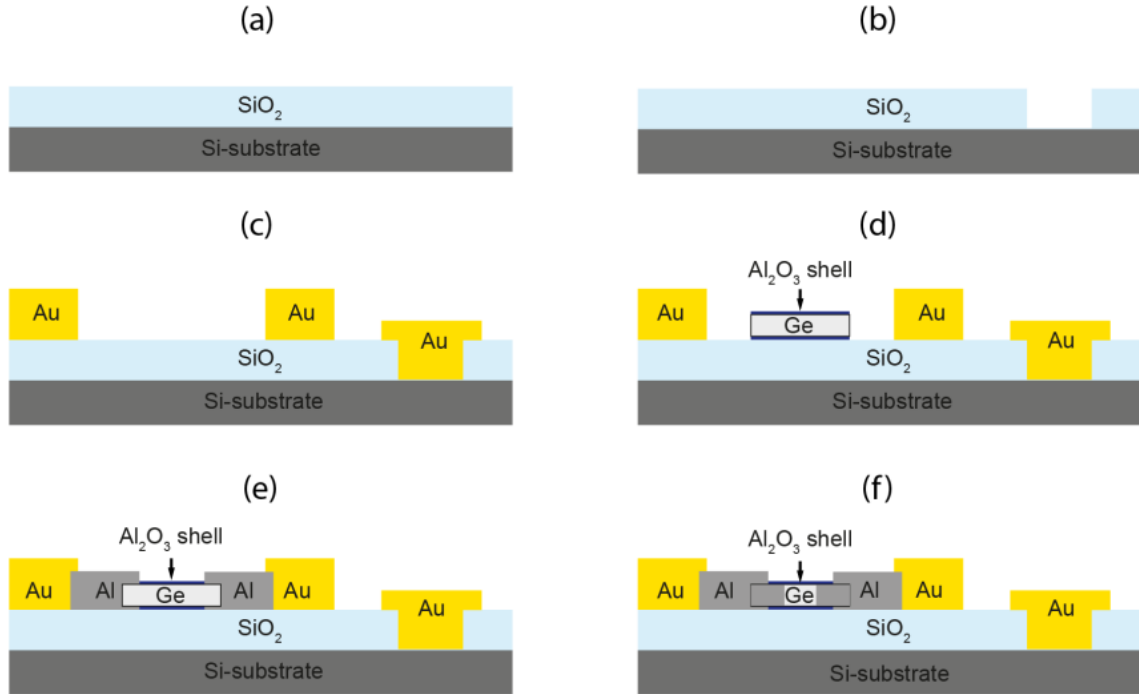


Figure 3.3 – Schematic of the fabrication process used to integrate Ge NWs into a FET architecture. (a) The highly *p*-doped Si substrate with a 100 nm SiO₂ insulating layer on-top. (b) Etched SiO₂ facilitating back-gate contact. (c) Au bonding pads deposited on the substrate. (d) Ge NW transfer by drop-casting. (e) Al contacts deposited to connect Ge NW to Au pads. (f) Formation of Al-Ge-Al NW heterostructure after thermal annealing process. Figure taken from Ref. [39]

To aid in the visualisation of the process outlined above, Figure 3.4 shows scanning electron microscope (SEM) images of increasing magnification of a sample with multiple Ge NWs integrated into a FET architecture. Figure 3.4(a) shows the large Ti/Au pads, which dominate the substrate and form a circular pattern. Also visible are the Al arms which make contact with the selected Ge NWs; in this SEM image, three Ge NWs have been contacted. A zoom on the Al arms, Figure 3.4(b), reveals the many NWs that are deposited by drop-casting and are unused. Figure 3.4(c) shows a zoom on one contacted NW.

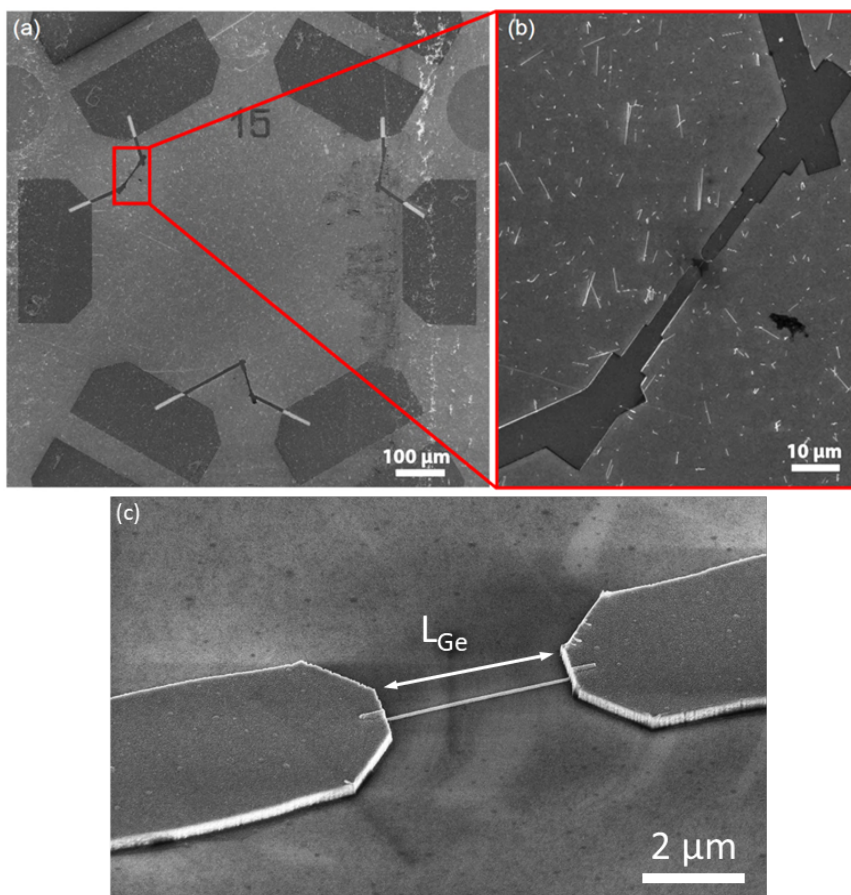


Figure 3.4 – SEM image with different magnifications of the FET sample illustrates the fabrication process. (a) shows the large Au pads fabricated using optical beam lithography. (b) Zoom on the Al leads which connect to the Ge NW that are fabricated using electron beam lithography (c) Zoom on the Ge NW and the Al leads.

3.4 Diffusion through Thermal Annealing

Critical to achieving Al-Ge-Al nanowire (NW) heterostructures with Ge segment lengths shorter than lithographic capabilities and highly transparent interfaces is the thermal annealing process. This process exploits the asymmetric diffusion properties of Al and Ge to realise monolithic Al-Ge-Al NWs.

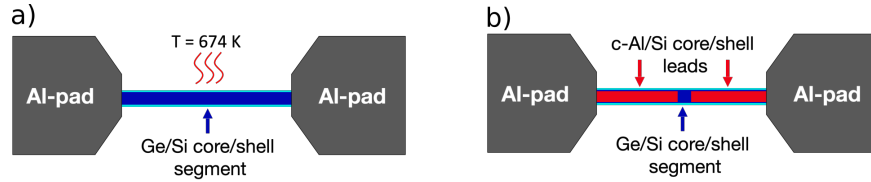


Figure 3.5 – Schematics presenting the thermal annealing process (a) that results in the diffusion of Ge out of the nanowire and into the Al pads. The diffused Ge is replaced by Al (b), forming monolithic Al-Ge-Al and Al-Ge/Si-Al core/shell NW heterostructures.

By heating the system to 624 K the controlled diffusion of Al from the contacts into the Ge NW can be induced. This is thanks to the diffusion coefficients of Al-Ge material systems, listed in Table 3.1. Inspecting Table 3.1 reveals the orders of magnitude difference between the diffusion of Ge in Al and the diffusion of Al in Al itself (self-diffusion) compared to the diffusion of Al in Ge and the self-diffusion of Ge. This significant asymmetry has distinct effects on the diffusion processes under thermal annealing conditions. The dominance of Ge diffusion through Al over the contrary leads to Ge diffusing out of the Ge NW and into the macroscopic Al pads. The displaced Ge is replaced by Al while the Al does not diffuse into the un-diffused Ge. Continuing the thermal annealing process leads to the Ge NW being steadily replaced by the Al. By controlling the thermal annealing time and temperature the length of the Ge segment L_{Ge} can be tuned down to 10 nm. Advantageously, the thermal annealing process can be repeated multiple times allowing greater control of L_{Ge} . Furthermore, by adjusting the lithographically defined gap between the Al contacts, Ge segment lengths between 500 nm and 10 nm can be achieved in a single thermal annealing step[39].

To enable high detailed imaging and structural characterisation of the Al-Ge-Al NW heterostructures' crystal structure and interfaces, the devices were also fabricated

Table 3.1 – Al-Ge diffusion coefficients at 623 K including the inter-diffusion; Al in Ge & Ge in Al as well as self-diffusion; Al in Al & Ge in Ge. The row labels represent the diffusing material and the column labels are the material through which it diffuses. From Ref. [106].

	Diffusing in Al (cm^2s^{-1})	Diffusing in Ge (cm^2s^{-1})
Al atoms	6.0×10^{-12}	1.3×10^{-25}
Ge atoms	3.2×10^{-11}	9.9×10^{-25}

on Si_3N_4 -membranes [39]. The membrane based devices enabled continuous in-situ scanning tunneling electron microscopy (STEM) analysis of the thermal annealing process of Al-Ge-Al heterostructures [107]. The thermal annealing was achieved by in-situ joule heating. The investigation revealed that the Ge segment shrank layer by layer, while maintaining a sharp interface.

Structural characterisation was carried out by applying energy-dispersive X-ray (EDX) spectroscopy to the Al-Ge-Al NW devices fabricated on membranes. A 3D chemical reconstruction model based on these spectroscopy measurements revealed that the Al NW leads formed a multi-shell structure. This NW structure consisted of a crystalline Aluminium (c-Al) core with a 2 nm thick Ge shell, followed by 1 nm thick Ge + Al_2O_3 shell and completed by the 3 nm Al_2O_3 shell that remained from the i-Ge NW [107]. The analysis revealed that during thermal annealing the c-Al core forms a diffusion front steadily replacing the depleting Ge via self-diffusion. The Ge diffuses out of the NW, also via self-diffusion, through the thin Ge shell.

Figure 3.6 shows STEM images of the devices after the thermal annealing process. The STEM images reveal that the Ge nanowire becomes an Al-Ge-Al NW heterostructure where the c-Al leads and Ge segment constitute a single NW. The formation of a single NW is why we describe these devices as monolithic Al-Ge-Al NW heterostructure.

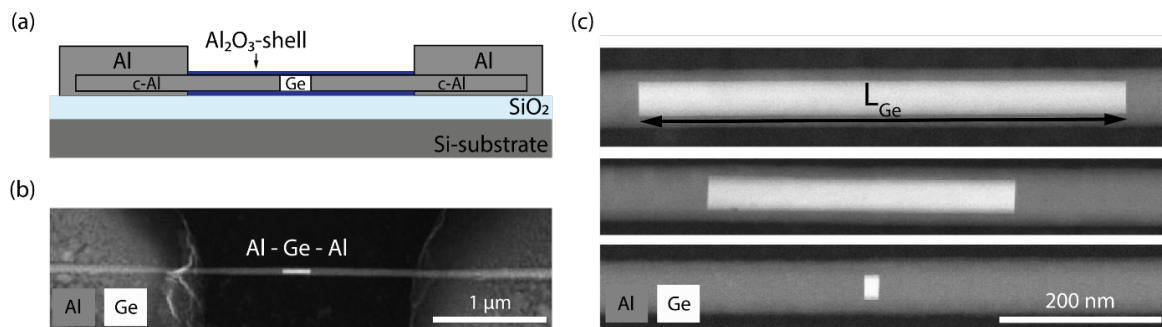


Figure 3.6 – (a) Schematic representation of the FET architecture after the annealing process. (b) STEM image of the architecture after the annealing process showing a monolithic Al-Ge-Al NW heterostructure coupled to large polycrystalline pads. (c) STEM image showing various Ge segments lengths achieved through the annealing process.

The thermal annealing process can also be deployed to Ge/Si core/shell NWs achieving similar results. In this case the Si shell remains intact during the process with only the Ge core being replaced by c-Al. As with Al-Ge systems, a thin Ge shell around the c-Al provides the channel through which the Ge self-diffuses. The final device then becomes a monolithic Al-Ge-Al NW heterostructure junction with a Si shell. EDX measurements, shown in Figure 3.7, reveal the stability of the Si shell and the purity of the respective segments.

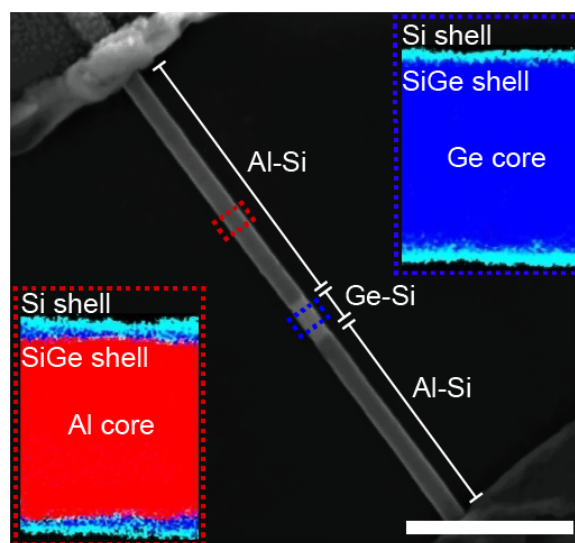


Figure 3.7 – STEM image of a monolithic Al-Ge-Al NW heterostructure core with a Si shell after the annealing process. Insets shows EDX measurements of the Ge segment and *c*-Al segment where Ge and Al cores with high purity are observed in the respective segments, which are wrapped by a continuous SiGe and Si shell. The scale bar is 200 nm.

3.5 Interface Quality

In the previous section we discussed how the thermal annealing technique allows Al-Ge-Al and Al-Ge/Si-Al core/shell nanowire heterostructures to be fabricated with semiconducting segment lengths shorter than lithographic capabilities. The nature of the diffusion that occurs under thermal annealing combined with the low probability of Al-Ge forming intermetallic phases, thanks to their low intersolubility [108], suggests that high quality semiconducting-metal interfaces should form.

3.5.1 i-Ge Interface

Figure 3.8 shows the results of high resolution imaging analysis of a Al-Ge-Al NW heterostructure after the annealing process. The high quality of the junction is immediately visible in Figure 3.8(a). This high junction quality is further endorsed by the EDX chemical maps shown in Figures 3.8(c-e) which reveal the purity of the Al and Ge segments and an absence of inter-metallic phases. Composition analysis showed no Al inside the Ge within the resolution limits of %1. The specs of Ge observed in the c-Al NW segments are attributed to the thin Ge shell that forms during thermal annealing rather than contamination. Figure 3.8.b shows a high-angle dark-field (HAADF) scanning transmission electron microscopy (STEM) image of the Al-Ge interface. The high quality interface is evident by the near atomic precision at which the NW transitions from c-Al to Ge.

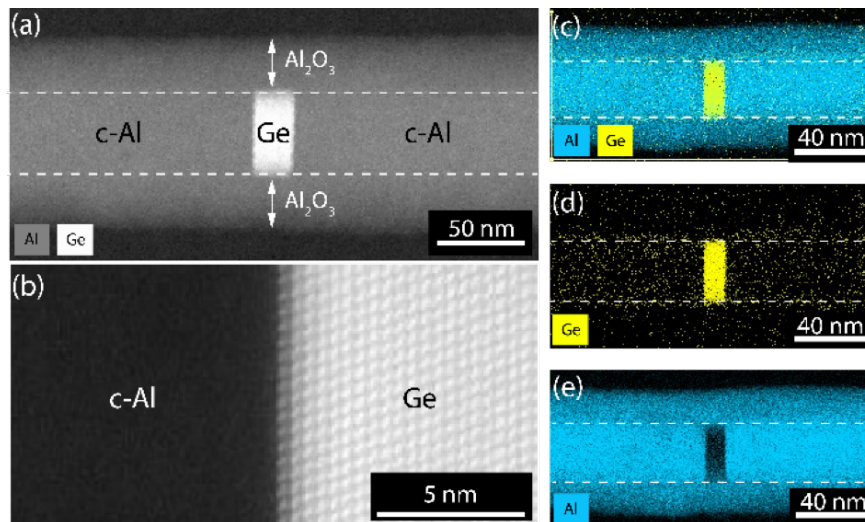


Figure 3.8 – Analysis of Al-Ge-Al heterostructure interface: (a) HAADF STEM image of an Al-Ge-Al NW heterostructure with an ultra-scaled Ge segment. (b) High-resolution HAADF STEM images recorded at the Al-Ge interface. (c-e) EDX chemical maps of the Al-Ge-Al NW heterostructure.

3.5.2 Ge/Si core/shell Interface

Figure 3.9 shows the results of high resolution imaging analysis of a Al-Ge/Si-Al core/shell NW heterostructure after the annealing process. The Ge/Si core/shell device shares the same high quality attributes as the i-Ge system [32]. The EDX chemical

maps shown in the inset of Figure 3.9 (a), which shows a schematic of the Al-Ge/Si-Al NW, reveal the purity of the respective segments. Figure 3.9 (c) shows the high-resolution HAADF STEM image at the Al-Ge interface of an Al-Ge/Si-Al NW, see cyan dashed box in Figure 3.9 (b). The improved visibility of the c-Al lattice, thanks to the strain induced by the Si shell, enables one to clearly observe the atomic precision of the interface. The sharpness of the interface is made further evident by the intensity profile obtained across the interface, see Figure 3.9(c).

The HAADF STEM imaging and EDX material analysis was carried out for both devices by our collaborators. More details of their material investigations of these devices can be found in Refs. [32, 107, 109, 39, 33].

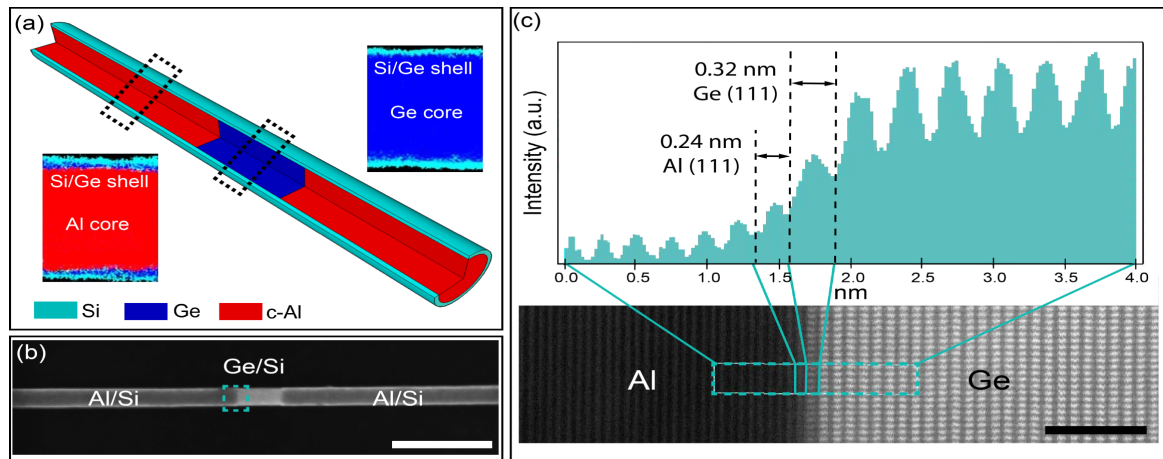


Figure 3.9 – (a) Schematic illustration of an axial Al-Ge-Al NW heterostructure with an ultrathin semiconducting shell wrapped around it. The insets show EDX chemical maps at the respective positions along the heterostructure indicating an intact semiconducting shell around the entire Al-Ge-Al heterostructure. (b) SEM image of the actual heterostructure arrangement. Scale bar is 200 nm. (c) High-resolution HAADF STEM obtained at the Al-Ge interface and corresponding intensity profile obtained at the cyan dashed square shown in (b). Scale bar is 2 nm.

3.6 Conclusion

This novel fabrication technique developed and implemented by our collaborators in Vienna enables the fabrication of germanium based nanowire FETs with ultra-scaled Ge or Ge/Si core/shell segments. Moreover, the exploitation of aluminium, a transition metal, for the leads adds further applications of these devices including JoFETs, Andreev Spin qubits, and the search for Majorana fermions. Beyond the high interface quality and reproducibility, this technique enables the fabrication of devices with semiconducting segment lengths down to 10 nm. Though devices with NW segment lengths of 30 nm to 50 nm can be achieved using electron-beam lithography to define the leads, the macroscopic size of the contacts results in substantial gate screening, which reduces the gate tuneability of the device[110]. As such NW FETs or NW JoFETs with lithographically defined contacts have typical segments longer than 100 nm[21]. The use of diffusion through annealing has been used to reduce the gate screening effect and achieve ultra-scaled semiconducting segments. F.A.Zwanenburg

et al. contacted a Si segment of length between 25 and 30 nm to NiSi leads through annealing[49]. More recently, Ridderbos et al. applied a similar annealing procedure to Ge/Si core/shell NWs with Al contacts[111] achieving a Ge/Si core/shell segment length of approximately 50 nm. However, asymmetric diffusion during the annealing process resulted in their devices having one bulk Al lead and a second NW Al lead.

In this thesis, we investigate the low temperature transport properties of these unique Al-Ge-Al nanowire heterostructures with various Ge segments lengths (L_{Ge}) of 162 nm and 40 nm. We consider the feasibility of these i-Ge devices as quantum devices including quantum dots and gate tuneable superconducting hybrid junctions. To make comparisons with the more prominent Ge/Si core/shell NWs we carry out and discuss low temperature investigations of Al-Ge/Si-Al core/shell nanowire heterostructures with Ge/Si segment lengths of 40 nm.

Experimental Set-Up

4

Contents

4.1 Cryogenics	82
4.2 Le Fridge: Table-top pumped helium-3 cryostat	82
4.2.1 Advantages & Disadvantages	83
4.2.2 Cool-down procedure	84
4.2.3 Reducing cool-down time: Exchange Gas	86
4.2.4 Stabilising ^4He flow	86
4.3 Measurement Set-up	90
4.3.1 Electronic measurements	90
4.3.2 Thermalisation & Filtering	94
4.4 Performing Measurements & Data Processing	95
4.4.1 LabView Measurement Program	95
4.4.2 Measurement Feedback	97
4.4.3 Data Correction	97
4.5 Sample Installation	98

4.1 Cryogenics

The nature of our Al-Ge-Al and Al-Ge/Si-Al core/shell nanowire heterostructures, which combine superconducting Al with highly confined Ge, motivates their investigation at sub-Kelvin temperatures. In this thesis, we make use of a novel table-top helium-3 cryostat, which was designed and built as a prototype at Institut Néel by Pierre Brosse-Marion with the expertise of Philippe Gandit. Nicknamed by myself as "*Le Fridge*", this unique refrigerator has a minimum working temperature of 350 mK and is discussed in detail below.

There are multiple helium based solutions. Such solutions include liquid helium-4 (^4He), which has a base temperature of 4 K. ^4He was first liquefied by Heike Kamerlingh Onnes in 1908 who later used its cryogenic properties to observe the superconducting transition of mercury [60]. Measurements performed between 300 K and 4 K by our collaborators, to discuss some of the classical transport properties of the Al-Ge-Al devices, will use a liquid helium-4 cryostat.

Favorably, it is possible to reduce the cooling temperature of liquid ^4He down to 1.2 K by reducing its vapour pressure through pumping. The lower temperature of pumped ^4He is often exploited in pumped ^3He systems to condense ^3He . In pumped ^3He cryostats the larger vapour pressure of ^3He compared to ^4He at the same temperature is exploited to reach sub-Kelvin temperatures. In fact the evaporation of ^3He is the simplest way to reach temperatures between 0.3 K and 1 K [112]. More details of the pumped ^3He cryostat used in this thesis will be discussed below.

The most important cryogenic technique for sub-Kelvin (5 mK to 1 K) temperatures exploits the cooling power of a ^3He - ^4He mixture [113]. The principle development of using a ^3He - ^4He mixture compared to pumped ^3He , the previous state of the art refrigeration technique, gave these systems the name of *dilution refrigerators*. Dilution refrigeration has evolved tremendously since its first realisation in Leiden in 1965 where a temperature of 0.22 K was reached [113]. Typical base temperatures of around 25 mK are now easily reached. These even lower working temperatures provide a significant reduction in thermal noise, which is necessary for many quantum experiments including quantum transport, circuit quantum electrodynamics, and superconducting qubits. Important for the advancement of these experiments is the successful commercialisation of such systems which has made low temperature science more accessible and helped the industrialisation of quantum technologies. More details of dilution refrigerators can be found in Ref. [113].

4.2 Le Fridge: Table-top pumped helium-3 cryostat

Figure 4.1(a) shows the table-top ^3He cryostat, nicknamed *Le Fridge*, used throughout this thesis. The internals of the cryostat are shown and labeled in Figure 4.1(b). The cryostat consists of two helium circuits: an open ^4He circuit and a closed ^3He circuit, shown schematically in Figure 4.2. In the open circuit ^4He flows from a 100 L reservoir through the cryostat and finally into the recuperation line where it is returned to the liquifier. The ^4He circuit cools down the 80 K and 4 K stages, the ^3He charcoal sorption pump, and the 1 K pot, labeled in Figures 4.1(b) & 4.2.

To reach sub-Kelvin temperatures, ^3He must be first condensed into its liquid phase. ^3He starts condensing at 3.19 K, which is below the temperature of liquid ^4He . To attain this temperature, the 1 K pot, which is strongly thermally coupled to the ^3He

circuit, is cooled below 4 K by the reduction in ^4He vapour pressure through external pumping. This technique achieves a minimum temperature of 1.2 K at which point the rate of evaporation is too low to reduce the temperature further. The pumped ^4He is sent to the liquifier through the recovery line. The ^3He condenses at the 1 K pot where it drips down into the ^3He pot, located below the 1 K pot. The ^3He reservoir is strongly thermally coupled to the sample stage by the cold finger. The condensation of ^3He is monitored by the pressure gauge labeled in Figure 4.1(a). At this step the condensed ^3He is at a temperature between 1.2 K and 2 K.

To achieve sub-Kelvin temperatures, the condensed ^3He must be pumped to reduce its vapour pressure. In our table-top cryostat, the ^3He is pumped by an internal sorption system consisting of activated charcoal enclosed in a neighboring container that is thermally coupled to the ^4He line. The vapour pressure of ^3He becomes too low at 300 mK for further cooling to occur. This defines the theoretical minimum temperature of a pumped ^3He cryostat. In our system, a bare temperature of about 300 mK was achieved when the measurement set-up was not yet mounted. In our transport measurements, we have reached a minimum temperature of 350 mK.

4.2.1 Advantages & Disadvantages

Though the table-top ^3He cryostat does not reach the base temperatures of dilution refrigerators, it is sufficient to observe quantum transport and the superconducting effects of Al and many other superconducting devices. The system has further advantages including that it is significantly cheaper to operate; taking only approximately 10 L of ^4He and has an optimized cool-down time of around 2.5 hours. However, once cold *Le Fridge* consumes approximately 2 L of ^4He per hour. Whereas, the Sionludi dilution refrigerators in the laboratory, their consumption of ^4He to cool-down ranges from 30 L to 100 L and cool-down times range from 6 - 10 hours. However, advantageously once cold their consumption is approximately 0.5 L per hour. Comparing the consumption and cool-down time it is clear that the table-top ^3He cryostat authorises very short measurement campaigns of one day. Indeed, the system was originally designed to quickly characterise superconducting tunnel junctions.

There are disadvantages to the table-top ^3He cryostat beyond just the higher working temperature. The cool-down process is completely manual, therefore a competent person must be present to manipulate the cryostat in order to achieve a successful cool-down. A detailed cool-down procedure is discussed below. Once cool the fridge requires regular manipulation to maintain the base temperature. This is due to the limited volume of ^4He in the 1 K pot and ^3He in the ^3He reservoir (5 L). The 1 K pot requires refilling every 2-3 hours depending on the temperature of the sample stage. The reserve of liquid ^3He is completely evaporated after approximately 8 hours, depending on the temperature of the sample stage. Refilling the reserve requires heating the activated charcoal to 40 K to release the ^3He gas to enable re-condensation. This procedure takes about half an hour before cooling down again. These aforementioned aspects reduces the continuous measurement time and ease of use of the table-top ^3He cryostat. Some of these limitations could be addressed by introducing automation procedures.

Another aspect of *Le Fridge* that further limits stable low temperature time is that the ^4He reservoir is a ^4He dewer. We use a 100 L dewer, which after cool-down provides approximately 40 hours of working time. Therefore, to continue low

temperature measurements the ^4He dewer must be replaced. This procedure is a race against time, without the flow of ^4He the cryostat quickly warms up. The ^4He dewer change process is outlined below. This limitation could be mitigated by using a larger dewer or introducing an internal ^4He reservoir that can be refilled without effecting the flow of ^4He . Such a system for example is used in the Sionludi dilution refrigerator.

4.2.2 Cool-down procedure

The temperature of the cryostat is monitored by five calibrated resistors, positioned at the 80K stage, 4K stage, ^3He charcoal pump, 1 K pot, and sample stage. The resistances are measured by MMR3, a device designed and built at Institut Néel, and a National Instruments fast voltage card. The respective temperatures are determined automatically through iMacRT^a and LabView respectively. The temperatures are recorded by LabView and presented as a real time plot. Heating of the sample stage and ^3He charcoal sorption pump is achieved by MGC3 a PID device that was also designed and built at Institut Néel. MGC3 is controlled by iMacRT.

As mentioned above cooling down is a manual process which requires delicate and timed adjustments of the valves. I was the first PhD student to carry out systematic and extensive measurements on this ^3He cryostat prototype. Over the many cool-downs I have tuned the processes to optimise the cool-down time and admittedly bonded to my dear *Le Fridge*. To aid future users of *Le Fridge* I have detailed a description of my optimal cool-down procedure.

1. Pump the cryostat chamber for around 30 minutes such that the pressure is below 4×10^{-2} mBar. Extended pumping time is important to degas the internal surfaces of the cryostat.
2. Introduce 20 mBar of ^4He exchange gas into the cryostat vacuum chamber and pump until a pressure of 8×10^{-2} mBar to have a first rinse of the vacuum chamber.
3. Reintroduce 20 mBar of ^4He exchange gas and pump until a pressure of 0.24 mBar.
4. Close the cryostat pumping valve.
5. Ensure all valves of the ^4He circulation line are fully open. Valves are labeled in Figure 4.1(a). Introduce the transfer line first into ^4He bottle then into cryostat. Ensure to maintain a pressure of at least 250 mBar in the bottle after completion of the introduction of the dip-stick. If needed the dewer pressure can be increased using the compressor.
6. When 4 K shield reaches 100 K turn shield valve to 1/4 open.
7. When charcoal reaches 150 K turn charcoal valve to 1/4 open.
8. When the 80 K and 4 K shields are below 100 K and 50 K respectively the rate of cooling of the sample stage slows. At this point the temperature of the 1 K pot dictates the sample stage temperature. To increase the ^4He flow to the 1 K pot the shield and charcoal valves should be reduced to 1/8 open.

^aA hardware and software package developed at Institut Néel.

9. The reduced flow through the shield valve (as it is 1/8 open) reduces the total draw of ^4He from the reservoir into the cryostat. This reduced flow can reduce the cooling rate of the 1 K pot. To increase the cooling rate one can increase the flow of ^4He through the cryostat by opening the shield valve for one minute and then re-closing to 1/8 open. This draws ^4He into the distribution chamber where it is forced through the 1 K pot.
10. Another tactic to increase the cooling rate of the 1 K pot is to turn on 1 K pot pump. I try to do this once the 1 K pot and sample stage is below 150 K. It is important that the temperature of the 1 K pot does not decrease too rapidly ahead of the sample stage temperature. If the temperature difference between the 1 K pot and sample stage is too great the cooling rate of the sample stage slows.
11. When charcoal approaches 40 K open charcoal valve to minimum to maintain charcoal above 40 K to prevent ^3He adsorption at this point; when the sample stage is too hot. It maybe necessary to use MGC3 to heat the charcoal container to maintain the temperature above 40 K.
12. When the 4 K shield approaches 30 K open shield valve to a minimum to maintain 4 K shield around 30 K.
13. When sample stage reaches near 30 K open shield valve to 1/4 open.
14. When 1 K pot reaches 2 K close the 1 K pot valve so the ^4He vapour pressure can be reduced. Note that the high temperature of the sample stage during the cool down will cause the ^4He of the 1 K pot to evaporate quickly. It is important to refill the 1 K pot as quickly as possible. Refilling is achieved by opening 1 K pot valve by 1/4 for 5 s and then re-closing the valve.
15. The 1 K pot should be kept stable around 1.2 K to ensure the condensation of ^3He which drips down into ^3He pot as it condenses at temperatures below 3.19 K.
16. Throughout the cool-down the pressure of the ^4He bottle must be at least 200 mBar.
17. Now one must wait until the sample stage stabilises below 2 K. Once below 2 K the sorption pumping of ^3He can be started. To start the ^3He pumping cycle the ^3He charcoal must be cooled to 4 K. This is achieved by turning off the heating element, if used, and opening the charcoal valve to 1/2 of a turn.
18. Once the sample stage's temperature has stabilised at its minimum (350 - 450 mK), introduce the pressure regulator on the ^4He bottle and adjust the shield and charcoal valves to maintain a stable temperature of around 4.2 K for the 4 K shield and ^3He charcoal. I set the pressure valve to 40 mBar and the shield and charcoal valves to around 1/5 of a turn. Adjustment should be made according to the respective stage temperatures, fluctuations of the 4 K shield and the ^3He charcoal temperature of around 0.1 K are okay.

Figure 4.3 shows the temperature evolution of the sample stage with respect to time during a cool-down using the procedure outlined above.

4.2.3 Reducing cool-down time: Exchange Gas

To reduce cool-down time, we introduce ^4He gas into the chamber after pumping the cryostat and before inserting the ^4He transfer line. The reasoning is that the ^4He gas acts as an exchange gas improving the thermal coupling between the sample stage and the shields which receive the largest ^4He flux. This increases the cool-down rate of the sample stage as it does not rely solely on the thermal conductivity of the ^3He through the cold finger.

The ^4He exchange gas loses its thermal conductivity as its temperature decreases. To remove the ^4He gas at low temperature, we introduced charcoal that is thermally coupled to the sample stage. Once the sample stage reaches 40 K, the charcoal starts to adsorb the exchange gas. This charcoal should not be confused with the activated charcoal of the ^3He sorption pump. The ^4He charcoal is fixed underneath the sample stage to which it is thermally coupled through a copper bracket (see Figure 4.4).

Redesigning the copper bracket

Upon my arrival in the lab there were issues with the cool-down of the fridge. We were unable to reach sub-Kelvin temperatures after ^3He condensation. The suspected culprit was the copper bracket holding the ^4He charcoal, which was touching the 4 K shield. To alleviate this issue, I redesigned the copper bracket to have an arm which couples thermally to the cold finger and bends downwards at an angle to avoid contact with the 4 K shield. After the installation of the redesigned bracket, shown in Figure 4.4, cool-downs were successful and I was able to reach a base temperature of 380-400 mK.

4.2.4 Stabilising ^4He flow

As discussed above, a 100 L ^4He dewer taken from the liquifier is the ^4He reservoir of the table-top cryostat. The ^4He flow rate into the cryostat is not only dependent on the open area of the valves controlled by knobs labeled in Figure 4.1 (a), but also dependent on the internal pressure of the dewer. Even without disturbance, the pressure of the dewer increases overtime as ^4He evaporates. To ensure optimal running of the cryostat and prevent the waste of ^4He , it is important that the ^4He flow rate is controlled. Too large, the ^4He flux and ice begins to build up around the external piping. Though in reasonable quantities it does not damage the system, it does block the manipulation of the valves and is a waste of ^4He . Too little the flux and the fridge will warm up.

To regulate the pressure of the cryostat, I make use of a pressure valve. Figure 4.5 shows a picture of the pressure valve in action. By manipulating the knob, the pressure at which the valve opens and ^4He gas is released to the recuperation line is set. I set a pressure of 40 mBar.

Using this pressure regulating technique, I have successfully kept the fridge cold overnight (approximately 12 hours). Predictably, after this time the ^3He has completely evaporated and the 1 K pot is empty of ^4He . Indeed, in the morning recondensation of ^3He is required. However, this procedure, of about half an hour, is much shorter than a full cool-down that would be otherwise required.

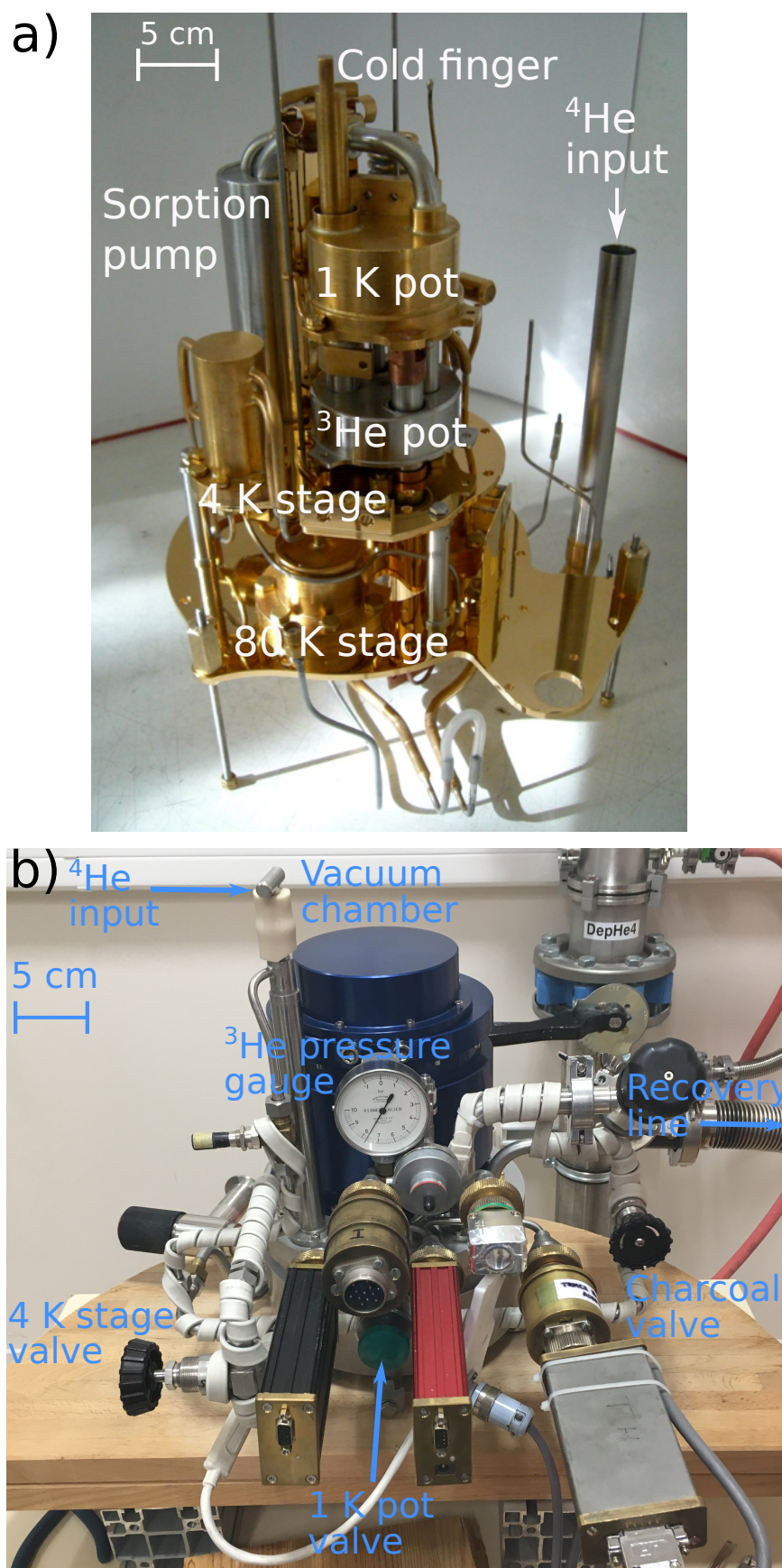


Figure 4.1 – Photos of the ^3He Table-top cryostat (a) The internals of the cryostat without the shields, the sample stage or outer vacuum seal with important internal components labeled. (b) In place in the laboratory. The valves used to manipulate the ^4He flow rate as well as other components are labeled.

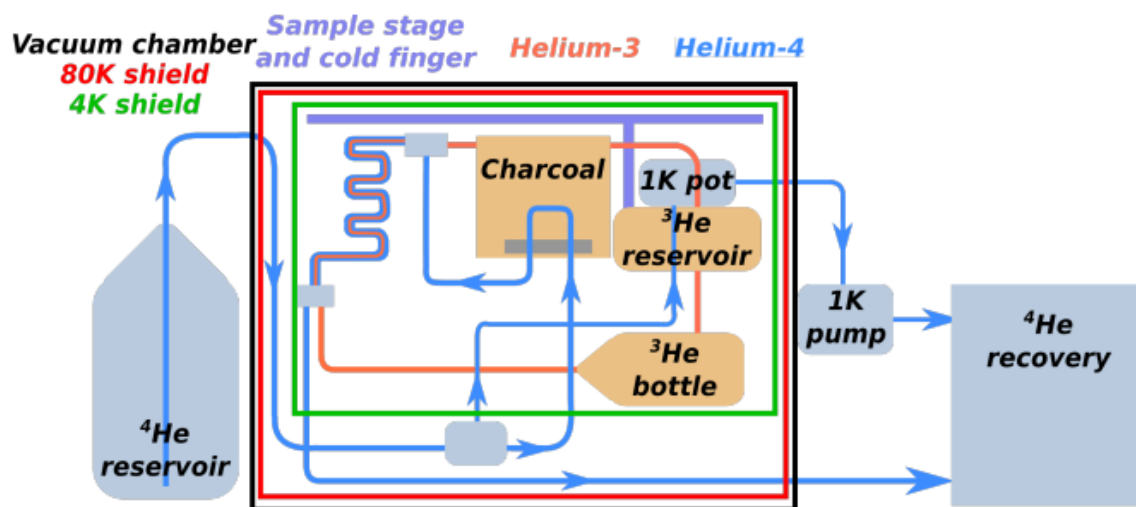


Figure 4.2 – Simplified schematic of the internal circuitry of the ^3He Table-top cryostat. The ^4He line is depicted in blue. Whereas, the ^3He line is depicted in orange. The 80 K shield and 4 K shield are depicted in red and green, respectively. The sample stage and cold finger are depicted in purple. In this schematic the ^3He pot is labeled as the ^3He reservoir. The ^3He Figure taken from Ref. [114].

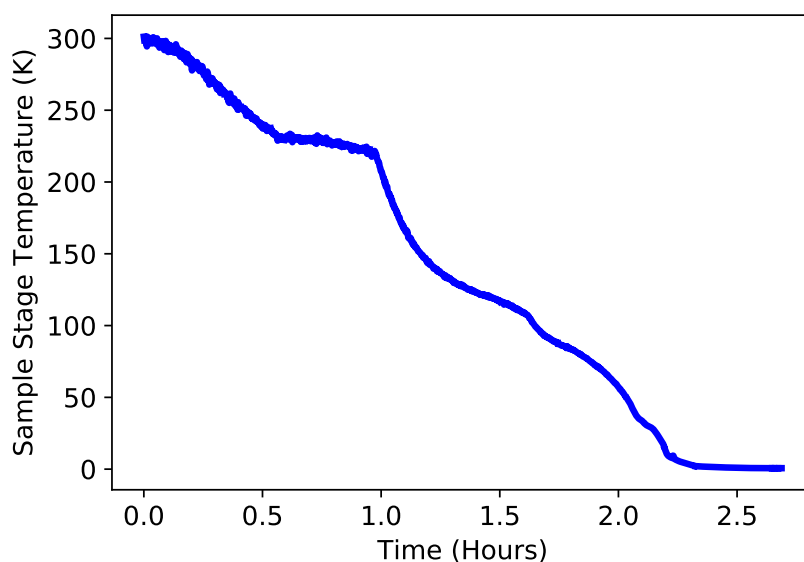


Figure 4.3 – Sample stage temperature versus time for an optimal cooldown.

4.2 LE FRIDGE: TABLE-TOP PUMPED HELIUM-3 CRYOSTAT



Figure 4.4 – Copper bracket encapsulating the charcoal sample.



Figure 4.5 – Pressure valve used to stabilise the ^4He flux.

4.3 Measurement Set-up

4.3.1 Electronic measurements

To investigate the transport properties of the Al-Ge-Al and Al-Ge/Si-Al core/shell nanowire heterostructures, two electrical measurement techniques were employed: voltage biasing (V-bias) and current biasing (I-bias). The two measurement techniques were employed in the same electrical set-up, which is shown schematically in Figure 4.6. The grey box with a red border, labeled measurement circuit, represents the electrical circuit used to carry out V-bias or I-bias measurements. As shown in Figure 4.6 the voltage source and voltmeter was a National Instruments (NI) PCI DAC/ADC high frequency card which has a range of ± 10 V. The NI voltage card is connected to the PC, where the DAC/ADC is installed, by a 68-pin I/O connector. The gate voltage V_G is provided by a Yokogawa programmable voltage source. BNC cables make all the room temperature electrical connections. The measurement circuit and the V_G source are connected to channels of the switch-box. The channels of the switch-box are connected to a Π -filter, which is connected to *Le Fridge*, through a 12-pin Jaeger connector. The switch-box enables each channel to be switched between the ground and signal. This feature is exploited to prevent electrical discharge when installing the sample, see Section 4.5 for details.

In Figure 4.6 the red dashed line represents the boundary of the cryostat. This outer-shield provides the vacuum seal of the cryostat. As such, the remaining stages of the cryostat share the same pressure. The internal fridge wiring is well thermalised at the 80 K, 4 K stages and at the 1 K pot. The wiring is then connected to the copper box which houses the sample and thermocoax via pin connectors.

4.3 MEASUREMENT SET-UP

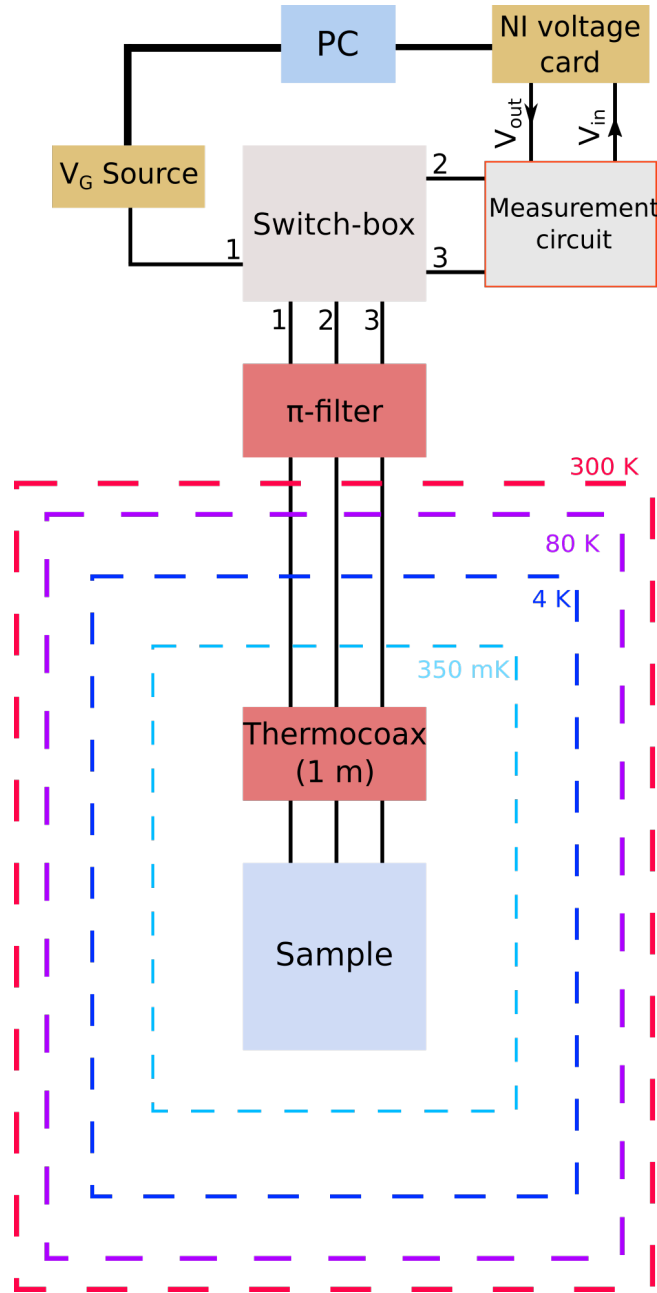


Figure 4.6 – Schematic of the measurement set-up which includes the fridge wiring which connects to the thermocoax that connects to the sample through micro-bonds within the copper box. The fridge wiring is thermalised to the stages of the fridge. At room temperature a π -filter with Jaeger connectors is used before entering the fridge. The switch-box is connected to the π -filter through a short lead with Jaeger connectors. The gate voltage V_G source is a Yokogawa programmable voltage source which is connected to line 1 of the switch-box through a BNC cable. The Yokogawa is connected to the PC through GPIB. The measurement circuit is connected to line 2 and line 3 of the switch-box through BNC cables. The measurement circuit used depends on whether voltage biasing or current biasing is employed. In both measurement cases, the voltage source and voltmeter is the NI instruments voltage card, which is connected to the PC by a 68-pin I/O connector that connects to a digital acquisition card installed in the PC.

Voltage biasing

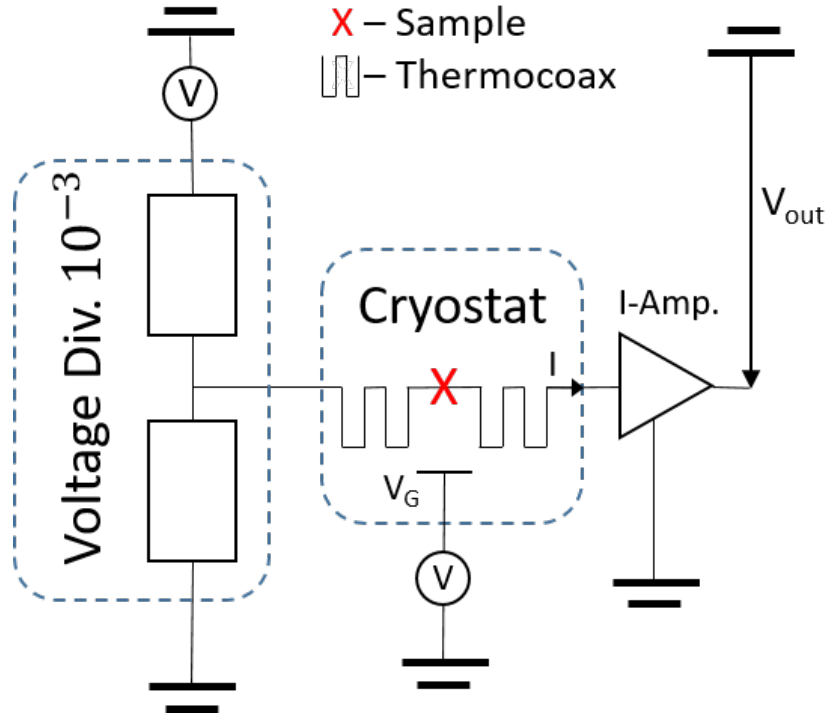


Figure 4.7 – Circuit diagram of the voltage biasing measurement circuit.

To carry out voltage biasing measurements, the sample is biased by applying a voltage source to one terminal and grounding the second terminal through a current amplifier, see Figure 4.7. At room temperature the applied voltage was scaled down by 1000 using an in-house built voltage divider of $50\ \Omega/50\text{k}\Omega$ providing a final V-bias range of $\pm 10\ \text{mV}$. The current that passes through the device is collected by the current amplifier and converted into a measurable voltage. The measured voltage is correlated to the current by $V_{\text{out}} \sim G_{\text{amp}} * I_{\text{out}}$, where G_{amp} is the gain of the amplifier. The voltage is measured using the same National Instruments card as the voltage source. The current amplifier used was a Femto variable gain transimpedance amplifier (DCPCA-200)^b.

This voltage biasing architecture provides reliable results when the resistance of the sample (R_{sample}) is much larger than the resistance of the amplifier ($R_{\text{amp}} \ll R_{\text{sample}}$). This condition ensures that the current circulates in the amplifier and the voltage bias across the sample is well defined. The maximum gain of $G_{\text{amp}} = 10^9$ ($R_{\text{amp}} = 10\text{k}\Omega$) was only used at very low conductances ($R_{\text{sample}} \gtrsim 1\text{M}\Omega$). The gain of $G_{\text{amp}} = 10^7$, ($R_{\text{amp}} = 150\Omega$) was used for the more conductive regions ($1\text{k}\Omega < R_{\text{sample}} < 10\text{k}\Omega$). Further, $R_{\text{sample}} \gg 50\Omega$ is required to ensure the voltage divider is working as rated. Given that the minimum normal resistance that we will measure is $R_{\text{N}} \approx 2.2\ \text{k}\Omega$, we estimate a voltage bias error of 3 % for a source bias of 1 V.

^bMore details can be found at www.femto.de

Current Biasing

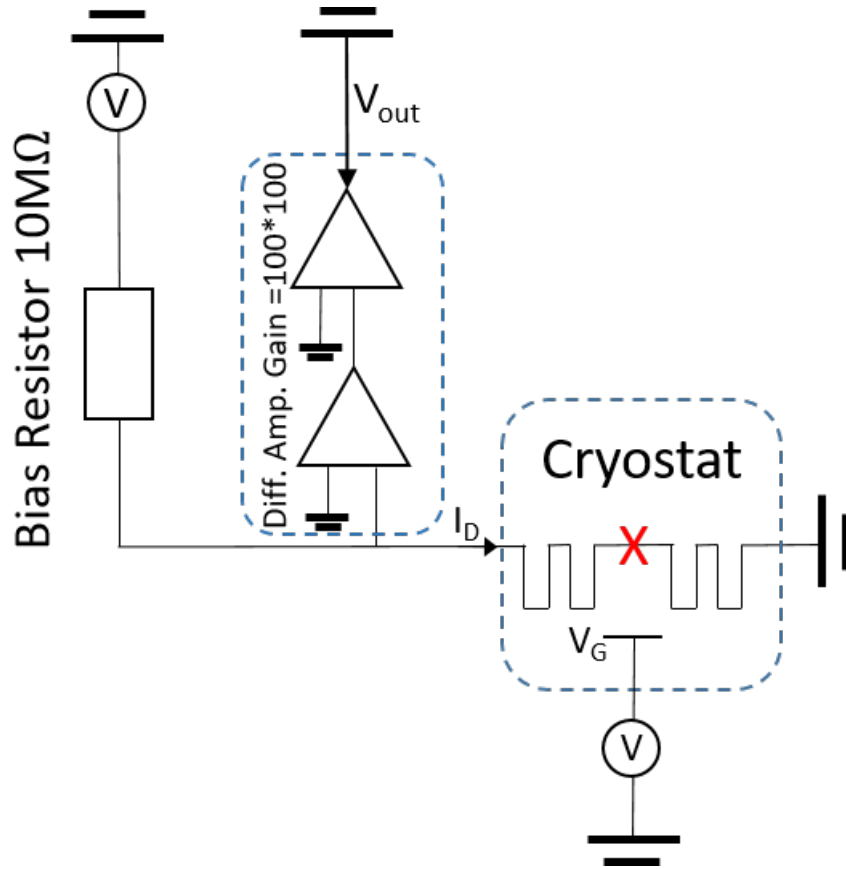


Figure 4.8 – Circuit diagram of the current biasing measurement circuit.

In the case of current biasing measurements, a voltage signal is applied to a polarising resistance ($R_{\text{polarising}}$) of $10\text{ M}\Omega$, which defines the current through the circuit, see Figure 4.8. The current is applied to the sample which is grounded at one end. To ensure the current is fixed and well defined, the polarising resistance must be chosen such that $R_{\text{polarising}} \gg R_{\text{sample}}$.

In the two-probe configuration, the voltage drop across the sample is determined by measuring the voltage at the input of the cryostat. To increase the voltage signal amplitude two differential amplifiers, each of gain 100, were used in series.

The voltage signal was provided and measured by the same National Instruments card as the voltage biasing measurements. The differential amplifiers were NF Electronic Instruments low noise preamplifiers (LI-75A) and have an input impedance of $R_{\text{amp}} = 100\text{ M}\Omega$. To ensure the applied current reaches the sample, it is necessary that $R_{\text{amp}} \gg R_{\text{sample}}$.

It is clear that the suitability of the two aforementioned measuring techniques depends on the resistance/conductance of the sample. The high tuneability of our devices, as will be demonstrated in the results chapter, requires both measuring techniques to investigate the transport properties of Al-Ge-Al and Al-Ge/Si-Al core/shell nanowire heterostructures over their full characteristic range.

In this thesis when discussing measurements and results, we use the symbols, V_G to define the back-gate voltage, V_D to define the applied bias voltage or measured voltage across the sample and I_D to define the applied bias current or measured

current through the sample.

4.3.2 Thermalisation & Filtering

When measuring devices at low temperature, it is necessary to consider the temperature of electrons that traverse the sample. Even if the sample is well thermalised at the base temperature, "*hot*" electrons coming from outside the cryostat can not only heat up the sample but increase the noise level of the measurements. There are two dominant mechanisms through which electron cooling occurs; the diffusion of electrons through the leads and electron-phonon coupling [115]. The large size of the leads and wiring means that they can be considered as thermal reservoirs where *hot* electrons can thermalise with the system. Therefore, it is important to reduce the temperature of the thermal reservoirs by well thermalising the electronic wiring to the cold stages of the cryostat.

In *Le Fridge*, the electronic wiring is thermalised to the 80 K, 4 K stages and 1 K pot. The wiring is thermalised to the sample stage through the thermocoax and sample holder, see discussion below.

Unfortunately, electron-phonon coupling is strongly diminished at low temperature, reducing the effectiveness of electron thermalisation. As a result, in most experiments, the electron temperature is greater than the base temperature. It was not possible to estimate the electron temperature in our set-up.

Outlined by many articles on experimental investigations of transport in mesoscopic and nanoscopic devices, it is critical to filter out parasitic electromagnetic radiation which is a major source of measurement noise. In our measurement set-up, we employed a room temperature π -filter and approximately 1 m of thermocoax for noise filtering. The thermocoax, with an outer grounded conductor of 1 mm in diameter, contains two conductive lines insulated from each other by aluminum oxide powder. Before measurements of nanowire heterostructures with ultra-short Ge segments, I realised a sample holder using a copper box fabricated by the workshop at Institut Néel. Figure 4.9 shows the finished sample holder positioned in the fridge. Three 1 m cables of thermocoax are wrapped around the copper box. The internal conductive lines are soldered to small boards; one next to where the sample is glued, inside the box and one to the outside side of the box. The side board is used to electrically couple, through soldering, the thermocoax to copper leads. The leads are soldered to pin connectors that connect to the fridge wiring. The Au/Ti contact pads of the device and the back-gate are micro-bonded to the internal sample board using Al wire with a diameter of $25\mu\text{m}$. The goal of the copper sample holder is that the sample is enclosed in a small box in which all entrances are thoroughly filtered by thermocoax. This prevents electromagnetic noise from tens of MHz to several hundreds of GHz to enter inside the sample holder and affect the transport properties of the device.

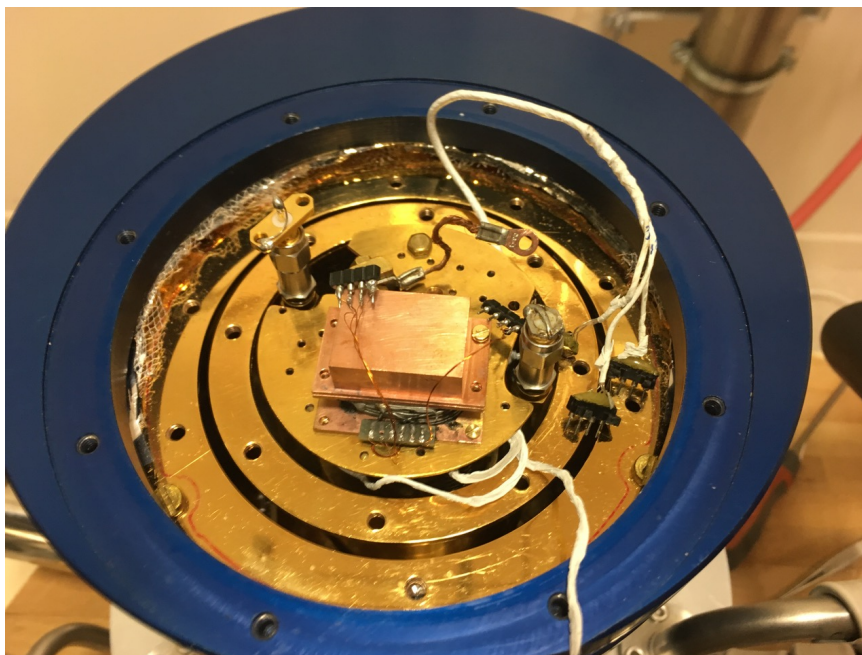


Figure 4.9 – Copper box sample holder

4.4 Performing Measurements & Data Processing

4.4.1 LabView Measurement Program

The measurement set-up was controlled by a Windows computer using a LabView program first built by Roman B. G. Kramer, a researcher of the QuantECA team. I modified this program to be more suitable for our needs. On the front panel of the LabView program, shown in Figure 4.10, the measurement parameters are set.

The adjustable measurement parameters that concern the sample bias and measurement include: the voltage source amplitude (V), the offset voltage (V), the magnitude of the voltage divider (1000 for V-bias measurements) and the gain of the current amplifier. The gate voltage V_G parameters can also be set which include the V_G source range, the starting V_G , the V_G span, and the number of V_G measurement slices. The waiting time after V_G has shifted and before I-V measurement can also be adjusted.

The first modification I made to the LabView program was to force the Yokogawa gate voltage source to increase the voltage amplitude from 0 V to the starting V_G of the measurement in intermediate V_G steps. The LabView program also forces the gate voltage source to decrease in voltage amplitude, from the final V_G of the measurement to 0 V, in intermediate V_G steps. These procedures were introduced to prevent a sharp change in V_G destroying the sample.

The other modification of the LabView program was to introduce an averaging method. I introduced two different averaging methods with the goal of reducing the measurement noise. The first method uses a LabView Virtual Instrument (VI) called *Decimate single shot VI*. The averaging occurs after the voltage source has been swept and the voltage response measured by the NI voltage card. The measured data object is an array that is inputted into the *Decimate single shot VI*. The VI reduces the number of samples from the initial sample number by a factor of decimation and outputs a new array with reduced sample points. The sample points of the reduced ar-

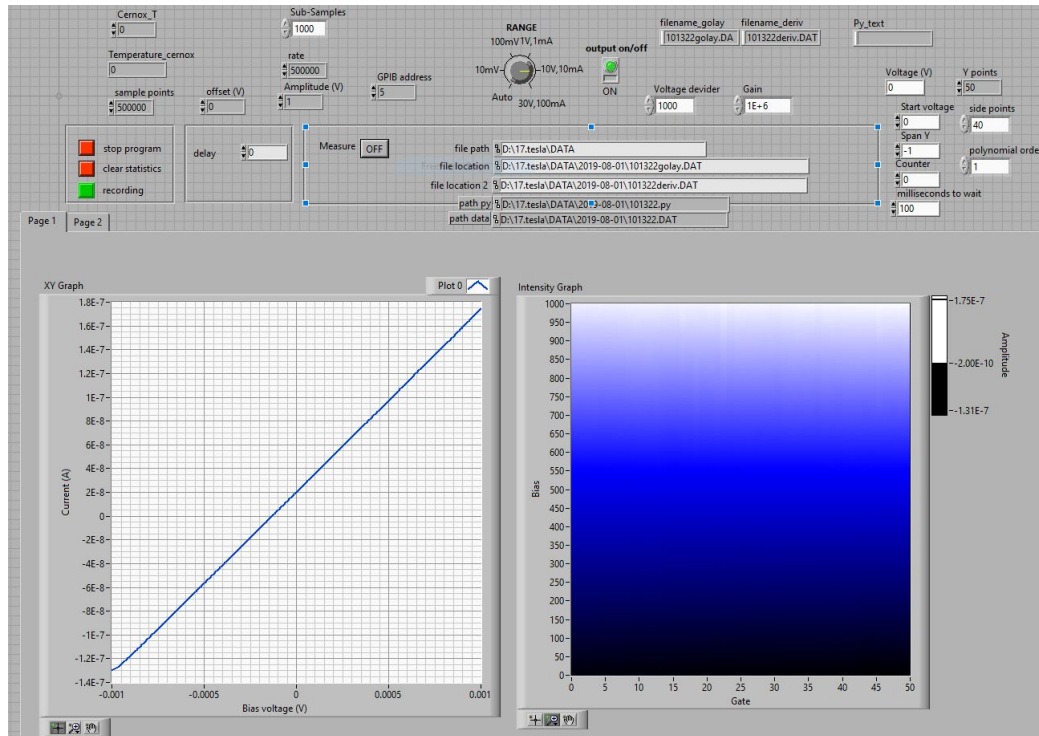


Figure 4.10 – Screen grab of the front panel of LabVIEW measurement program. Here the user can input measurement parameters

ray are calculated by averaging the sample points of the input array over the decimate interval (dt) which is equivalent to the factor of decimation and thus the decimate interval is determined by $dt = \text{samples}/\text{sub-samples}$. The number of sample and sub-samples can be adjusted on the front panel of the measurement LabVIEW program. The sampling rate, the frequency at which data points are measured can also be adjusted on the front panel. It is necessary that the number of samples is larger than the rate of sampling otherwise experimental artifacts are observed.

The second averaging method uses standard averaging techniques. Instead of sweeping the voltage source, the voltage source is fixed at each discrete voltage bias. The voltage biases are defined by the bias range and the number of samples. At each fixed voltage bias, the voltage is measured m number of times by the NI voltage card and then averaged by the LabVIEW program. The averaged data point is then recorded by the program and the voltage source moves to the next voltage bias and measurements recommence. This process continues until the end of the voltage bias range. The number of averaged measurements is defined by the sub-samples input on the front panel of the measurement LabVIEW program.

For both averaging methods, the data after the averaging processes goes through a Savitzky Golay filter. The smoothed data and its numerical derivative produced by the Savitzky Golay filter are exported as .dat files. The raw data before the filter is also exported as a .dat file.

The two aforementioned averaging methods were used depending on the goal of the measurement and time constraints. The second averaging method though more effective in reducing noise and measuring delicate transport features is considerably time intensive compared to the first averaging method. If the measurement focused

on a small V_G range and required high precision then the second method was used, otherwise the first method was used.

4.4.2 Measurement Feedback

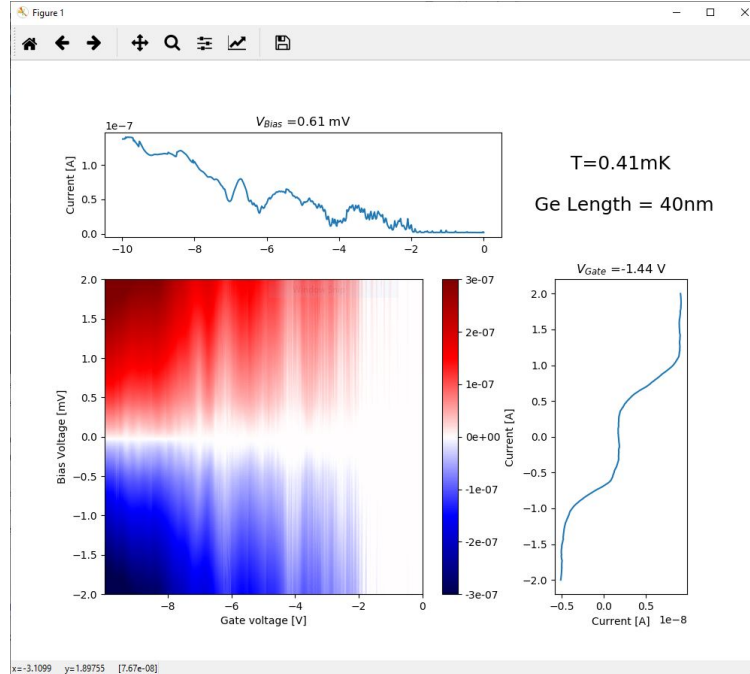


Figure 4.11 – Graphical User Interface (GUI) produced by the python script `'diamonds.py'` showing a density plot of $I_D(V_G$ with V_G and V_D slices plotted to the right and top, respectively. A user can click on the density plot to select V_G and V_D slices.

To provide immediate measurement feedback, I developed a python script that enables a user to easily view, in the case of voltage biasing measurements, the density plots of the measured current I_D and numerical differential conductance G versus V_D and V_G .

Figure 4.11 shows the graphical user interface (GUI) of the measured current. By clicking on the density plot the user can select a (V_G, V_D) coordinate. The program uses this coordinate to plot V_G and V_D slices to the right and top, respectively. The user can select different coordinates freely. The GUI also provides the standard functionality of a `matplotlib` plot such as saving the figure, changing the colorbar scale, zoom, pan and more. The same functionality works in the conductance GUI. This python script also works for current biasing measurements. Further details on how to run the python script can be found in Appendix B.

4.4.3 Data Correction

The measurements carried out in *Le Fridge* were 2-probe measurements. As such one must take into account the resistance of the wiring of the ^3He set-up, $R_{\text{fridge}} = 390 \Omega$, before analysing the measurement data. The finite resistance of the fridge wiring causes a finite voltage drop across the fridge wiring. Therefore, for V-bias

measurements, the applied voltage is not equal to the true voltage bias across the sample V_D . Whereas, for I-bias measurements the measured voltage is not equal to the true voltage drop across the sample V_D .

To correct the measured data, I adjusted the voltage response of I-bias measurements and the applied voltage of V-bias measurements. Further, I corrected the data to remove the zero-bias offset associated with the voltage source and the current offset associated with the current amplifier. By making these adjustments, I ensured that the voltages discussed in these measurements is the true voltage drop across the Al-Ge-Al nanowire heterostructures. Details of the procedure that I implemented are discussed in Appendix B.

4.5 Sample Installation

The fragility of the Al-Ge-Al and Al-Ge/Si-Al nanowire heterostructures that were measured during this thesis necessitates considerable care when installing them into the ^3He cryostat. Firstly, the sample must be carefully fixed to the sample holder while maintaining electrical isolation between the highly doped silicon wafer and the sample box. Secondly, due to the sensitivity of the device to static discharge a careful bonding routine must be followed. Finally, care should be taken when installing, the sample holder and sample into the cryostat. To ensure successful sample installation we developed a detailed routine which is described below in three stages: Fixing sample to sample box, Bonding sample and Installation of the sample in the fridge. To help explain the routine, Figure 4.12 shows the circuit diagram of the switch-box and shortening-link used to mitigate electrical discharge. The implementation of this procedure resulted in a sample installation success rate of approximately 90 %. Throughout my thesis I successfully installed and measured five Ge nanowire devices.

Fixing sample to sample box

- Glue a piece of cigarette paper to the sample holder using resist and glue the sample onto cigarette paper using the same resist. The cigarette paper is used to electrically isolate the highly doped silicon wafer, which will be polarised by the gate voltage, from the copper sample holder.
- Wait for 2 h for the resist to dry. One can use microscope lamp to speed up the process.

Bonding Sample

- Wear antistatic wrist strap connected to the ground of the micro-bonder.
- Link the ground of the portable switch-box and the work-holder to the ground of the bonding machine.
- Connect the switch-box to the sample using connector 1.
- Put in resistors (1 M Ω) to all used lines of the switch-box and switch to signal.
- First bond the back-gate.
- Second bond Ti/Au pads that contact the Al leads.

4.5 SAMPLE INSTALLATION

- Switch the lines to ground using the switch-box.
- Insert shortening links to connector 2.
- Attached copper box lid.
- Disconnect the sample from the switch-box.

Installation of the sample in the fridge

- Wear antistatic wrist strap connected to the fridge.
- Do not use plastic gloves.
- Put in resistors to all used lines of switch-box installed in set-up and switch to signal.
- Mount the sample holder to the fridge and connect cables to connector 1 of the sample.
- Switch all used lines to ground.
- Remove shortening-links.
- Wrap all open connections with Teflon-tape.
- Install the first (4K) shield to the fridge.
- Start the measurement program.
- Remove the resistors from the switch-box.
- Connect the cables of the measurement systems to the switch-box.
- Switch all used lines to signal.
- Run the measurement program to check the device.
- Ground device before cool-down.
- Always wear antistatic wrist strap before touching the fridge or the switch-box.
- Ground switch box before disconnecting or connecting the cables.

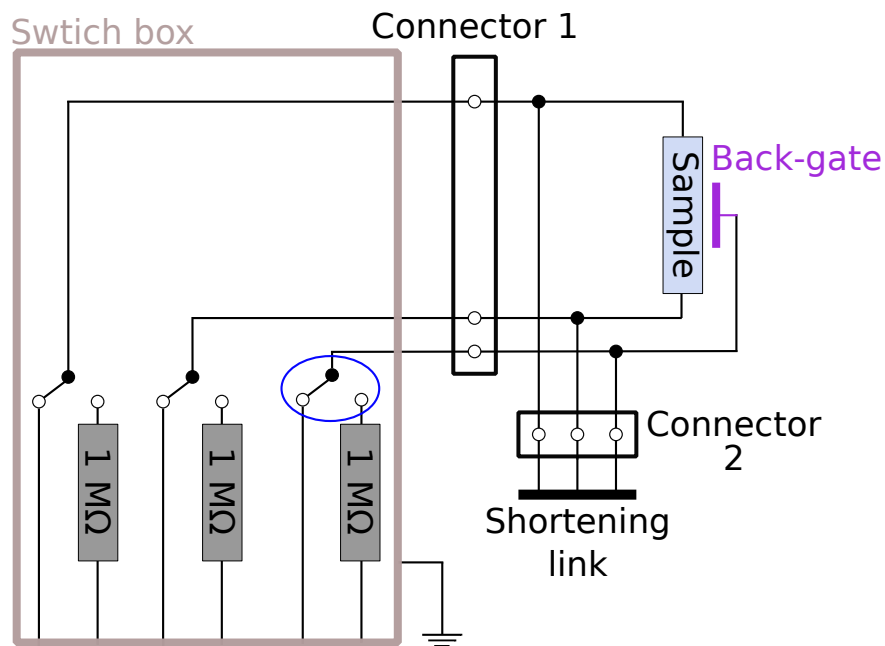


Figure 4.12 – Circuit diagram of the connections between the switch-box and sample holder connectors. The switch box has switches, circled in blue, that allow one to switch the input line between terminating through a short or a resistance of $1\text{ M}\Omega$. The lines of the switch box are connected to the switch box. The switch box is grounded to the bonding machine during bonding.

Transport properties of Al-Ge-Al Nanowire heterostructures

5

Contents

5.1	Al-Ge-Al heterojunction: A back-to-back Schottky diode	102
5.1.1	Schottky-Mott rule	102
5.1.2	Surface States	104
5.1.3	Charge transport through a Schottky barrier	106
5.1.4	Modeling Al-Ge-Al as a back-to-back Schottky diode	108
5.1.5	Quantum dot formation	110
5.2	Transport properties at high temperature	111
5.2.1	Long vs short Ge segment lengths	111
5.2.2	Temperature dependence on Al-Ge-Al transport ($G-V_G$)	113
5.3	Transport Overview at 400 mK	116
5.4	Coulomb Blockade	120
5.4.1	Addition Energy	124
5.4.2	Odd-even filling effect	127
5.4.3	Excited charge state resonant tunneling	128
5.4.4	Temperature evolution of Coulomb blockade	128
5.4.5	Coulomb blockade with superconducting leads	130
5.5	Supercurrent Regime	132
5.5.1	Multiple Andreev Reflection (MAR)	132
5.5.2	Supercurrent	139
5.6	Intermediate Regime	142
5.7	Sub-gap features in the Coulomb blockade regime	145
5.8	Conclusion	147

This chapter provides a detailed discussion of the transport properties of monolithic Al-Ge-Al nanowire heterostructures. The exceptional quality of these novel NW devices, highlighted in Chapter 3, motivates a detailed investigation of their transport properties. The goal of this investigation is to examine and understand the transport properties of these devices, while assessing their potential as quantum devices or systems of interest for further experimental measurements.

The chapter will begin by the introduction of the Schottky barrier, a potential barrier that forms at metal-semiconductor interfaces. The Schottky barrier plays an important role in explaining the experimental transport results of the Al-Ge-Al NW devices. We will show that the back-to-back Schottky barriers are key for the formation of a quantum dot at low temperatures. We will then present the electrical characterization of Al-Ge-Al NW heterostructures from room temperature down to 4 K. These measurements were carried out by our collaborators in Vienna.

The following sections, will focus on the low temperature transport properties, down to 350 mK, based on measurements that were carried out at Institut Néel. We will show that at low temperature, the Al-Ge-Al NW heterostructures can be tuned from a completely insulating regime, through a low conductive regime that exhibits properties of a single-hole filling quantum dot, to a supercurrent regime resembling a Josephson field effect transistor. We will describe in detail the properties of the three major transport regimes: the Coulomb blockade regime, the supercurrent regime and the intermediate regime.

5.1 Al-Ge-Al heterojunction: A back-to-back Schottky diode

The existence of a potential barrier at a metal-semiconducting contact was first reported by Schottky, Strömer and Waibel in 1931 [116]. They observed that the entire potential drop across a metal-semiconducting junction occurred at the interface. The rectifying behaviour observed in previous metal-semiconducting contacts was explained by Schottky and Mott independently in 1938 to be due to electron passing over the barrier through drift or diffusion, rather than quantum tunnelling which predicted current flowing in the opposite direction.

Schottky's significant involvement in the investigation of potential barriers at metal-semiconducting interfaces has resulted in the term Schottky barrier being used indiscriminately to describe most barriers at metal-semiconductor interfaces, independent of their cause.

To improve my understanding of the Schottky barrier at the Al-Ge interface, I have made particular use of *Metal-semiconducting Contacts* by Rhoderick [116] and the Master thesis of Raphael Böckle [117]. Böckle, under the supervision of Masiar Sistani, investigated the Al-Ge Schottky barrier in detail. This work has provided further insight into the band structure of our Al-Ge-Al nanowire heterostructures.

5.1.1 Schottky-Mott rule

To explain the potential barrier at the interface, Mott (1938) proposed that the barrier forms due to the necessary compensation of the difference between the work functions of the metal and the semiconductor. He suggested that the barrier region had no charged impurities as such the electric field was constant [118].

Mott's proposition enabled one to estimate the barrier height based on the difference between the respective work functions. This prediction for an ideal junction became to be known as the Schottky-Mott rule of barrier formation and is based on the following assumptions:

- The metal-semiconducting contact is ideal and intimate with no intermediary layers such as an oxide.
- There is no interdiffusion of the metal and semiconductor and no mixing of electronic states.
- There are no impurities at the interface.

Figure 5.1 shows schematically the Schottky barrier formation in the band diagram formalism. The neutral and isolated crystals are depicted on the left side of Figure 5.1, with the metal work function (φ_m), electron affinity (χ) and semiconductor work function labelled (φ_s). Isolated, the metal and semiconductor have differing Fermi energies, which must be equilibrated when in contact. To achieve equilibrium excess charge must flow between the metal and the semiconductor. The lowering (n -type) and raising (p -type) of E_F to achieve equilibrium induces a respective shifting of the semiconducting bands to maintain a constant electron affinity which is an intrinsic constant of the semiconductor. However, this band shift results in a discontinuity of the resting energy of a particle in the vacuum at the surface of the solid E_{vac} , which is not physically possible. To compensate, the bands must bend upwards (n -type) or downwards (p -type) to achieve E_{vac} continuity while maintaining a constant electron affinity, thus resulting in a parabolic potential, see right side of Figure 5.1. The contact region with a parabolic potential are variously referred to as the barrier region, the space-charge region, or the depletion region.

According to the Schottky-Mott rule the Schottky barrier height for electrons (B_n) and holes (B_p) is given by

$$q\varphi_{Bn} = q(\varphi_m - \chi) \quad (5.1)$$

$$q\varphi_{Bp} = E_g q(\varphi_m - \chi), \quad (5.2)$$

respectively. Here, E_g is the band gap energy. The difference in E_{vac} between the metal and semiconductor results in an internal potential difference (V_{bi}). It behaves similarly to a threshold voltage and defines the minimum bias voltage required to achieve a flat band in the semiconductor. In this ideal model V_{bi} is given by

$$V_{bi} = \varphi_m - \varphi_s. \quad (5.3)$$

Experimental investigations of a diverse range of semiconductors revealed that the barrier height was generally independent of the metal's work function, exposing the inaccuracy of the Schottky-Mott rule. On the other hand, Schottky (1939) suggested that the barrier contained a high density of charged impurities which resulted in a linearly increasing electric field. Therefore a quadratically increasing potential in accordance with Poisson's equation, contrary to the linearly increasing potential proposed by Mott. Though impurities have a significant effect on barrier height measurements on high purity devices also revealed discrepancies.

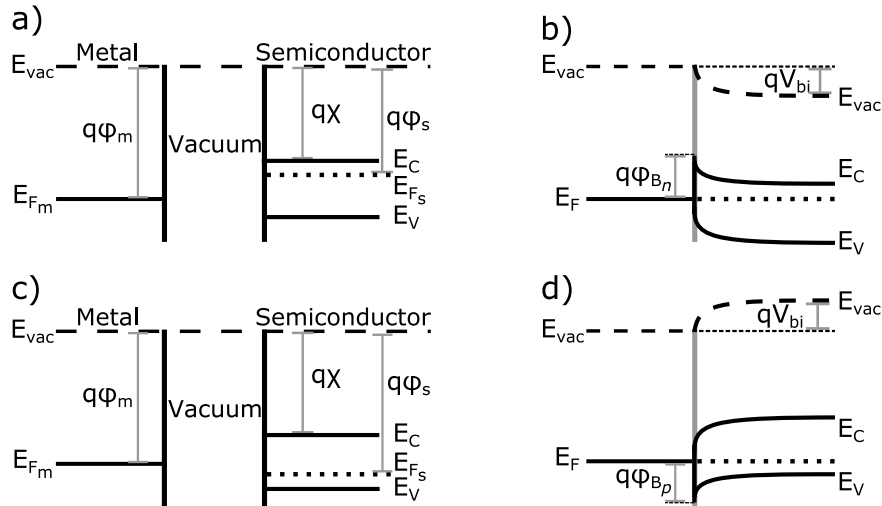


Figure 5.1 – Band diagrams depicting the formation of a Schottky barrier at an ideal metal-semiconductor contact using the Schottky-Mott rule. (a) & (c) show the band diagrams of the isolated metal and n -type & p -type semiconductors, respectively. Whereas (b) & (d) show the band diagrams when the metal-semiconducting contact is made for n -type & p -type semiconductors, respectively. (b) & (d) reveal the respective band bending.

Bardeen explained the discrepancy of the Schottky-Mott rule in 1947 as resulting from surface states which effectively screened the interior of the semiconductor from the metal and compensating for the contact potential difference. Given a large density of surface states, the Schottky barrier would be effectively independent of the metal work function. To understand their effect on the metal-semiconductor contact barrier, we will first introduce surface states.

5.1.2 Surface States

Surface states predicted by Tamm and Shockley in the 1930s [119] are a natural consequence of the finite dimensions of crystals. The crystal edge (surface) interrupts the perfect periodicity of an infinite crystal lattice. This interruption breaks down the model of a solid as an infinite Bravais lattice, which is a key assumption of Bloch's theorem (Section 2.1.3). The reduced validity of Bloch's theorem near the surface leads to the possibility of electronic states existing within the semiconductor's band-gap. In fact, electrons inside the surface region have solutions to Schrödinger's equation with band-gap energies. However, the eigenstates have imaginary wavevector values, which decay exponentially in space similar to wavevectors of tunnelling charges. As such, in a perfect but finite semiconductor, these states are localised near the surface and do not affect the band structure of the bulk.

In accordance with maintaining a constant density of states (DOS), the new surface states are made up of wave functions that would otherwise constitute the valence and conduction band states of an infinite crystal, as such the DOS in these bands are diminished near the surface. It can be considered that the surface states form their own band structure; a detailed three-dimensional treatment of surface states revealed the formation of a two-dimensional band with a continuous range of energy states

which can overlap the valence and conduction bands [120].

The filling of these surface states with electrons defines the net charge of the surface. The charge neutral level (CNL), defines the energy level $q\varphi_0$ to which surface states must be filled for the surface to be neutral. The CNL helps to determine the charge on the surface: If states are filled with electrons above $q\varphi_0$ then the surface is negatively charged (acceptor type), whereas if states are filled below $q\varphi_0$ then the surface is positively charged (donor type).

Surface charges have a significant effect on the local band structure. If the surface charges fill the surface states above or below the CNL then the charged surface will express an electric field, which will induce local band bending. If the surface charge is negative, then the bands will bend upwards, thus reducing the electron concentration at the surface compared to the bulk. On the other hand, if the surface charge is positive, then the bands will bend downwards, thus increasing the electron concentration at the surface compared to the bulk. In the case of very large density of surface states such bending dominates the semiconductor's band structure profile at the surface, which effectively pins E_F close to the CNL. This results in the metal-semiconducting Schottky barrier strength being nearly independent of the metal.

In the case of a metal contact, the filling of the surface states occurs up to the Fermi level of the metal, which, as described above, must be aligned with E_F of the semiconductor, see Figure 5.2. As without the contact, the filling with respect to the CNL determines the charge of the surface states. To maintain electrical neutrality between the metal and semiconductor, the positive charge of the semiconductor donors (Q_d) must compensate for the additional charge of the surface (Q_{ss}). For instance, in Figure 5.2, the CNL is higher than E_F resulting in a net positive surface charge, thus Q_d must be reduced. This is achieved by reducing the width of the depletion region, which reduces the amount of band bending that would otherwise occur, decreasing the barrier height. This has an overall effect of pushing $q\varphi_0$ towards E_F .

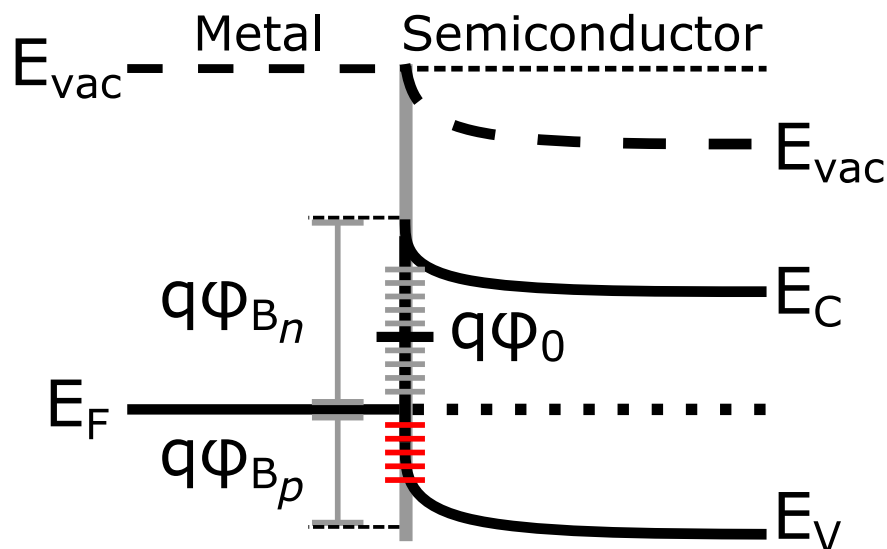


Figure 5.2 – Band diagrams depicting the effect of surface states on the formation of a Schottky barrier resulting in Fermi level pinning.

In the opposite case, if E_F is above $q\varphi_0$ then the negative Q_{ss} must be compensated by an increase in (Q_d), which is achieved by increasing the depletion width. This leads

to greater band bending as $q\varphi_0$ is pulled up towards E_F , resulting in a larger barrier height than without surface states.

5.1.3 Charge transport through a Schottky barrier

We can now consider the Schottky barrier's effect on charge transport through a junction. First, we will consider the transport across a single metal-semiconductor junction where a Schottky barrier of height ϕ_{Bn} has formed. There are multiple ways charge can be transported across a Schottky barrier. Figure 5.3 shows schematically the different transport mechanisms which are labelled by integers from (1) to (4). At room temperature the principle mechanism of transport is thermionic emission, labelled by (1). Introduced theoretically by Bethe in 1942, thermionic emission current is produced by thermal fluctuation which makes the electrons passing over the Schottky barrier and into the metal. Secondly, quantum mechanical charge carrier tunneling contributes to the current, labelled (2). The tunneling rate is dependent on the width (a) and height (ϕ_{Bn}) of the barrier, which can be expressed in terms of transmission probability by $T \propto e^{-a\phi_{Bn}}$. Though of less significance, electron-hole recombination (3) and diffusion (4) also contribute to the current across a metal-semiconductor junction.

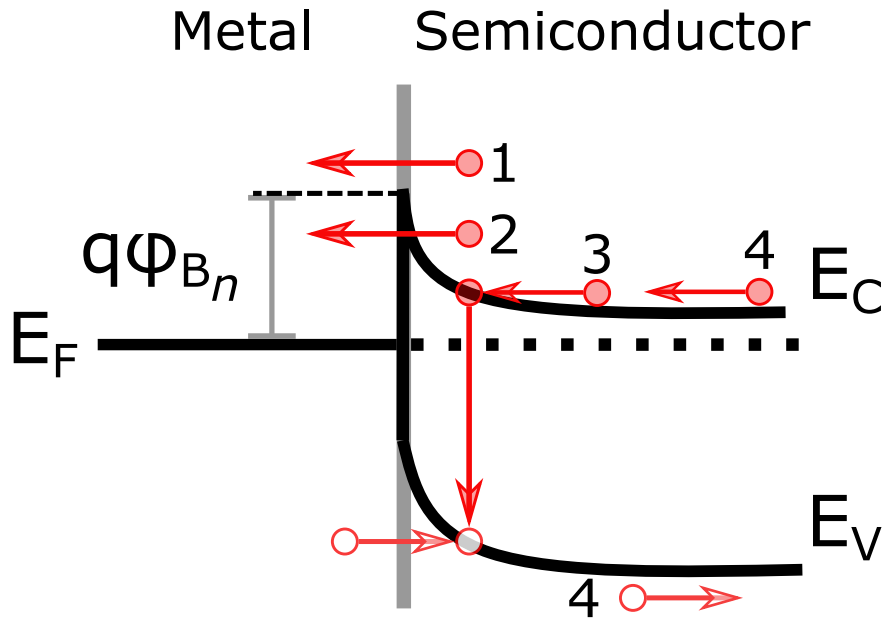


Figure 5.3 – Schematic showing the possible transport mechanisms across a Schottky barrier. Such as, thermionic emission (1), tunneling (2), electron-hole recombination (3) and diffusion (4).

Experimentally, it is difficult to distinguish between these different transport mechanisms as only the total current is measured as a function of the bias voltage. However, we can gain a general understanding of the current through a metal-semiconductor interface by reviewing the expressions for current density J deduced from thermionic emission theory:

$$J = J_0 e^{qV/k_B T} - 1 \quad (5.4)$$

where J_0 is defined as

$$J_0 = A^* T^2 e^{-q(\varphi_{Bn})/k_B T}, \quad (5.5)$$

where A^* is the Richardson constant and T is the temperature.

Inspecting the prefactor J_0 given by Eq. 5.5 reveals that the current density decreases, hence the resistivity increases, with temperature. This can be understood in terms of the energy of the charge carriers; as the temperature decreases, the reduced thermal energy of the charge carriers reduces their chance of having sufficient energy to overcome the Schottky barrier by thermionic emission, thus reducing the current through the junction and increasing the resistivity.

Another consequence of the Schottky barrier is that it exhibits rectifying transport characteristics. That is, current is more favourable under forward bias compared to reverse bias. In Eq. 5.4 this directional dependence is represented by the current density's exponential dependence on voltage bias V , resulting in highly non-linear I-V curves which are asymmetric with respect to V . This directional dependence is characteristic of rectifiers and gives metal-semiconductor contacts with Schottky barriers the name of Schottky diodes. Figure 5.4 shows a typical I-V curve of a Schottky diode. We can clearly see the characteristic features of the large potential barrier. An exponential increase of current under forward bias and a suppression of current under reverse bias resulting in a strong non-linear and asymmetric I-V curve. At sufficiently large reverse bias junction breakdown occurs.

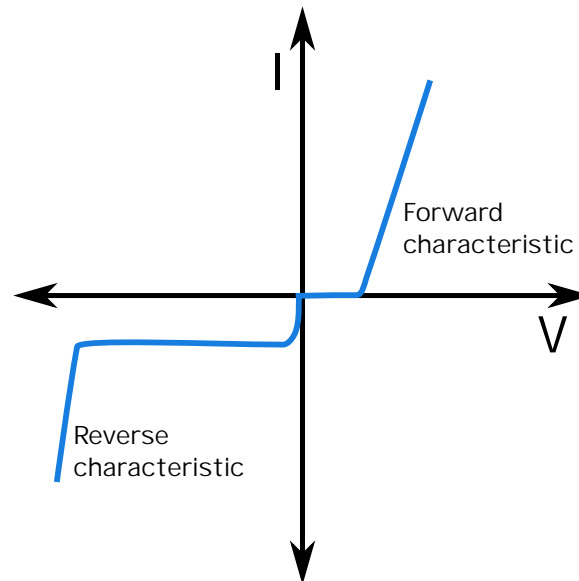


Figure 5.4 – Schematic plot of the I-V characteristics of a Schottky diode.

5.1.4 Modeling Al-Ge-Al as a back-to-back Schottky diode

From the introduction of the previous section, we can now consider Schottky barriers in the context of Al-Ge interfaces and their influence on the transport properties of Al-Ge-Al nanowire (NW) heterostructures. Figure 5.5 shows a characteristic I_D - V_D curve, measured at 300 K with $V_G = 0$ V by our collaborators in Vienna. Here the Al-Ge-Al NW heterostructure has a Ge segment length of 550 nm fabricated using the annealing process. Clearly, the curve is highly non-linear suggesting the influence of a Schottky barriers on the NW transport properties. However, in combination with the non-linearity the curve is symmetric with respect to V_D . From the discussion above we expect asymmetry for a single Schottky diode, whereas a symmetric non-linear I_D - V_D curve is regularly associated with back-to-back Schottky diodes [121, 34]. This explanation is consistent with our Al-Ge-Al NWs if we consider that the two Al-Ge interfaces form near identical back-to-back Schottky barriers as schematically represented in inset of Figure 5.5.

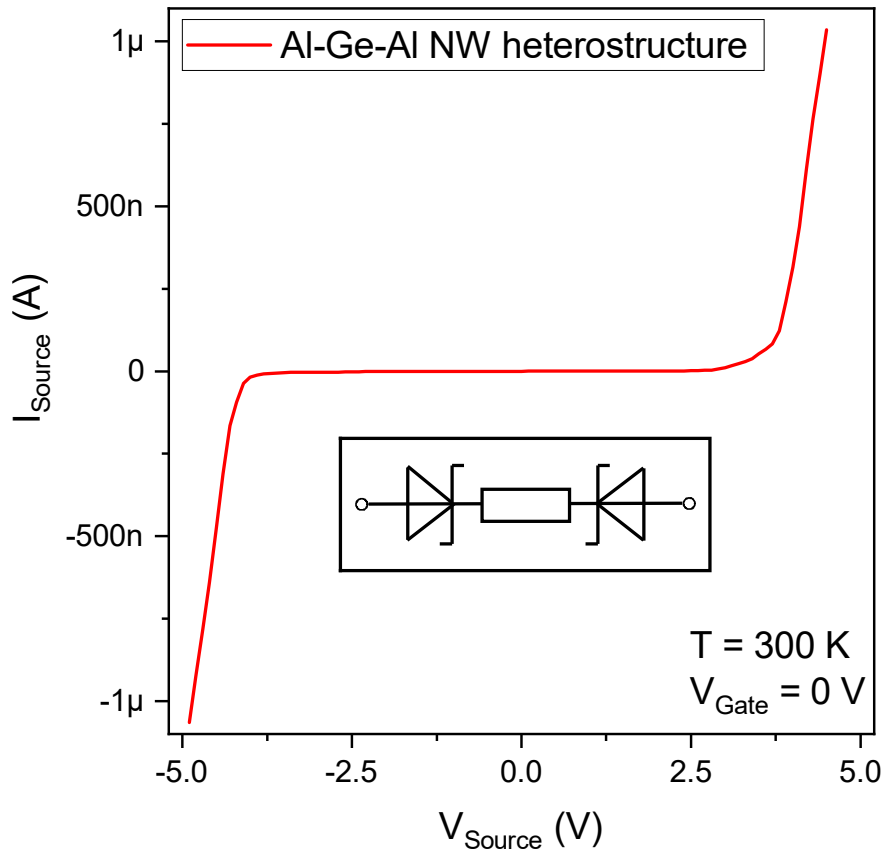


Figure 5.5 – Characteristic I_D - V_D curve of a Al-Ge-Al nanowire heterostructure with a Ge segment length of 550 nm after the annealing process measured at room temperature ($T \approx 300$ K) and $V_G = 0$ V. Figure taken from Ref. [39].

With evidence of back-to-back Schottky barriers we can begin to build a preliminary band diagram of the device. Figure 5.6 shows a schematic of an Al-Ge-Al nanowire heterostructure, below which an energy diagram reveals the band bending expected for a Ge NW contacted by two Al leads. Fundamental to the band diagram is the strong Fermi level pinning, which results in the valence band being pinned just below the Fermi level of the Al leads. As discussed above, the Fermi level pinning is

5.1 AL-GE-AL HETEROJUNCTION: A BACK-TO-BACK SCHOTTKY DIODE

a consequence of surface states on the semiconductor. In the case of Ge, Thanailakis and Northrop identified a density of surface states of $2 \times 10^{17} \text{ eV}^{-1}\text{m}^{-2}$ with a charge neutral level (CNL) just 0.13 eV above the valence band [29]. Further investigations of Ge endorsed the position of the CNL close to the valence band and the subsequent strong Fermi level pinning of the Schottky barrier, which results in the dominance of *p*-type transport in metal-Ge systems [93, 122].

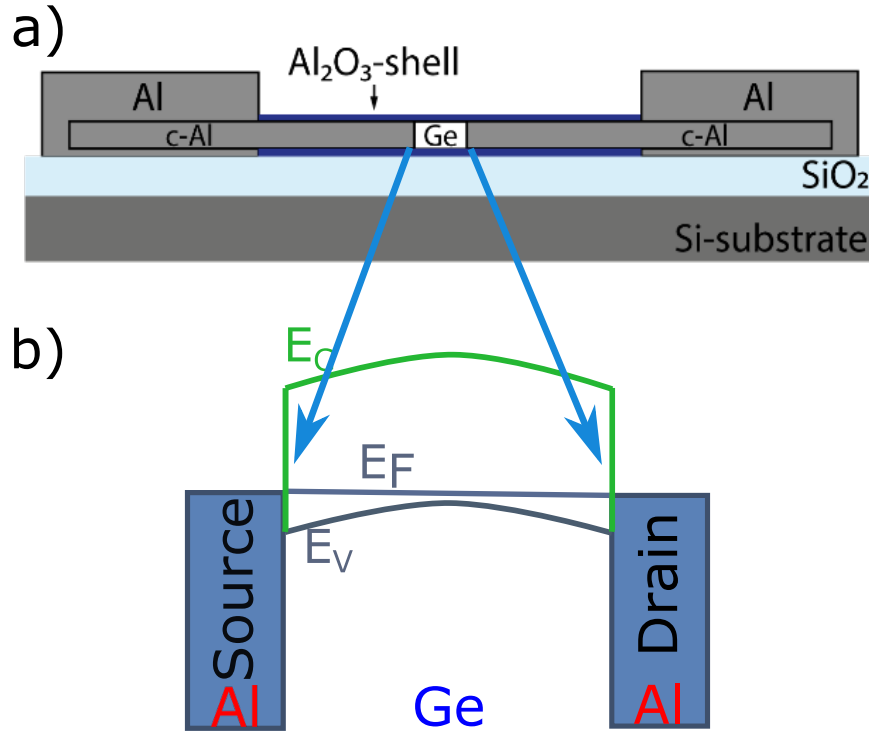


Figure 5.6 – (a) Schematic of an Al-Ge-Al nanowire heterostructure implemented into a back-gated field effect transistor (FET) with a band diagram (b) depicting the back-to-back Schottky barriers associated with the two Al-Ge interfaces. The valence band is pinned close to E_F of the Al leads due to Fermi level pinning.

5.1.5 Quantum dot formation

Interestingly and fundamental to this thesis, the band formation of the Al-Ge-Al nanowire heterostructures, due to the back-to-back Schottky barriers over a very short Ge segment, combined with the strong confinement, due to the ultra-small diameter (25 nm), results in the formation of quantum dot (QD) devices. The integration of these NW systems into a field effect transistor (FET) architecture enables the tuning of the QD size using a back-gate.

Figure 5.7 depicts schematically the increasing size of the QD, due to the evolution of the valence band under more negative V_G . The band bending occurs because the Fermi level pinning forces E_V to be pinned just below E_F of the Al leads. As such the whole valence band can not move above E_F of Ge in a way that maintains a flat band, as is usually depicted for bulk semiconductors. Therefore, to compensate for the negative electrostatic field of the back gate, the Ge bands must bend away from the back-gate forming a parabolic shape and pushing the parabola's vertex above E_F . This band bending increases the volume of hole states above E_F , thus increases the size of the QD which explains the reducing E_C as V_G decreases.

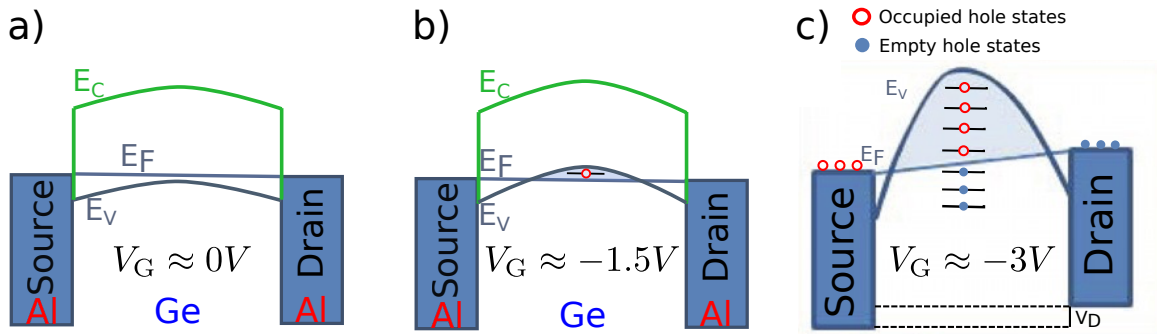


Figure 5.7 – Schematic of the QD formation in the Al-Ge-Al NW heterostructure due to the band bending of the valence band E_V resulting from the combination of the negative electrostatic field of the back-gate and Fermi level pinning. (a) At $V_G \approx 0$ V there are no available states in the Ge as $E_V < E_F$, therefore blocking current, pinch-off. (b) At $V_G \approx -1.5$ V, E_V is bent just above E_F forming a small QD and providing hole states through which transport can occur. (c) As V_G decreases the QD becomes larger as the volume of hole states above E_F increases. The large depletion region formed by the Schottky barrier results in a very small tunnel rate and low current. The band bending also effects the strength of the Schottky barrier. Increased band bending reduces the width of the depletion region, reducing the strength of the Schottky barrier, which in turn increases the tunnel rate and observed current.

5.2 Transport properties at high temperature

5.2.1 Long vs short Ge segment lengths

As discussed in Section 2.2, the transport properties of a metallic system is also dependent on its dimensions. The small diameter (≈ 25 nm) of the Ge NWs results in significant radial confinement. Furthermore, the nature of the fabrication technique allows one to tune the length of the Ge segment (L_{Ge}). Adjusting L_{Ge} has a considerable effect on the transport properties of the device, some of which can be observed at room temperature.

Figure 5.8 shows $I_{\text{D}}-V_{\text{D}}$ curves of Al-Ge-Al devices with various Ge segment lengths. The measurements were taken at room temperature with $V_{\text{G}} = 0$ V by our collaborators in Vienna. The plot reveals the significant effect L_{Ge} has on the conductivity of the device, further emphasising the dominance of the Ge segment on the transport properties of the device. As L_{Ge} becomes smaller, the strength of the non-linearity of the $I_{\text{D}}-V_{\text{D}}$ curve is reduced, becoming approximately linear for $L_{\text{Ge}} < 45$ nm. This reduction in non-linearity suggests a reduction in the strength of the back-to-back Schottky barrier.

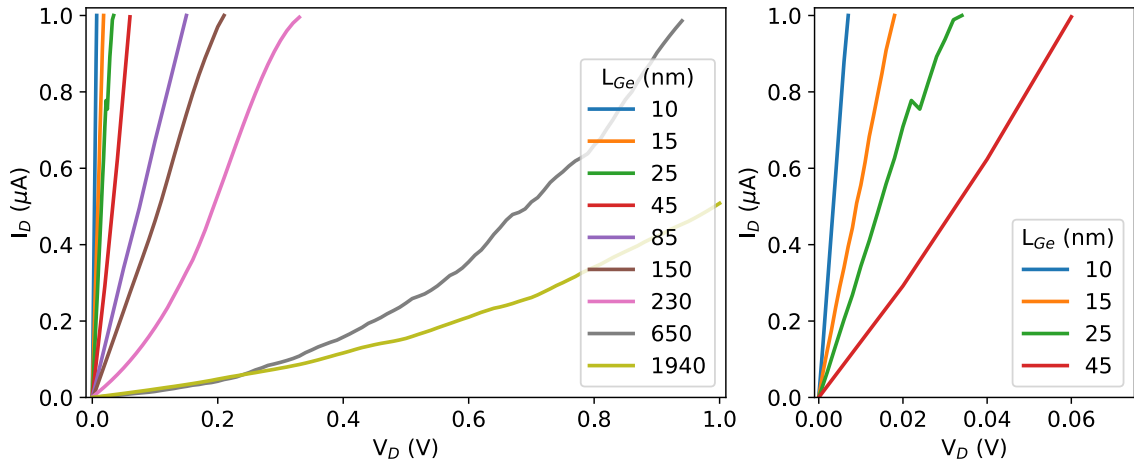


Figure 5.8 – $I_{\text{D}}-V_{\text{D}}$ curves of Al-Ge-Al devices with a range of Ge segment lengths at room temperature ($T \approx 300$ K) with $V_{\text{G}} = 0$ V. *Right* shows a zoom of the $I_{\text{D}}-V_{\text{D}}$ curves of the Al-Ge-Al devices with $L_{\text{Ge}} < 45$ n. Data taken from Ref. [39].

In accordance with Ohm's law the resistance of the NWs decreases with decreasing L_{Ge} . This behavior is clarified by Figure 5.9, which plots the resistance, calculated from the $I_{\text{D}}-V_{\text{D}}$ curves near zero-bias versus L_{Ge} . To account for variations in Ge NW diameters effecting resistance, the calculated resistance is multiplied by the NW's cross-sectional area. Figure 5.9 reveals a near linear relationship between R and L_{Ge} , consistent with Ohm's law. However, notably, devices with $L_{\text{Ge}} < 45$ nm diverge from this linear relationship converging to a fixed resistance independent of L_{Ge} . This peculiarity, highlighted by the inset of Figure 5.9, is an indication of ballistic transport. Ballistic transport occurs when the dimensions of a conductor are smaller than the mean free path (ℓ). Interestingly, the short devices converge to a resistance near the quantum resistance $R_{\text{Q}} = \frac{h}{2e^2} = 12.9$ k Ω . The concurrence of the converging resistance and fundamental resistance quantum provides further evidence that the devices

with ultra-short Ge segments are in the ballistic regime. As such, we approximate the mean free path of our Ge NWs to be $\ell_{\text{Ge}} \approx 45$ nm.

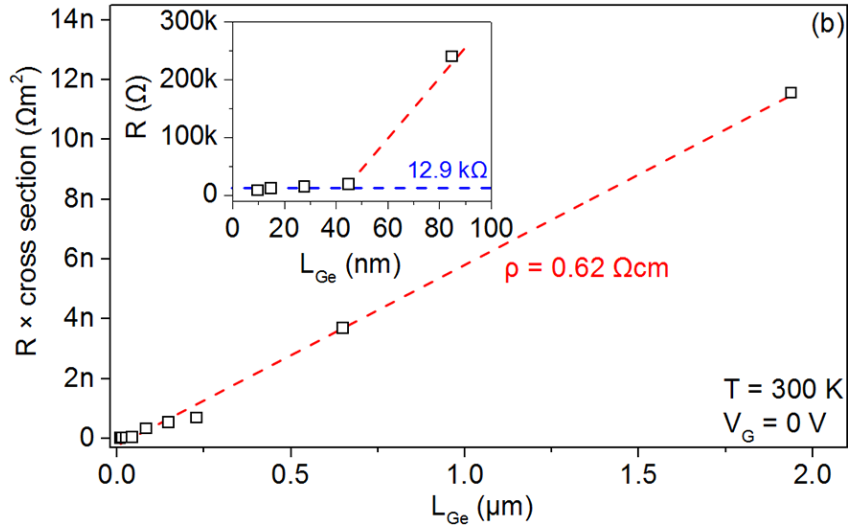


Figure 5.9 – Resistance, calculated from I_D - V_D curves of Figure 5.8 and multiplied by the Ge NW's cross sectional area, versus L_{Ge} . Inset shows a zoom of actual resistance R versus L_{Ge} of devices with $L_{\text{Ge}} < 100$ nm. Figure taken from Ref. [104].

Using this estimation of ℓ_{Ge} , we organise the Al-Ge-Al nanowire heterostructures into two categories of short and long devices. We define long devices as Al-Ge-Al NWs with Ge segment lengths of $L_{\text{Ge}} \gg \ell_{\text{Ge}}$ that are evidently in the diffusive transport regime. Whereas short devices with Ge segment lengths of $L_{\text{Ge}} \lesssim \ell_{\text{Ge}}$ are thus at the borderline between diffusive and ballistic transport or are completely ballistic.

5.2.2 Temperature dependence on Al-Ge-Al transport ($G-V_G$)

Temperature has a considerable effect on the physical properties of the germanium NWs. Metallic systems experience a reduction in resistivity as temperature decreases. This is owing to the electron's increasing mean free path ℓ as electron-phonon coupling is reduced by lowering the temperature. On the contrary, the resistivity of semiconductors, including Ge, increases with temperature.

Figure 5.10 shows the resistivity ρ of Al-Ge-Al devices, measured by our collaborators in Vienna, with various Ge segment lengths L_{Ge} versus temperature T . The resistivity of the Al-Ge-Al NWs increases as temperature decreases, contrary to the resistivity of the c-Al NW device, a conductor, which is also plotted in Figure 5.10 (black line).

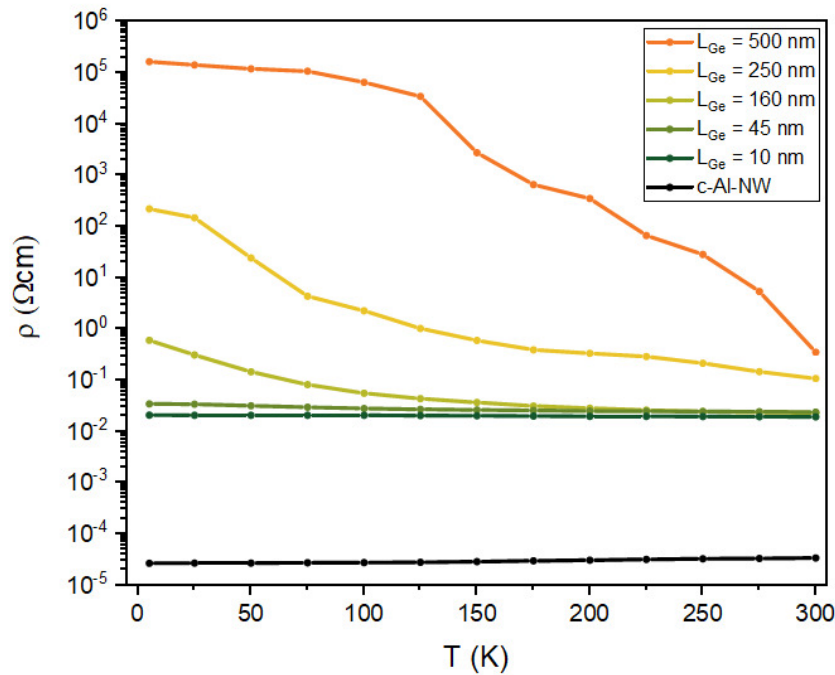


Figure 5.10 – Resistivity (ρ) versus temperature (T) of Al-Ge-Al devices with a range of Ge segment lengths (L_{Ge}). The resistivity was calculated by taking a linear fit of an I_D-V_D curve measured at $V_G = 0$ V. Also plotted is ρ vs T for a fully exchanged NW device (c-Al-NW).

Interestingly, the rate of increase in resistivity depends strongly on the Ge length L_{Ge} . Devices near or within the ballistic limit ($L_{Ge} < 45$ nm) reveal little change in resistivity, only experiencing a small increase at lower temperatures. Figure 5.11 highlights the change in resistivity of the short devices, showing the resistivity, normalised by the resistivity at 300 K ($\rho/\rho(300K)$), in semilog and linear plots. For comparison, the c-Al NW device is also plotted. It clearly shows the decrease in ρ as T decreases, which is in stark contrast to even the shortest Al-Ge-Al device.

The increase in resistivity of the devices with long Ge segments is attributed to semiconducting properties of the germanium. However, the increasing resistivity of the devices with short Ge segments, which are in the ballistic regime, is understood to be due to the Schottky barriers that define the Al-Ge contacts. As discussed in

Section 5.1 the current density due to thermionic emission across a Schottky barrier, defined by Eq. 5.5, decreases with decreasing temperature.

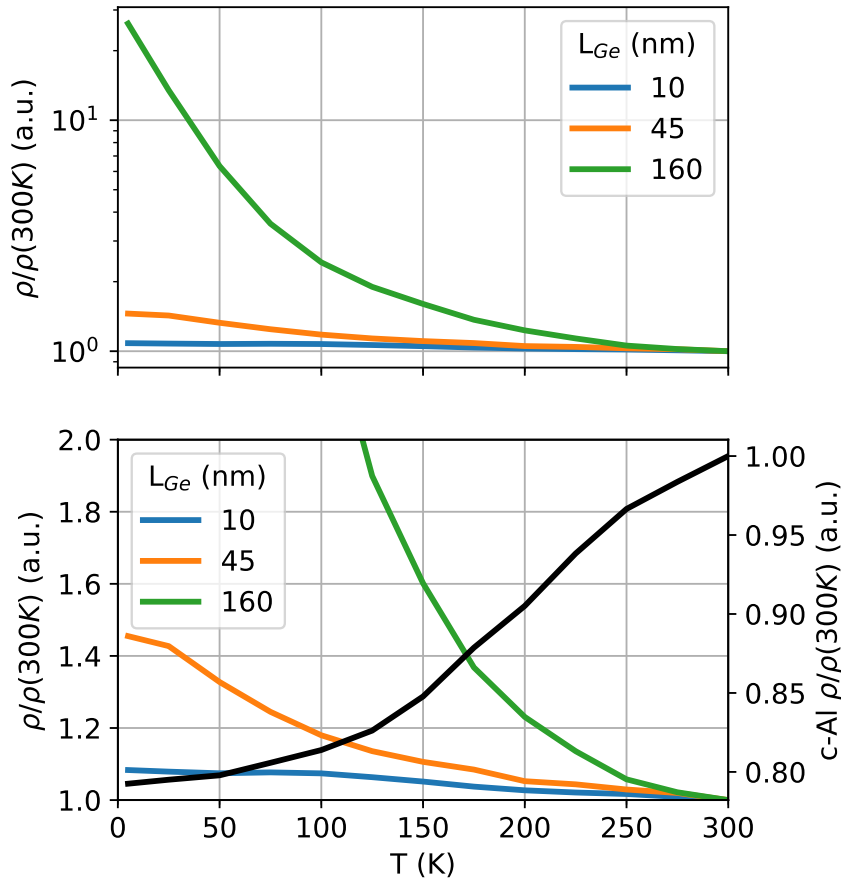


Figure 5.11 – Normalised resistivity ($\rho/\rho(300\text{K})$) versus temperature (T) of selected Al-Ge-Al devices from Figure 5.10, highlighting the temperature evolution of shorter devices. *Upper* Figure has a semilog scale whereas *lower* Figure has a linear scale with the c-Al NW device plotted in black whose scale is on the right axis.

Beyond observing the characteristic change in resistivity, reducing the temperature reveals physical features of mesoscopic systems that would be otherwise hidden by thermal noise. More specifically one of the requirements to observe confinement effects in a QD is to have a charging energy $E_C = e^2/C_\Sigma$ larger than the system's thermal energy $k_B T$. We can make a rough estimate of E_C of the QD and thus know the maximum temperature at which quantised charge effects could be observed. Roughly approximating the Ge NW segment to be a sphere of radius $R = L_{Ge}/2$ we can estimate the total capacitance by $C = 4\pi\epsilon_r\epsilon_0 R$, where ϵ_r is the dielectric constant of the material [123], which we take as that of bulk germanium, 16.2. Considering an Al-Ge-Al NW heterostructure with $L_{Ge} = 250$ nm; given an approximate charging energy of $E_C \approx 700\mu\text{eV}$, one would require measurements below $T = 8\text{K}$ to observe transport features associated with charge quantisation such as Coulomb blockade.

Figure 5.12 shows the temperature dependent evolution of $G-V_G$ curves of Al-Ge-Al devices; (a) in the diffusive limit ($L_{Ge} = 250$ nm) and (b) well within the ballistic limit ($L_{Ge} = 15$ nm). Beyond decreasing conductivity and a shifting of the gate voltage

response, features typical of semiconducting devices, little extra physics is revealed in the diffusive device by the lower temperatures, down to 5 K. On the other hand, the ballistic device reveals extra conductance features as the temperature decreases, distinctly a feature at approximately $0.85G_0$, beyond the distinct conductance plateau observed at 300 K. The causes of these features are beyond the scope of this thesis and are briefly discussed in Ref. [104]. In addition, the slope and overall conductance $G-V_G$ remains relatively constant with temperature, contrary to the diffusive device. This independence with temperature combined with the clear conductance plateau near G_0 further reinforces that the device is in the ballistic limit.

Despite being below the temperature ceiling of 8 K, at which we expect to see confinement effects, close inspection of the $G-V_G$ curves of both devices, down to 5 K, reveals a notable absence of Coulomb blockade effects such as conductance oscillations. The lack of conductance oscillations can be firstly associated with the relatively high temperature of the measurement; 5 K is of the order of 8 K. Secondly, the measurements presented here were carried out by our collaborators in a continuous flow liquid ^4He cryostat (Cryo Industries CRC-102) that was not designed for low noise measurement of nanoscopic devices. As such the lack of sufficient wire thermalisation and filtering could result in noise destroying the CB effects.

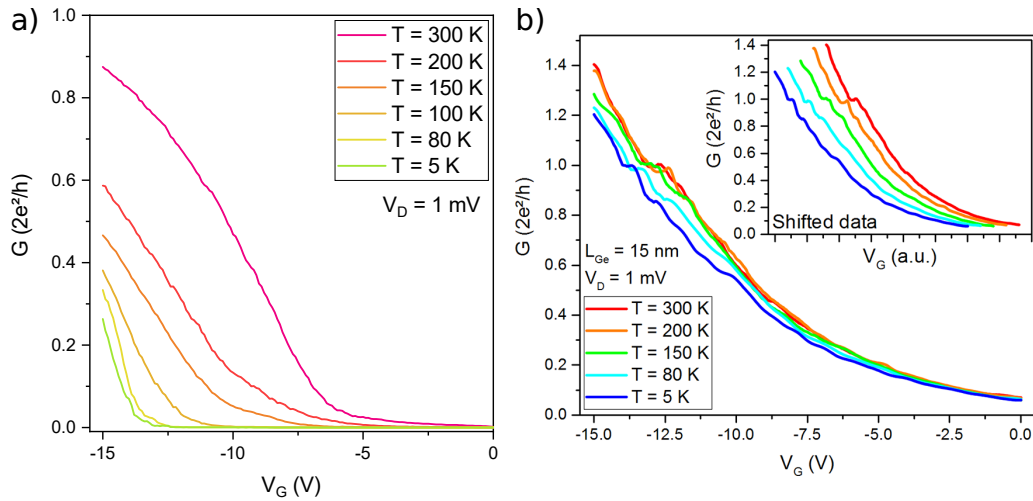


Figure 5.12 – Characteristic $G-V_G$ curves measured for $V_D = 1$ mV over a range of temperatures (T) of Al-Ge-Al devices with (a) long ($L_{\text{Ge}} = 250$ nm) and (b) short ($L_{\text{Ge}} = 15$ nm) Ge segment lengths. Figure taken from Ref. [104].

In order to observe CB effects in the Al-Ge-Al nanowire heterostructure devices it is necessary to improve the measurement set-up. Indeed, the anticipation of richer physics and the possible observation of quantum transport by reducing the external energy scales, in this case temperature $k_B T$, improving thermalisation and filtering, motivated our investigating of the Al-Ge-Al NW devices using our pumped ^3He cryostat. Given that the c-Al leads are transition metals, one would expect to see evidence of superconductivity when reducing the temperature below the superconducting critical temperature T_C of c-Al, further motivating measurements at sub-Kelvin temperatures.

5.3 Transport Overview at 400 mK

The low temperature investigation of Al-Ge-Al nanowire heterostructures is the significant focus of my thesis. In the following, we will discuss the transport properties of Al-Ge-Al NWs with both long and short Ge segments measured using the pumped He³ cryostat detailed in Chapter 4. In particular, for the long Ge device we will focus our discussion on a device with a Ge segment length of $L_{\text{Ge}} \approx 162$ nm, which is in the diffusive regime. Whereas for the short Ge device we will consider two devices with Ge segment lengths of $L_{\text{Ge}} \approx 40$ nm, which is just within the ballistic regime.

The discussion will be organised into sections that reflect the different transport regimes of the devices. We will begin by providing a transport overview of the devices. Then we will discuss in the detail the different transport regimes, making comparisons between the long and short devices where appropriate.

Investigations of long Ge devices involved measurements of multiple Al-Ge-Al NW heterostructures with Ge segments lengths ranging from 100 nm to 800 nm. The similar behavior of these devices permits us to represent their transport properties by analysing a single long Ge device with a segment length of $L_{\text{Ge}} \approx 162$ nm. This device will be labeled Sample L1. Two short Ge devices with comparable Ge lengths of 42 nm and 37 nm were measured to investigate the transport properties of short devices. The two samples will be labeled in the following sections as Sample S1 and Sample S2, respectively. Samples S1 and S2 also behaved similarly to each other. Comparisons between the short and long devices revealed both similarities and differences that will be highlighted throughout the chapter.

Using a 2-probe configuration, outlined in Section 4.3, the current I_{D} was measured as a function of the back-gate voltage V_{G} and source-drain bias voltage V_{D} . Figure 5.13 shows the field effect on the conductance induced by the gate voltage for Sample L1, a device with $L_{\text{Ge}} = 162$ nm (blue), and Sample S2 $L_{\text{Ge}} = 37$ nm (orange) for a bias voltage, V_{D} , of 0.5 mV and 1 mV at $T = 350$ mK and $T = 400$ mK, respectively. The numerical differential conductance was obtained from the measured current according to $G = dI_{\text{D}}/dV_{\text{D}}$ and is plotted in units of $G_0 = \frac{2e^2}{h}$.

A characteristic of semiconducting devices is the ability to switch off the current by tuning the gate voltage such that the conductance band or, more applicable to our devices, the valence band is pushed below the Fermi energy, see Figure 5.7 (a). For Sample L1 the pinch-off gate voltage was estimated to be -1.5 V; this estimate is based on additional measurements where it was observed that between $V_{\text{G}} = +5$ V and -1.5 V the conductance is below the noise threshold of $10^{-5}G_0$. On the other hand the current pinch-off for the short devices was observed to be approximately $V_{\text{G}} \approx 0.274$ V and measurements up to $V_{\text{G}} = +5$ V of both samples (S1 and S2) revealed again the conductance below the noise threshold of $10^{-5}G_0$, suggesting that current is also completely blocked.

As the gate voltage decreases from the pinch-off region, peaks appear in the G - V_{G} curves. A zoom on this region depicted by the inset of Figure 5.13 reveals the nature of these features. The oscillatory character of these conductance peaks combined with them being separated by periods of near zero conductance suggests that they result from the Coulomb blockade (CB) phenomenon (discussed in Section 2.3.4). With a further decrease of the gate voltage, the conductance of the devices rises and the periodic conductance peaks typical of CB, disappear.

The increase in conductance as V_{G} becomes more negative is in clear agreement

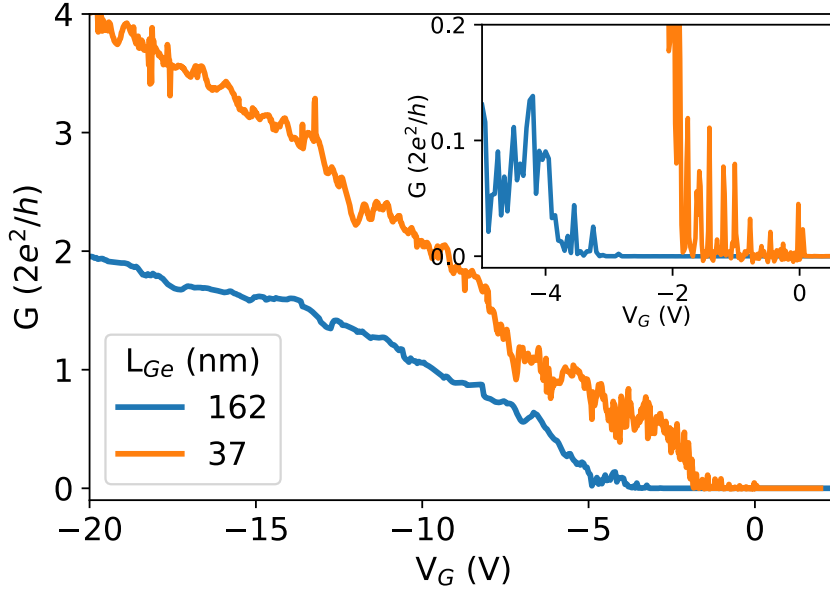


Figure 5.13 – **Transport overview** Conductance plotted in units of G_0 as a function of back-gate voltage (V_G) of an Al-Ge-Al heterostructure with a Ge segment of $L_{Ge} \approx 162$ nm (blue) and $L_{Ge} \approx 37$ nm (orange) for a bias voltage of 0.5 mV and 1 mV recorded at $T = 350$ mK and $T = 400$ mK, respectively. The inset shows a zoom of the conductance features just after pinch-off (-5.0 V $< V_G < 0.5$ V).

with the behavior of Al-Ge-Al devices at higher temperatures shown in Figure 5.12. As such, we conclude that both short and long devices maintain their p -type semiconductor behavior at cryogenic temperatures. Comparing the long and short devices, it is notable that the conductance of the short Ge device diverges significantly from that of the long Ge device as V_G decreases. For instance, at $V_G = -20$ V, $G(L_{Ge} = 162$ nm) is approximately half of $G(L_{Ge} = 37$ nm). This is likely due to Sample L1 being in the diffusive regime.

Further insight into the general transport properties of the Al-Ge-Al devices can be acquired by inspecting density plots, also referred to as colormaps, of G versus V_D and V_G . Figure 5.14 shows the differential conductance (G), in units of quantum conductance, versus bias voltage V_D and V_G of Samples S1 (a) and S2 (b) recorded at $T = 390$ mK and 410 mK, respectively. The plots reveal that the two devices display similar highly tuneable transport properties with four distinguishable regimes 1) a full blockade regime for $V_G > 0.5$ V, 2) a CB regime from the first hole to a few tens of holes in the QD (-4.5 V $< V_G < 0.5$ V), 3) an intermediate regime with various sub-gap features (-15 V $< V_G < -4.5$ V) and 4) a supercurrent regime at very negative gate voltages. We also observe peaks in conductance due to Andreev reflections at $eV = 2\Delta/n$, where n is the order of reflection (see Section 2.5.3).

To compare with the long Ge devices a density plot of Sample L1 is shown in Figure 5.14 (c). Like the short Ge segment devices, after pinch-off, we observe Coulomb blockade (CB) in the low conductance regime. As V_G becomes more negative, the Ge segment becomes more conductive. The CB features fade out and we begin to see sub-gap transport. However, contrary to the short devices the sub-gap transport of Sample L1 does not evolve into supercurrent, instead remaining suppressed compared

to the normal conductivity.

Having presented an overview of the low temperature transport properties of the devices, we will now focus on each of the multiple transport regimes listed above. The regimes will be presented in the following order; first the Coulomb blockade regime, second the superconducting regime and thirdly the intermediate regime.

5.3 TRANSPORT OVERVIEW AT 400 mK

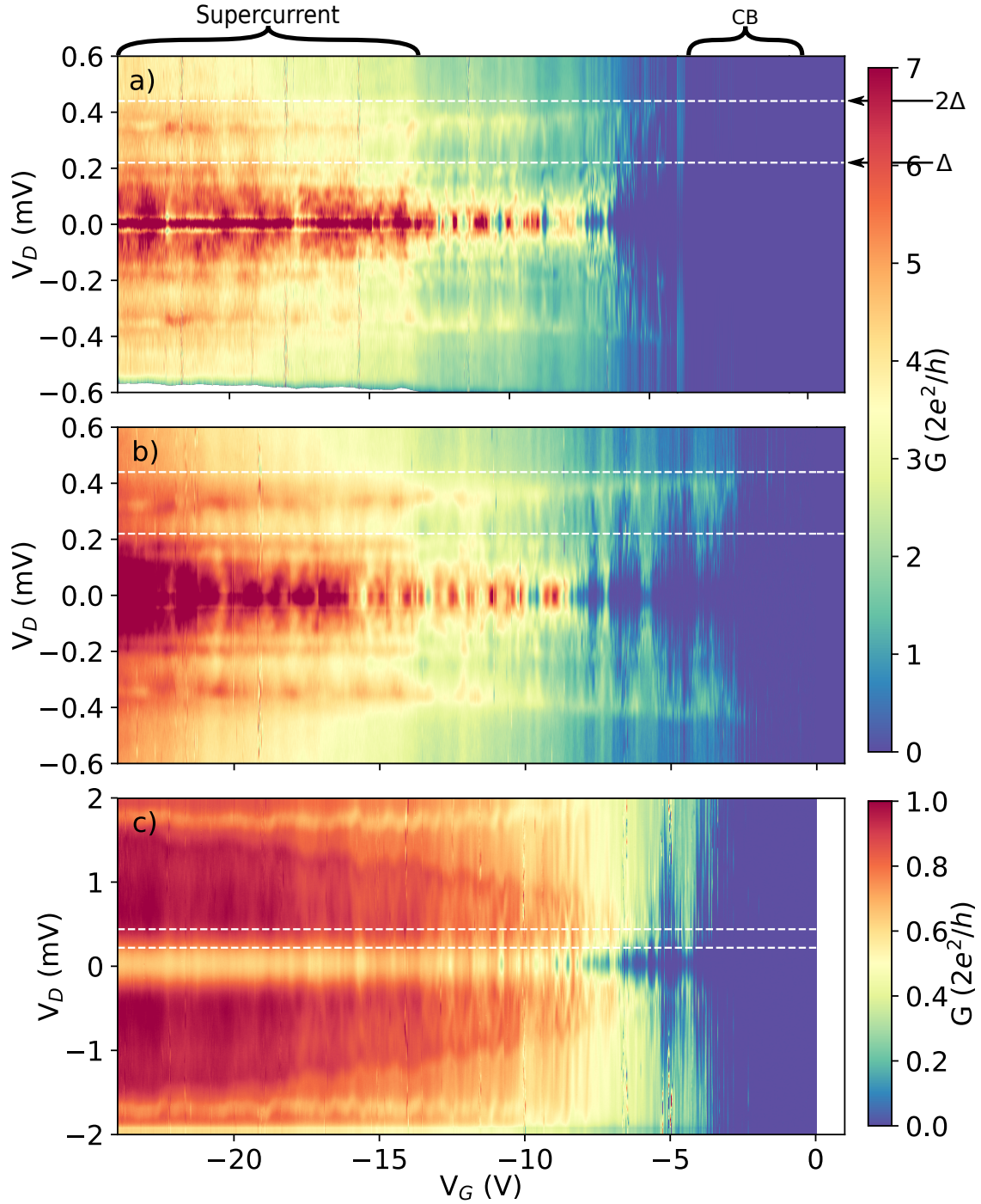


Figure 5.14 – **Transport Overview.** Density plot of differential conductance (G) with respect to bias voltage (V_D) and gate voltage (V_G) of Sample S1 recorded at 390 mK, Sample S2 recorded at 410 mK and Sample L1 recorded at 350 mK. The dashed white lines mark $V_D = 0.44$ mV and $V_D = 0.22$ mV, 2Δ and Δ , respectively. In Sample S1 & S2 we observe four distinct regimes: A full blockade regime for $V_G > 0.5$ V. A Coulomb blockade regime (-4.5 V $< V_G < 0.5$ V), an intermediate regime (-15 V $< V_G < -4.5$ V) and a supercurrent regime ($V_G < -15$ V). In Sample L1, similar to Samples S1 & S2, we observe multiple regimes: a full blockade regime for $V_G > -1.5$ V, a Coulomb blockade regime (-4 V $< V_G < -2$ V), and an intermediate regime with signs of sub-gap transport (-6 V $< V_G < -4$ V) that evolves into a steady transport regime without supercurrent.

5.4 Coulomb Blockade

Figure 5.15 shows a color map representation of I_D as a function of the back-gate voltage V_G and the applied source-drain voltage V_D of Sample L1 measured at $T = 350$ mK. The gate voltage window has been selected to be in the center of the Coulomb diamond regime described in the transport overview. Density plots revealing Coulomb blockade are often referred to as stability diagrams in the literature as they depict regions where charge on the QD is stable. In Figure 5.15 the regions of charge stability, therefore zero current and consequently zero conductance, are represented by white in the density plots. Clear diamond like shapes at the boundary between zero and non-zero current can be observed. Such features, are character characteristic of Coulomb blockade and are called Coulomb diamonds (see Section 2.3.3).

The density plot of Figure 5.15 (a). reveals richer physics than the standard Coulomb blockade expected for a single electron transistor (SET). First, a global decay of the Coulomb diamond height is observed as V_G is decreased from -3.0 V to -4.5 V. Superimposed on this general decay are periodic fluctuations of the height of the diamonds.

When -4 V $< V_G < -3.4$ V, we observe diamond pairing where the addition of a hole from a $2N$ state to a $2N + 1$ state requires additional energy beyond just the charging energy E_C due to the Pauli exclusion principle. This additional energy is associated with the energy spacing of the QD's energy levels (single level spacing δ_N). The different energies between odd and even charge filling gives this phenomenon the name of odd-even filling.

When -4.5 V $< V_G < -4$ V, we observe hints of a second periodicity with higher diamond peaks at the $4N$ and $4N + 1$ hole filling points. This extra periodicity maybe associated with atomic-like electron/hole filling that is often observed in high quality quantum dots [124, 125]. In the case of Ge, light-hole-heavy-hole (LH-HH) degeneracy is known to be lifted by confinement or strain [126, 25]. Combined with the possible lifting of spin degeneracy due to Coulomb repulsion results in a lifting of fourfold degeneracy. Such a lifting would result in a large addition energy to fill the $4N+1$ hole, thus explaining the periodic higher diamond energies.

Similarly, an investigation of Sample S1 near pinch-off reveals Coulomb blockade features. Figure 5.16 a-b-c show stability diagrams of the differential conductance versus V_D over a V_G range, in the low conducting regime, of -3.75 V $< V_G < 0.4$ V at 390 mK. Indeed, we clearly observe Coulomb diamonds analogous to those of Sample L1 suggesting that device also acts as a QD with single hole filling. In Sample S1, we observe the first charge degeneracy point at $V_G = 0.224$ V (see Figure 5.16 (a)).

We estimate the number of holes inside the QD by counting the number of charge degeneracy points. The estimated number of holes on the QD is labeled on the stability diagrams of Figure 5.16. Although the occurrence of charge jumps during the measurement causes uncertainty, we estimate that this number is accurate to ± 2 .

As described in Section 2.3.3, the characteristic parameters of the SET or SHT can be determined from the periodicity of the diamonds and the slope of their edges. From the periodicity of the diamonds as a function of V_G , we extract a gate capacitance (see Eq. 2.45) of $C_G = 3 \times 10^{-18}$ F and $C_G = 2.1 \times 10^{-18}$ F in the many hole regime of Samples L1 and S1, respectively. This is in reasonable agreement with an estimate of the gate capacitance of 7×10^{-18} F and 2×10^{-18} F for Samples L1 and S1, respectively. This estimate is based on modeling the Ge NW segment as a microwave

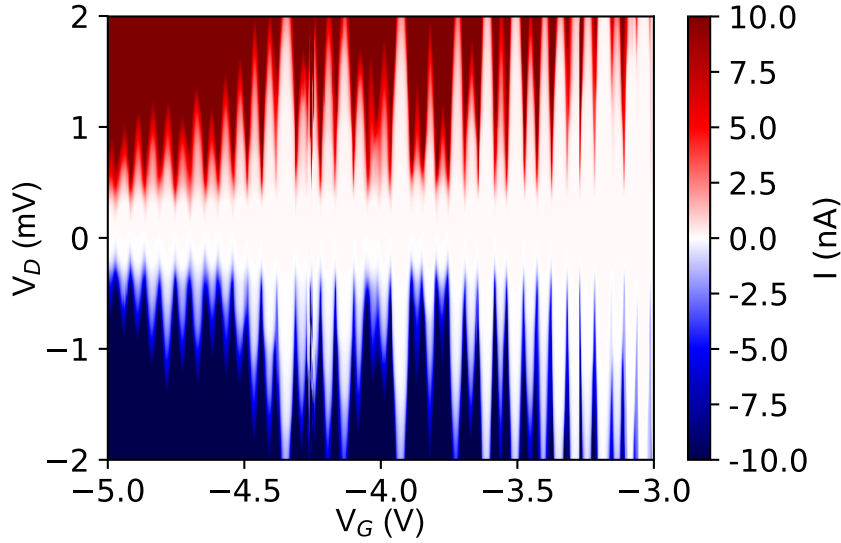


Figure 5.15 – **Stability diagram** Showing the measured current versus V_D and V_G of an heterostructure device with $L_{Ge} = 162$ nm (Sample L1) recorded at $T = 350$ mK.

microstrip with a width w and distance from the ground plane (d) through a medium with a relative dielectric constant ϵ_r . When $w/d > 0.06$, a well defined expression gives the capacitance per length between the microstrip and the ground[127]. Considering the Ge NW segment as the microstrip of length 40 nm, we take the NW diameter of 25 nm to be the width and the SiO_2 , of thickness $d = 100$ nm and $\epsilon_r = 3.8$ to be the medium between the microstrip and the ground.

Figure 5.17 shows a zoom of the gate region -4.9 V $< V_G < -4.7$ V of Sample L1 in which we superimposed on the experimental data the extracted slopes of the Coulomb diamonds. Within the constant interaction model of an SET, the slopes of the diamonds give the ratio of the source C_S and drain C_D capacitances to the gate capacitance C_G , see Eqs. 2.50 and 2.51. C_G is first calculated by $C_G = e/\Delta V_G$, where ΔV_G is determined from the periodicity of the Coulomb diamonds (see Figure 2.6 (c)). We then extracted the slopes of the diamonds from the stability diagrams revealing that C_S and C_D increase from approximately 15×10^{-18} F to 100×10^{-18} F when V_G decreases from -3 V to -5 V. In this V_G range of Sample L1, an average $C_G = 3 \times 10^{-18}$ F was determined.

For Sample S1, a strong V_G dependence on the capacitances is also observed, C_S and C_D increase from 2×10^{-18} F and 3×10^{-18} F, respectively for the first diamond ($N = 1$) at $V_G = 0.224$ V, to 37×10^{-18} F and 67×10^{-18} F for the $N = 32$ diamond at $V_G = -3.645$ V. A significant V_G dependence on C_G is also observed for Sample S1. C_G ranges from 0.5×10^{-18} F in the few hole regime to 2.1×10^{-18} F in the many hole regime. In the few hole regime of Sample S1 we observe strong fluctuations in ΔV_G , which results in fluctuations of C_G . These fluctuations are discussed in more detail later. On the other hand, for Sample L1, the C_G fluctuations are minimal. However, we could not measure clear Coulomb diamonds in the few hole regime of Sample L1.

To further illustrate the CB in this regime, we show in Figure 5.18 (a) a plot of I_D versus V_G of Sample S1, by taking voltage bias slices at $V_D = 0.48$ mV. Each colour

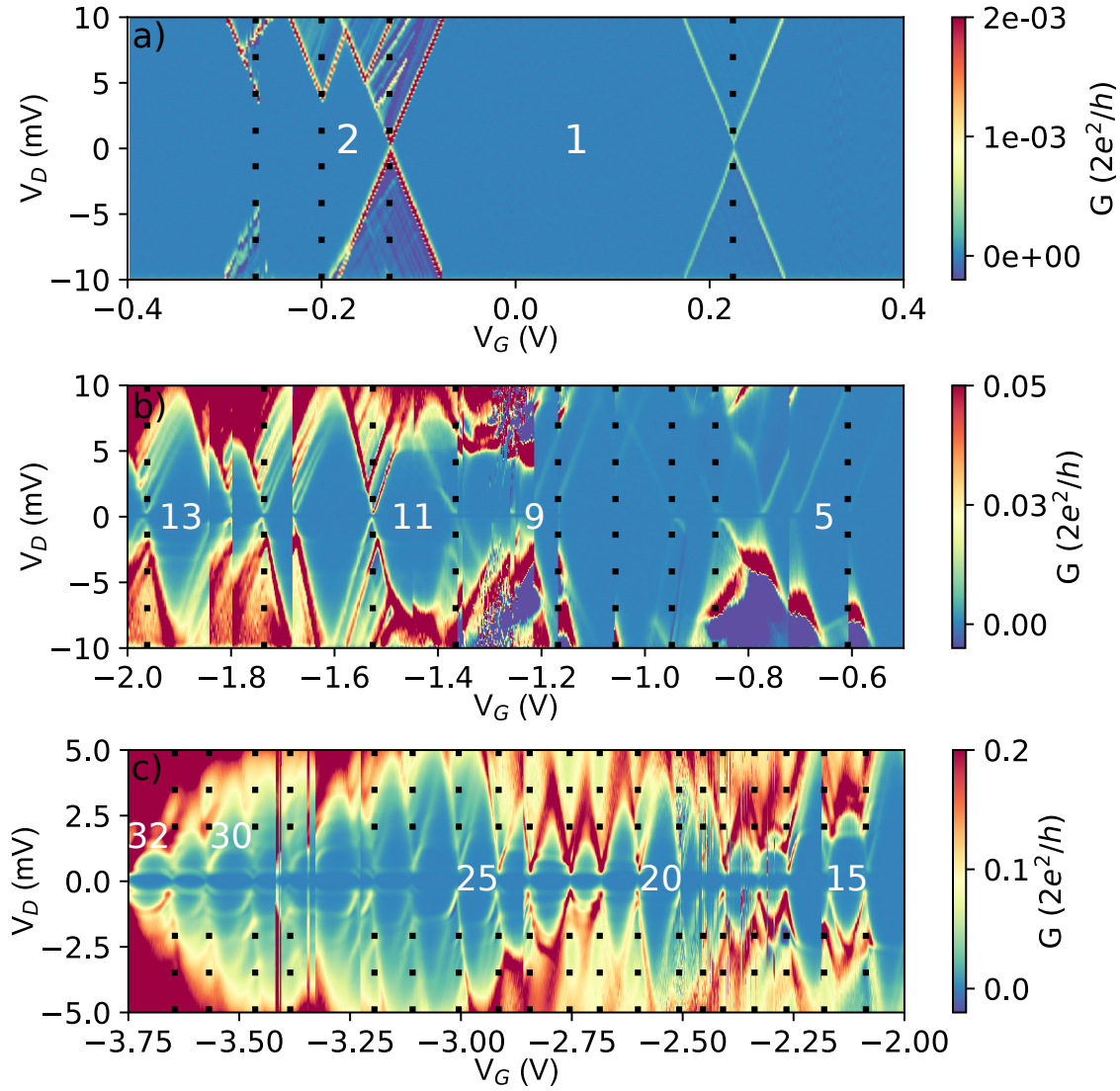


Figure 5.16 – **Coulomb diamonds** Stability diagram of the differential conductance ($G = dI_D/dV_D$) with respect to bias voltage (V_D) and gate voltage (V_G) in the Coulomb blockade regime: (a) In the first hole QD regime, (b) the few hole filling regime, (c) many hole filling regime. The numerical labels show the estimated number of holes (N) on the quantum dot (QD) for a sample of stable charge states. The black vertical dotted lines represent the charge degeneracy points where we estimate that a new hole has been introduced to the QD, while considering the occurrence of repeated or incomplete diamonds due to charge jumps.

of the plot represents independent measurements taken during the same cooldown. The plot reveals periodic current peaks separated by near-zero current regions typical of CB and in accordance with the conductance peaks observed in Figure 5.13. To compare with Sample L1, I_D versus V_G is plotted in Figure 5.18 (b). We observe strong similarities between the two devices; both showing periodic current peaks consistent with CB as well as showing an overall increase in the current as V_G decreases. Clearly Sample L1 is more stable with respect to V_G compared to Sample S1. This likely due to the fact that the longer Ge segment is less sensitive to movement in surface charges,

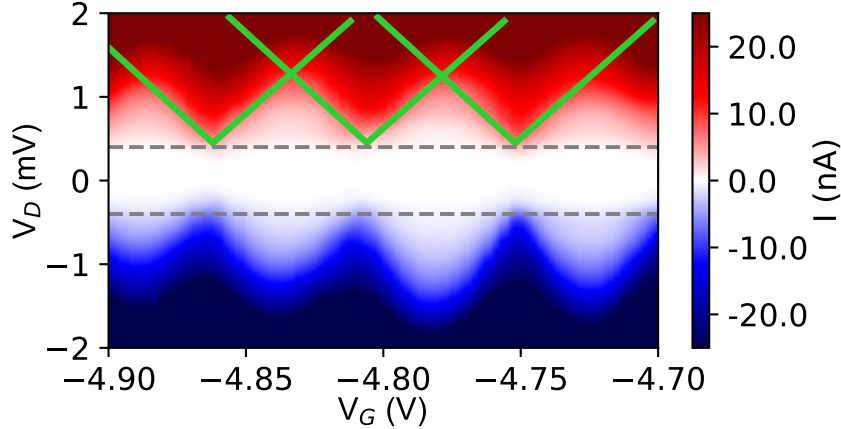


Figure 5.17 – **Coulomb diamond zoom** A zoom onto a few diamonds of Sample L1 revealing with greater clarity the transport gap due to the superconducting leads. The gap is traced by two grey dashed lines. Green lines that depict the extracted slopes used to calculate the capacitances are superimposed on the stability diagram.

resulting in charge jumps compared to the shorter device. This effect is made more acute by the fewer holes on the QD of Sample S1 compared to Sample L1 which is in the many hole regime with approximately 50 holes on the QD at $V_G = 4$ V.^a

Figure 5.18 (a) also highlights the significant tunability of the QD's conductance. For Sample S1, the first current peak, at $V_G = 0.224$ V, has a magnitude of approximately 5 pA whereas the final current peak at $V_G = -3.645$ V has a magnitude of approximately 1 nA. In the blockade regions, the current increases from zero to 0.4 nA around $V_G = -3.6$ V. This dynamic is shared by Sample L1 with the first current peak, of the plot, at $V_G = -3.014$ V, has a magnitude of approximately 0.2 nA whereas the penultimate current peak at $V_G = -4.916$ V has a magnitude of approximately 7.0 nA. In the blockade regions, the current increases from zero, below the noise threshold, to 1.1 nA around $V_G = -4.94$ V.

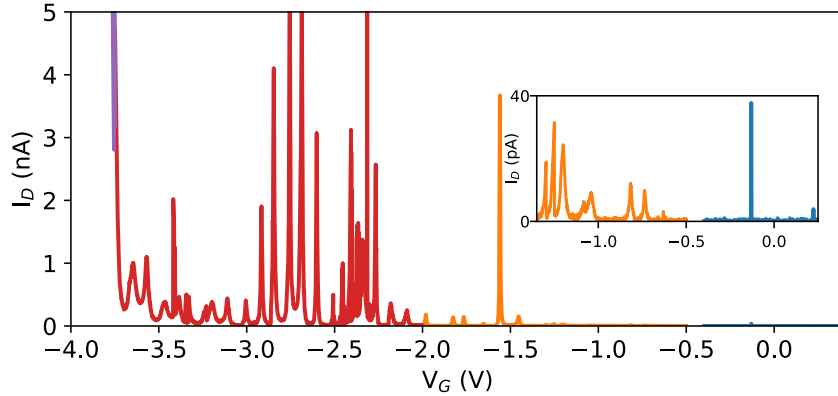
The evolution of the current is explained by the decreasing strength of the Schottky barrier as V_G decreases. The decreasing strength occurs due to the band bending induced by the back gate. This band bending reduces the width of the depletion region that defines the Schottky barrier (see Figure 5.7). As discussed in Section 5.1, the tunnel rate Γ , which regulates the current, is dependent on the Schottky barrier's width a and height ϕ_b , which defines the overall strength of the barrier. These barrier properties determine the charge carrier transmission probability by $T \propto e^{-a\phi_b}$, which is related to Γ .

To estimate Γ experimentally, we used different techniques for few hole and many hole regime. In the few hole regime, when $2\Delta < eV_D < \delta_N$ and $k_B T \ll E_C$ is satisfied, the limiting current of the QD is bias independent. Given a spin degenerate QD, the tunnel coupling of the left (Γ_L) and right (Γ_R) leads can be calculated from the current limit of a charge degeneracy point [128]. We determine a tunnel coupling of $\Gamma_L = 5.0\mu\text{eV}$ and $\Gamma_R = 7.4\mu\text{eV}$ for the charge degeneracy point of $N/N+1 = 1/2$. Comparing to $E_C(N=2)$ of 32 meV and $\Delta = 220\mu\text{eV}$, we are thus clearly in the weak

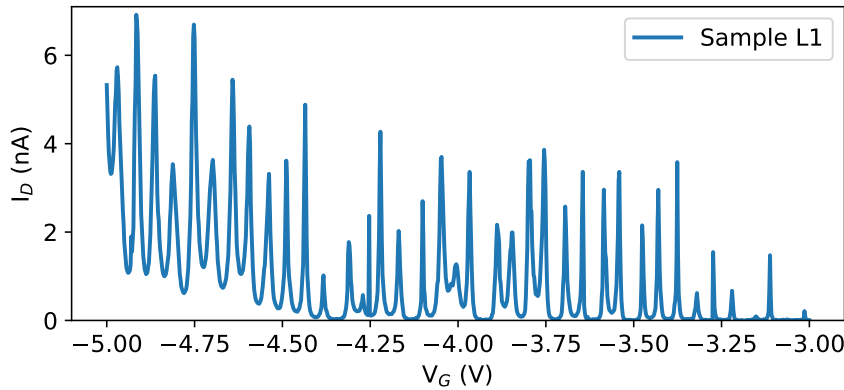
^aThis is estimated from the pinch-off gate voltage (1.5 V) using the average periodicity of the Coulomb diamonds ΔV_G

coupling regime.

In the many hole regime, the limiting current becomes poorly defined and as a result cannot be used to calculate the tunnel coupling. Alternatively, we estimate the tunnel coupling from the width of the G peak of the diamond edge retrieving tunnel couplings of $\Gamma = 82, 102$ and $250 \mu\text{eV}$ for the charge states $N = 17, 24$ and 31 , respectively. Notably, in the many hole regime ($N \geq 24$) we are no more in the weak coupling regime with respect to superconductivity as $\Gamma \sim \Delta$. As a first conclusion, the significant evolution of the tunnel coupling further endorses the strong gate tuneability of the device.



(a) Sample S1



(b) Sample L1

Figure 5.18 – I_D - V_G slice at $V_D = 0.48$ mV of (a) Sample S1 and (b) Sample L1. (a) For Sample S1 Each color represents a different measurement taken during the same cool-down. (Inset) zoom of I_D (V_G) for $0.25 \text{ V} < V_G < -1.45 \text{ V}$.

5.4.1 Addition Energy

The addition energy E_{add} , first introduced in Section 2.3 of the theory chapter, is the total energy cost of adding an additional charge to the QD. E_{add} , defined by Eq. 2.41, is the sum of the energy to overcome the electrostatic Coulomb repulsion of the dot, the charging energy E_C and the spacing of the energy levels due to quantum confinement, the single-particle level spacing δ_N .

Figure 5.19 shows α_G versus the estimated hole number N and V_G . Here, α_G is calculated by $\alpha_G = E_{\text{add}}/e\Delta V_G$, where E_{add} is the addition energy and ΔV_G is the

5.4 COULOMB BLOCKADE

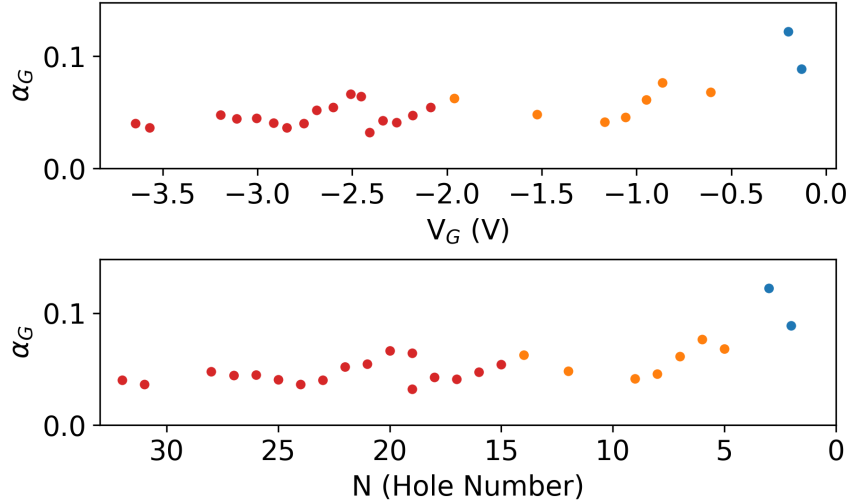


Figure 5.19 – **Gate lever arm** α_G versus V_G & N for three independently measured datasets. $\alpha_G = 0.49$ calculated by averaging α_G in the gate region of (-3.75 V < V_G < -2 V)

periodicity of the charge degeneracy points. E_{add} and ΔV_G are extracted directly from the stability diagrams, see Figure 2.6 and the related discussion in Section 2.3.4. With many holes on the QD $N > 20$, α_G is quite constant. However, we can not extract α_G from every Coulomb diamond due to the difficulty of determining E_{add} from some Coulomb diamonds. To estimate a constant α_G for the QD system, we determined the average value in the region where there are many holes on the QD (-3.75 V < V_G < -2 V). Retrieving a ratio of $\langle \alpha_G \rangle = 0.049$. With this estimate of $\langle \alpha_G \rangle$, we can calculate E_{add} for the whole Coulomb blockade regime from the measured ΔV_G .

Figure 5.20 shows E_{add} calculated using $E_{\text{add}}(N) = e\langle \alpha_G \rangle \Delta V_G(N)$ and E_{add} extracted directly from the Coulomb diamonds versus V_G . In the many hole regime $N > 20$, there is good agreement between the two addition energies. However, in the few hole regime, we observe a significant divergence between the addition energies. This is due to the discrepancy of α_G between the many and few hole regimes.

Figure 5.21 shows the calculated addition energy $E_{\text{add}}(N)$ versus the hole number on the QD N . In the few hole regime ($N < 10$), E_{add} is sporadic, moving between 3 and 17 meV. With approximately 10 holes on the QD, E_{add} begins to decay steadily until $N \approx 20$ where it converges into an even-odd hole filling effect. We associate the evolution of E_{add} to the evolution of the charging energy E_C . Similarly to the long Ge segment heterostructures, the valence band bends further above the Fermi energy when V_G decreases. This induces an increase of the QD size (see Figure 5.7). Consequently, the magnitude of C_S and C_D increases leading to a reduction of E_C .

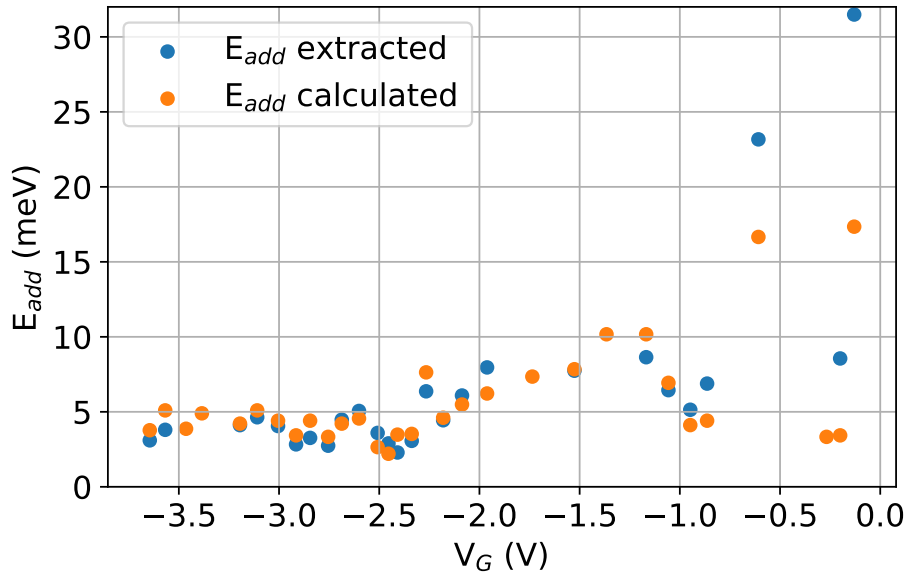


Figure 5.20 – E_{add} calculated using $E_{add}(N) = \langle \alpha_G \rangle \Delta V_G(N)$ and E_{add} extracted directly from Coulomb diamonds versus V_G .

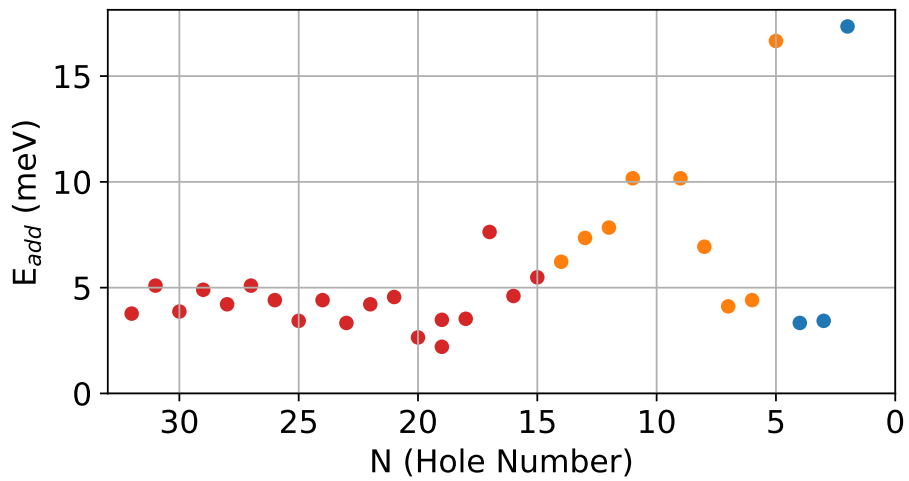


Figure 5.21 – E_{add} calculated using $E_{add}(N) = \langle \alpha_G \rangle \Delta V_G(N)$, versus hole number (N).

5.4.3 Excited charge state resonant tunneling

As discussed in Section 2.3.3, another way to extract the energy levels of a QD is to analyse resonant tunneling through excited charge states, which manifest as conductance lines that run parallel to diamond edges. In the short Ge devices, we observe such features throughout the stability diagrams. Figure 5.23 shows density plots focused on two Coulomb diamonds, as seen in Figure 5.16, revealing extra conductance resonances which we associate with excited state charge transport. From the conductance features at $V_G = -1.53$ V with $N \approx 12$, we calculate the energy of the first excited hole state to be $\Delta E = 2.0$ meV. Whereas, in the many hole regime ($N > 20$), the average energy of the observed first excited states is 1.2 ± 0.6 meV, which agrees with $\langle \delta_N \rangle$ estimated from the even-odd effect.

Assuming that the energy spacing is dominated by quantum confinement $\Delta E \sim h^2/m_{\text{eff}}L^2$ [49], we coarsely estimate the effective mass m_{eff} of the holes given a QD of $L = 40$ nm to be $0.9m_e$, where m_e is the electron mass. This estimate is larger than the reported values of $0.28m_e$ [102] for holes in Ge/Si core/shell NWs and $0.08m_e$ [26] obtained from Hall measurements on SiGe/Ge/SiGe planar junctions. Further experiments and analysis are required to more accurately determine m_{eff} in our device, which are beyond the scope of this thesis.

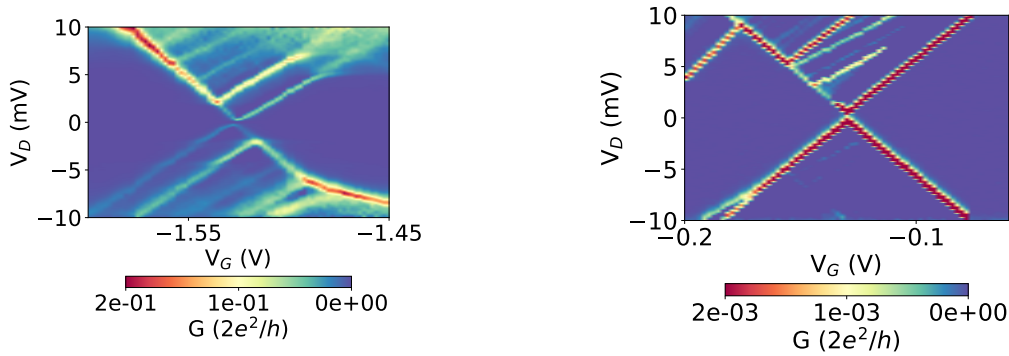


Figure 5.23 – Density plots of Sample S1 focused on two Coulomb diamonds showing extra conductance resonances due to excited state resonant tunneling.

Investigations of Sample L1, shown in Figure 5.24, reveal also possible evidence of excited state resonant tunneling. However, the poor clarity of the measurement makes it difficult to confirm the nature of these extra resonances.

5.4.4 Temperature evolution of Coulomb blockade

Figure 5.25 shows density plots in the V_G range of the Coulomb blockade regime of Sample L1 at different temperatures above 350 mK; $T = 2$ K, 5 K and 10 K. Interestingly, the diamond like shapes typical of CB, seen at 350 mK (see Figure 5.15) persist up to 10 K. In this long segment sample, the charging energy at $V_G \approx -3$ V has been estimated to be $E_C \approx 4.84$ meV. This large value explains why we continue to observe Coulomb blockade up to 10 K.

5.4 COULOMB BLOCKADE

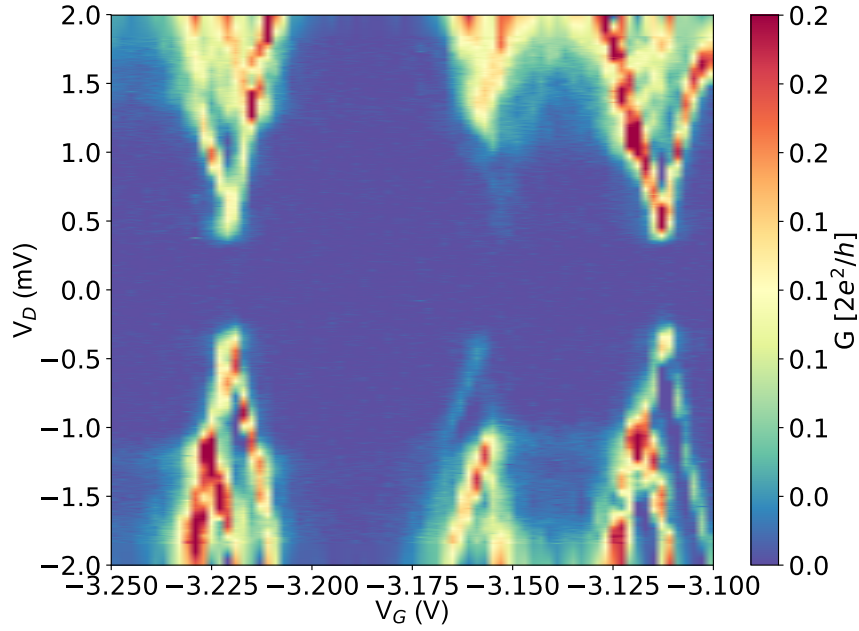


Figure 5.24 – Density plot of Sample L1 focused on a few Coulomb diamonds showing possible evidence of excited state resonant tunneling.

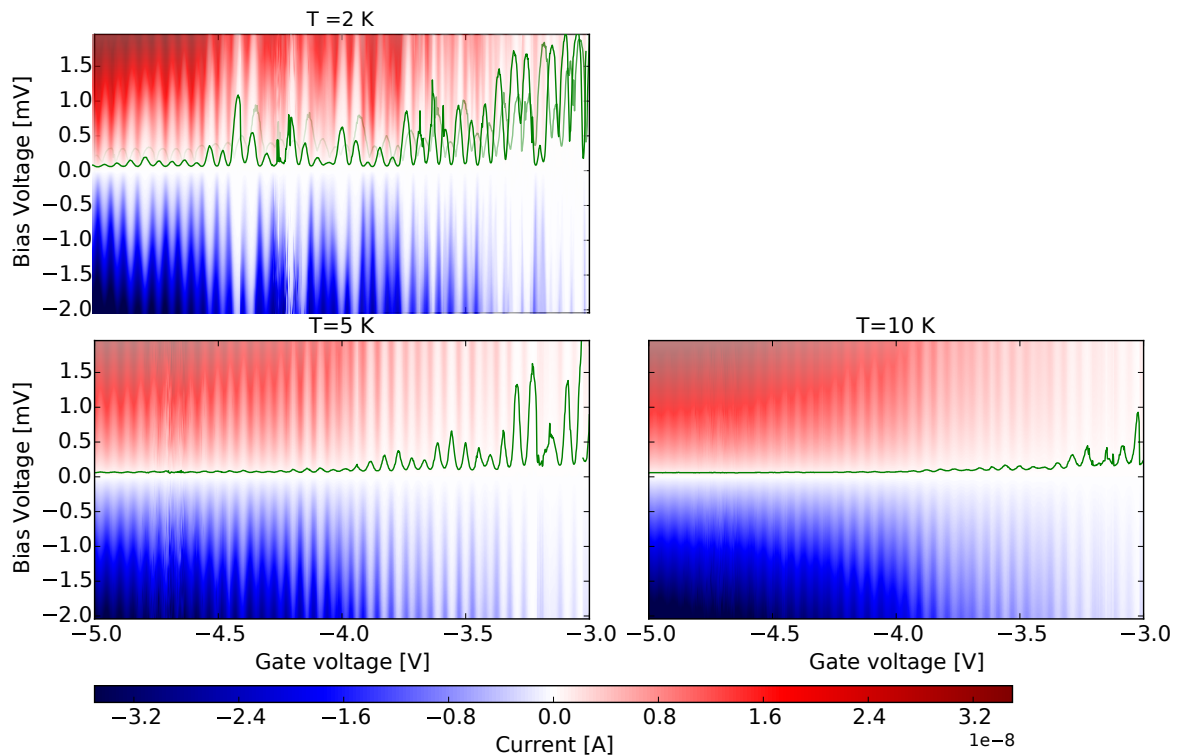


Figure 5.25 – Stability diagrams showing Coulomb diamonds of the device at different temperatures. Showing the measured current versus V_D and V_G of an heterostructure device with $L_{Ge} = 162$ nm recorded at $T = 350$ mK, 2 K, 5 K and 10 K. Green lines are iso-current curves extracted from the 2D plots. For these curves the current through the nanowire is equal to 0.5 nA.

5.4.5 Coulomb blockade with superconducting leads

In the stability diagrams of Samples L1 and S1 measured at $T = 350$ mK and $T = 390$ mK (see Figures 5.15, 5.17 & 5.17) a clear gap is observed. The gap is symmetric around $V_D = 0$ V. This transport gap is due to the superconducting gap in the density of states (DOS) of the c-Al leads of the heterostructure. It results in the charge degeneracy resonances occurring at a non-zero bias voltage of $eV_D = \pm 2\Delta$. In Figure 5.25, the stability diagrams, which are measured above the critical temperature of the c-Al NW $T_C^{\text{c-Al}} = 1.46$ K [129], exhibit no transport gap in the DOS of the c-Al leads, leading to transport in the low energy, $|eV| < 2\Delta$, range.

For greater comparison between the superconducting and non-superconducting regimes, I_D - V_D curves of Sample L1, measured at 350 mK and 2 K at the charge degeneracy point of $V_G = -4.866$ V, are plotted in Figure 5.26 (a). The numerical differential conductance of the I_D - V_D curves is also plotted in Figure 5.26 (b). At 350 mK, in the superconducting regime, we observe a clear suppression of the current for voltages $|eV| < 2\Delta$. Whereas, at 2 K the I_D - V_D remains approximately linear. In conductance, the suppression of current translates to a region of low conductance bounded by two peaks. This behavior can be explained by the suppression of quasi-particles through the NW for $|eV| < 2\Delta$ due to the gap of the superconducting c-Al leads. The separation between the two peaks is expected to be approximately 4Δ , from this we extract an estimate for the superconducting gap of $\Delta = 202 \mu\text{eV}$, which is consistent with the superconducting gap of Aluminium.

In the case of Sample S1, $\Delta = 220 \pm 10 \mu\text{eV}$ is extracted from the voltage gap between the diamond peaks, which is consistent, though larger, with the observed gap of Sample L1. Further, the measured Δ agrees with the BCS gap of $222 \mu\text{eV}$ derived from the critical temperature of $T_C = 1.46$ K using Eq. 2.62. This T_C was determined for a pure c-Al nanowire sample. In this sample, the diffusion time had been extended such that the Ge had diffused out of the nanowire and into the bulk Al pads [129].

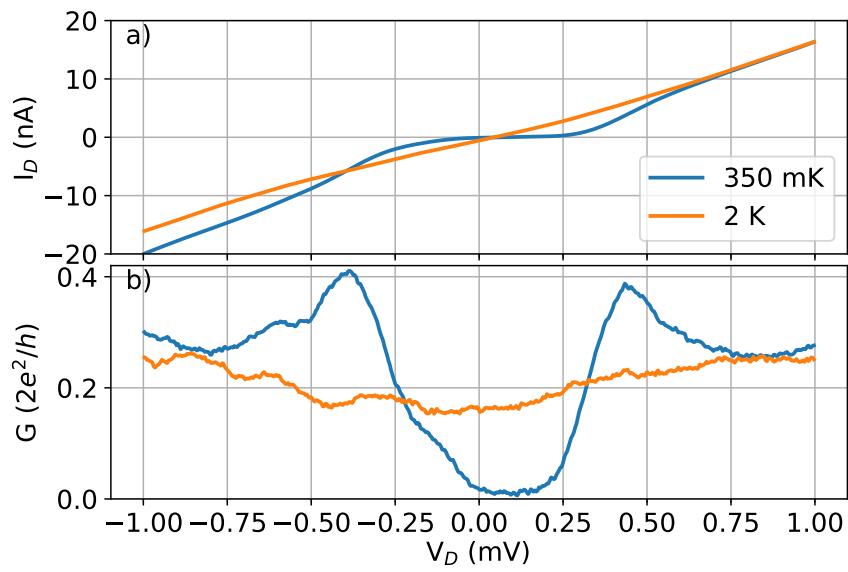


Figure 5.26 – (a) I_D - V_D curves of Sample L1 taken from the density plots at $V_G = -4.866$ V at $T = 350$ mK (blue curve) and $T = 2$ K (orange curve). (b) G - V_D curves, where G is the numerical differential conductance calculated from the I_D - V_D curves.

5.5 Supercurrent Regime

One of the significant differences between the Al-Ge-Al NW heterostructure devices with short and long Ge segments is the observation of supercurrent in the short devices. In order to investigate the supercurrent regime, current biasing measurements were carried out. Figure 5.27 shows a density plot of the differential resistance (dV_D / dI_D) with respect to the current bias (I_D) and V_G across the device at 390 mK. This provides an overview of the transport in this regime. For $V_G < -10$ V, a continuous region of zero dV_D / dI_D is observed for a range of bias currents symmetric around $I_D = 0$, indicating dissipationless transport through the Ge segment. Whereas for $V_G > -10$ V this low I_D bias window is dominated by regions of large resistance (resistance peaks), which are periodically separated by regions of zero-resistance.

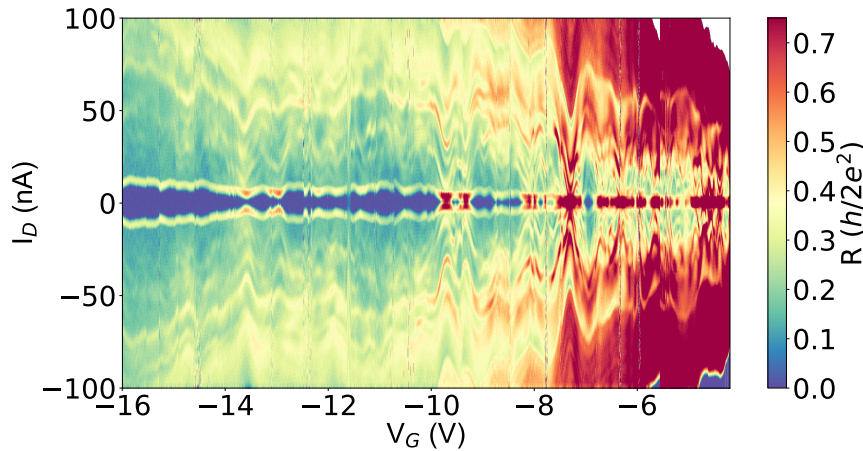


Figure 5.27 – **Overview of the superconducting regime:** Colorplot of differential resistance (R) vs bias current (I_D) and back gate voltage (V_G). We observe the zero-bias resistance peaks due to low bias blockade evolving into low bias zero resistance region due to superconducting transport as V_G decreases. This superconducting region results from the proximity effect of the Al contacts and the removal of Schottky barrier by the large negative back gate voltage.

5.5.1 Multiple Andreev Reflection (MAR)

Outside this dissipationless current region of Figure 5.27, we observe resonant features that are continuous with respect to V_G . These resonant features appear as fluctuations in resistance that trace the density plot in a snake like fashion as V_G is adjusted. To further understand these features, G versus V_D curves are plotted in Figure 5.28. The numerical differential conductance ($G = dI_D / dV_D$) was calculated from the I_D - V_D curves of Sample S1 (blue curves) and S2 (orange curve). The curves reveal that the resonant features observed in Figure 5.27 are due to bias dependent conductance peaks. They are symmetric around a large zero-bias conductance peak corresponding to *infinite conductivity* of the supercurrent state. Further, the resonant features are exceptionally consistent between Samples S1 and S2. Indeed, the curves of the two samples present very nice reproducibility in conductivity for similar $V_G \approx -15$ V.

These conductance peaks can be explained by Multiple Andreev Reflection (MAR). We superimpose on Figure 5.28 vertical dashed lines at the expected V_D position of

sub-gap conductance resonances associated with MAR. The peak positions are given by $V_D = 2\Delta/ne$, where Δ is the superconducting gap at the Al-Ge interface and n is the MAR order (see Section 2.5.3 of the Theory chapter). A superconducting gap of $\Delta^* = 185\mu\text{eV}$ was determined by finding the Δ that best aligned the dashed vertical lines with the conductance peaks. The clear alignment of up to three consecutive MAR conductance peaks with near constant V_D positions over a large gate range and across two independently measured samples highlights the quality of these heterostructures.

In Figure 5.28, we observe two extra conductance peaks beyond those associated with the first three orders of MAR. In fact, the two remaining peaks line-up with higher order MAR peaks of 5 and 14, however as the peaks are not consecutive it is unclear to which order they truly belong. As such we have only shown the expected MAR V_D positions up to 3rd order. There has been similar observations of non-consecutive higher order MAR conductance peaks [21]. However, the cause of such peaks is still unknown.

The Δ^* estimated from the fit of the MAR peaks of Figure 5.28 differs significantly from the $\Delta = 220 \pm \mu\text{eV}$ and $\Delta = 202 \pm \mu\text{eV}$ extracted in the CB regime of the short and long Ge segments, respectively. This difference is understood to be due to the reduction of the induced superconducting gap at the Al-Ge interface resulting from superconducting proximity effect, see Section 2.5.1. The absence of the Schottky barrier in the strong coupling regime permits the proximity effect through the interaction of the QD and superconducting leads, thus resulting in the observations of an induced gap of $\Delta^* = 185\mu\text{eV}$, which is, as expected, less than the BCS gap of the c-Al leads.

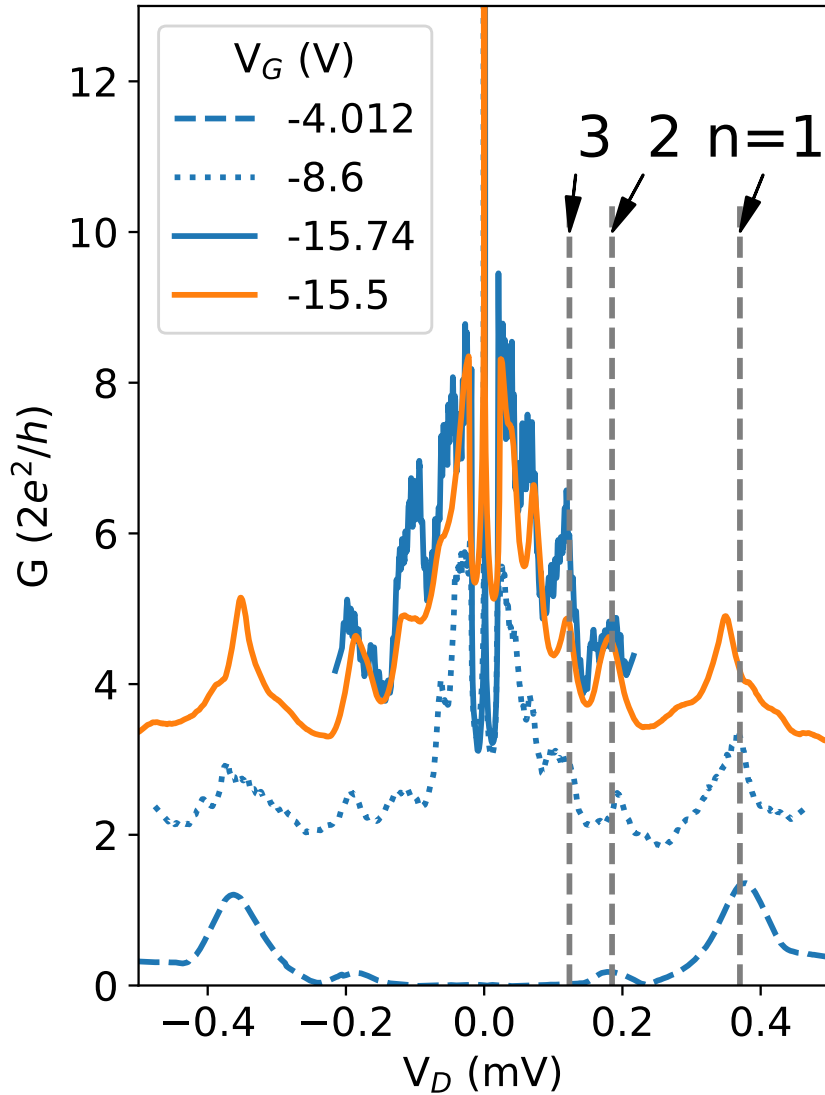


Figure 5.28 – $G(V_D)$ curves for four V_G slices. For comparison both Sample 1 (blue curves) and Sample 2 are shown (orange curve). We see clear conductance peaks which we associate with MAR. The vertical grey dashed lines indicate the expected voltage position $V_n = 2\Delta/ne$ of the first three MAR peaks for $\Delta = 185\mu\text{eV}$.

MAR Fits

The stable and multiple MAR conductance peaks indicates that the Al-Ge interfaces are highly transparent. As the Ge NW is a few channel device, due to the strong radial confinement, we can estimate the transparencies of each of the conductance channels. To acquire the transparencies, we use a Monte-Carlo based simulated annealing algorithm, which fits the non-linear I_D - V_D curves. This program has been realised by the group of Gabino Rubio, see Ref. [35] and used by a few groups to extract the transparencies τ of few channel devices [130, 131, 132].

Before initialising the algorithm, the user must set an estimate of the number of conducting channels N and an estimate of the superconducting gap Δ . The number of channels should be overestimated to be sure to account for all the channels of the weak-link. When the algorithm has converged it presents the unused channels as having negligible transparency $\tau < 0.01$. The fitting procedure starts with a random set of transparencies $\{\tau_n\}$. From this set of transparencies a random walk is performed, where the transparencies are changed. At each fitting step, the error between the I-V curve that is calculated from $\{\tau_n\}$ and the measured I_D - V_D curve, is determined by the root mean-square of their deviation χ^2 . The resulting error is then compared to the previous fit. If the new χ^2 is smaller, then the fit is accepted and $\{\tau_n\}$ is adjusted accordingly. The annealing algorithm continues until χ^2 is within the error tolerance or the maximum number of iterations has been reached. These quantities are set by the user. Once finished, the set of channel transparencies of the final fit are reported to the user.

To fit the non-linear I_D - V_D curves, an estimate of the superconducting gap Δ must be supplied. Fortunately, the program provides a tool called "*Gap search*" that determines an optimal gap to fit the I_D - V_D curve. The program works by carrying out the simulated annealing fitting procedure for different gap values. In this case, the algorithm stops after a set number of iterations and records the final fit error χ^2 . Finally the tool produces a plot of fit error versus Δ . The optimal gap is then supplied to the fitting algorithm that fits the non-linear I_D - V_D curves and determines an estimate for the channel transparencies. See Appendix C for details on using the fitting program.

We first applied the *Gap search* tool to the fits of the I_D - V_D curves of $V_G = -8.6$ V and $V_G = -15.5$ V. Figure 5.29 shows the results of the *Gap search* where we provided $\Delta = 185$ μeV as the estimate of the gap energy. The gaps with the minimum fit error were $\Delta = 181$ μeV and $\Delta = 185$ μeV for $V_G = -8.6$ V and $V_G = -15.5$ V, respectively. Inspection of the $V_G = -8.6$ V fit error versus Δ curve reveals a second fit error minimum at $\Delta = 113$ μeV . Though the fit error of the two minimums is 0.002, we took $\Delta = 181$ μeV for $V_G = -8.6$ V as it is most reasonable.

Figure 5.30 shows the fits of the I_D - V_D using the respective gaps. The fits provide similar high transparencies of the first channel of 95% and 96%, respectively. Figure 5.31 shows a bar chart of the respective channel transparencies obtained from the fits of Figure 5.30. Consistent with the transport properties of a majority hole carrier semiconductor, more conduction channels contribute to the transport at $V_G = -15.5$ V than $V_G = -8.6$ V. Further, the transparency of the mutually active channels (2, 3, 4) are significantly higher at $V_G = -15.5$ V than $V_G = -8.6$ V. This suggests that the Schottky barrier strength decreases as V_G decreases. In addition new conduction channels appear as V_G decreases. In conclusion, the high transparency of the first and second channel in the case of $V_G = -15.5$ V endorses the high quality of these

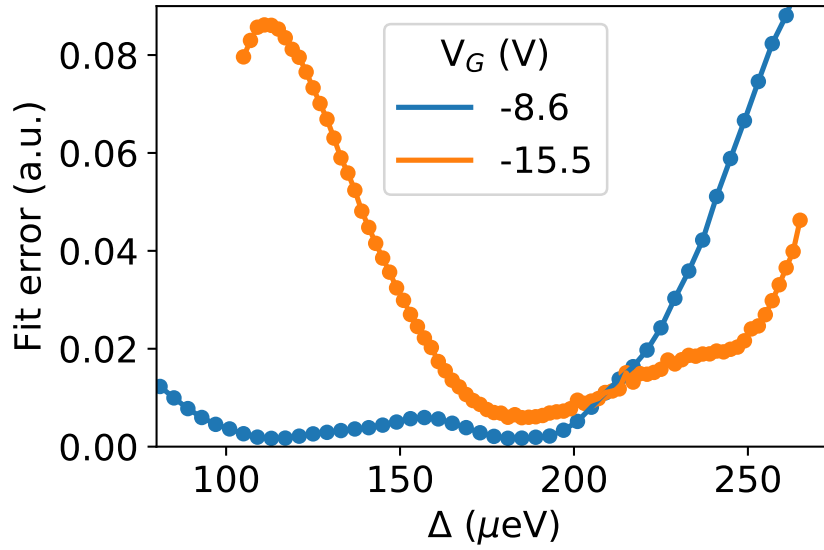


Figure 5.29 – Plot of fit error versus Δ for fits of I_D - V_D curves at $V_G = -8.6$ V and $V_G = -15.5$ V. The data was obtained from the *Gap search* to of the Monte-Carlo based fitting program.

heterostructures.

The transparencies extracted from the fitting algorithm can be compared to the results of the BTK model presented in Section 2.5.3. To employ the BTK model the normalised excess current, $\frac{eI_{exc}R_N}{\Delta}$, where R_N is the normal resistance and I_{exc} is the excess current, must be calculated. The normal resistance R_N is determined by fitting V_D - I_D curves in the linear regime above the superconducting gap ($V_D > 2\Delta/e$). The excess current I_{exc} is extracted from the V_D - I_D by finding the x-axis intercept ($V_D = 0$ V) of the linear fit, see Figure 6.11. Once $\frac{eI_{exc}R_N}{\Delta}$ is calculated, an estimate of the barrier strength (Z) can be determined using the curve of Figure 2.10 (c). The transmission probability T is then determined by $T = 1/(1 + Z^2)$.

By this BTK method transparencies of 60 % and 90 % were extracted from $V_G = -8.6$ V and $V_G = -15.5$ V, respectively. A quantitative agreement with the MAR fits method is obtained by taking an average of the transparencies of the first three channels, giving 60% for $V_G = -8.6$ V and 80% for $V_G = -15.5$ V. This is justified by the fact that the BTK method gives an average transparency which is dominated by the most transparent channels.

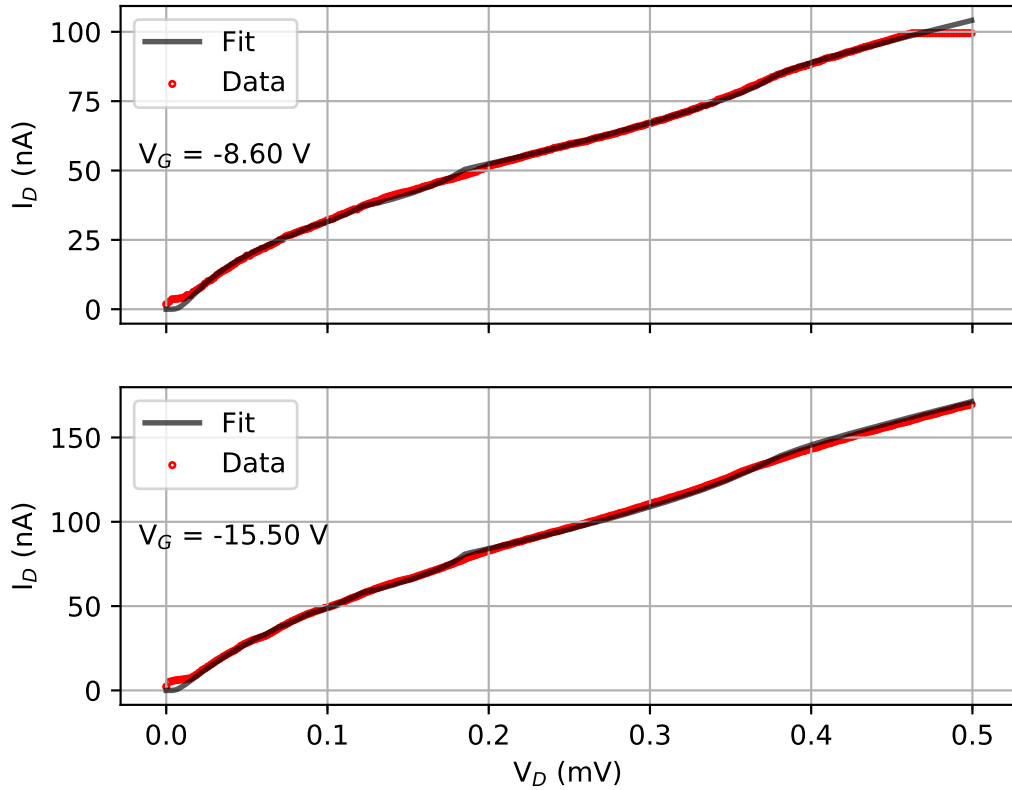


Figure 5.30 – **MAR fits** Shows fits (black) of I-V curves (red) at selected gate voltages. The fits were made using a program developed by Ref (AevCarlo) which uses Monte Carlo to converge to a fit of smallest error. The program provides an estimate of the number of conducting channels involved in the transport and the transparency of each channel (see Figure 5.31).

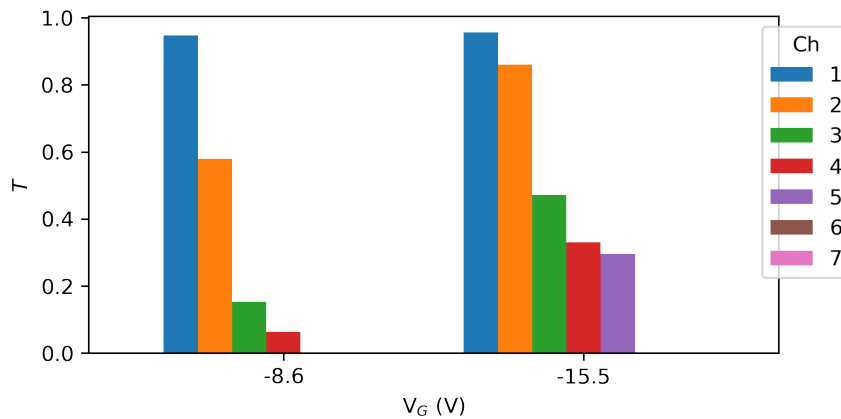


Figure 5.31 – Estimated transparency (T) of each active conducting channel for four different gate voltages. Note that $V_G = -15.5$ V is of sample 2 and the remaining are from sample 1.

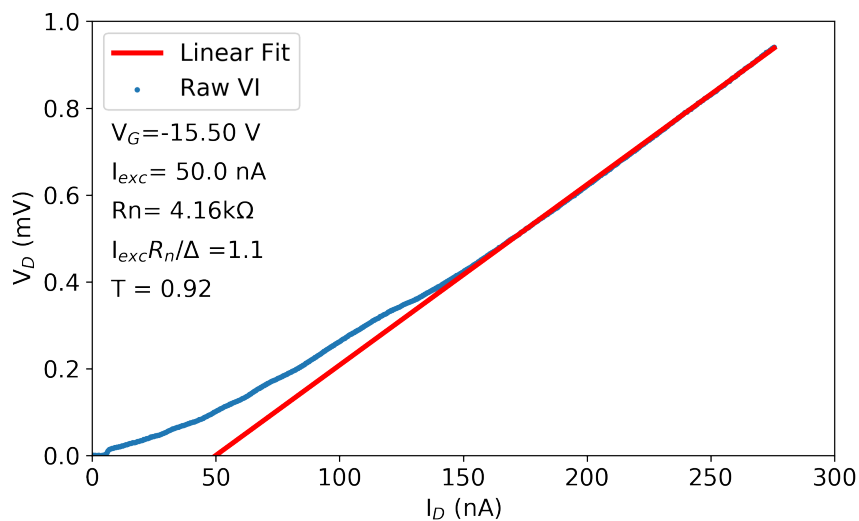


Figure 5.32 – Raw V_D - I_D curve at $V_G = -15.5$ V and linear fit of the curve in the normal regime $V_D > 2\Delta/e$. From the linear fit, R_N and I_{exc} is determined. $R_N = 4.16$ k Ω is the gradient of linear fit and $I_{exc} = 50$ nA is the x-axis intercept.

5.5.2 Supercurrent

Figure 5.33 shows plots of V_D versus I_D for Sample S1 and S2. The three gate voltages of Sample S1 (blue curves) highlight the gate tunability of the supercurrent. Further, the two samples present very similar behavior with the appearance of non-zero critical current for the same V_G range with comparable tuneability. As discussed in the supercurrent paragraph of Section 2.5.3, the critical current I_c is the maximum dissipationless current that can pass through a superconducting junction. Current larger than I_c will suppress the superconducting properties of the junction, thus giving the junction its finite normal resistance. This transition at I_c manifests itself experimentally as a measurable voltage drop across the junction as the current becomes dissipative. In the density plot of Figure 5.27, the transition is visualised by a peak of differential resistance that border the dissipationless region. The retrapping current I_r is complimentary to I_c ; defined as the minimum current at which a superconducting junction transitions from a dissipative regime to a supercurrent regime. I_r is observed when the current bias is swept from a high to low magnitude and I_c is observed in the opposite sweep direction (from low to high magnitude). We observe that the critical and retrapping currents are near equal in magnitude for all the V_D - I_D curves. We observe gate tunable critical current up to 10 nA for Sample S1 and 6 nA for Sample S2.

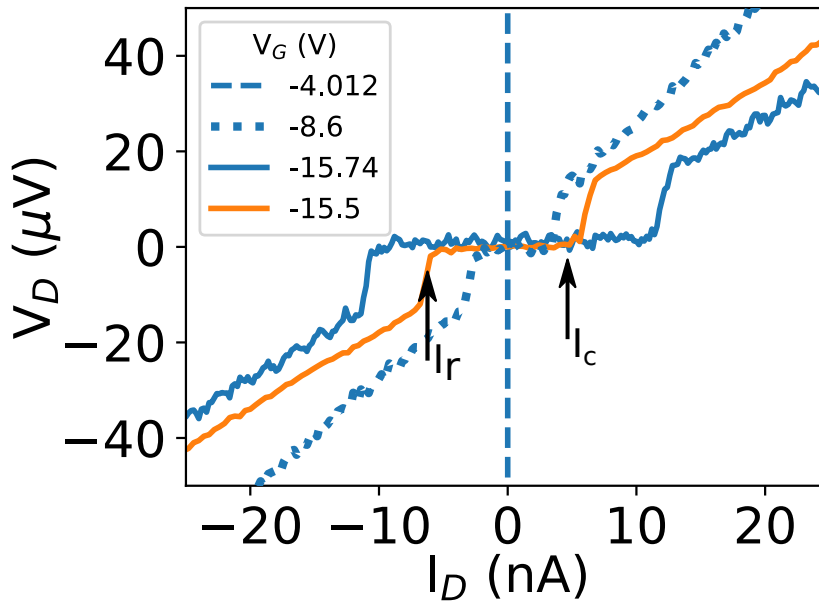


Figure 5.33 – V_D versus I_D for four V_G slices showing the onset of supercurrent. For comparison both Sample 1 (blue curves) and Sample 2 are shown (orange curve). Retrapping I_r and critical current I_c are labeled.

The observation of supercurrent at very negative V_G implies that in this regime $\Gamma \gg \Delta$, E_C . This suggests that the back-to-back Schottky barriers that dominated the transport characteristics in the Coulomb blockade regime are no longer present. In accordance with our model of the Al-Ge-Al nanowire heterostructure, described in Figure 5.7, we expect that at very negative gate voltages the valence band bending due to the negative V_G is sufficient to reduce the depletion region of the Schottky

barriers. This makes the Schottky barriers negligible, thus resulting in a near Ohmic contact at the Al-Ge interface.

In a superconducting-QD-superconducting junction, the resonant critical current is given by $I_c = (\pi e/h)\Gamma\Delta/(\Delta + \Gamma/2)$ which holds for any Γ and Δ ratio if E_C can be neglected [74]. In the case where $\Gamma \gg \Delta$, it simplifies to $I_c = (\pi\Delta/e)G_0$. We retrieve here the supercurrent for a quantum point contact (QPC) superconducting junction. This is equivalent to the $I_c R_N$ product, which relates I_c to Δ by $eI_c R_N = \pi\Delta/2$ and is often used in the literature as a figure of merit for accessing S-N-S junctions. Applying this figure of merit, we obtain product values which are 20 and 30 times smaller than Δ . This suggests that I_c is considerably suppressed possibly due to residual measurement noise and/or thermal fluctuation at $T = 390$ mK overcoming the Josephson energy $\frac{\hbar}{2e}I_c$.

Superconducting coherence length

The coherence length of a junction is another important consideration when analysing superconducting hybrid junctions. To introduce this discussion, we will first consider coherence length of superconducting Aluminium.

Superconductors can be categorised into clean or dirty limits depending on the relative scale of the superconducting coherence length ξ_s to the mean free path ℓ_s . The *clean* limit is defined as $\xi_s \ll \ell_s$ whereas the *dirty* limit is defined as $\xi_s \gg \ell_s$. In the *clean* limit, the superconductor's coherence length is given by the Pippard coherence length ξ_0

$$\xi_0 = 0.18 \frac{\hbar v_F}{k_B T_c} \quad (5.6)$$

From measurements of the c-Al NW, a mean free path of $\ell_{Al} \approx 15$ nm was determined. Comparing to the coherence length of Al $\xi_0 = 1600$ nm, we are clearly in the *dirty* limit. In this limit the superconductor's coherence length is approximated by

$$\xi_s^d = \sqrt{\xi_0 \ell_s}. \quad (5.7)$$

Therefore, we estimate the superconducting coherence length of the c-Al NW to be $\xi_{Al} \approx 160$ nm.

Superconducting junctions with normal metal or semiconducting weak-links are categorised into short or long junction limits. These limits depend on the length L of the weak-link compared to the coherence length of the junction ξ_N . The short junction limit is achieved by having $L \ll \xi_N$, whereas for the long junction limit $L \gg \xi_N$. However, coherence length that defines the limit depends on whether the weak-link is in the diffusive or ballistic regime. The coherence lengths are expressed as [133]

$$\xi_N^d = \sqrt{\frac{\hbar \mathcal{D}_N}{\Delta}} = \sqrt{\frac{\hbar v_F \ell_N}{3\Delta}} \quad (5.8)$$

and

$$\xi_N^b = \frac{\hbar v_F}{\Delta}, \quad (5.9)$$

for the diffusive and ballistic regimes, respectively. The two regimes define the energy scales of the Andreev bound states (ABS) and the junction's critical current I_c [133].

Assuming the minimum Fermi energy E_F of 10 meV to be the energy of the first sub-band, which is estimated from the energy levels of the 1D modes in the Ge nanowire due to radial confinement [102] and a maximum effective mass of heavy-holes m_{HH} of $0.28m_e$, we estimate a minimum $v_F = \sqrt{2E_F/m_{HH}}$ of $1.1 \times 10^5 \text{ ms}^{-1}$. Considering that the Ge segment is in the ballistic limit, we estimate a coherence length for a single Ge channel to be approximately $\xi_N^b = 2500 \text{ nm}$. Whereas, in the diffusive limit we estimate a coherence length of $\xi_N^b = 190 \text{ nm}$ using $\ell_{Ge} = 45 \text{ nm}$. This result confirms that Samples S1 and S2 are in the short junction limit.

The dependence of $\xi_N^{d,b}$ on v_F means that ξ_N can be tuned by adjusting the carrier density of the weak-link. In the case of semiconducting weak-links such as Ge, the carrier density is readily tuned by an electrostatic gate field. The tuneability of ξ is the basis of Josephson field effect transistors (JoFETs) which can be employed to build a gatemon. A gatemon is a gate tuneable transmon. The critical current's I_c relationship with ξ_N enables I_c to be adjusted by tuning ξ_N through V_G .

5.6 Intermediate Regime

Between the Coulomb blockade (CB) and superconducting regimes of the Al-Ge-Al nanowire heterostructures with short Ge segments, Samples S1 and S2, we observe an intermediate regime. The onset of the intermediate regime is marked by the fading of Coulomb blockade features as V_G becomes more negative. The transition from the Coulomb blockade regime to the intermediate regime is evident in Figure 5.34. The I_D - V_G slice at $V_D = 0.48$ mV shows a clear increase of current magnitude in the sample. Though we continue to observe current oscillations, the current minimums are now of the order of 10 nA. It is an order of magnitude larger compared to 0.4 nA in the many-hole CB regime. The observation of oscillations with the absence of current blockade implies we have entered an intermediate coupling regime. Here, the charging energy E_C is no longer the dominant energy scale but is now comparable to the tunnel rate Γ . From previous analysis, Γ is close to the superconducting gap Δ when $V_G = -3.5$ V (see Page 123).

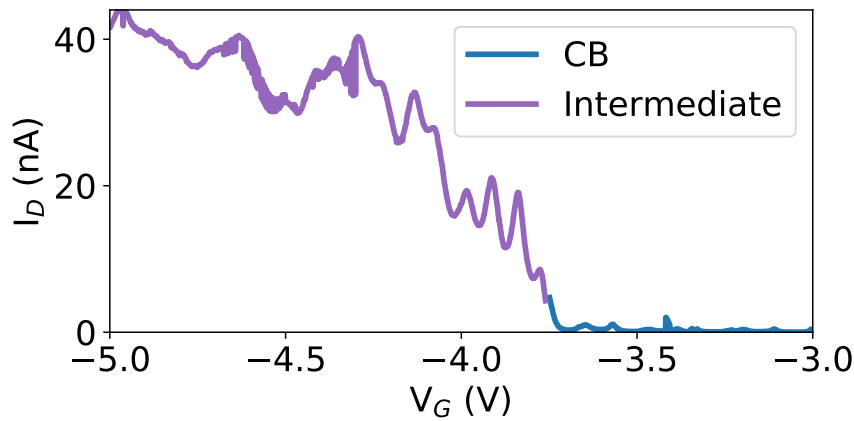


Figure 5.34 – I_D - V_G slice of Sample S1 at $V_D = 0.48$ mV revealing the large magnitude of the current oscillations at the beginning of the intermediate regime.

In Figure 5.35 (b) the differential conductance versus V_D and V_G is plotted. For $V_G < -3.8$ V, sub-gap conductance peaks appear with periodic modulation with respect to V_G . These resonances forming arcs bending towards zero-bias at the charge degeneracy points are interpreted as the experimental signature of single hole filling of the QD in the intermediate coupling regime. Similar to the CB regime, we estimate E_{add} from ΔV_G (see Figure 5.35 (a)) and observe a continuation of the even-odd filling with comparable energies. In this V_G range, we estimate the QD is filled by over thirty holes.

As the QD is filled with more holes, the sub-gap features evolve: the magnitude of the conductance resonances increases and new conductance peaks emerge at lower bias voltages resulting in a reduction of the blockade region. This gate voltage dependence of the conductance peaks shows that these resonances are not simple multiple Andreev reflections (MAR) which should appear at constant bias voltage. In spectroscopy measurements performed on carbon nanotube QDs contacted by superconducting leads, such sub-gap facing bell-shaped resonances are associated with Andreev bound states (ABS) which occur in a S-QD system in equilibrium through the coupling of discrete

electronic states to the leads [6]. The similarity of these results to our measurements suggests that the sub-gap features could be due to resonant coupling to the ABS.

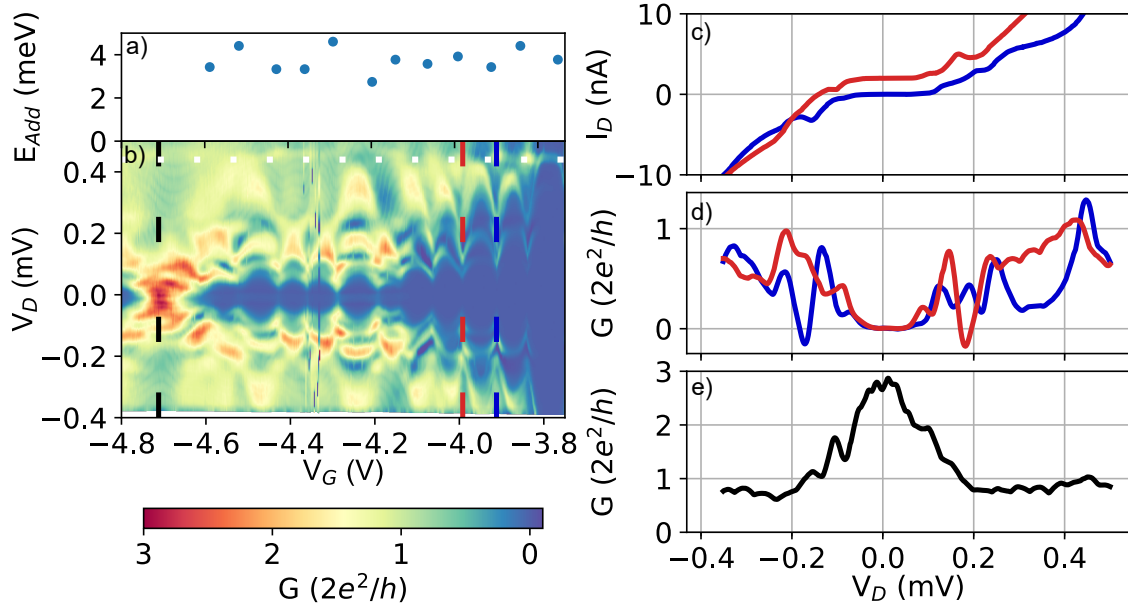


Figure 5.35 – **Intermediate regime**(a) E_{add} , calculated using $\alpha_G \Delta V_G$, versus V_G . (b) Density plot of differential conductance with respect to bias voltage (V_D) and gate voltage (V_G) in the intermediate regime. White dashed line shows $eV_D = \pm 2\Delta$ for $\Delta = 220 \mu\text{eV}$. We observe sub-gap conductance features that evolve with V_G . (c) $I_D(V_D)$ & (d) $G(V_D)$ slices at $V_G = -3.91 \text{ V}$ (dark blue) and $V_G = -3.99 \text{ V}$ (red). The red $I_D(V_D)$ curve has been offset by $+5 \text{ nA}$ for clarity. (e) $G(V_D)$ curve at $V_G = -4.72 \text{ V}$.

The blue curves of Figure 5.35 (c) and 5.35 (d) show the current and the conductance as a function of the bias voltage for V_G adjusted to the degeneracy points (see vertical blue dashed line in Figure 5.35 (b)). The I_D - V_D measurements, shown in Figure 5.35 (c) reveal a current peak at a bias voltage of about $-160 \mu\text{eV}$ close to $\frac{2}{3}\Delta \approx 147 \mu\text{eV}$, for $\Delta = 220 \mu\text{eV}$. Related to this peak, negative conductance is observed in Figure 5.35 (d). As discussed in Section 2.5.4 such resonances have been predicted to occur in S-QD-S systems when Γ is of the order of Δ [80] and result from the interplay between MAR resonances (the 3rd order occurs at $V_D \sim \frac{2}{3}\Delta$) and resonant tunneling.

Further inspection reveals that the resonant peak is not symmetric with respect to V_D . Negative conductance shows up only at negative bias voltage and not at positive bias (blue curve). More interestingly, this asymmetry is inverted when a single hole is added inside the QD (red curve in Figure 5.35.c and Figure 5.35.d). As previously, we observe a current and negative conductance peak but this time at positive bias voltage. In combination, these individually asymmetric curves share significant symmetry: by reflecting the red G - V_D curve about the y-axis of $V_D = 0 \text{ V}$, we observe the underlying symmetry between the resonance features of the blue and red G - V_D curves (see Figure 5.36). The intriguing symmetry between the curves of two consecutive charge degeneracy points, that is observed in both samples, needs

further investigation and measurements with a magnetic field or interface gates to confirm the nature of these transport characteristics.

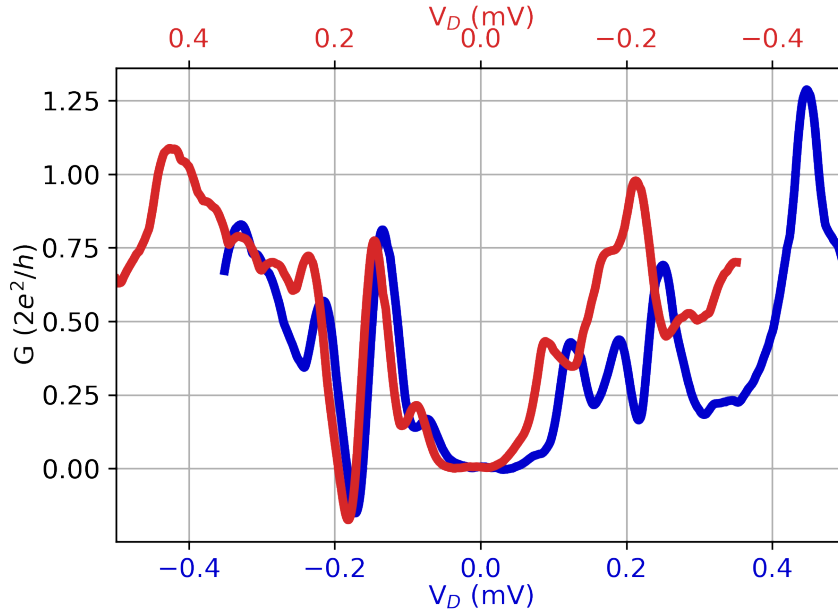


Figure 5.36 – Differential conductance slices ($G(V_D)$) at, $V_G = -3.91$ V and $V_G = -3.99$ V, the charge degeneracy points of the sub-gap blockade of the QD in the intermediate regime (see dashed lines in Figure 5.36.b of the main text). The $G(V_D)$ slice at $V_G = -3.99$ V (red curve) is reflected about $V_D = 0$ V. This reflection is achieved by plotting the $V_G = -3.99$ V slice (red curve) with an independent V_D axis (red axis labels) which is inversed with respect to the V_D axis (blue axis labels) of the $V_G = -3.91$ V slice (blue curve). The alignment of the negative conductance features reveals the underlying symmetry between the curves of two consecutive charge degeneracy points.

The sub-gap bell-shaped resonances continue until $V_G = -4.72$ V where the low voltage blockade is replaced by a zero-bias conductance peak shown on Figure 5.35 (e). We associate this feature as superconducting transport across the QD.

Figure 5.37 shows the differential conductance versus V_D and V_G at lower gate voltage. In this plot the intermediate regime shows regions of sub-gap features periodically separated by superconducting resonances until the supercurrent transport begins to overcome the blockade and large zero-bias conductance is observed continuously with respect to V_G , marking the beginning of the supercurrent regime.

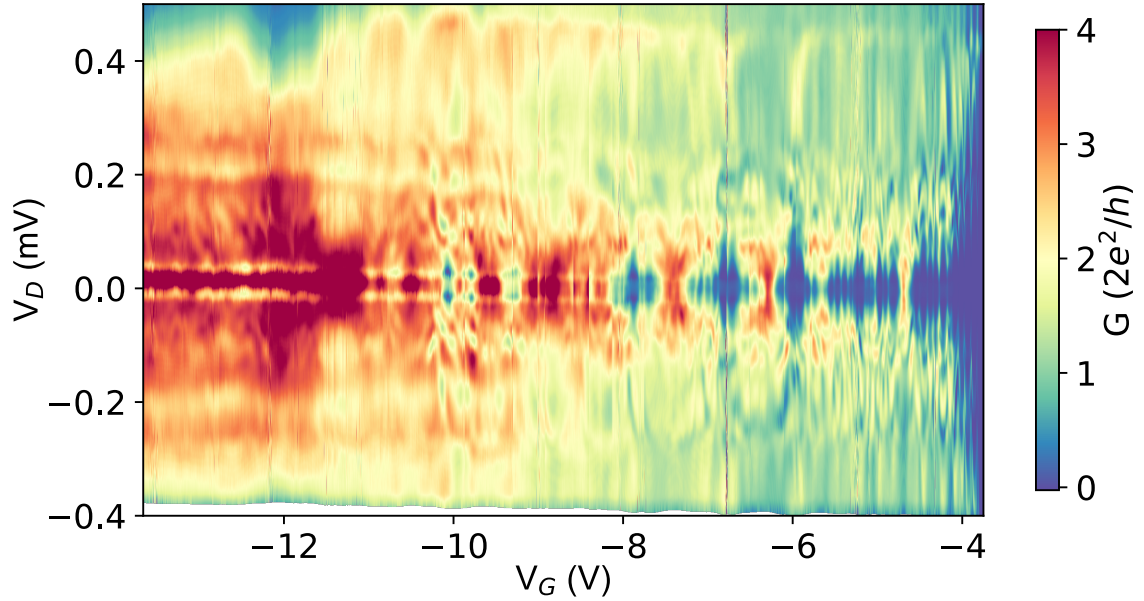


Figure 5.37 – **Intermediate regime transport overview:** Colorplot of differential conductance (G) vs bias voltage (V_D) and back gate voltage (V_G). We observe large sub-gap conductance with Coulomb blockade like features at low V_D bias evolving into large zero-bias conductance peaks as V_D decreases.

5.7 Sub-gap features in the Coulomb blockade regime

Closer inspection in the Coulomb blockade regime reveals also the appearance of sub-gap states with only a few holes on the QD. Interestingly, as Γ becomes comparable to the superconducting gap ($\Gamma \sim \Delta < E_C$), a zoom on the superconducting gap reveals sub-gap conductance resonances that meet at $eV_D \approx \pm\Delta$ and occur at the charge degeneracy points. Given these features are within the superconducting gap, they are likely mediated by Andreev reflections.

Figure 5.38 (a-b) shows the sub-gap features with a few holes on the QD. These sub-gap features trace a triangle shape with a blockade region between the opposing apexes spanning $V_D = 450 \pm 20 \mu\text{V}$. Comparing the V_D width with the measured Δ of $220 \mu\text{V}$ we conclude that the apex of the conductance resonances occur at $eV_D = \pm\Delta$. This suggests that these sub-gap features are indeed related to Andreev states rather than quasiparticle poisoning. Figure 5.38 (c-d) show I_D - V_D slices that cross the apex of two sub-gap triangles: $V_G = -1.448 \text{ V}$ and -0.82 V , respectively (see blue dashed lines on Figure 5.38 (a-b)). Both slices show current features at $eV_D \approx \pm\Delta$, which results in the observed conductance resonances. Interestingly, there is significant asymmetry with respect to V_D ; the current feature at $eV_D \approx -\Delta$ is a well defined current peak whereas the current feature at $eV_D \approx +\Delta$ is a current jump. These I_D - V_D features result in the conductance resonance of $-2\Delta < eV_D \leq -\Delta$ being accompanied by a region of negative differential conductance contrary to the conductance resonance of $\Delta < eV_D \leq +2\Delta$, which is accompanied by a region of near zero differential conductance.

Figure 5.39 shows the sub-gap features with about twenty to thirty holes on the QD. We continue to observe the triangular sub-gap conductance resonances at the

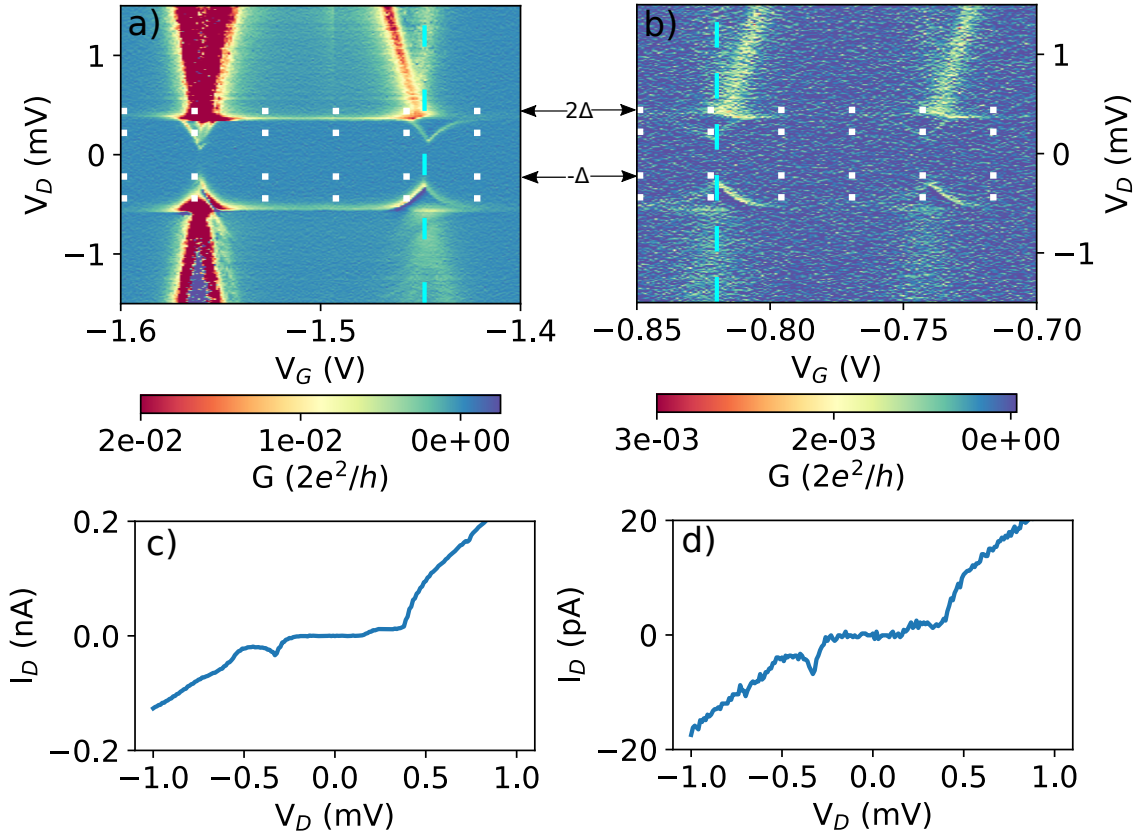


Figure 5.38 – (a-b, e) Colorplot of differential conductance (G) zoomed onto the charge degeneracy points of the Coulomb blockade regime with few holes on the quantum dot a-b showing sub-gap conductance resonances. In this case, G is determined using the Savitzky-Golay filter with a smoothing window of 3 data points which provides more sensitivity to the transport features. White horizontal dotted lines show $eV_D = \pm 2\Delta$, Δ for $\Delta = 220\mu\text{eV}$. (c & d) shows I-V curves at the apex of two sub-gap triangles: $V_G = -1.448$ V & -0.82 V respectively (see blue dashed lines on (a & b)). The V_D position of the sub-gap apexes and the current peaks suggests that these sub-gap features are due to Andreev reflection.

charge degeneracy points. However, around $V_G = -3.2$ V with $N \approx 27$ holes on the QD, we begin to observe differences between the V_D position of the conductance resonances of the odd and even charge states. The resonance of the odd charge state begins to pull away from the superconducting gap at $eV_D \approx \pm 2\Delta$ compared to the even charge state which remains anchored to $eV_D \approx \pm 2\Delta$. This difference is most notable for the charge state of $N \approx 27$ around $V_G = -3.6$ V. These odd charge state features have similarities to the Andreev bound states of an S-QD-S junction in the Kondo regime, see Figure 2.20. Using Eq. 2.89 and taking $E_C \approx 3$ meV and $\Gamma \approx 250$ μeV , we estimate a Kondo temperature, assuming $\epsilon_0 = 0$ of $T_K \approx 7$ K. As such we could expect to observe Kondo effects when there are an odd number of holes on the QD. However, more investigation is required to confirm the observation of Kondo effects.

Finally, we note that the V_D position of the 2Δ and Δ resonances in the colormaps are slightly shifted from their expected position. We associate this shift with a bias

offset in the measurement.

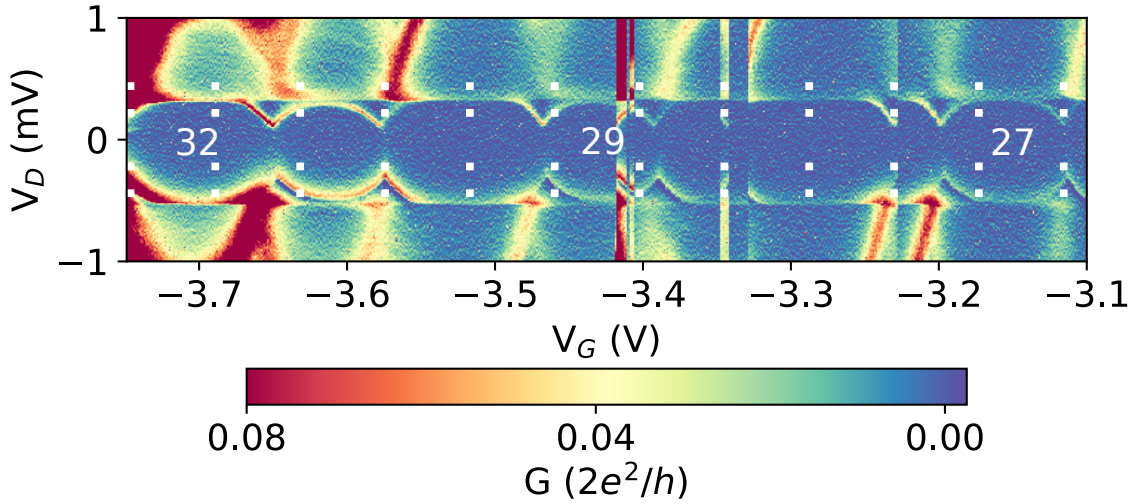


Figure 5.39 – Colorplot of differential conductance (G) zoomed onto the superconducting gap in the many hole Coulomb blockade regime. In this case, G is determined using the Savitzky-Golay filter with a smoothing window of 3 data points which provides more sensitivity to the transport features. Shows sub-gap conductance and the progressive shifting of the conductance resonance from the $V_D = \pm 2\Delta$ edge in the odd charge state as V_G decreases. White horizontal dotted lines show $eV_D = \pm 2\Delta$, Δ for $\Delta = 220\mu\text{eV}$.

5.8 Conclusion

In this chapter, we have reported on the transport properties of monolithic Al-Ge-Al NW heterostructures with intrinsic germanium (i-Ge) segments. In particular, we have presented the low temperature (400 mK) transport properties of a device in the diffusive regime and devices at the edge of the ballistic regime. The device in the diffusive regime, labeled Sample L1, has an i-Ge segment length of approximately 162 nm. Whereas, the devices at the edge of the ballistic regime have i-Ge segment lengths of 42 nm and 37 nm, labeled Sample S1 and Sample S2, respectively. We have shown that by using a single back-gate, we can tune the devices from a completely insulating regime, through a low conductive regime that exhibits properties of a single-hole filling quantum dot, to a supercurrent regime, resembling a Josephson field effect transistor [134].

We described how the dynamic transport observed in these devices is attributed to the band structure of the Al-Ge-Al nanowire heterostructure. In Section 5.1.4, we showed that the band structure of the Al-Ge-Al nanowire heterostructure is defined by back-to-back Schottky barriers at the Al-Ge interfaces. Importantly, Fermi level pinning results in a weak Schottky barrier to holes, allowing hole transport through our device. We then showed, in Section 5.1.5, how this band structure leads to the formation of a quantum dot. Here, the Schottky barriers define the tunnel junctions between the Al leads and the Ge quantum dot. The quantum dot is defined by Ge's valence band. Moreover, the tunnel rate Γ between the leads and the quantum dot is

dependent on the strength of the Schottky barriers. While the charging energy E_C is dependent on the size of the quantum dot [135].

We showed that by shifting the back-gate voltage V_G to be more negative, we can push the valence band above the Fermi energy. This valence band bending increases the size of the quantum dot, while simultaneously decreasing the strength of the Schottky barriers. This gate dependence explains our observation of multiple transport regimes at low temperature.

In the Coulomb blockade regime (Section 5.4), we presented stability diagrams, which displayed clear Coulomb diamonds. From the stability diagrams, we determined the characteristics of the Ge quantum dot. Beyond discussing the characteristic capacitances, we showed that the addition energy E_{add} decreases as V_G becomes more negative. We associated the evolution of E_{add} with the decreasing E_C due to the increasing size of the quantum dot as V_G becomes more negative. In Sample S1, we estimated that E_C ranges from approximately 32 meV in the few hole regime to 3 meV in the many hole regime. By comparing E_C , Γ and the superconducting gap Δ of the Al leads, we showed that the Coulomb blockade regime is defined, in terms of energy, by $E_C \gg \Delta > \Gamma$.

We also revealed evidence of the effects of strong confinement on Ge's hole states. This included, the observation of the even-odd filling effect, which suggests that we are observing single hole filling of the Ge segment. From the even-odd effect, we estimated the average single-level spacing of Sample S1 to be $\langle \delta_N \rangle \approx 1.0 \pm 0.3$ meV. Further, we discussed the observation of resonant tunnelling through excited charge states. In the Coulomb blockade regime, we extracted the superconducting gap of the c-Al leads to be $\Delta = 220 \pm 10$ μeV and $\Delta = 202 \pm \mu\text{eV}$ for Samples S1 and L1, respectively. The extracted Δ is in good agreement with the BCS gap of 222 μeV , which was determined using the critical temperature of a c-Al nanowire of 1.46 K [129].

In Section 5.5, we showed that by applying a large negative back-gate voltage, we can tune Samples S1 and S2 to be in a supercurrent regime. In this regime, we observe gate tuneable supercurrent up to 10 nA. The observation of supercurrent suggests that in this regime, the tunnel coupling is the dominating energy scale, with $\Gamma \gg \Delta, E_C$. Furthermore, we described the observation of sub-gap conductance peaks, which we associated with multiple Andreev reflection (MAR). We revealed that three consecutive conductance peaks were well aligned with the expected V_D position of MAR, using an induced gap of $\Delta^* = 185$ μeV . The observation of stable MAR, up to third order and over a large V_G range, provides further evidence towards the high quality of the Al-Ge interfaces. Using a Monte Carlo based fitting algorithm, to fit the non-linear I_D - V_D curves measured in the supercurrent regime, we estimated the transmission of Ge's conducting channels. From these fits, we obtained a transmission above 90 % for the first channel, which agreed with transmission estimates using the BTK model.

In Section 5.6, we discussed the intermediate regime, which is observed in the V_G range that is between the Coulomb blockade and superconducting regimes. Estimates of Γ revealed that the intermediate regime occurs when the energy scales are $\Gamma \sim \Delta \lesssim E_C$. This results in the observation of significant transport features within the superconducting gap. We showed that the nature of these sub-gap transport features suggests that, in the intermediate regime, sub-gap transport does not solely occur by multiple Andreev reflection (MAR) but by a combination of MAR and resonant tunneling through the quantum dot.

In conclusion, the results presented in this chapter, demonstrate the potential of

5.8 CONCLUSION

these novel Al-Ge-Al nanowire heterostructures for the study of quantum phenomena and their application as quantum devices. In particular, the impressive tuneability and high quality of the Al-Ge interfaces enables the investigation of the rich physics provided by the subtle interplay between Coulomb blockade and Andreev mediated superconductivity.

Transport properties of Al-Ge/Si-Al core/shell Nanowire heterostructures

6

Contents

6.1	Introduction	152
6.2	Transport Overview	152
6.3	Quantised Conductance	154
6.4	Low Conductance Regime	158
6.5	High Conductance Regime	159
6.6	Conclusion	164

6.1 Introduction

In this chapter, I will discuss the transport properties of Al-Ge/Si-Al core/shell NW heterostructures with ultra-short Ge segments of approximately 40 nm. Though similar in dimension to the Al-Ge-Al NW heterostructures, discussed in Chapter 5, the 1D hole gas created by the Si shell leads to significant differences between their respective transport properties. We will present all the transport properties that this new devices has revealed at low temperature.

6.2 Transport Overview

We begin by discussing the overall transport features of the measured device. Figure 6.1 shows a density plot of the differential conductance, in units of quantum conductance ($G_0 = 2e^2/h$), versus bias voltage V_D of the Ge/Si core/shell sample with $L_{\text{Ge/Si}} = 40$ nm recorded at $T = 390$ mK over a full gate voltage V_G range. The plot reveals highly tuneable transport with similarities to that of the ultra-short intrinsic Ge (*i*-Ge) NW devices of Figure 5.13. When V_G is swept from positive to negative, the conductance increases. In agreement with *i*-Ge, the Ge/Si core/shell device behaves like a *p*-type accumulation FET. For the Al-Ge/Si-Al core/shell NW heterostructure we split the transport properties into a low conductance regime at positive V_G and a high conductance regime at negative V_G . The regimes are labeled in Figure 6.1. Although charging and hysteresis effects should be significantly suppressed by passivating a Ge NW with a Si shell [22], we note that a dependence on the V_G sweep direction for our Ge/Si core/shell NW heterostructure devices was found.

As with the *i*-Ge devices, we observe features resulting from the superconducting property of the leads. In particular, continuous conductance resonances are observed that run parallel to the V_G axis. These features are symmetric around $V_D = 0$ V and are correspondingly associated with MAR. Interestingly, even in the low conductance regime ($15 \text{ V} < V_G < 30 \text{ V}$) we observe no evidence of Coulomb blockade or pinch-off. The blockade occurs only at low energies within the superconducting gap ($|eV_D| < 2\Delta$) where particle states are forbidden due to the superconducting leads. As V_G is reduced, the low energy blockade transitions disappear and a zero-bias conductance peak emerges. It is associated with supercurrent through the Ge/Si core/shell segment.

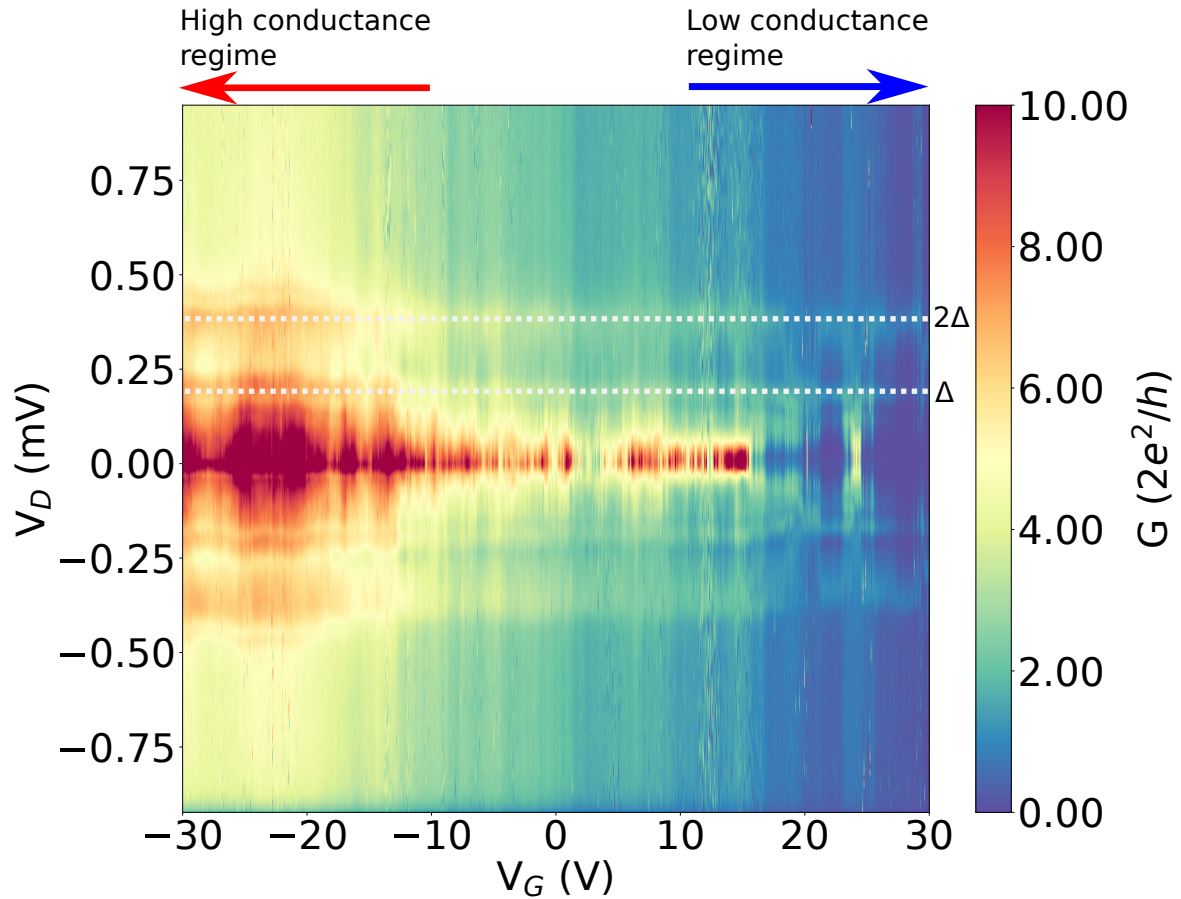


Figure 6.1 – **Transport Overview.** Density plot of differential conductance (dI_D/dV_D) with respect to bias voltage (V_D) and gate voltage (V_G) of (a) Ge/Si core/shell NW sample recorded at 390 mK. We observe two distinct regimes: A low conductance regime $V_G > 20$ V and a supercurrent (high conductance) regime ($V_G < 10$ V).

6.3 Quantised Conductance

To investigate the Ge/Si core/shell nanowire's transport properties, the conductance was measured as V_G was swept from -30 V to 30 V with an applied constant V_D bias of 1 mV at various temperatures from 300 K to 5 K. These measurements were made by our collaborators in their ^4He cryostat using a lock-in amplifier. Figure 6.2 shows the resulting G - V_G curves. As observed in Figure 6.1, the conductance increases as V_G goes from positive to negative. Notably, at $T = 150$ K the G - V_G curve begins to reveal plateau-like features compared to the smooth higher temperature curves. These plateaus become more pronounced as the sample is cooled further. The position and nature of these features suggests that they relate to quantised conductance. Furthermore, the G - V_G measurement recorded at $T = 5$ K hints at a conductance anomaly at $0.7G_0$, which is often observed in ballistic mesoscopic devices [136].

We discussed in Section 2.2.1 the conditions that must be met to observe quantum ballistic transport. Firstly, the NW must be in the ballistic regime, where the dimensions of the NW are smaller than the mean free path ℓ . Secondly, the diameter d of the NW must be of the order of the Fermi wavelength λ_F . In the literature the reported mean free path of Ge/Si core/shell NWs ranges from 70 nm to 500 nm [36, 22], putting our Ge/Si device firmly in the ballistic regime. This suggests that we are indeed observing in the Ge/Si core/shell system one-dimensional spin-degenerate sub-band-resolved quantum ballistic transport.

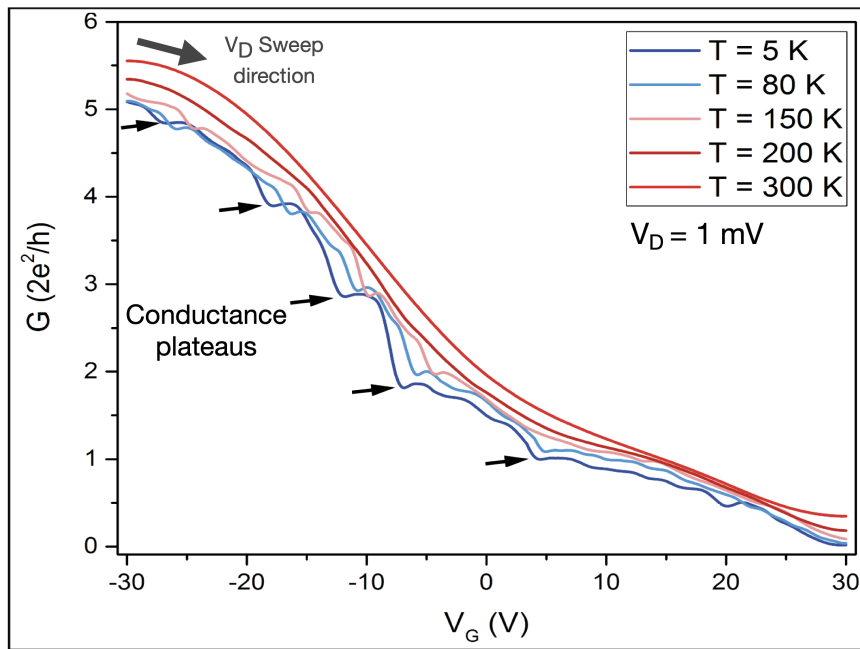


Figure 6.2 – G - V_G characteristics of the Al-Ge/Si-Al heterostructure device with a channel length of $L_{\text{Ge/Si}} = 40$ nm measured at different temperatures between $T = 5$ and 300 K. The conductance G was directly obtained from the measured current as the V_G is swept from -30 V to 30 V according to $G = dI_D/dV_D$ and is plotted in units of G_0 . The black arrows indicate the quantised conductance plateaus, and the blue arrow indicates the $0.7 G_0$ plateau at 5 K.

In Figure 6.3, the resistance of the conductance plateaus $R = 1/G$ taken at the

points marked by black arrows marked on Figure 6.2 are plotted against the inverse of the conducting channel number, associated with that plateau $1/n$. By applying a linear fit to R versus $1/n$ the average transparency of the Al-Ge interfaces can be estimated. The gradient of the linear fit gives a value of $1.04 R_0$, where $R_0 = h/2e^2$ is the quantised resistance. From the gradient an average transparency of approximately 96 % is determined.

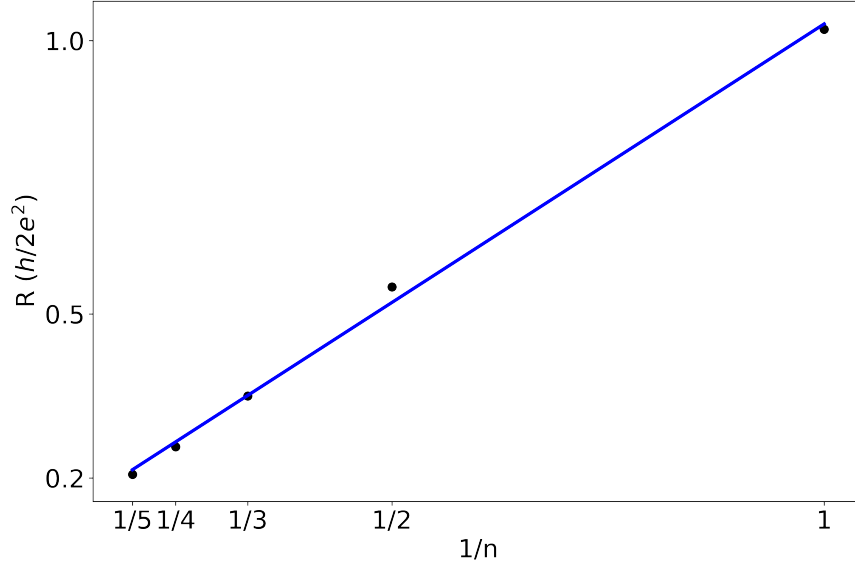


Figure 6.3 – Resistance (R) of the quantised conductance plateaus of Fig. 6.2 vs the inverse of the conducting channel number ($1/n$). The linear fit is used to estimate the interface transparency.

The procedure to estimate the transparency is based on Landauer’s formula (Eq. 2.29). Landauer’s formula can be expressed in terms of resistance R [40],

$$R = (R_0 + R_1) / n, \quad (6.1)$$

where $R_1 = R_0(1 - T)/T$ is the excess resistance due to scattering resulting from finite transmission of ballistic conductor T . By assuming that the excess resistance in our Ge/Si core/shell NW is due to finite interface transparency, we can estimate the transparency of the Al-Ge interface from the gradient of the linear R versus $1/n$ curve. By Eq. 6.1 the gradient is equal to $R_0(1 + (1 - T)/T)$, therefore T can be easily determined.

Investigations of quantised conductance continued in the low temperature regime using the pumped ^3He set-up. Figure 6.4 shows traces of the bias voltage dependent differential conductance $G = I_D/V_D$ for fixed gate voltages ranging from $V_G = 30$ V to -30 V with a step size of $167 \mu\text{V}$ at $T = 450$ mK. The waterfall plot clearly shows conductance traces bunching into five thick lines of constant conductance separated by regions of low trace density. We associate each bunch to the opening of each of the five conductance channels, observed as plateaus in Figure 6.2. Each bunching region occurs near an integer multiple of G_0 . The waterfall plot also reveals the zero-bias conductance peaks associated with superconducting transport through the Ge/Si core/shell segment. In accordance with Figure 6.1 zero-bias conductance peaks

appear after a certain gate voltage. In addition we observe a drop in conductance in the vicinity to the zero-bias peak. This drop could be related to the superconducting gap, which strongly reduces conductance. However, the voltage window does not correspond to the expected $4\Delta/e$.

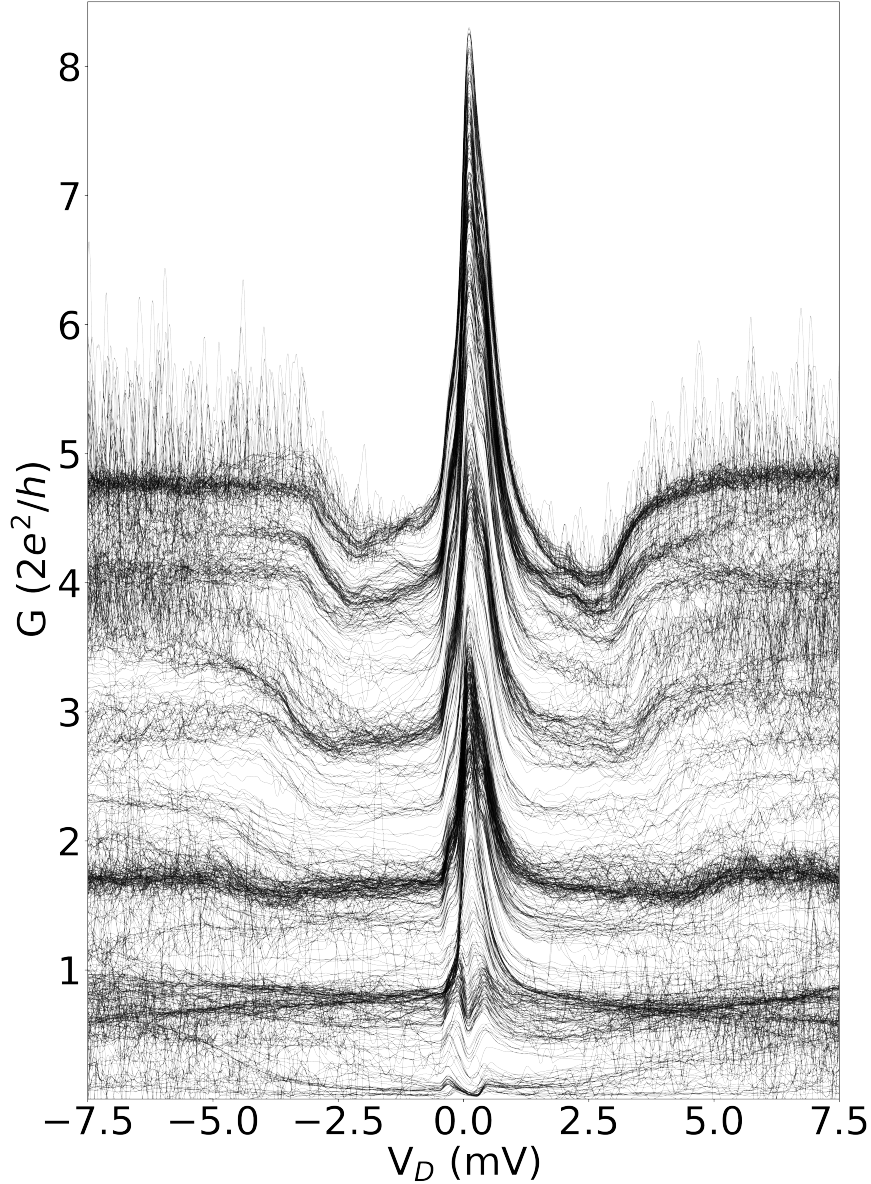


Figure 6.4 – Differential conductance (G) with series resistance of 370Ω subtracted waterfall plot from $V_G = 30 \text{ V}$ to -30 V in $167 \mu\text{V}$ steps measured at $T = 450 \text{ mK}$.

As a last remark, these low-temperature measurements were performed two and a half years after the measurements of Figure 6.2. Impressively, they still present conductance plateaus with only a slightly lower transparency of 86 %. This endorses the high quality of the devices. For easy comparison Figure 6.5 shows $G-V_G$ characteristic curves of the Ge/Si NW heterostructure extracted from $G(V_D, V_G)$ measurements made in the pumped ^3He set-up.

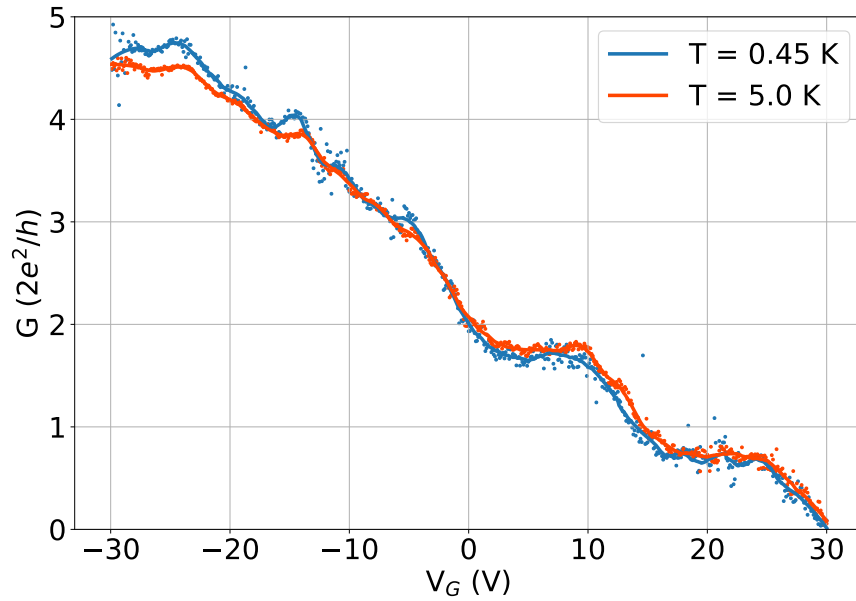


Figure 6.5 – G - V_G characteristic curves of the Al-Ge/Si-Al heterostructure device measured in the pumped ^3He set-up at $T = 0.45\text{ K}$ and $T = 0.5\text{ K}$. The curves were extracted from the $G(V_D, V_G)$ measurements by taking an average of V_D slices of $G(V_D, V_G)$ in the range $4.95\text{ mV} < V_D < 5.05\text{ mV}$, scatter plot. The average interface transparency of each conduction channel is approximately 86%. To smooth the data a Savitzky-Golay filter is applied (solid curve). In this measurement, V_G was swept from 30 V to -30 V.

6.4 Low Conductance Regime

In this section, we will consider the transport properties of the Al-Ge/Si-Al core/shell NW in the low conductance regime. The low conductance regime is reached by applying a large positive gate voltage V_G (see Figure 6.1). This regime is characterised by a small normal conductance G_N , which is less than the conductance quantum $G_0 = 2e^2/h$. However, in the low conductance regime, there is no evidence of Coulomb blockade effects suggesting the absence of a QD. This is contrary to the transport properties of the *i*-Ge NWs where clear Coulomb blockade was observed. This observation is supported by the significant conductivity outside the superconducting gap at $V_G = 28$ V of $0.3G_0$. Figure 6.6 shows I_D - V_D slices at $V_G = 28, 20$ and 10 V further revealing the transport dynamics in this regime. The linear nature of curve outside the superconducting gap further suggests an absence of Coulomb blockade with all non-linearities coming from the superconducting effects at low-energies, for $|V_D| < 400 \mu\text{V}$.

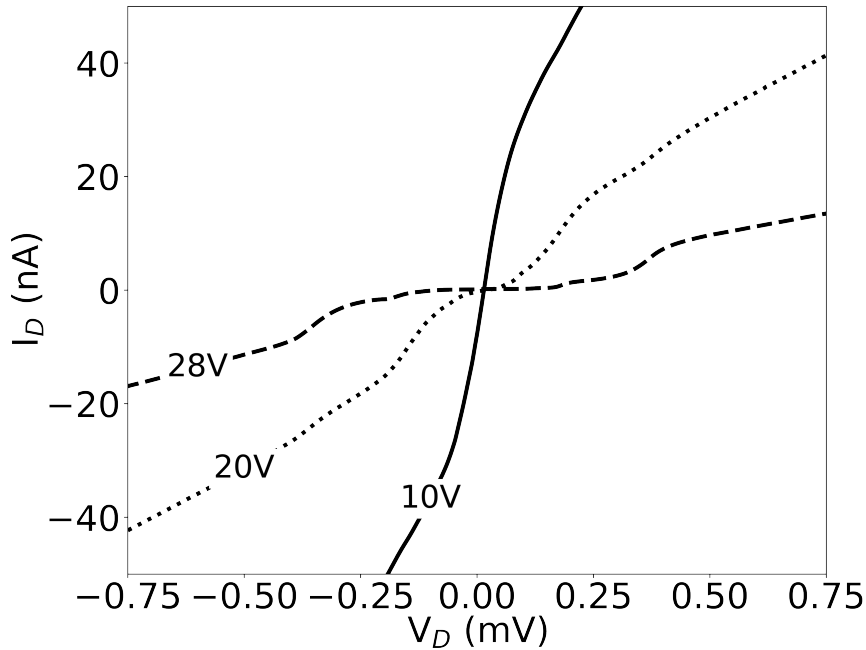


Figure 6.6 – I_D versus V_D for three different V_G (10, 20, 28 V) slices taken from Figure 6.1.

In the low conducting regime, $25 \text{ V} < V_G < 30 \text{ V}$, transport is significantly suppressed for energies within the superconducting gap. Figure 6.7 shows a G - V_D slice at $V_G = 28$ V. The conductance peaks seen in Figure 6.7 are associated with Andreev reflection and will be discussed in conjunction with the discussion of the high conductance regime. At low bias voltage $|V_D| < 100 \mu\text{V}$, we observe a suppression of conductance compared to the normal conductance G_N . The strength of this suppression, referred to in the literature as *gap hardness* is quantified by the ratio between the normal and sub-gap conductance: $\langle G_G \rangle / \langle G_N \rangle$ where $\langle G_G \rangle$ is the average conductance inside the gap and $\langle G_N \rangle$ is the average conductance outside the gap. We calculate the respective quantities by taking the average G across a V_D range from -0.05 to 0.05 mV for $\langle G_G \rangle$ and a V_D range from -0.7 to -0.6 mV for $\langle G_N \rangle$ for all the V_G slices in

the range $25 \text{ V} < V_G < 30 \text{ V}$. The rectangles overlaid on Figure 6.7 highlights the averaged regions. We determine a minimum gap ratio of $\langle G_G \rangle / \langle G_N \rangle = 0.03$.

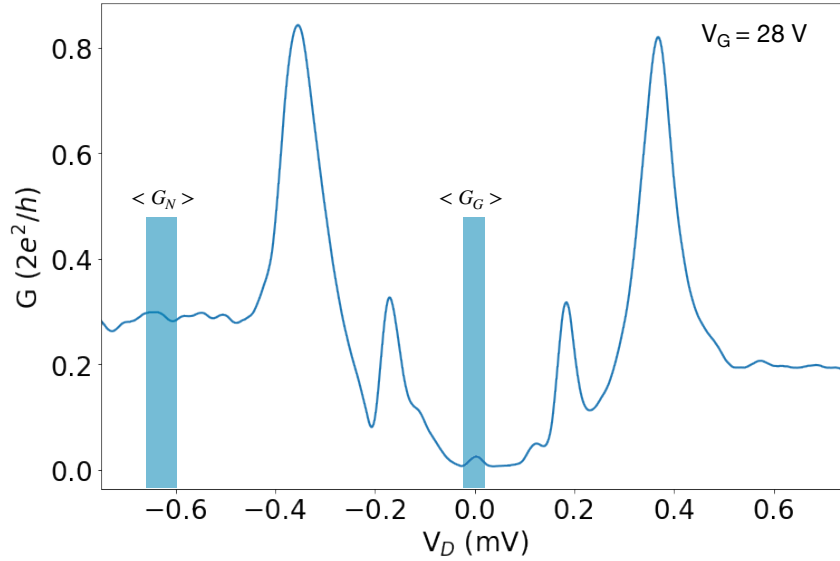


Figure 6.7 – Differential conductance slice (dI_D/dV_D) with respect to V_D for $V_G = 28 \text{ V}$ measured at 450 mK . The highlighted regions show where the average conductance is taken for each V_G slice to calculate the *gap hardness*.

6.5 High Conductance Regime

To investigate the high conductance regime, we carried out current biasing measurements in the range $-30 \text{ V} < V_G < 0 \text{ V}$ at $T = 420 \text{ mK}$. Figure 6.8 shows a density plot of the differential resistance $R = dV_D/dI_D$ versus I_D and V_G . For this measurement I_D was swept from -400 nA to 400 nA and the voltage drop across the device measured for each V_G . Similarly to the ultra-short *i*-Ge devices, a region of near-zero resistance centred around $I_D = 0 \text{ nA}$ begins to form as V_G becomes more negative. For $V_G < -20 \text{ V}$, this region becomes continuous (i.e. is not separated by regions of finite resistance) and extends through an extended V_G range. This suggests that there is a supercurrent regime where dissipationless supercurrent passes through the Ge/Si core/shell segment, as observed in the *i*-Ge NW heterostructures.

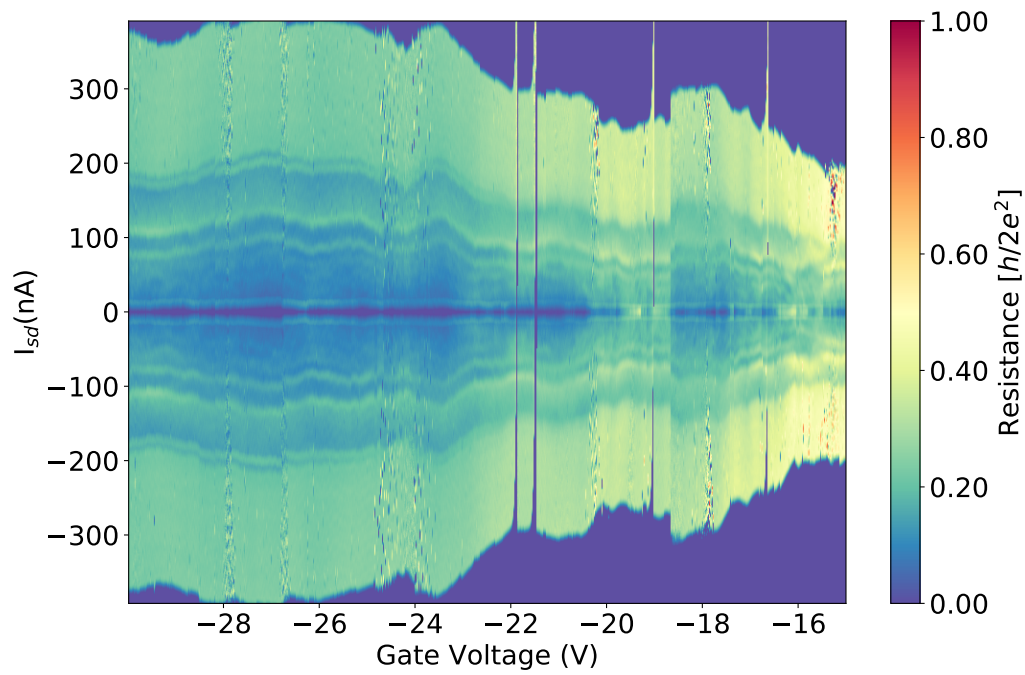


Figure 6.8 – Transport overview of superconducting regime. Density plots of differential resistance $R = dV_D/dI_D$ plotted in units of the quantum resistance versus I_D and V_G .

6.5 HIGH CONDUCTANCE REGIME

To further investigate the supercurrent regime, measurements were made with smaller I_D ranges. Figure 6.9 shows the differential resistance density plot where I_D was swept from -50 nA to 50 nA. In this Figure, we more clearly see the onset of supercurrent and the dependence of the critical current I_C on V_G .

These dynamics are illustrated further by insets of Figure 6.9. The lower inset shows a resistance slice at $I_D = 0$ nA. Between $V_G = 0$ V and -3 V, a regime of high zero-bias resistance, on the order of several quantum of resistance, is observed. As V_G decreases from -3 V, the zero-bias resistance of the device drops abruptly and finally converges to a small finite resistance of 25Ω . We attribute this finite resistance to thermally activated phase slips. Such phase slips are of significance in Josephson junctions, when the Josephson energy $E_J \approx 5 \times 10^{-24}$ J is on the order of the thermal energy $k_B T \approx 6 \times 10^{-24}$ J [60]. The Josephson energy is estimated by $E_J = \varphi_0 I_C / 2\pi$, where $\varphi_0 = h/2e$ is the magnetic flux quantum.

The upper inset highlights the dependence of I_C on V_G . It shows I_D - V_D characteristics of the heterostructure device for a selection of gate voltages, revealing the ability to tune I_C with an electrostatic field. We observe a maximum critical current of $I_C = 15$ nA, which saturates at $V_G = -25$ V.

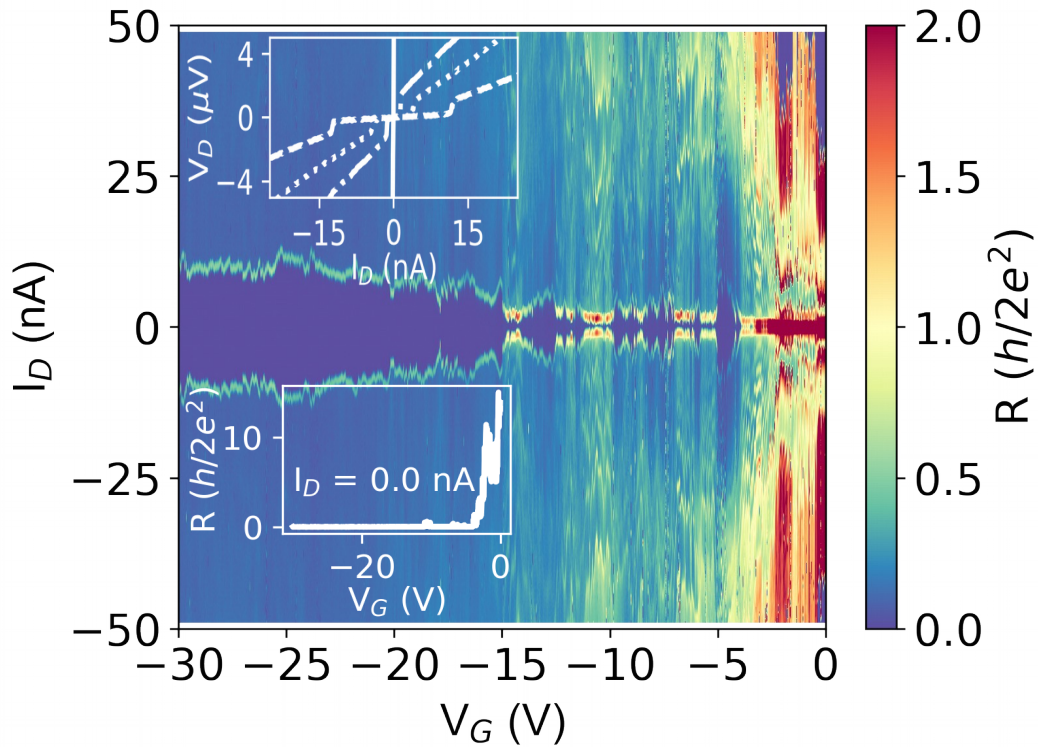


Figure 6.9 – (a) Differential resistance (dV_D/dI_D), with a wiring resistance of 370Ω subtracted, plotted in units of the quantum resistance versus I_D and V_G . I_D was swept from negative to positive and V_G from 0 V to -30 V measured at 420 mK. The dark blue regions correspond to zero resistance and indicate superconductivity induced into the Ge/Si core/shell channel. The upper inset shows V_D versus I_D for four different V_G (0, -10, -15, -29 V). The lower inset shows a slice of differential resistance (dV_D/dI_D) at $I_D = 0$ nA with respect to V_G .

Outside the low I_D bias region, clear resonant features that are continuous with respect to V_G are observed. The nature of these features that are symmetric about $I_D = 0$ nA and their similarities with those of Figure 5.27 suggests that they are due to MAR. Figure 6.10 shows a G - V_D slice at $V_G = -29.5$ V taken from Figure 6.8. Indeed, the features of the density plot appear as conductance peaks symmetric around a large conductance peak at $V_D = 0$ V. The main peak, which is larger than $200G_0$, corresponds to the *infinite conductivity* of the superconducting state of the Ge/Si core/shell channels. A comparison with the conductance peaks of the low conducting regime is also made in Figure 6.10 by plotting the G - V_D curve at $V_G = 28$ V. The V_D position of the peaks are compared to the expected peak position given by $V_D = \frac{2\Delta}{ne}$. In this case Δ/e is taken to be half of, $V_D = 0.37$ mV, the position of the first conductance peak ($n = 1$), giving $\Delta = 185 \mu\text{eV}$. Using this Δ , three consecutive conductance peaks of both G - V_D slices agree with their expected positions at $n = 1, 2, 3$ (see Figure 6.10). In the G - V_D slice at $V_G = -29.5$ V, further conductance peaks are observed at lower energy, $V_D < 0.1$ mV. These peaks line up with V_D positions expected for MAR of orders $n = 7$ & 12. However, as they do not appear consecutively after the first three peaks it is not possible to rule out other causes of the lower energy features. Interestingly, we observe a small conductance feature at 0.44 mV that would indicate a slightly larger superconducting gap of $220 \mu\text{eV}$.

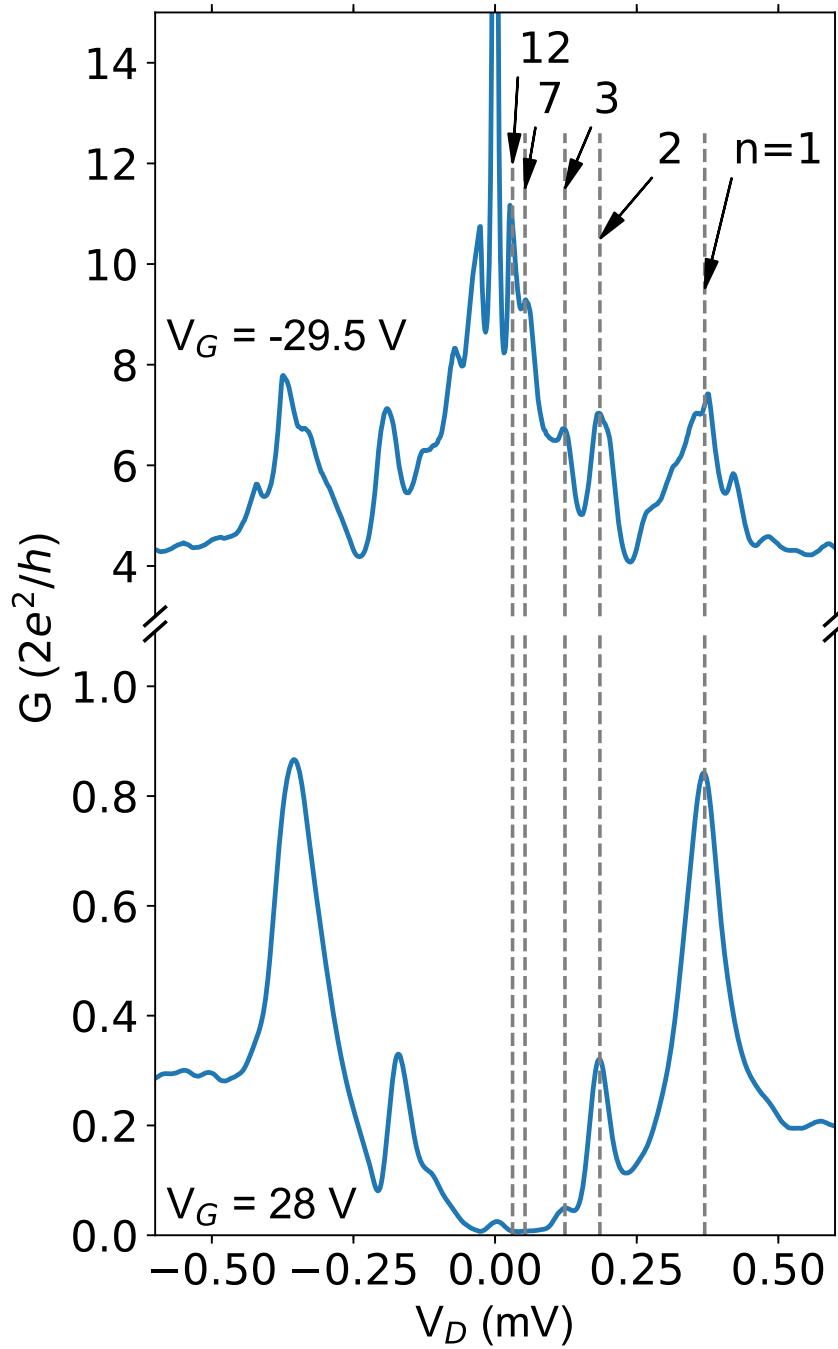


Figure 6.10 – Differential conductance slices (dI_D/dV_D) with respect to V_D for $V_G = -29.5$ V and 28 V measured at 450 mK. Vertical dashed lines at $V_D = \frac{2\Delta}{ne}$ show the expected position of conductance peaks due to MAR for $\Delta = 185\mu\text{eV}$.

The alignment of the MAR conductance peaks in Figure 6.10 agrees with the stability of the conductance resonances, with respect to V_G , shown in Figure 6.1. The remarkable stability of the MARs through 60 V of gate tuning further endorses the exceptional interface quality that has been achieved. To estimate the interface transparency, we again make use of the BTK model. The normal resistance R_N is calculated by fitting V_D - I_D curves in the linear regime above the superconducting gap ($|eV_D| > 2\Delta$) with the excess current I_{exc} being determined as the x-axis intercept ($V_D = 0$ V) of the linear fit. This was carried out for all gate voltages satisfying $V_G < 0$ V where we observe R_N converging to 2.98 k Ω at $V_G = -25$ V. Figure 6.11 shows an example of the fitting procedure. Applying the BTK model, we retrieve a barrier strength of $Z = 0.1$, giving an estimate of the transparency of 99 %, which is consistent with the transparency calculated from the quantised conductance.

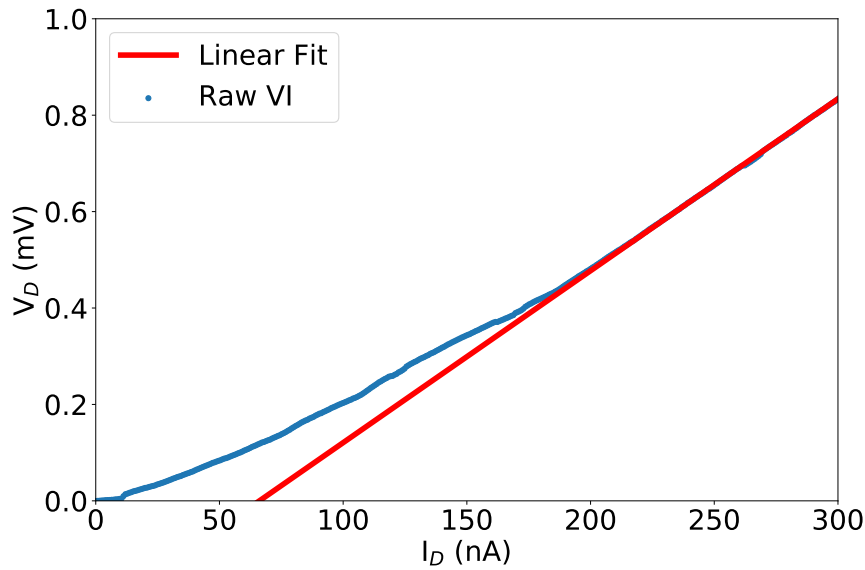


Figure 6.11 – Raw V_D - I_D curve at $V_G = -29$ V and linear fit of the curve in the normal regime $V_D > 2\Delta/e$. From the linear fit, R_N and I_{exc} is determined. $R_N = 3.6$ k Ω is the gradient of linear fit and $I_{exc} = 66$ nA is the x-axis intercept.

6.6 Conclusion

In this chapter, we have discussed the transport properties of a Al-Ge/Si-Al core/shell nanowire heterostructure with a Ge/Si core/shell segment length of 40 nm. This work has been published in ACS Nano, see Ref. [137]. In Section 6.3, we revealed the observation of quantised conductance, which suggests that we are observing quantum ballistic transport. Using the Landauer formula, we estimated an average interface transparency greater than 96 %. Low temperature measurements at highly negative V_G , revealed similarities to the Al-Ge-Al devices, including gate tuneable supercurrent up to 15 nA at 420 mK and stable MAR up to third order. High interface transparency, estimated by applying the BTK model to the MAR I_D - V_D curves, further endorses the great quality of these Al-Ge/Si-Al core/shell nanowire heterostructures. We showed that by applying a large positive gate voltage, we could enter the low conductance regime. In this regime, we observed a low energy transport gap with a gap ratio

6.6 CONCLUSION

of $\langle G_G \rangle / \langle G_N \rangle = 0.03$, which is promising for the observation of sub-gap modes, including Majorana zero modes [86]. Moreover, the absence of Coulomb blockade effects in the transport properties of this device, suggests that there is an Ohmic contact between the Al and Ge/Si core/shell. The existence of an Ohmic contact, not only affirms the great device quality and high contact transparency, which is necessary for quantum devices, but also demonstrates a significant divergence between the Ge/Si core/shell and intrinsic Ge (i-Ge) devices.

Conclusion & Perspectives

7

7.1 Conclusion

In this thesis, we have presented the results of our investigations of the low temperature transport properties of novel superconducting hybrid junctions, based on germanium nanowires. These impressive devices were fabricated by our collaborators in Vienna using a selective, thermally induced Al-Ge substitution process [34]. This process enables the fabrication of monolithic Al-Ge-Al nanowire heterostructures. These nanowires feature crystalline Al (c-Al) leads connected to a crystalline Ge segment, by near atomically abrupt interfaces [33]. Two kinds of Ge nanowire heterostructures have been investigated in this thesis; intrinsic Ge (i-Ge) nanowires passivated by a thin shell of Al₂O₃ and Ge/Si core/shell nanowires. Material characterisation of these devices, carried out by our collaborators, has revealed the high purity of the c-Al leads and Ge segment [32, 107]. Their demonstration of the high quality of these devices was one of our motivations to carry out low temperature investigations.

Succinctly, we have demonstrated that these remarkable devices, do indeed have promising transport characteristics. We have shown that the Al-Ge-Al nanowire heterostructures, with i-Ge segment lengths of 40 nm, can be tuned from a completely insulating regime, through a low conductive regime that exhibits properties of a single-hole filling quantum dot, to a supercurrent regime [134]. We attributed this dynamic transport to the band structure of the Al-Ge-Al nanowire heterostructure. The band structure, defined by a back-to-back Schottky barrier, is highly tuneable, allowing access to multiple transport regimes. In this thesis, we reported on three major transport regimes; the Coulomb blockade regime, the supercurrent regime and the intermediate regime. We showed that these regimes can be defined in terms of the characteristic energies of the device. In the Coulomb blockade regime, $E_C \gg \Delta > \Gamma$, whereas in the superconducting regime, $\Gamma \gg \Delta, E_C$ and in the intermediate regime $\Gamma \sim \Delta \lesssim E_C$.

Analysis of the Coulomb blockade regime, revealed a significant gate dependence on the addition energy of the Ge quantum dot [135, 134]. The decreasing addition energy, as the back-gate voltage V_G became more negative, was associated with the decreasing charging energy E_C . E_C decreased as the size of the QD increased as V_G became more negative. In this regime, we also observed evidence of quantum confinement on Ge's hole states. This included the even-odd effect and resonant tunnelling through excited states. These results demonstrate the strong confinement effects provided by the small diameter of the Ge nanowires of approximately 25 nm. These

[Link back to Table of contents →](#)

quantum features endorses the potential of Al-Ge-Al nanowire heterostructures as quantum devices.

In the supercurrent regime, at large negative V_G , we observed gate tuneable supercurrent up to 10 nA, leading to a Josephson field effect transistor. The confirmation of gate tuneable Josephson current in Al-Ge-Al nanowire heterostructures, makes these devices, to the best of our knowledge, the first superconducting-semiconducting Josephson junctions based on intrinsic germanium. Furthermore, we described the observation of sub-gap conductance peaks due to multiple Andreev reflection (MAR). Fits to the non-linear I_D - V_D curves, in this regime, revealed high interface transparencies of up to 96 % for the first conducting channel. This high transparency suggests that the Schottky barriers, which had a dominating effect on the transport in the Coulomb blockade regime, have been tuned away by the back-gate.

Between the Coulomb blockade and superconducting regimes, we observed the intermediate regime. Here, we observed significant transport features within the superconducting gap. However, the bell-shape nature of these conductance features suggested that they had more complex origins than standard MAR. We attributed these features to a combination of MAR and resonant tunneling through the quantum dot. The cause of the intriguing asymmetry with respect to V_D and quantum dot parity, observed in this regime, requires further investigation.

Transport investigations of a Al-Ge/Si-Al core/shell nanowire heterostructure with a Ge/Si core/shell segment length of 40 nm [137], revealed similarities and differences to the i-Ge devices. Observations of stable MAR and quantized conductance affirmed the great quality of the interface and a high contact transparency, which was estimated to be greater than 96 %. Similar to the i-Ge devices, we observed gate tuneable supercurrent up to 15 nA, in the Ge/Si core/shell device. By applying a large positive gate voltage, we could enter the low conductance regime. In this regime, we observed a low energy transport gap, with a gap ratio of $\langle G_G \rangle / \langle G_N \rangle = 0.03$, which is promising for the observation of sub-gap modes, including Majorana zero modes [86]. Contrary to the i-Ge nanowire devices, we did not observe Coulomb blockade in this regime. This suggests that there is an Ohmic contact between Al and the Ge/Si core/shell nanowire. An Ohmic contact implies that the Si shell has modified the Schottky barrier, to the extent where it is unobservable in our measurements. Further investigation is required to fully understand the effect of the Si shell on the Schottky barrier.

The results presented in this thesis, demonstrates the potential of these novel germanium nanowire based superconducting-semiconducting hybrid junctions as quantum devices and for the study of quantum phenomena. In particular, the impressive tuneability and high quality of the Al-Ge devices enables the investigation of the rich physics provided by the subtle interplay between Coulomb blockade and Andreev mediated superconductivity. These results add further weight to the growing evidence that Ge has significant potential as a key material in future quantum experiments and technologies [138].

7.2 Perspectives

The diverse transport properties of our germanium nanowire based superconducting-semiconducting hybrid junctions motivates further experimental investigation. Future investigations should include high magnetic field measurements at dilution refrigerator temperatures (20 mK). By reducing the temperature, we would expect to observe an

improvement on the signal to noise ratio due to the reduced electron temperature. Furthermore, the device may become more stable due to the freezing out of surface charges that result in charge jumps. A reduced temperature, would help towards understanding if the relatively low critical current measured in the our devices is suppressed due to the high working temperature of 400 mK.

The application of a high magnetic field would provide a mechanism to investigate the effects of charge spin on the Ge quantum dot. By lifting the spin degeneracy, the observation of single hole filling, suggested by the even-odd effect, could be confirmed. Moreover, the magnetic field can be used to examine the origins of the higher energy conductance resonances that were attributed to excited state tunnelling. In the intermediate regime the magnetic field could be used to help understand the asymmetry of the negative differential conductance, with respect to V_D and quantum dot parity. By using a magnetic field, we could investigate if spin-orbit coupling is responsible for this asymmetry. Furthermore, we could use the magnetic field to remove superconductivity, allowing one to investigate the Kondo effect more easily. It is understood that superconductivity strongly suppresses the Kondo effect [75]. Finally, a high magnetic field could be used to investigate whether we can observe Majorana bound states in these superconducting hybrid junctions [88].

Beyond further experimental investigations, we could integrate these Ge nanowire based superconducting hybrid junctions into quantum devices such as a gate tuneable transmon qubit, known as a gatemon. We have begun preliminary measurements on a Ge/Si core/shell transmon, which was fabricated by our collaborators in Vienna. The transmon consists of a Al-Ge/Si-Al core/shell nanowire heterostructure, with a Ge/Si segment length of 20 nm, shunted by a capacitance provided by two large Al contact pads. The device is fabricated on an un-doped Si wafer to reduce damping of the resonator due to the wafer's finite resistance. The device is installed in a 3D cavity, which acts as the resonator, which couples to the transmon. Through the microwave resonator qubit control and readout can be performed. In the current set-up we do not have the ability to tune the density of charge carries in the Ge/Si core/shell segment. However, preliminary measurements produced interesting results. We observed an increase in the cavity resonance as the microwave drive power of the single-tone spectroscopy was increased. This is evidence of the cavity interacting with a non-linear element, possibly the transmon. Furthermore, we observed some evidence of qubit transitions in two-tone spectroscopy measurements. However, extra cavity resonances were observed near the estimated qubit frequency. These extra resonances must be understood and further measurements carried out before a claim of a Ge/Si core/shell transmon qubit can be made. Furthermore, I strongly suggest that a gate field is introduced, which will enable the charge carrier density of the Ge/Si core/shell segment to be tuned, which would improve future experiments.

Appendices

Introduction to BCS theory



Leon Cooper's discovery, in 1956, that the ground state of a Fermi sea is unstable in the presence of an attractive electronic potential, became the basis of the microscopic description of superconductivity (BCS theory) [60]. Defined as a Cooper pair, this lower energy electron bound state, is guaranteed to form in an electronic system at $T = 0$, with attractive interaction, irrelevant of its strength.

The formation of a lower energy ground state can be understood by considering two electrons, with energies above the Fermi energy E_F . Suppose these electrons experience a small local attractive interaction between themselves and are added to the Fermi sea. Further, it is assumed that the additional particles do not interact with the Fermi sea, except for obeying Pauli's exclusion principle. By Bloch's theorem, the minimum energy state must have net zero momentum. Therefore, the two new particles must have equal and opposite momentum. By taking into account the antisymmetry of electron exchange due to the Fermion statistics of electrons. A two-electron singlet wavefunction can be built to describe the two particle system,

$$\psi(\vec{r}_1 - \vec{r}_2) = \left[\sum_{\vec{k} > k_F} g_{\vec{k}} \cos(\vec{k} \cdot (\vec{r}_1 - \vec{r}_2)) \right] (\alpha_1 \beta_2 - \beta_1 \alpha_2), \quad (\text{A.1})$$

where α and β represent the spin up and spin down configurations respectively. The weighting coefficient $g_{\vec{k}}$ is related to the interaction potential $V_{\vec{k}\vec{k}'}$ between the two electrons by

$$(E - 2\epsilon_{\vec{k}})g_{\vec{k}} = \sum_{\vec{k}' > k_F} V_{\vec{k}\vec{k}'} g_{\vec{k}'}, \quad (\text{A.2})$$

where, $\epsilon_{\vec{k}}$ are the eigenenergies of the unperturbed electron states. The electron eigenstates are plane waves as discussed above. Whereas, E is the energy of the electron pair. By solving this expression, one can determine $g_{\vec{k}}$ and E . Importantly, a bound-pair state forms if there exists a set of $g_{\vec{k}}$ with $E < 2E_F$.

To solve Eq. A.2, Cooper assumed a constant and attractive interaction potential of $V_{\vec{k}\vec{k}'} = -V$, for all \vec{k} states up to a cutoff energy of $\hbar\omega_D$ above E_F and zero otherwise. Here, ω_D is the Debye frequency of the solid, which is the frequency of the phonon whose wavelength is the size of the lattice unit cell. In aluminium, the Debye

[Link back to Table of contents](#) →

frequency is approximately 10 THz. This simplifies Eq. A.2 to

$$g_{\vec{k}} = V \frac{\sum g_{\vec{k}'}}{2\epsilon_{\vec{k}} - E}. \quad (\text{A.3})$$

This allows one to determine the eigenenergy of the bound state in the weak coupling case $\rho(0)V \ll 1$, where $\rho(0)$ is the density of states near E_F , to be

$$E \approx 2E_F - 2\hbar\omega_D e^{-2/\rho(0)V}. \quad (\text{A.4})$$

This result reveals that two electrons with $k > k_F$ form a bound state with lower energy than E_F , independent of the magnitude of the attractive potential V . This makes the normal ground state unstable.

Examination of the wavefunction, reveals that the probability of a bound state forming, is proportional to the weighting factor $(2\xi_{\vec{k}} + E')^{-1}$, where $\xi_{\vec{k}} = \epsilon_{\vec{k}} - E_F$ is the particle energy relative to the Fermi energy and $E' = 2E_F - E > 0$ is the binding energy relative to $2E_F$. Therefore, the maximum probability (max weighting factor = $\frac{1}{E'}$) occurs for particles around E_F . As $E' \ll \hbar\omega_D$ for $\rho(0)V < 1$, the weighting factor quickly decays for particles above E_F . Therefore, there is a small window where binding occurs, which justifies the approximation of the constant interaction potential. Further, this small binding window agrees with Pippard's description of the Cooper pair size, with a minimum size of $\sim \hbar v_F / E'$, where v_F is the Fermi velocity. As $k_B T_c \sim E'$, the size of the Cooper pair is $\xi_0 = \hbar v_F / k_B T_c$, where T_c is the temperature at which the superconducting condensate forms, known as the critical temperature.

The source of the attractive potential between electrons, required for pairing, was not obvious, especially given the strong repulsive nature of Coulomb interaction. Frölich suggested in 1950 that electron-ion interactions could result in an attractive potential sufficient to overcome Coulomb repulsion [60].

With the discovery of the existence of a Cooper pair and the possibility of having an electronic system with an attractive interaction, the next challenge was expanding this to many Cooper pairs. The number of Cooper pairs in a superconducting metal must reach a finite maximum, after which there is no energy gain by the addition of another pair. This large number of Cooper pairs would clearly change the Fermi sea, thus treating bound pairs independently from the Fermi sea, could not be maintained.

To model this complex system, Bardeen, Cooper and Schrieffer exploited second quantisation of quantum mechanics to develop the BCS wavefunction. Second quantisation is a powerful tool when dealing with many-particle systems of bosons or fermions. In the fermionic case; the anti-symmetry, must be maintained for an N-electron system. Through the use of creation (annihilation) operators, the workhorse of second quantisation, which create (destroy) particles, many-body quantum states are built while maintaining their symmetric or anti-symmetric nature.

The key second quantisation operators used for electronic systems including superconductors are as follows:

- $\hat{c}_{\vec{k}\uparrow}^\dagger$ **creation operator**: Creates a fermion with momentum \vec{k} and spin $\frac{1}{2}$ (up).
- $\hat{c}_{\vec{k}\downarrow}$ **annihilation operator**: Destroys a fermion with momentum \vec{k} and spin $-\frac{1}{2}$ (down).

- $\hat{n}_{\vec{k}\sigma} = \hat{c}_{\vec{k}\sigma}^\dagger \hat{c}_{\vec{k}\sigma}$ **particle number operator**: counts the number of particles with momentum \vec{k} and spin $\sigma = \uparrow, \downarrow$.

Importantly, the fermionic operators must obey the anti-commutator relation

$$\{\hat{c}_{\vec{k}\sigma}, \hat{c}_{\vec{k}'\sigma'}^\dagger\} = \delta_{\vec{k}\vec{k}'} \delta_{\sigma\sigma'}, \quad (\text{A.5})$$

where $\delta_{i,j}$ is the Kronecker delta, defined as

$$\delta_{i,j} = \begin{cases} 0 & \text{if } i \neq j \\ 1 & \text{if } i = j. \end{cases} \quad (\text{A.6})$$

In the formalism of second quantisation, the two-electron singlet wavefunction of Eq. A.1 is written as

$$|\psi_0\rangle = \sum_{\vec{k} > \vec{k}_F} g_{\vec{k}} \hat{c}_{\vec{k}\uparrow}^\dagger \hat{c}_{-\vec{k}\downarrow}^\dagger |F\rangle, \quad (\text{A.7})$$

where $|F\rangle$ is the Fermi sea where all states are filled to \vec{k}_F . Expanding this to an N -electron wavefunction

$$|\psi_N\rangle = \sum_{\vec{k}} g(\vec{k}_i \dots \vec{k}_\ell) \hat{c}_{\vec{k}_i\uparrow}^\dagger \hat{c}_{-\vec{k}_i\downarrow}^\dagger \dots \hat{c}_{\vec{k}_\ell\uparrow}^\dagger \hat{c}_{-\vec{k}_\ell\downarrow}^\dagger |\phi_0\rangle, \quad (\text{A.8})$$

where $|\phi_0\rangle$ is the vacuum state, the complexity becomes clear. Given the large number of possible ways to achieve $N/2$ pairs, determining $g(\vec{k}_i \dots \vec{k}_\ell)$ is a near impossible task.

This is where the ingenuity of BCS theory comes to light; by using the mean-field approximation, where the occupancy of a \vec{k} state is dependent on the average occupancy of other states, the particle number N can be treated statistically and thus Cooper pair occupancy can also be treated statistically. This approach results in the BCS ground state of

$$|\psi_G\rangle = \prod_{\vec{k}} (u_{\vec{k}} + v_{\vec{k}} \hat{c}_{\vec{k}\uparrow}^\dagger \hat{c}_{-\vec{k}\downarrow}^\dagger) |\phi_0\rangle, \quad (\text{A.9})$$

where $|v_{\vec{k}}|^2$ is the probability that a pair ($\vec{k} \uparrow, -\vec{k} \downarrow$) is occupied, whereas the probability of not being occupied is $|u_{\vec{k}}|^2$. By the nature of probabilities, the condition $|u_{\vec{k}}|^2 + |v_{\vec{k}}|^2 = 1$ must be met.

For finite $u_{\vec{k}}$ and $v_{\vec{k}}$ there is a finite probability of any number of free particles M from 0 to $2N$ where N is the number of Cooper pairs. However the coefficients peak at the average number of Cooper pairs given by

$$\bar{N} = \sum_{\vec{k}} 2|v_{\vec{k}}|^2. \quad (\text{A.10})$$

Through the Heisenberg uncertainty principle an important relationship between Cooper pair number N and superconducting phase φ can be made

$$\Delta N \Delta \varphi \geq \frac{1}{2} \quad (\text{A.11})$$

To determine fully the ground state of Eq. A.9, one must calculate $u_{\vec{k}}$ and $v_{\vec{k}}$. This is achieved by minimising the expectation value of the "pairing Hamiltonian" or "reduced Hamiltonian" with respect to the system in the ground state. That is

$$\delta \langle \psi_G | \hat{H} | \psi_G \rangle = 0, \quad (\text{A.12})$$

where \hat{H} is the pairing Hamiltonian, where the chemical potential μ is taken to be the point of zero kinetic energy:

$$\hat{H} = \sum_{k, \sigma=\uparrow, \downarrow} \xi_{\vec{k}\sigma} \hat{c}_{\vec{k}\sigma}^\dagger \hat{c}_{\vec{k}\sigma} + \sum_{\vec{k}, \vec{k}'} V_{\vec{k}\vec{k}'} \hat{c}_{\vec{k}\uparrow}^\dagger \hat{c}_{-\vec{k}\downarrow}^\dagger \hat{c}_{\vec{k}'\uparrow} \hat{c}_{-\vec{k}'\downarrow}, \quad (\text{A.13})$$

where, $\xi_{\vec{k}} = \epsilon_{\vec{k}} - \mu$, is the energy of the particle state above μ .

In the original BCS paper, a variational method was taken to determine the coefficients: $u_{\vec{k}}$ and $v_{\vec{k}}$. However, in this thesis I will take another approach, that was developed after BCS theory but achieves the same result. This method uses a canonical transformation.

In its current form, the pairing Hamiltonian of Eq. A.13 has a quartic term in the interaction component, making it overly complex to solve. By introducing a mean-field approximation, the interaction can be simplified into a bilinear form, where the creation and annihilation of pairs of Bloch states ($\vec{k} \uparrow, -\vec{k} \downarrow$) are separated.

The mean-field approximation is justified by the phase-coherence of the BCS ground state. For more details on the mean-field approximation, see Ref. [60]. In this approximation, one defines the parameter,

$$\Delta_{\vec{k}} = - \sum_{\vec{\ell}} V_{\vec{k}\vec{\ell}} \langle \hat{c}_{-\vec{k}\downarrow} \hat{c}_{\vec{\ell}\uparrow} \rangle. \quad (\text{A.14})$$

$\Delta_{\vec{k}}$ has similarities to the order parameter introduced in Ginzburg-Landau theory of superconductivity. For superconductors with s-wave pairing, such as aluminium, the order parameter is defined by $\Delta_{\vec{k}} = |\Delta| e^{i\varphi}$, where φ is the superconducting phase.

By introducing the order parameter into the quartic term of the pairing Hamiltonian and relabeling the subscripts, one gets a simpler BCS Hamiltonian

$$\hat{H} = \sum_{\vec{k}, \sigma=\uparrow, \downarrow} \xi_{\vec{k}\sigma} \hat{c}_{\vec{k}\sigma}^\dagger \hat{c}_{\vec{k}\sigma} - \sum_{\vec{k}} \left(\Delta_{\vec{k}}^\dagger \hat{c}_{-\vec{k}\downarrow} \hat{c}_{\vec{k}\uparrow} + \Delta_{\vec{k}} \hat{c}_{\vec{k}\uparrow}^\dagger \hat{c}_{-\vec{k}\downarrow}^\dagger - \Delta_{\vec{k}} \langle \hat{c}_{\vec{k}\uparrow}^\dagger \hat{c}_{-\vec{k}\downarrow}^\dagger \rangle \right). \quad (\text{A.15})$$

The simplified \hat{H} is then diagonalised using the canonical transformation. This transformation was used by Bogliubov and Valatin independently but has become to be known as the Bogoliubov transformation. In the canonical transformation the particle creation $\hat{c}_{\vec{k}\uparrow}^\dagger, \hat{c}_{-\vec{k}\downarrow}^\dagger$ and annihilation $\hat{c}_{\vec{k}\uparrow}, \hat{c}_{-\vec{k}\downarrow}$ operators in terms of creation $\gamma_{\vec{k}\sigma}^\dagger$ and annihilation $\gamma_{\vec{k}\sigma}$ operators of quasiparticle excitations, given by:

$$\hat{c}_{\vec{k}\uparrow} = u_{\vec{k}}^* \gamma_{\vec{k}\uparrow} + v_{\vec{k}} \gamma_{\vec{k}\downarrow}^\dagger \quad \hat{c}_{-\vec{k}\downarrow} = u_{\vec{k}}^* \gamma_{\vec{k}\downarrow} - v_{\vec{k}} \gamma_{\vec{k}\uparrow}^\dagger \quad (\text{A.16})$$

$$\hat{c}_{-\vec{k}\downarrow}^\dagger = -v_{\vec{k}}^* \gamma_{\vec{k}\uparrow} + u_{\vec{k}} \gamma_{\vec{k}\downarrow}^\dagger \quad \hat{c}_{\vec{k}\uparrow}^\dagger = v_{\vec{k}}^* \gamma_{\vec{k}\downarrow} + u_{\vec{k}} \gamma_{\vec{k}\uparrow}^\dagger. \quad (\text{A.17})$$

with the canonical transformation the diagonalised Hamiltonian becomes

$$\hat{H} = \sum_{\vec{k}} (E_{\vec{k}} \hat{\gamma}_{\vec{k}\uparrow}^\dagger \hat{\gamma}_{\vec{k}\uparrow} + E_{\vec{k}} \hat{\gamma}_{\vec{k}\downarrow}^\dagger \hat{\gamma}_{\vec{k}\downarrow}) + \sum_{\vec{k}} (\xi_{\vec{k}} - E_{\vec{k}} + \Delta_{\vec{k}} \langle \hat{c}_{\vec{k}\uparrow}^\dagger \hat{c}_{-\vec{k}\downarrow}^\dagger \rangle), \quad (\text{A.18})$$

with the condition that

$$2\xi_{\vec{k}} u_{\vec{k}} v_{\vec{k}} + \Delta_{\vec{k}}^* v_{\vec{k}}^2 - \Delta_{\vec{k}} u_{\vec{k}}^2 = 0, \quad (\text{A.19})$$

where $E_{\vec{k}} = \sqrt{(\xi_{\vec{k}}^2 + |\Delta_{\vec{k}}|^2)}$. By solving the conditional statement of the diagonalised \hat{H} the coefficients are found to be

$$|v_{\vec{k}}|^2 = 1 - |u_{\vec{k}}|^2 = \frac{1}{2} \left(1 - \frac{\xi_{\vec{k}}}{E_{\vec{k}}} \right), \quad (\text{A.20})$$

which is in agreement with the original variational method of BCS. The order parameter $\Delta_{\vec{k}}$, defined in the mean-field approximation, is found self consistently using the Bogliubov transformations

$$\Delta_{\vec{k}} = - \sum_{\vec{\ell}} V_{\vec{k}\vec{\ell}} u_{\vec{\ell}}^* v_{\vec{\ell}} \left(1 - \langle \hat{\gamma}_{\vec{\ell}\uparrow}^\dagger \hat{\gamma}_{\vec{\ell}\uparrow} \rangle \langle \hat{\gamma}_{\vec{\ell}\downarrow}^\dagger \hat{\gamma}_{\vec{\ell}\downarrow} \rangle \right). \quad (\text{A.21})$$

At $T = 0$ K, when there are no quasiparticle excitations, the order parameter reduces to the same expression as that in the variational method, given by

$$\Delta = \frac{\hbar\omega_D}{\sinh(1/\rho(0)V)} \approx 2\hbar\omega_D e^{-1/\rho(0)V}. \quad (\text{A.22})$$

Eq. A.21 shows that the superconducting gap is dependent on the state of the system, thus depends on how many quasiparticles exist.

Returning to the Hamiltonian of Eq. A.18, we can gain an understanding of how it describes the system. The sum on the right of Eq. A.18 is a constant, which differs from the normal state at $T = 0$ K, where $\Delta_{\vec{k}} = 0$, by the condensation energy of the superconducting state. Therefore we can express Eq. A.18 as

$$\hat{H} = \sum_{\vec{k}} (E_{\vec{k}} \hat{\gamma}_{\vec{k}\uparrow}^\dagger \hat{\gamma}_{\vec{k}\uparrow} + E_{\vec{k}} \hat{\gamma}_{\vec{k}\downarrow}^\dagger \hat{\gamma}_{\vec{k}\downarrow}) + \Xi, \quad (\text{A.23})$$

where Ξ can be considered as a constant offset energy. The Hamiltonian now describes the superconducting system in terms of energy above the ground-state due to quasiparticle like excitations of the system. These one-particle like excitations are referred to as Bogoliubons, as they come from the Bogoliubov transformation.

The two possible Bogoliubons $\hat{\gamma}_{\vec{k}\uparrow}$ and $\hat{\gamma}_{\vec{k}\downarrow}$, each increase the system energy by $E_{\vec{k}} = \sqrt{(\xi_{\vec{k}}^2 + |\Delta_{\vec{k}}|^2)}$. A Bogoliubon introduces a linear superposition of electron and holes into the system. However, their effect on the total momentum $\sum_{\vec{k}} \vec{k}$ and spin S_z of the system is different. $\hat{\gamma}_{\vec{k}\uparrow}^\dagger$ either creates a Fermion with momentum $+\vec{k}$ and spin 1/2 (up) or destroys a Fermion with $-\vec{k}$ and spin -1/2 (down). Therefore, $\hat{\gamma}_{\vec{k}\uparrow}^\dagger$ has the net result of increasing the system momentum by \vec{k} and increasing S_z by $\hbar/2$. On the other hand $\hat{\gamma}_{\vec{k}\downarrow}^\dagger$, has the opposite effect; reducing the system momentum and total

spin by \vec{k} and $\hbar/2$, respectively. This shift is either achieved by creating a Fermion with $-\vec{k}$ and spin $-1/2$ (down) or destroying a Fermion with $+\vec{k}$ and spin $1/2$ (up).

For instance, $\hat{\gamma}_{\vec{k}\uparrow}^\dagger \hat{\gamma}_{\vec{k}\uparrow}$ counts the number of spin-up quasi-particles (excitations that increase momentum and spin). Whereas, $\hat{\gamma}_{\vec{k}\downarrow}^\dagger \hat{\gamma}_{\vec{k}\downarrow}$ counts the number of spin-down quasi-particles (excitations that decrease momentum and spin). However, both excitations introduce the same additional energy to the system. Inspecting $E_{\vec{k}}$, we see that $\Delta_{\vec{k}}$ acts as the minimum energy required for an excitation to occur. Supposing a quasi-particle is created at the Fermi surface, where the minimum energy given all other states are filled at $T = 0$. Then $\xi_{\vec{k}} = 0$ and the eigenenergy is $E_{\vec{k}} = |\Delta_{\vec{k}}| > 0$, which is the minimum energy.

At finite temperature, the order parameter can be derived using the Fermi-Dirac function Eq. 2.15. The Fermi-Dirac equation defines the probability of quasi-particle excitation at temperature T . For $T > 0$, $\Delta_{\vec{k}}$ becomes,

$$\Delta_{\vec{k}} = - \sum_{\vec{\ell}} V_{\vec{k}\vec{\ell}} u_{\vec{\ell}}^* v_{\vec{\ell}} \left(1 - \langle \hat{\gamma}_{\vec{\ell}\uparrow}^\dagger \hat{\gamma}_{\vec{\ell}\uparrow} \rangle \langle \hat{\gamma}_{\vec{\ell}\downarrow}^\dagger \hat{\gamma}_{\vec{\ell}\downarrow} \rangle \right) \quad (\text{A.24})$$

$$= - \sum_{\vec{\ell}} V_{\vec{k}\vec{\ell}} u_{\vec{\ell}}^* v_{\vec{\ell}} \left[1 - 2f(E_{\vec{\ell}}) \right] \quad (\text{A.25})$$

$$= - \sum_{\vec{\ell}} V_{\vec{k}\vec{\ell}} \frac{\Delta_{\vec{\ell}}}{2E_{\vec{\ell}}} \tanh \frac{\beta E_{\vec{\ell}}}{2}, \quad (\text{A.26})$$

where $\beta = k_B T$. Using the BCS approximation of a constant negative interaction potential ($V_{\vec{k}\vec{\ell}} = -V$) which leads to $\Delta_{\vec{k}} = \Delta_{\vec{\ell}}$ the self consistency equation at finite temperature becomes

$$\frac{1}{V} = \frac{1}{2} \sum_{\vec{k}} \frac{\tanh \frac{\beta E_{\vec{k}}}{2}}{E_{\vec{k}}}. \quad (\text{A.27})$$

Determination of T_c

The critical temperature (T_c) is defined as the temperature at which $\Delta(T) \rightarrow 0$. By substituting $E_{\vec{k}} = |\xi_{\vec{k}}|$ into Eq. A.27 and solving by integrating over $\xi_{\vec{k}}$, one resolves an expression for T_c of

$$kT_c = 1.13 \hbar \omega_D e^{-1/N(0)V}. \quad (\text{A.28})$$

Combining with Eq. A.22, we retrieve an expression for T_c in terms of $\Delta(0)$ of

$$T_c = \frac{\Delta(0)}{1.764 k_B}. \quad (\text{A.29})$$

The numerical factor of 1.764 has been reasonably well supported by various experiments on standard superconductors, with measured factors ranging from 1.5 to 2.25, with most accumulating around 1.75 [60].

The temperature dependence of the gap can be determined by numerically computing the integral of Eq. A.27 over $\xi_{\vec{k}}$. The result, which is universal for superconductors

in the weak coupling regime, reveals that near $T = 0$ the decay of $\Delta(T)$ is exponentially slow and nearly insensitive to T . As T approaches T_c , $\Delta(T)$ decays rapidly, reaching a vertical tangent. In fact, near T_c , $\Delta(T)$ is approximated by

$$\frac{\Delta(T)}{\Delta(0)} \approx 1.74 \left(1 - \frac{T}{T_c}\right)^{1/2}, T \approx T_c. \quad (\text{A.30})$$

BCS Density of States

Now we have a definition for the superconducting gap, we can define the density of states (DOS) of a superconductor. From our theoretical analysis, we understand that there exists a region where no quasi-particles can exist. From the density of states of a normal metal $\rho_N(0)$, which we assume to be constant, we obtain the DOS of a superconductor by introducing the energy states of the superconductor giving

$$\rho_S(E) = \frac{1}{2}\rho_N(0) \begin{cases} \frac{|E|}{\sqrt{E^2 - \Delta^2}} & \text{if } |E| > \Delta \\ 0 & \text{otherwise.} \end{cases} \quad (\text{A.31})$$

Figure 2.7 shows the DOS of a superconductor.

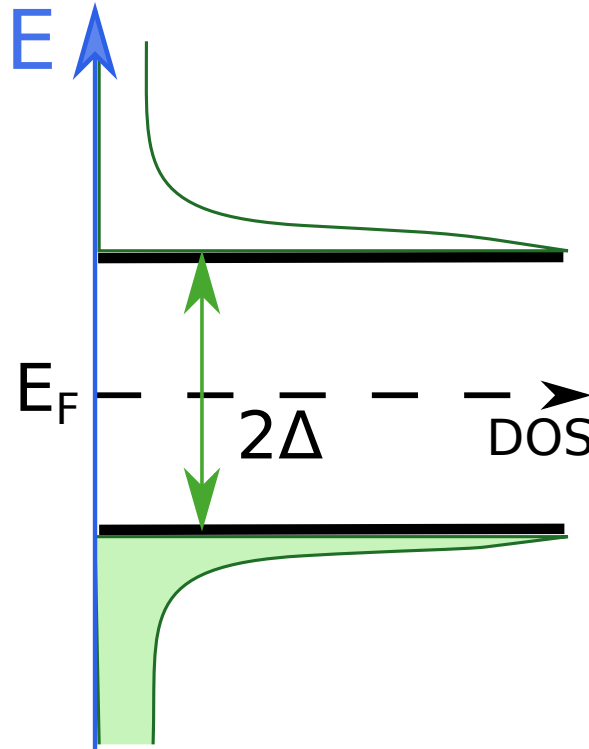


Figure A.1 – Quasiparticle spectrum of the superconducting ground state in the one-particle representation. In the ground state, all the quasiparticle states below E_F are filled, whereas all states above E_F are empty. Notably, all quasiparticle states of energy $|E - E_F| < \Delta$ are forbidden. This defines the superconducting gap.

Measurement Feedback and Data Correction Procedure

B

B.1 Measurement Feedback

As discussed in Chapter 4 of the main text, I developed a python script to provide immediate measurement feedback. The script enables a user to easily view, in the case of voltage biasing measurements, the density plots of the measured current I_D and numerical differential conductance G versus V_D and V_G . In this section of the Appendix, I will describe how to run the python script to observe the target data.

To use the python script, called '*diamonds.py*' it must be copied to the same directory as the measurement data for which the user wishes to plot. Then the user must run the python script that is produced by the LabView measurement program when the target measurement was made. The name of the measurement python script is defined by the time of the measurement e.g. *165903.py*. Once run the measurement python script calls the *diamonds.py* script and two graphical user interface (GUI) panels will appear on the user's screen. One GUI will show the measured $I_D(V_G, V_D)$ and the second will show the measured $G(V_G, V_D)$. Figure 4.11 shows the GUI of the measured current. By clicking on the density plot the user can select a (V_G, V_D) coordinate. The program uses this coordinate to plot V_G and V_D slices to the right and top, respectively. The user can select different coordinates freely. The GUI also provides the standard functionality of a *matplotlib* plot such as saving the figure, changing the colorbar scale, zoom, pan and more. The same functionality works in the conductance GUI. This python script also works for current biasing measurements.

B.2 Data Correction

As discussed in Chapter 4 of the main text I carried out a data correction procedure. This procedure was implemented to ensure that the measured current and voltage was the true current and voltage at the device under measure. Here, I detail, using technical terms associated with the python packages used, the data correction procedures I used.

To correct the measured data, I adjusted the voltage response of I-bias biased measurements and the applied voltage of V-bias measurements. Further, I corrected the data to remove the zero-bias offset associated with the voltage source and the current offset associated with the current amplifier. By making these adjustments, I ensured that the voltages discussed in these measurements is the true voltage drop across the Al-Ge-Al and Al-Ge/Si-Al nanowire heterostructures.

[Link back to Table of contents](#) →

Voltage Biasing

Correcting zero bias offset: To correct for the zero bias offset, I shifted the voltage bias (V-bias) index such that $I(V\text{-bias} = 0) = 0$ A. To achieve this, I created a python function, which calculates the offset and subtracts this value from the original voltage index of the dataset. The offset is calculated by finding the V-bias value associated with the minimum I-measured of each V_G slice. Assuming that the offset is constant with respect to V_G , the V-bias values are averaged to obtain a single offset value. This process is only carried out in the non-blockade region of the data set. Indeed, the zero current over a finite V-bias makes finding the V-bias offset value from the minimum I-measured unreliable.

Correcting current offset: To correct for the current offset of the current amplifier, I determined the current offset from an average of the measured current in the blockade and/or pinch-off regions of the measurement. In these regions, I assume that the measured current is an experimental artifact due to the amplifier. I then use the determined current offset to correct the measured current in order to obtain the true current through the device I_D . Correcting for current offset was only possible for datasets with a blockade or pinch-off region. On the other hand, in the more conductive regimes of the devices, the current offset is negligible compared to the measured current.

Correcting wiring resistance: To correct for the wiring resistance of the fridge R_{fridge} and determine the true V_D across the devices, I subtracted from the V-bias index values, that have already been corrected for the zero bias offset, $I_D \times R_{\text{fridge}}$ where I_D is the measured current corrected for current offset and $R_{\text{fridge}} = 390 \Omega$. As I_D is dependent on V_D and V_G , the new V_D indexes are different for each V_G slice, thus expanding the index of Pandas DataFrame object through which I have stored the data on python. As a result the function to remove the fridge resistance called *correct_fridge_R_V_bias* returns a new DataFrame with each column being the true V_D indexes of the labeled V_G slice. To improve the organisation of the data I combined the true V_D and I_D values into a single DataFrame with a V_D index using the function called *single_index_df*. To reduce the size of the index I rounded the V_D values to three decimal places. In instances when there are duplicates of the V_D index in a single V_G slice (which are illegal in the Pandas DataFrame object) I used V_D values rounded to four decimal places to replace the duplicates.

Current Biasing

Correcting voltage offset: To correct for the zero bias offset which results in the measurement of a non-zero voltage at I-bias = 0 A. One should recall that the I-bias is created by the same voltage card as the V-bias. To remove the zero bias offset I subtracted the measured voltage at I-bias = 0 A from all the measured voltage values of that V_G slice. This process is carried out by the function called *correct_zero_bias_offset*.

Correcting wiring resistance: To determine the true voltage drop across the devices V_D , I subtracted from the measured voltage values that have been corrected for the zero bias offset $I_D \times R_{\text{fridge}}$ where I_D is the I-bias, index of the DataFrame. and $R_{\text{fridge}} = 393 \Omega$. This process is carried out by the function called *correct_fridge_R*.

Using the Monte Carlo fitting program



In Chapter 5 of the main text we used the Monte Carlo fitting programme created by Gabino Rubio to fit the IV curves in the superconducting regime of the Al-Ge-Al nanowire heterostructures. Here, I explain in detail how I used the program.

Figure C.1 shows the GUI of the programme. There are multiple features of the programme that I made use of: Fitting IV curves and simulating IV curves for arbitrary channels and transmissions values.

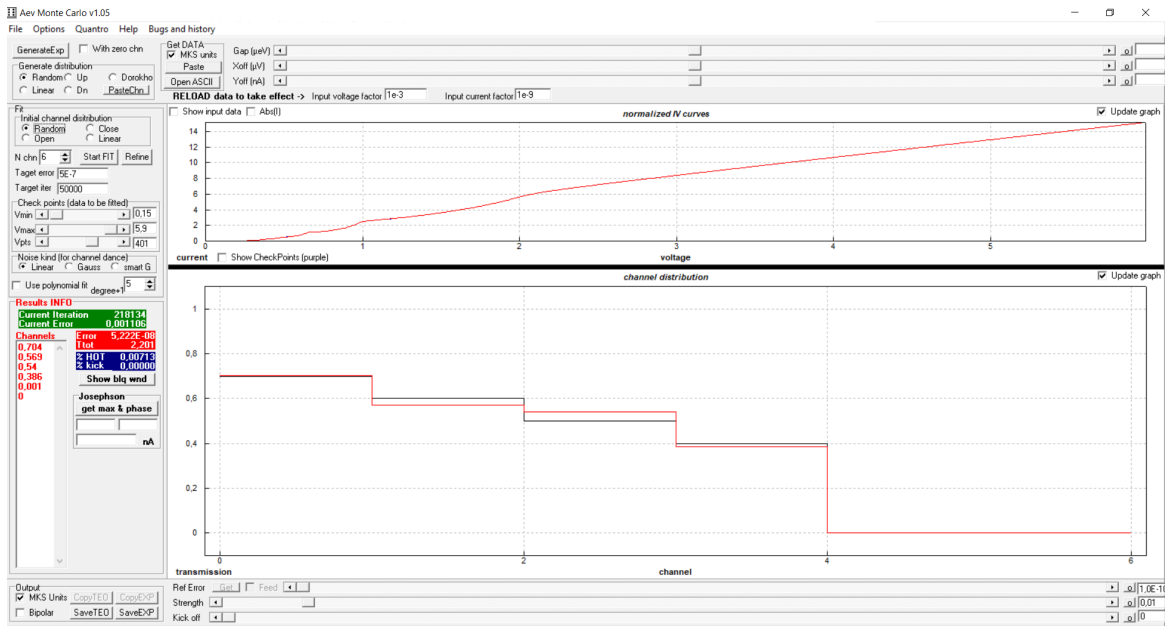


Figure C.1 – Screenshot of AevCarlo programme.

Fitting IV Curves The raw data is uploaded to AevCarlo by pressing the Open ASCII button and selecting the desired file which has two columns V(mV) & I(nA). It is important that the data is adjusted to ensure that the V (mV) column is the true voltage drop across the device ((i.e. removing voltage drop due to fridge resistance). AevCarlo smooths the data into 600 points up to 6Δ where Δ is the gap chosen by the user using the scroll bar labeled 'Gap (μeV)'. The smoothed data is then plotted on the first graph in blue. The input voltage factor and input current factor must be set to ensure the data is in SI units before fitting takes place. The fitting procedure has multiple parameters to adjust the fit: Initial channel distribution - Defines how

[Link back to Table of contents →](#)

the initial transmission will be set, N chn - Number of channels to be fitted, Target error, Target iteration, Vmin (Δ/e)- The minimum voltage to fit from loaded and smoothed data, Vmax (Δ/e)- The maximum voltage to fit from loaded and smoothed data, Vpts - The number of data points of loaded and smoothed data. The button "Start Fit" is clicked to initiate the fit; the Monte Carlo process ends when either Target error or Target iteration is reached. The "Refine" button can be used to run the fit continuously beyond the target iteration to reduce the error the fit must be stopped manually. The fitting curve is plotted in red on both graphs; the second graph shows the transmission Vs. channel number.

Gap Search: AevCarlo also provides a tool to find the optimum gap energy to fit the IV curve. The tool can be selected by clicking "Quantro" then "Gap Search". One can select the number of iterations either side of the provided gap energy and the width of these iterations in μeV . Launching the search causes AevCarlo to fit the IV curve for each gap value and record the Error of the fit producing data of Error Vs. Gap which can be copy & pasted into a txtfile for saving.

Simulating Curves: To simulate IV curves one can copy the transmission values of an arbitrary number of channels from a txtfile and pasting such channels by clicking PasteChn (note decimals are separated by commas (",") not dot points (".")). One can also choose different ways to generate channel transmission distributions; Random, Linear, etc. This results in a normalized IV curve plot and channel distribution plot.

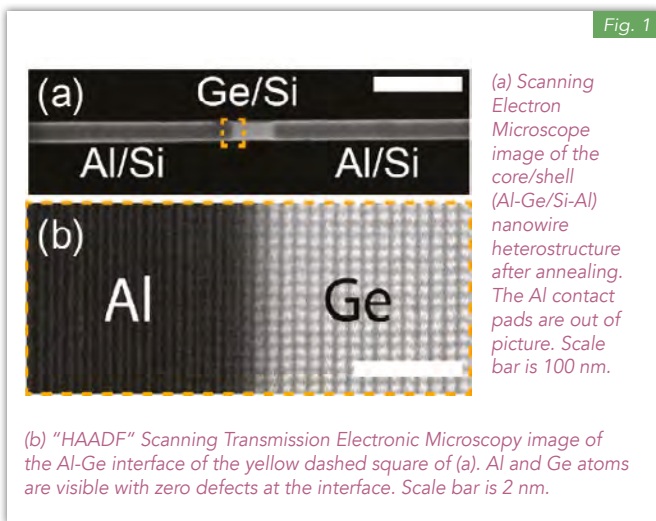
Saving Data: The theory (fitting) curve and experimental (loaded & smoothed) curve can be saved by clicking "SaveTEO" and "SaveEXP" respectively. The channel transmissions are saved by copying and pasting the Channels into an independent txtfile and saving such file.

Article in Highlights 2019



The following page, is an article that I wrote in 2019 for Institut Néel's annual *Highlights* magazine. The magazine article is based on our transport investigations of Al-Ge/Si-Al core/shell nanowire heterostructures, discussed in Chapter 6. The goal of this article, is to explain our research to the scientific and non-scientific communities inside and outside the institute.

Hybrid superconducting-semiconducting systems are promising candidates for nano-electronic quantum devices including quantum bits ("qubits") and quantum circuits. However, their successful realisation requires devices with very few defects. In these hybrid devices, significant defects result from poor quality interfaces between the superconductor and semiconductor. Reducing defects by improving the interface provides a significant challenge.

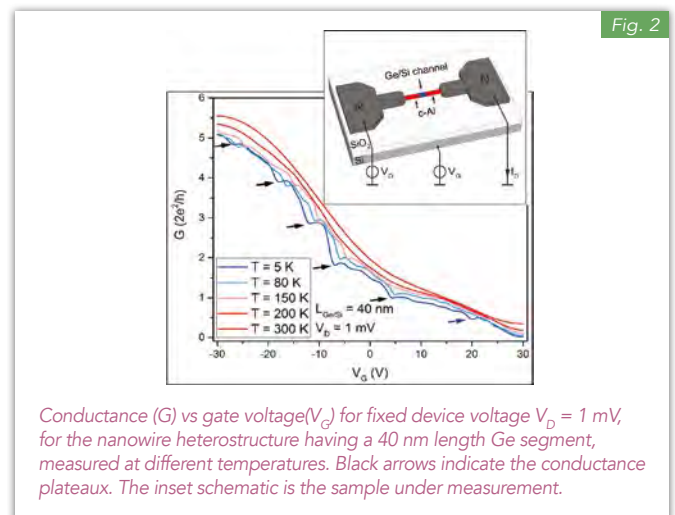


In collaboration with the Institute of Solid State Electronics at TU Wien, Vienna, Austria, and the Laboratoire d'Etude des Matériaux par Microscopie Avancée, CEA-Grenoble, we have fabricated and characterised hybrid nanowire heterostructures having extremely high quality interfaces. Developed in Vienna, a novel technique facilitates the fabrication of superconducting-semiconducting hybrid nanowires (NWs) with atomically precise interfaces. We start with a 3 micron long nanowire consisting of a germanium (Ge) core with a diameter of 30 nm and a silicon (Si) shell with a thickness of 3 nm. Then we apply two aluminium (Al) contact pads onto the two ends of the wire, using electron beam lithography. Through annealing, we can enable and control the replacement of germanium of the nanowire by aluminium from Al pads. The controlled substitution of Ge by Al results in a monolithic nanowire having the form of a short, central Ge segment, of desired length, connected on both sides by monocrystalline aluminium (c-Al) nanowire segments serving as leads, while maintaining its Si shell (Fig. 1a and inset of Fig. 2). A substantial breakthrough of this method is the atomically precise contacts between the Al and the Ge, which we can observe using a tunnelling electron microscope (Fig. 1b).

To highlight the high quality of these devices and their quantum phenomena we carried out temperature dependent electrical measurements on a nanowire with a Ge segment of length 40 nm between the two Al contact leads. By applying a voltage difference (V_D) across the device and measuring the current (I_D), we can calculate its conductance (the inverse of its resistance) here $G = I_D/V_D$. As germanium is a semiconductor, we can control its conductivity, its ability to conduct charge, by applying an electric field, the gate field. The electric field is induced by applying a voltage bias (the gate voltage V_G) to the highly doped underlying silicon wafer, see the inset of Fig. 2. Germanium in its natural state behaves like a *p*-type semiconductor, so it is easier for positive charges (holes) to transverse the Ge segment. As such, as shown in Fig. 2, applying a more negative gate voltage increases the conductivity of the device.

As we decrease the temperature of the sample from 300 K, we begin to observe structures within the conductance

curves at temperatures as high as 150 K. These structures become more pronounced as the temperature is reduced to 5 K. The structures, indicated by black arrows (Fig. 2), are known as quantized conductance plateaux and are a phenomenon of "one dimensional" nanostructures explained by quantum mechanics. The plateaux conductance is then given by two fundamental constants, e the electron charge and h the Planck constant: $G_n = n2e^2/h$ where n is an integer. The ability to observe such features up to 150 K demonstrates the high quality of the sample and its interfaces. From the measured conductance of the plateaux, we estimate the transparency of the Al to Ge interface to be greater than 96%.



Measurements below 1.2 K reveal that the aluminium contacts become superconducting, resulting in the connected Ge segment experiencing *proximity-induced*, superconducting transport properties, such as dissipationless current.

We have demonstrated the exceptional electrical transport characteristics of these high quality core/shell (Al-Ge/Si-Al) nanowires fabricated using a novel annealing technique. Having overcome the limitations of interface defects, these devices can be integrated into quantum devices and used for future investigations of superconducting-semiconducting phenomena.

CONTACTS

Olivier Buisson
olivier.buisson@neel.cnrs.fr
Cécile Naud
cecile.naud@neel.cnrs.fr
Ph.D.
Jovian Delaforce

FURTHER READING...

- M. Sistani, J. Delaforce, R. B. G. Kramer, N. Roch, M. A. Luong, M. I. den Hertog, E. Robin, J. Smoliner, J. Yao, C. M. Lieber, C. Naud, A. Lugstein and O. Buisson "Highly Transparent Contacts to the 1D Hole Gas in Ultrascaled Ge/Si Core/Shell Nanowires" *ACS Nano*, doi: 10.1021/acsnano.9b06809.

Bibliography

- [1] R. Dassonneville, T. Ramos, V. Milchakov, L. Planat, A. Dumur, F. Foroughi, J. Puertas, S. Leger, K. Bharadwaj, J. Delaforce, C. Naud, W. Hasch-Guichard, J. García-Ripoll, N. Roch, and O. Buisson. Fast High-Fidelity Quantum Nondemolition Qubit Readout via a Nonperturbative Cross-Kerr Coupling. *Physical Review X*, 10(1):011045, February 2020.
(Cited on page 1.)
- [2] Luca Planat, Arpit Ranadive, Romy Dassonneville, Javier Puertas Martínez, Sébastien Léger, Cécile Naud, Olivier Buisson, Wiebke Hasch-Guichard, Dennis M. Basko, and Nicolas Roch. Photonic-Crystal Josephson Traveling-Wave Parametric Amplifier. *Physical Review X*, 10(2):021021, April 2020.
(Cited on page 1.)
- [3] J. Basset, M. Kuzmanović, P. Virtanen, T. T. Heikkilä, J. Estévez, J. Gabelli, C. Strunk, and M. Aprili. Nonadiabatic dynamics in strongly driven diffusive Josephson junctions. *Physical Review Research*, 1(3), October 2019.
(Cited on page 1.)
- [4] Yong-Joo Doh, Jordan A. van Dam, Aarnoud L. Roest, Erik P. A. M. Bakkers, Leo P. Kouwenhoven, and Silvano De Franceschi. Tunable Supercurrent Through Semiconductor Nanowires. *Science*, 309(5732):272–275, July 2005.
(Cited on page 1.)
- [5] B. Irmer, R. H. Blick, F. Simmel, W. Gützel, H. Lorenz, and J. P. Kotthaus. Josephson junctions defined by a nanoplough. *Applied Physics Letters*, 73(14):2051–2053, October 1998.
(Cited on page 1.)
- [6] J-D. Pillet, C. H. L. Quay, P. Morfin, C. Bena, A. Levy Yeyati, and P. Joyez. Andreev bound states in supercurrent-carrying carbon nanotubes revealed. *Nature Physics*, 6(12):965–969, December 2010.
(Cited on pages 1, 69, and 143.)
- [7] Hubert B. Heersche, Pablo Jarillo-Herrero, Jeroen B. Oostinga, Lieven M. K. Vandersypen, and Alberto F. Morpurgo. Bipolar supercurrent in graphene. *Nature*, 446(7131):56–59, March 2007.
(Cited on page 1.)
- [8] T. D. Clark, R. J. Prance, and A. D. C. Grassie. Feasibility of hybrid Josephson field effect transistors. *Journal of Applied Physics*, 51(5):2736, 1980.
(Cited on page 1.)

BIBLIOGRAPHY

- [9] B.D. Josephson. Possible new effects in superconductive tunnelling. *Physics Letters*, 1(7):251–253, July 1962.
(Cited on page 1.)
- [10] Jens Koch, Terri M. Yu, Jay Gambetta, A. A. Houck, D. I. Schuster, J. Majer, Alexandre Blais, M. H. Devoret, S. M. Girvin, and R. J. Schoelkopf. Charge-insensitive qubit design derived from the Cooper pair box. *Physical Review A*, 76(4):042319, October 2007.
(Cited on page 2.)
- [11] T. W. Larsen, K. D. Petersson, F. Kuemmeth, T. S. Jespersen, P. Krogstrup, J. Nyg rd, and C. M. Marcus. Semiconductor-Nanowire-Based Superconducting Qubit. *Physical Review Letters*, 115(12), September 2015.
(Cited on page 2.)
- [12] G. de Lange, B. van Heck, A. Bruno, D. J. van Woerkom, A. Geresdi, S. R. Plissard, E. P. A. M. Bakkers, A. R. Akhmerov, and L. DiCarlo. Realization of Microwave Quantum Circuits Using Hybrid Superconducting-Semiconducting Nanowire Josephson Elements. *Physical Review Letters*, 115(12):127002, September 2015.
(Cited on page 2.)
- [13] Lucas Casparis, Malcolm R. Connolly, Morten Kjaergaard, Natalie J. Pearson, Anders Kringh j, Thorvald W. Larsen, Ferdinand Kuemmeth, Tiantian Wang, Candice Thomas, Sergei Gronin, Geoffrey C. Gardner, Michael J. Manfra, Charles M. Marcus, and Karl D. Petersson. Superconducting gatemon qubit based on a proximitized two-dimensional electron gas. *Nature Nanotechnology*, 13(10):915–919, October 2018.
(Cited on page 2.)
- [14] A. Kringh j, T. W. Larsen, B. van Heck, D. Sabonis, O. Erlandsson, I. Petkovic, D. I. Pikulin, P. Krogstrup, K. D. Petersson, and C. M. Marcus. Controlled dc Monitoring of a Superconducting Qubit. *Physical Review Letters*, 124(5):056801, February 2020.
(Cited on page 2.)
- [15] M. Hays, V. Fatemi, D. Bouman, J. Cerrillo, S. Diamond, K. Serniak, T. Connolly, P. Krogstrup, J. Nyg rd, A. Levy Yeyati, A. Geresdi, and M. H. Devoret. Coherent manipulation of an Andreev spin qubit. *arXiv:2101.06701 [cond-mat, physics:quant-ph]*, January 2021. arXiv: 2101.06701.
(Cited on page 2.)
- [16] J. Dalibard, D. Est ve, and J.-M. Raimond. Preface. In Daniel Est ve, Jean-Michel Raimond, and Jean Dalibard, editors, *Les Houches*, volume 79, pages xv–xviii. Elsevier, January 2004.
(Cited on page 2.)
- [17] I. M. Georgescu, S. Ashhab, and Franco Nori. Quantum Simulation. *Reviews of Modern Physics*, 86(1):153–185, March 2014. arXiv: 1308.6253.
(Cited on page 2.)

BIBLIOGRAPHY

- [18] SÅbastien Leger. *Quantum Electrodynamics of a Josephson junction coupled to a strongly dissipative environment*. These, UniversitÅI Grenoble Alpes, 2021.
(Cited on page 2.)
- [19] D. Deutsch. Quantum Theory, the Church-Turing Principle and the Universal Quantum Computer. *Proceedings of the Royal Society of London. A. Mathematical and Physical Sciences*, 400(1818):97 LP – 117, 1985.
(Cited on page 2.)
- [20] Frank Arute, Kunal Arya, Ryan Babbush, Dave Bacon, Joseph C. Bardin, Rami Barends, Rupak Biswas, Sergio Boixo, Fernando G. S. L. Brandao, David A. Buell, Brian Burkett, Yu Chen, Zijun Chen, Ben Chiaro, Roberto Collins, William Courtney, Andrew Dunsworth, Edward Farhi, Brooks Foxen, Austin Fowler, Craig Gidney, Marissa Giustina, Rob Graff, Keith Guerin, Steve Habegger, Matthew P. Harrigan, Michael J. Hartmann, Alan Ho, Markus Hoffmann, Trent Huang, Travis S. Humble, Sergei V. Isakov, Evan Jeffrey, Zhang Jiang, Dvir Kafri, Kostyantyn Kechedzhi, Julian Kelly, Paul V. Klimov, Sergey Knysh, Alexander Korotkov, Fedor Kostritsa, David Landhuis, Mike Lindmark, Erik Lucero, Dmitry Lyakh, Salvatore MandrÅ, Jarrod R. McClean, Matthew McEwen, Anthony Megrant, Xiao Mi, Kristel Michielsen, Masoud Mohseni, Josh Mutus, Ofer Naaman, Matthew Neeley, Charles Neill, Murphy Yuezhen Niu, Eric Ostby, Andre Petukhov, John C. Platt, Chris Quintana, Eleanor G. Rieffel, Pedram Roushan, Nicholas C. Rubin, Daniel Sank, Kevin J. Satzinger, Vadim Smelyanskiy, Kevin J. Sung, Matthew D. Trevithick, Amit Vainsencher, Benjamin Villalonga, Theodore White, Z. Jamie Yao, Ping Yeh, Adam Zalcman, Hartmut Neven, and John M. Martinis. Quantum supremacy using a programmable superconducting processor. *Nature*, 574(7779):505–510, October 2019.
(Cited on page 2.)
- [21] Jie Xiang, A. Vidan, M. Tinkham, R. M. Westervelt, and Charles M. Lieber. Ge/Si nanowire mesoscopic Josephson junctions. *Nature Nanotechnology*, 1(3):208–213, December 2006.
(Cited on pages 3, 69, 79, and 133.)
- [22] D Kotekar-Patil, B-M Nguyen, J Yoo, S A Dayeh, and S M Frolov. Quasiballistic quantum transport through Ge/Si core/shell nanowires. *Nanotechnology*, 28(38):385204, September 2017.
(Cited on pages 3, 11, 69, 152, and 154.)
- [23] Folkert K. de Vries, Jie Shen, Rafal J. Skolasinski, Michal P. Nowak, Daniel Varjas, Lin Wang, Michael Wimmer, Joost Ridderbos, Floris A. Zwanenburg, Ang Li, Sebastian Koelling, Marcel A. Verheijen, Erik P. A. M. Bakkers, and Leo P. Kouwenhoven. SpinÅOrbit Interaction and Induced Superconductivity in a One-Dimensional Hole Gas. *Nano Letters*, 18(10):6483–6488, October 2018.
(Cited on pages 3 and 69.)
- [24] Joost Ridderbos, Matthias Brauns, Jie Shen, Folkert K. de Vries, Ang Li, Erik P. A. M. Bakkers, Alexander Brinkman, and Floris A. Zwanenburg. Josephson Effect in a Few-Hole Quantum Dot. *Advanced Materials*, 30(44):1802257,

BIBLIOGRAPHY

- November 2018.
(Cited on pages [3](#) and [69](#).)
- [25] Hannes Watzinger, Christoph Kloeffel, Lada VukuÅaiÄĖ, Marta D. Rossell, Violetta Sessi, Josip KukuÄDka, Raimund Kirchschrager, Elisabeth Lausecker, Alisha Truhlar, Martin Glaser, Armando Rastelli, Andreas Fuhrer, Daniel Loss, and Georgios Katsaros. Heavy-Hole States in Germanium Hut Wires. *Nano Letters*, 16(11):6879–6885, November 2016.
(Cited on pages [3](#), [69](#), and [120](#).)
- [26] N. W. Hendrickx, D. P. Franke, A. Sammak, M. Kouwenhoven, D. Sabbagh, L. Yeoh, R. Li, M. L. V. Tagliaferri, M. Virgilio, G. Capellini, G. Scappucci, and M. Veldhorst. Gate-controlled quantum dots and superconductivity in planar germanium. *Nature Communications*, 9(1):2835, December 2018.
(Cited on pages [3](#), [68](#), and [128](#).)
- [27] Florian Vigneau, Rasei Mizokuchi, Dante Colao Zanuz, Xuhai Huang, Susheng Tan, Romain Maurand, Sergey Frolov, Amir Sammak, Giordano Scappucci, Francois Lefloch, and Silvano De Franceschi. Germanium Quantum-Well Josephson Field-Effect Transistors and Interferometers. *Nano Letters*, 19(2):1023–1027, February 2019.
(Cited on pages [3](#) and [68](#).)
- [28] Kushagra Aggarwal, Andrea Hofmann, Daniel Jirovec, Ivan Prieto, Amir Sammak, Marc Botifoll, Sara Marti-Sanchez, Menno Veldhorst, Jordi Arbiol, Giordano Scappucci, Jeroen Danon, and Georgios Katsaros. Enhancement of Proximity Induced Superconductivity in a Planar Ge Hole Gas. *Physical Review Research*, 3(2):L022005, April 2021. arXiv: 2012.00322.
(Cited on pages [3](#) and [68](#).)
- [29] A. Thanailakis and D.C. Northrop. Metal-germanium Schottky barriers. *Solid-State Electronics*, 16(12):1383–1389, December 1973.
(Cited on pages [3](#), [69](#), and [109](#).)
- [30] N. Neophytou, Jing Guo, and M.S. Lundstrom. Three-dimensional electrostatic effects of carbon nanotube transistors. *IEEE Transactions On Nanotechnology*, 5(4):385–392, July 2006.
(Cited on pages [3](#) and [69](#).)
- [31] T. Burchhart, A. Lugstein, C. Zeiner, Y. J. Hyun, G. Hochleitner, and E. Bertagnolli. Nanowire-metal heterostructures for high performance MOSFETs. *e & i Elektrotechnik und Informationstechnik*, 127(6):171–175, June 2010.
(Cited on pages [3](#) and [69](#).)
- [32] M. Sistani, M. A. Luong, M. I. den Hertog, E. Robin, M. Spies, B. Fernandez, J. Yao, E. Bertagnolli, and A. Lugstein. Monolithic Axial and Radial Metal-ÅSemiconductor Nanowire Heterostructures. *Nano Letters*, 18(12):7692–7697, December 2018.
(Cited on pages [3](#), [69](#), [78](#), [79](#), and [167](#).)

BIBLIOGRAPHY

- [33] M.A. Luong, E. Robin, N. Pauc, P. Gentile, M. Sistani, A. Lugstein, M. Spies, B. Fernandez, and M. I. Den Hertog. In-Situ Transmission Electron Microscopy Imaging of Aluminum Diffusion in Germanium Nanowires for the Fabrication of Sub-10 nm Ge Quantum Disks. *ACS Applied Nano Materials*, 3(2):1891–1899, February 2020.
(Cited on pages [3](#), [69](#), [79](#), and [167](#).)
- [34] S. Kral, C. Zeiner, M. StÄúger-Pollach, E. Bertagnolli, M. I. den Hertog, M. Lopez-Haro, E. Robin, K. El Hajraoui, and A. Lugstein. Abrupt Schottky Junctions in Al/Ge Nanowire Heterostructures. *Nano Letters*, 15(7):4783–4787, July 2015.
(Cited on pages [3](#), [69](#), [108](#), and [167](#).)
- [35] J. J Riquelme, L. de la Vega, A. Levy Yeyati, N AgraÄít, A Martin-Rodero, and G Rubio-Bollinger. Distribution of conduction channels in nanoscale contacts: Evolution towards the diffusive limit. *Europhysics Letters (EPL)*, 70(5):663–669, June 2005.
(Cited on pages [8](#), [54](#), and [135](#).)
- [36] Jie Xiang, Wei Lu, Yongjie Hu, Yue Wu, Hao Yan, and Charles M. Lieber. Ge/Si nanowire heterostructures as high-performance field-effect transistors. *Nature*, 441(7092):489–493, May 2006.
(Cited on pages [11](#), [71](#), and [154](#).)
- [37] N. W. Ashcroft and N. D. Mermin. *Solid State Physics*. Holt-Saunders, 1976.
(Cited on pages [16](#) and [21](#).)
- [38] S. M Sze and Kwok K Ng. *Physics of semiconductor devices*. John Wiley & Sons, New York, 2007. OCLC: 488586029.
(Cited on page [22](#).)
- [39] Masiar\$\$QSistani Sistani, Masiar\$\$10000-0001-5730-234X. *Transport in ultra-scaled Ge quantum dots embedded in Al-Ge-Al nanowire heterostructures*. Elektrische Transportuntersuchungen an monolithischen Al-Ge-Al Nanodrahtheterostrukturen. Wien, Wien, 2019. Journal Abbreviation: Transport in ultra-scaled Publication Title: Transport in ultra-scaled.
(Cited on pages [23](#), [26](#), [70](#), [71](#), [73](#), [75](#), [76](#), [79](#), [108](#), and [111](#).)
- [40] Supriyo Datta. *Electronic Transport in Mesoscopic Systems*. Cambridge University Press, Cambridge, 1995. OCLC: 855502561.
(Cited on pages [25](#) and [155](#).)
- [41] William M Haynes and David R Lide. *CRC handbook of chemistry and physics: a ready-reference book of chemical and physical data*. 2011. OCLC: 1118477973.
(Cited on page [26](#).)
- [42] Ilse van Weperen, SÄlbastien R. Plissard, Erik P. A. M. Bakkers, Sergey M. Frolov, and Leo P. Kouwenhoven. Quantized Conductance in an InSb Nanowire. *Nano Letters*, 13(2):387–391, February 2013.
(Cited on page [27](#).)

BIBLIOGRAPHY

- [43] Leo P. Kouwenhoven, Charles M. Marcus, Paul L. McEuen, Seigo Tarucha, Robert M. Westervelt, and Ned S. Wingreen. Electron Transport in Quantum Dots. In Lydia L. Sohn, Leo P. Kouwenhoven, and Gerd SchÅn, editors, *Mesoscopic Electron Transport*, NATO ASI Series, pages 105–214. Springer Netherlands, Dordrecht, 1997.
(Cited on pages 29 and 30.)
- [44] C G Smith, M Pepper, H Ahmed, J E F Frost, D G Hasko, D C Peacock, D A Ritchie, and G A C Jones. The transition from one- to zero-dimensional ballistic transport. *Journal of Physics C: Solid State Physics*, 21(24):L893–L898, August 1988.
(Cited on pages 29 and 30.)
- [45] Daniel Jirovec, Andrea Hofmann, Andrea Ballabio, Philipp M. Mutter, Giulio Tavani, Marc Botifoll, Alessandro Crippa, Josip Kukucka, Oliver Sagi, Frederico Martins, Jaime Saez-Mollejo, Ivan Prieto, Maksim Borovkov, Jordi Arbiol, Daniel Chrastina, Giovanni Isella, and Georgios Katsaros. A singlet-triplet hole spin qubit in planar Ge. *Nature Materials*, 20(8):1106–1112, August 2021.
(Cited on page 30.)
- [46] Matthias Brauns, Joost Ridderbos, Ang Li, Wilfred G. van der Wiel, Erik P. A. M. Bakkers, and Floris A. Zwanenburg. Highly tuneable hole quantum dots in Ge-Si core-shell nanowires. *Applied Physics Letters*, 109(14):143113, October 2016.
(Cited on page 30.)
- [47] Emmanuel Chanrion, David J. Niegemann, Benoit Bertrand, Cameron Spence, Baptiste Jadot, Jing Li, Pierre-AndrÅ Mortemousque, Louis Hutin, Romain Maurand, Xavier Jehl, Marc Sanquer, Silvano De Franceschi, Christopher BÅduerle, Franck Balestro, Yann-Michel Niquet, Maud Vinet, Tristan Meunier, and Matias Urdampilleta. Charge Detection in an Array of CMOS Quantum Dots. *Physical Review Applied*, 14(2):024066, August 2020.
(Cited on page 30.)
- [48] David H. Cobden and Jesper NygÅrd. Shell Filling in Closed Single-Wall Carbon Nanotube Quantum Dots. *Physical Review Letters*, 89(4):046803, July 2002.
(Cited on page 30.)
- [49] F. A. Zwanenburg, A. A. van Loon, G. A. Steele, C. E. W. M. van Rijmenam, T. Balder, Y. Fang, C. M. Lieber, and L. P. Kouwenhoven. Ultrasmall silicon quantum dots. *Journal of Applied Physics*, 105(12):124314, June 2009.
(Cited on pages 30, 69, 80, and 128.)
- [50] Nicolas Roch, Serge Florens, Vincent Bouchiat, Wolfgang Wernsdorfer, and Franck Balestro. Quantum phase transition in a single-molecule quantum dot. *Nature*, 453(7195):633–637, May 2008.
(Cited on page 30.)
- [51] G. Katsaros, P. Spathis, M. Stoffel, F. Fournel, M. Mongillo, V. Bouchiat, F. Lefloch, A. Rastelli, O. G. Schmidt, and S. De Franceschi. Hybrid superconductor–semiconductor devices made from self-assembled SiGe nanocrystals

BIBLIOGRAPHY

- on silicon. *Nature Nanotechnology*, 5(6):458–464, June 2010.
(Cited on page 30.)
- [52] Jean-Noël Patillon and Dominique Maily. Alternative Electronics. In Claire Dupas, Philippe Houdy, and Marcel Lahmani, editors, *Nanoscience: Nanotechnologies and Nanophysics*, pages 417–446. Springer Berlin Heidelberg, Berlin, Heidelberg, 2007.
(Cited on page 30.)
- [53] H. Van Houten, C. W. J. Beenakker, and A. A. M. Staring. Coulomb-Blockade Oscillations in Semiconductor Nanostructures. In Hermann Grabert and Michel H. Devoret, editors, *Single Charge Tunneling: Coulomb Blockade Phenomena In Nanostructures*, NATO ASI Series, pages 167–216. Springer US, Boston, MA, 1992.
(Cited on page 30.)
- [54] Thomas Ihn. Introduction to electron transport through quantum dots. In Thomas Ihn, editor, *Electronic Quantum Transport in Mesoscopic Semiconductor Structures*, pages 67–85. Springer New York, New York, NY, 2004.
(Cited on page 30.)
- [55] R. Hanson, L. P. Kouwenhoven, J. R. Petta, S. Tarucha, and L. M. K. Vandersypen. Spins in few-electron quantum dots. *Reviews of Modern Physics*, 79(4):1217–1265, October 2007.
(Cited on page 30.)
- [56] John F. Cochran and D. E. Mapother. Superconducting Transition in Aluminum. *Physical Review*, 111(1):132–142, July 1958.
(Cited on page 38.)
- [57] W. Meissner and R. Ochsenfeld. Ein neuer Effekt bei Eintritt der Supraleitfähigkeit. *Naturwissenschaften*, 21(44):787–788, November 1933.
(Cited on page 38.)
- [58] F. London, H. London, and Frederick Alexander Lindemann. The electromagnetic equations of the supraconductor. *Proceedings of the Royal Society of London. Series A - Mathematical and Physical Sciences*, 149(866):71–88, March 1935. Publisher: Royal Society.
(Cited on page 38.)
- [59] J. Bardeen, L. N. Cooper, and J. R. Schrieffer. Theory of Superconductivity. *Physical Review*, 108(5):1175–1204, December 1957.
(Cited on page 38.)
- [60] Michael Tinkham. *Introduction to Superconductivity*. Dover Publications, 2 edition, June 2004. Published: Paperback.
(Cited on pages 38, 82, 161, 173, 174, 176, and 178.)
- [61] Jean-Damien Pillet. *Tunneling spectroscopy of the Andreev Bound States in a Carbon Nanotube*. Theses, Université Pierre et Marie Curie - Paris VI, December 2011.
(Cited on page 42.)

BIBLIOGRAPHY

- [62] Landry Bretheau. *Localized Excitations in Superconducting Atomic Contacts: PROBING THE ANDREEV DOUBLET*. Theses, Ecole Polytechnique X, February 2013.
(Cited on pages [42](#), [44](#), and [52](#).)
- [63] D.B Szombati. *Superconducting InSb nanowire devices*. PhD thesis, Delft University of Technology, 2017. OCLC: 7792852475.
(Cited on pages [42](#), [50](#), [55](#), and [59](#).)
- [64] Theodore Van Duzer and C. W Turner. *Principles of superconductive devices and circuits*. Elsevier, New York, 1981. OCLC: 558588485.
(Cited on page [42](#).)
- [65] N. R. Werthamer. Theory of the Superconducting Transition Temperature and Energy Gap Function of Superposed Metal Films. *Physical Review*, 132(6):2440–2445, December 1963.
(Cited on page [42](#).)
- [66] R. Holm and W. Meissner. Messungen mit Hilfe von flüssigem Helium. XIII. *Zeitschrift für Physik*, 74(11):715–735, November 1932.
(Cited on page [42](#).)
- [67] P. G DE GENNES. *SUPERCONDUCTIVITY OF METALS AND ALLOYS*. CRC Press, Place of publication not identified, 2019. OCLC: 1110683745.
(Not cited.)
- [68] G. E. Blonder, M. Tinkham, and T. M. Klapwijk. Transition from metallic to tunneling regimes in superconducting microconstrictions: Excess current, charge imbalance, and supercurrent conversion. *Physical Review B*, 25(7):4515–4532, April 1982.
(Cited on pages [45](#) and [47](#).)
- [69] C. W. J. Beenakker and H. van Houten. Josephson current through a superconducting quantum point contact shorter than the coherence length. *Physical Review Letters*, 66(23):3056–3059, June 1991.
(Cited on pages [48](#), [49](#), and [50](#).)
- [70] M. Büttiker, Y. Imry, R. Landauer, and S. Pinhas. Generalized many-channel conductance formula with application to small rings. *Physical Review B*, 31(10):6207–6215, May 1985.
(Cited on page [49](#).)
- [71] D. Averin and A. Bardas. ac Josephson Effect in a Single Quantum Channel. *Physical Review Letters*, 75(9):1831–1834, August 1995.
(Cited on page [54](#).)
- [72] J. C. Cuevas, A. Martín-Rodero, and A. Levy Yeyati. Hamiltonian approach to the transport properties of superconducting quantum point contacts. *Physical Review B*, 54(10):7366–7379, September 1996.
(Cited on pages [54](#) and [60](#).)

BIBLIOGRAPHY

- [73] E. N. Bratus', V. S. Shumeiko, E. V. Bezuglyi, and G. Wendin. dc-current transport and ac Josephson effect in quantum junctions at low voltage. *Physical Review B*, 55(18):12666–12677, May 1997.
(Cited on page [54](#).)
- [74] Silvano De Franceschi, Leo Kouwenhoven, Christian SchÅűnenberger, and Wolfgang Wernsdorfer. Hybrid superconductor–quantum dot devices. *Nature Nanotechnology*, 5(10):703–711, October 2010.
(Cited on pages [55](#), [56](#), and [140](#).)
- [75] A. MartÅűn-Rodero and A. Levy Yeyati. Josephson and Andreev transport through quantum dots. *Advances in Physics*, 60(6):899–958, December 2011.
(Cited on pages [55](#), [57](#), [58](#), [59](#), [60](#), [65](#), and [169](#).)
- [76] P. W. Anderson. Localized Magnetic States in Metals. *Physical Review*, 124(1):41–53, October 1961. Publisher: American Physical Society.
(Cited on page [55](#).)
- [77] M. Buttiker. Coherent and sequential tunneling in series barriers. *IBM Journal of Research and Development*, 32(1):63–75, January 1988.
(Cited on page [57](#).)
- [78] L. I. Glazman and K. A. Matveev. Resonant Josephson current through Kondo impurities in a tunnel barrier. *ZhETF Pisma Redaktsiiu*, 49:570, May 1989.
(Cited on page [58](#).)
- [79] D. B. Szombati, S. Nadj-Perge, D. Car, S. R. Plissard, E. P. A. M. Bakkers, and L. P. Kouwenhoven. Josephson φ_0 -junction in nanowire quantum dots. *Nature Physics*, 12(6):568–572, June 2016.
(Cited on page [59](#).)
- [80] A. Levy Yeyati, J. C. Cuevas, A. LÅűpez-DÅűvalos, and A. MartÅűn-Rodero. Resonant tunneling through a small quantum dot coupled to superconducting leads. *Physical Review B*, 55(10):R6137–R6140, March 1997.
(Cited on pages [60](#) and [143](#).)
- [81] A. Martin-Rodero, A. Levy Yeyati, and J.C. Cuevas. General transport properties of superconducting quantum point contacts: a Green functions approach. *Superlattices and Microstructures*, 25(5-6):925–936, May 1999.
(Cited on page [64](#).)
- [82] A. Levy Yeyati, A. MartÅűn-Rodero, and E. Vecino. Nonequilibrium Dynamics of Andreev States in the Kondo Regime. *Physical Review Letters*, 91(26):266802, December 2003.
(Cited on page [65](#).)
- [83] Alexander Cyril Hewson. *The Kondo Problem to Heavy Fermions*. Cambridge Studies in Magnetism. Cambridge University Press, Cambridge, 1993.
(Cited on page [65](#).)

BIBLIOGRAPHY

- [84] J. R. Petta, A. C. Johnson, J. M. Taylor, E. A. Laird, A. Yacoby, M. D. Lukin, C. M. Marcus, M. P. Hanson, and A. C. Gossard. Coherent Manipulation of Coupled Electron Spins in Semiconductor Quantum Dots. *Science*, 309(5744):2180–2184, September 2005. Publisher: American Association for the Advancement of Science.
(Cited on page 68.)
- [85] Kaveh Gharavi, Gregory W Holloway, Ray R LaPierre, and Jonathan Baugh. Nb/InAs nanowire proximity junctions from Josephson to quantum dot regimes. *Nanotechnology*, 28(8):085202, February 2017.
(Cited on page 68.)
- [86] W. Chang, S. M. Albrecht, T. S. Jespersen, F. Kuemmeth, P. Krogstrup, J. NygÅerd, and C. M. Marcus. Hard gap in epitaxial semiconductorÅ§superconductor nanowires. *Nature Nanotechnology*, 10(3):232–236, March 2015.
(Cited on pages 68, 165, and 168.)
- [87] P. Krogstrup, N. L. B. Ziino, W. Chang, S. M. Albrecht, M. H. Madsen, E. Johnson, J. NygÅerd, C.ÅM. Marcus, and T. S. Jespersen. Epitaxy of semiconductorÅ§superconductor nanowires. *Nature Materials*, 14(4):400–406, April 2015.
(Cited on page 69.)
- [88] V. Mourik, K. Zuo, S. M. Frolov, S. R. Plissard, E. P. A. M. Bakkers, and L. P. Kouwenhoven. Signatures of Majorana Fermions in Hybrid Superconductor-Semiconductor Nanowire Devices. *Science*, 336(6084):1003–1007, May 2012.
(Cited on pages 69 and 169.)
- [89] Ånder GÅijl, Hao Zhang, Folkert K. de Vries, Jasper van Veen, Kun Zuo, Vincent Mourik, Sonia Conesa-Boj, MichaÅC P. Nowak, David J. van Woerkom, Marina Quintero-PÅrez, Maja C. Cassidy, Attila Geresdi, Sebastian Koelling, Diana Car, SÅlbastien R. Plissard, Erik P. A. M. Bakkers, and Leo P. Kouwenhoven. Hard Superconducting Gap in InSb Nanowires. *Nano Letters*, 17(4):2690–2696, April 2017.
(Cited on page 69.)
- [90] Yong-Joo Doh, Silvano De Franceschi, Erik P. A. M. Bakkers, and Leo P. Kouwenhoven. Andreev Reflection versus Coulomb Blockade in Hybrid Semiconductor Nanowire Devices. *Nano Letters*, 8(12):4098–4102, December 2008.
(Cited on page 69.)
- [91] Eduardo J. H. Lee, Xiaocheng Jiang, Manuel Houzet, RamÅsn Aguado, Charles M. Lieber, and Silvano De Franceschi. Spin-resolved Andreev levels and parity crossings in hybrid superconductorÅ§semiconductor nanostructures. *Nature Nanotechnology*, 9(1):79–84, January 2014.
(Cited on page 69.)
- [92] A. Eichler, M. Weiss, S. Oberholzer, C. SchÅünenberger, A. Levy Yeyati, J. C. Cuevas, and A. MartÅjn-Rodero. Even-Odd Effect in Andreev Transport through a Carbon Nanotube Quantum Dot. *Physical Review Letters*, 99(12), September 2007.
(Cited on page 69.)

BIBLIOGRAPHY

- [103] Masiar Sistani, Philipp Staudinger, and Alois Lugstein. Polarity Control in Ge Nanowires by Electronic Surface Doping. *The Journal of Physical Chemistry C*, 124(36):19858–19863, September 2020.
(Cited on pages 71 and 72.)
- [104] Masiar Sistani, Philipp Staudinger, Johannes Greil, Martin Holzbauer, Hermann Detz, Emmerich Bertagnolli, and Alois Lugstein. Room-Temperature Quantum Ballistic Transport in Monolithic Ultrascaled Al_{0.5}Ge_{0.5}Al Nanowire Heterostructures. *Nano Letters*, 17(8):4556–4561, August 2017.
(Cited on pages 71, 112, and 115.)
- [105] Shixiong Zhang, Francisco J. Lopez, Jerome K. Hyun, and Lincoln J. Lauhon. Direct Detection of Hole Gas in Ge_{0.5}Si Core_{0.5}Shell Nanowires by Enhanced Raman Scattering. *Nano Letters*, 10(11):4483–4487, November 2010.
(Cited on page 72.)
- [106] William F Gale and T. C Totemeier. *Smithells metals reference book*. Elsevier Butterworth-Heinemann, Oxford; Burlington, MA, 2003. OCLC: 982152158.
(Cited on page 75.)
- [107] Khalil El hajraoui, Minh Anh Luong, Eric Robin, Florian Brunbauer, Clemens Zeiner, Alois Lugstein, Pascal Gentile, Jean-Luc Rouvière, and Martien Den Hertog. In Situ Transmission Electron Microscopy Analysis of Aluminum_{0.5}Germanium Nanowire Solid-State Reaction. *Nano Letters*, 19(5):2897–2904, May 2019.
(Cited on pages 76, 79, and 167.)
- [108] A. J. McAlister and J. L. Murray. The Al-Ge (Aluminum-Germanium) system. *Bulletin of Alloy Phase Diagrams*, 5(4):341–347, August 1984.
(Cited on page 78.)
- [109] Minh Anh Luong. *Investigation of Al thermal diffusion in Ge and SixGe1-x alloy nanowires using in-situ transmission electron microscopy*. PhD thesis, Université Grenoble Alpes, 2019.
(Cited on page 79.)
- [110] Floris A. Zwanenburg, Cathalijn E. W. M. van Rijmenam, Ying Fang, Charles M. Lieber, and Leo P. Kouwenhoven. Spin States of the First Four Holes in a Silicon Nanowire Quantum Dot. *Nano Letters*, 9(3):1071–1079, March 2009.
(Cited on page 79.)
- [111] Joost Ridderbos, Matthias Brauns, Folkert K. de Vries, Jie Shen, Ang Li, Sebastian Käßling, Marcel A. Verheijen, Alexander Brinkman, Wilfred G. van der Wiel, Erik P. A. M. Bakkers, and Floris A. Zwanenburg. Hard Superconducting Gap and Diffusion-Induced Superconductors in Ge_{0.5}Si Nanowires. *Nano Letters*, 20(1):122–130, January 2020.
(Cited on page 80.)

BIBLIOGRAPHY

- [112] Frank Pobell. Helium-3 Cryostats. In Frank Pobell, editor, *Matter and Methods at Low Temperatures*, pages 139–147. Springer Berlin Heidelberg, Berlin, Heidelberg, 2007.
(Cited on page 82.)
- [113] Frank Pobell. The ^3He – ^4He Dilution Refrigerator. In Frank Pobell, editor, *Matter and Methods at Low Temperatures*, pages 149–189. Springer Berlin Heidelberg, Berlin, Heidelberg, 2007.
(Cited on page 82.)
- [114] Kitti Ratter. *Epitaxial Rhenium, a clean limit superconductor for superconducting Qbits*. phdthesis, Universit t Grenoble Alpes, October 2017.
(Cited on page 88.)
- [115] B. Huard, H. Pothier, D. Esteve, and K. E. Nagaev. Electron heating in metallic resistors at sub-Kelvin temperature. *Physical Review B*, 76(16):165426, October 2007.
(Cited on page 94.)
- [116] E. H. Rhoderick. *Metal-semiconductor Contacts*. Clarendon Press, 1978.
(Cited on page 102.)
- [117] Raphael B uckle. *Ge-based reconfigurable transistors: a platform enabling negative differential resistance*. Wien, 2021.
(Cited on page 102.)
- [118] N. F. Mott. Note on the contact between a metal and an insulator or semiconductor. *Mathematical Proceedings of the Cambridge Philosophical Society*, 34(4):568–572, 1938. Edition: 2008/10/24 Publisher: Cambridge University Press.
(Cited on page 102.)
- [119] Abraham Many, Yehuda Goldstein, and Norman B. Grover. *Semiconductor Surfaces, by A. Many, Y. Goldstein, and N.B. Grover*. 1965. Google-Books-ID: CeM_cgAACA AJ.
(Cited on page 104.)
- [120] Volker Heine. Electrons at surfaces of solids. *Proc. R. Soc. Lond.*, A331307–320:14, 1972.
(Cited on page 105.)
- [121] C. Y. Nam, D. Tham, and J. E. Fischer. Disorder Effects in Focused-Ion-Beam-Deposited Pt Contacts on GaN Nanowires. *Nano Letters*, 5(10):2029–2033, October 2005.
(Cited on page 108.)
- [122] Tomonori Nishimura, Koji Kita, and Akira Toriumi. Evidence for strong Fermi-level pinning due to metal-induced gap states at metal/germanium interface. *Applied Physics Letters*, 91(12):123123, September 2007.
(Cited on page 109.)

BIBLIOGRAPHY

- [123] Lydia L. Sohn, Leo P. Kouwenhoven, and Gerd SchÅn, editors. *Mesoscopic Electron Transport*. Springer Netherlands, Dordrecht, 1997.
(Cited on page [114](#).)
- [124] Seigo Tarucha, David Guy Austing, Takashi Honda, Rob van der Hage, and Leonardus Petrus Kouwenhoven. Atomic-Like Properties of Semiconductor Quantum Dots. *Japanese Journal of Applied Physics*, 36(Part 1, No. 6B):3917–3923, June 1997.
(Cited on page [120](#).)
- [125] S. Moriyama, T. Fuse, M. Suzuki, Y. Aoyagi, and K. Ishibashi. Four-Electron Shell Structures and an Interacting Two-Electron System in Carbon-Nanotube Quantum Dots. *Physical Review Letters*, 94(18), May 2005.
(Cited on page [120](#).)
- [126] Jing Wang, A. Rahman, G. Klimeck, and M. Lundstrom. Bandstructure and orientation effects in ballistic Si and Ge nanowire FETs. In *IEEE International-Electron Devices Meeting, 2005. IEDM Technical Digest.*, pages 4 pp.–533, December 2005. ISSN: 0163-1918, 2156-017X.
(Cited on page [120](#).)
- [127] S. Ramo, J. R. Whinnery, and T. Van Duzer. *Fields and Waves in Communication Electronics*. Wiley, 1994.
(Cited on page [121](#).)
- [128] Edgar Bonet, Mandar M. Deshmukh, and D. C. Ralph. Solving rate equations for electron tunneling via discrete quantum states. *Physical Review B*, 65(4):045317, January 2002.
(Cited on page [123](#).)
- [129] Florian M Brunbauer, Emmerich Bertagnolli, Johannes Majer, and Alois Lugstein. Electrical transport properties of single-crystal Al nanowires. *Nanotechnology*, 27(38):385704, September 2016.
(Cited on pages [130](#) and [148](#).)
- [130] J. G. Rodrigo, V. Crespo, H. Suderow, S. Vieira, and F. Guinea. Topological Superconducting State of Lead Nanowires in an External Magnetic Field. *Physical Review Letters*, 109(23):237003, December 2012.
(Cited on page [135](#).)
- [131] M F Goffman, C Urbina, H Pothier, J NygÅrd, C M Marcus, and P Krogstrup. Conduction channels of an InAs-Al nanowire Josephson weak link. *New Journal of Physics*, 19(9):092002, September 2017.
(Cited on page [135](#).)
- [132] TÅmea NÅra TÅrÅk, MiklÅs Csontos, PÅlter Makk, and AndrÅs Halbritter. Breaking the Quantum PIN Code of Atomic Synapses. *Nano Letters*, 20(2):1192–1200, February 2020.
(Cited on page [135](#).)

BIBLIOGRAPHY

- [133] Anil Murani. *Superconducting proximity effect in monocrystalline bismuth nanowires*. phdthesis, Universit  Paris Saclay (COMUE), April 2017.
(Cited on pages [140](#) and [141](#).)
- [134] Jovian Delaforce, Masiar Sistani, Roman B. G. Kramer, Minh A. Luong, Nicolas Roch, Walter M. Weber, Martien I. den Hertog, Eric Robin, Cecile Naud, Alois Lugstein, and Olivier Buisson. Al-Ge-Al Nanowire Heterostructure: From Single-Hole Quantum Dot to Josephson Effect. *Advanced Materials*, 33(39):2101989, 2021. [_eprint: https://onlinelibrary.wiley.com/doi/pdf/10.1002/adma.202101989](https://onlinelibrary.wiley.com/doi/pdf/10.1002/adma.202101989).
(Cited on pages [147](#) and [167](#).)
- [135] M. Sistani, J. Delaforce, K. Bharadwaj, M. Luong, J. Nacenta Mendivil, N. Roch, M. den Hertog, R. B. G. Kramer, O. Buisson, A. Lugstein, and C. Naud. Coulomb blockade in monolithic and monocrystalline Al-Ge-Al nanowire heterostructures. *Applied Physics Letters*, 116(1):013105, January 2020.
(Cited on pages [148](#) and [167](#).)
- [136] A P Micolich. What lurks below the last plateau: experimental studies of the $0.7 \frac{e^2}{h}$ conductance anomaly in one-dimensional systems. *Journal of Physics: Condensed Matter*, 23(44):443201, November 2011.
(Cited on page [154](#).)
- [137] Masiar Sistani, Jovian Delaforce, Roman B. G. Kramer, Nicolas Roch, Minh Anh Luong, Martien I. den Hertog, Eric Robin, J ijrgen Smoliner, Jun Yao, Charles M. Lieber, Cecile Naud, Alois Lugstein, and Olivier Buisson. Highly Transparent Contacts to the 1D Hole Gas in Ultrascaled Ge/Si Core/Shell Nanowires. *ACS Nano*, 13(12):14145–14151, December 2019.
(Cited on pages [164](#) and [168](#).)
- [138] Giordano Scappucci, Christoph Kloeffel, Floris A. Zwanenburg, Daniel Loss, Maksym Myronov, Jian-Jun Zhang, Silvano De Franceschi, Georgios Katsaros, and Menno Veldhorst. The germanium quantum information route. *Nature Reviews Materials*, December 2020.
(Cited on page [168](#).)